Room and Elevated Temperature Constitutive Response of Polycrystalline Materials Exhibiting Tension-Compression Asymmetry under Monotonic Loading

by
Dariush Ghaffari Tari

A thesis
presented to the University of Waterloo
in fulfilment of the
thesis requirement for the degree of
Doctor of Philosophy
in
Mechanical Engineering

Waterloo, Ontario, Canada, 2014

This thesis consists of material all of which I authored or co-authored: see Statement of Contributions included in the thesis. This is a true copy of the thesis, including any required final revisions, as accepted by my examiners.

I understand that my thesis may be made electronically available to the public.

Dariush Ghaffari Tari

STATEMENT OF CONTRIBUTIONS

The following co-authors have contributed to the current work;

Professor Michael Worswick supervised this PhD thesis.

Dr. Sooky Winkler assisted the author with optical microscopy and interpretation of microscopy images.

Mr. Usman Ali assisted the author in developing the Matlab optimization code and investigation of optimization algorithms within Matlab.

Dr. Michael Gharghouri performed texture measurements on AZ31B-O material specimens using the Neutron Diffraction Scattering method at AECL; furthermore, he assisted the authors in proof reading parts of this work.

The balance of the research is my own work.

ABSTRACT

A continuum plasticity yield function is developed that captures tension/compression asymmetry and its evolution as exhibited by HCP materials such as magnesium alloy sheet. The model, referred to herein as “CPB06ex3ev”, is based upon the CPB06 [1] yield surface which is extended in this research to consider evolution of asymmetry and anisotropy under monotonic loading. The model is further modified to incorporate thermal softening and strain rate effects.

Mechanical characterization experiments are performed to acquire uniaxial tensile and compressive stress-strain data along a range of in-plane and through-thickness loading orientations. Experiments are performed for a range of strain rates (0.001-1s^{-1}) and temperatures (23-250°C). A strong, evolving asymmetry is observed at room temperature when comparing tensile and compressive flow stresses and *r*-values, while asymmetry and anisotropy are reduced dramatically as temperature is increased. AZ31B exhibits moderate strain rate sensitivity at room temperature, however, the rate sensitivity increases with temperature.

The CPB06ex3ev model is applied to simulate AZ31B magnesium alloy sheet. An error minimization scheme is used to fit the yield function and evolution coefficients over the entire data set. The calibrated model is shown to capture the evolving asymmetric/anisotropic response of both flow stresses and *r*-values in tension and compression, while also fitting the flow stress at the biaxial tension and pure shear locations on the yield locus. The model, which uses three stress transformations, is implemented within a user defined material model (UMAT) and linked to the commercial finite element software LS-DYNA.

In order to assess the finite element implementation of the CPB06ex3ev model, a series of validation experiments were performed and corresponding finite element models were developed: (i) room temperature three-point bending; (ii) elevated temperature (250°C) limiting dome height experiments; and, (iii) warm cup drawing experiments. The three point bend simulations demonstrated the importance of capturing material asymmetry and the associated shift in neutral axis. Comparison between the warm forming experiments and models revealed qualitative agreement between the predicted punch load-displacement and strain distributions. The CPB06ex3ev formulation was able to capture the anisotropy trends in terms of the differences in strains measured along the sheet rolling versus transverse directions.

Beyond the constitutive characterization and modeling effort, the cup draw formability experiments have provided interesting insight into the effect of temperature and temperature distribution within the AZ31B sheet. The current work has served to show the existence of a process window in which the blank center temperature must lie below the die temperature but above the temperature for activation of non-basal slip systems (to avoid low temperature fracture). Two modes of failure have been identified at the process window boundaries in which the cup either fractures due to low temperature (brittle) failure or a high temperature (necking) failure.

ACKNOWLEDGEMENTS

I would like to thank my advisor Prof. Michael Worswick for giving me such a life-changing opportunity. I am grateful for his patience; wisdom and mentorship through the years which helped me develop myself not just to a better scientist but also to a better person.

None of this could be possible if it was not because of my caring parents who devoted their lives to the well-being of their children. Their unconditional support and love has enabled me to dream high and challenge myself. I would like to thank my dear sisters for all their love, care and encouragements.

This research was carried out under the framework of the Research Program of the Magnesium Network (MagNET), Canada. Financial support from MagNET, the Natural Sciences and Engineering Research Council (NSERC), the Canada Research Chairs Secretariat and the Ontario Research Fund is gratefully acknowledged.

I would like to use this opportunity to thank Prof. Poole of UBC whose leadership provided this amazing experience for me and many other young researchers. I would like to thank Prof. Hamid Jahed and Prof. Mahmoud Farzin whose teachings have been my guide throughout this work, Dr. Sooky Winkler for introducing me to the world of metallography. I appreciate the opportunities that Prof. Greg Glinka provided me to learn from him. I thank Elmar Beeh from German Aerospace center (DLR) who graciously hosted me to learn from his team. Many thanks to Dr. Michael Gharghouri from Neutron beam center at Chalk river laboratories for his helpful comments on my work and for helping me with generating the pole figures. The advice and helpful comments from my colleagues in the University of Waterloo are highly appreciated, especially Dr. Srihari Kurukuri, Reza Bagheriasl, Kamyar Ghavam, Jon Rossiter, Usman Ali, Jose Imbert, Alex Bardelcik and Dan Hasenpouth. I would like to thank Eckhard Budziarek, Tom Gawel, Andy Barber, Mark Kuntz, Richard Forgett, and Mark Griffet at the University of Waterloo for their experimental support. I also would like to thank Laurie Wilfong and Debbie Burgess for all their help, patience, and administrative support.

To my dear father and mother

TABLE OF CONTENTS

LIST OF FIGURES

Synopsis

1. Introduction

The application of lightweight materials in the automotive industry can help to improve fuel economy and reduce emissions. Among the different candidates to replace mild steel, magnesium alloys have a high strength-to-density ratio which makes them a good alternative to the currently used steel and aluminum alloys [2].

The first use of magnesium alloys in the automotive industry dates back to the Second World War era [3]. However, at present the application of magnesium alloys is mostly limited to extruded parts and castings [4]. Unfortunately, magnesium alloys have a limited deformation capability at room temperature. The formability improves at higher temperatures; however, warm forming requires more complex tooling setup which increases the cost of the forming operation. A warm formed magnesium part has the potential to reduce the weight of vehicle structural members, but there is currently little published work on the mechanical response of magnesium alloys under different load path, temperature and strain rate conditions. Moreover, there exists an ongoing effort to develop new material models that capture the complex mechanical response observed from magnesium alloys.

The general goal of the proposed research is to support the application of magnesium alloys in the automotive industry by improving understanding of the deformation characteristics of magnesium alloys at room and elevated temperatures. In particular, characterization of the AZ31B deformation response, development of a continuum based material model considering tension/compression asymmetry and validating these models based on forming experiments performed at elevated temperatures are the goals of the proposed research.

This thesis has been written in a “manuscript-based” style which consists of four parts. First part comprises this synopsis of the thesis research containing major results, discussion and overall conclusions. Appendices A, B and C are three published or submitted peer-reviewed manuscripts which contain greater detail documenting each aspect of the research. This synopsis comprises a review of the current state of the art in characterization of the mechanical behavior and continuum-based modelling of asymmetric materials, focusing specifically on magnesium alloy sheet. A statement of the objectives of this research is then provided, followed by a summary of the research results, discussion, and the major conclusions and future work. Appendix A documents work done on warm deep draw behavior of magnesium alloy sheet. Appendices B and C present the constitutive characterization studies and models for room and elevated temperatures, respectively.

2. Literature Review

2.1. Magnesium Alloys

Magnesium, with a density of 1.73 g/cm^3 is a good potential candidate to fabricate lighter structures. Moreover, magnesium alloys have a high strength-to-weight ratio and display good castability, machinability and good magnetic resistance properties [2].

On the other hand, low formability at room temperature and limited corrosion resistance are the key issues that limit the application of magnesium, particularly for automotive applications. The use of formed parts, especially sheet metal products, is limited due to the low ductility of magnesium at room temperature. A significant tension-compression asymmetry in the material behaviour has been reported for wrought magnesium alloys under tension and compression modes of deformation [5]. This observed asymmetry is due to the Hexagonal Closed Packed (HCP) structure and twinning behaviour of magnesium alloys [6]. In addition to common slip deformation systems which are active at room temperature, an additional deformation system, namely twining, is active. Additional slip systems become active at elevated temperatures which improves the formability to a great extent [7]. The slip systems of a hexagonal closed packed crystal unit are illustrated in Figure 1. The basal slip system is illustrated at (a) in the plane {0001}. The prismatic slip system is illustrated at (b). The pyramidal slip system is hard to activate at room temperature due to a high critical resolved shear stress (CRSS) [8].

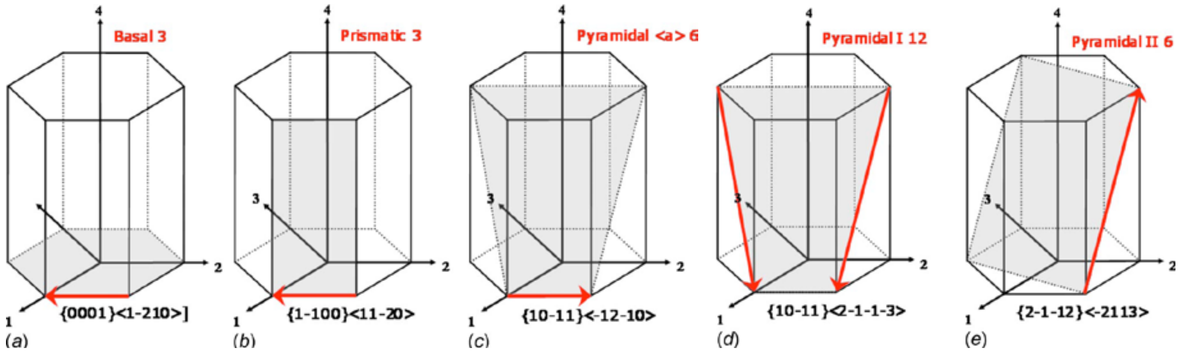

Figure 1. Slip system families in hexagonal structures, a) basal, b) prismatic <a>, c) pyramidal <a> d) pyramidal<c+a>/I and e) pyramidal <c+a>/II [9].

2.2. Metallurgy and Microstructure

At room temperature, mainly basal and prismatic slip systems are active. These deformation mechanisms do not fulfill the Taylor criterion which states that five independent deformation mechanisms are required for homogeneous deformation of a polycrystalline aggregate [10]. Twinning is the other deformation mechanism that helps satisfy the Taylor criterion for hexagonal materials [11]; however, the amount of strain accommodated by twinning is limited which is the source of limited ductility at room temperature [5].

Wrought magnesium alloy sheets are known to have a strong basal texture, which indicates that the *c*-axes of the crystals are predominately oriented normal to the sheet surface [6]. A weaker basal texture improves formability as more <*a*> slip, systems are activated [12]. The anisotropy observed in wrought magnesium sheets is mainly due to the initial texture retained from previous rolling operations. Pole figure studies along the (0 0 0 2) axis suggests a slight off-basal shift of the c-axes toward the rolling direction [12] which creates the in-plane anisotropic behaviour of wrought magnesium. This tilt of basal planes towards the rolling direction favours basal slip over non-basal prismatic slip and leads to a lower *r*-value along the rolling direction [12]. The strong anisotropy observed at room temperature reduces as temperature increases. The activation of non-basal <*c*+*a*> slip systems explains the observed changes in the anisotropy coefficients when the temperature is increased [14].

The texture evolution in magnesium alloy AZ31B at elevated temperature under a compressive deformation was investigated by Jiang et al. [15]. It was concluded that non-basal <*c*+*a*> slip gains more importance when a sample is deformed beyond a strain of 0.2 since twinning deformation systems become saturated.

Jain and Agnew [16] performed compression tests under a wide range of temperature varying from 22-250˚C. The onset of yield was reported to be insensitive to temperature which suggests that a temperature independent deformation mechanism is active during yielding. In addition, a very low *r*-value was measured which is known to be a signature of twinning. Rapid work hardening observed at room temperature during deformation leads to high stresses which ultimately caused strain instability and crack initiation [5].

2.3. Mechanical characterization of magnesium alloys

Understanding material behaviour is of great importance in engineering design and manufacturing. The choice of material for a component depends on the expected properties and the required function. To understand and predict material behaviour under different deformation conditions, a number of standard tests are recommended. For understanding forming operations performed in multiple stages, material tests involving loading and unloading modes are needed [17].

The uniaxial monotonic tensile test is a standard material test performed to define the flow stress of the material under deformation. Compression tests are suggested for cases where the material response in tension and compression is not the same. Compression tests performed on magnesium alloy AZ31 show that the asymmetry of the material at higher temperatures reduces. The strain rate sensitivity increases with the temperature change and it also affects the asymmetry [18].

Khan et al. [19] characterized AZ31B alloy at temperatures between room temperature and 150˚C. Texture measurements were performed on the as-received samples as well as deformed specimens. The texture intensity strengthened after tensile tests along the rolling direction, even at low strain rates.

Lou et al. [5] used an experiment setup proposed by Boger et al. [20] to test tension followed by compression and compression followed by tension loading conditions (Figure 2). The asymmetry of AZ31 magnesium alloy is seen in the figures. A transition region due to untwining activity was observed after the change from the compression to tension mode. In the same two figures, different modes of deformation such as slip, twin and untwin can be recognised from the mechanical behaviour when loading and unloading is applied. The activity of different deformation mechanisms in the stress-strain curves are in agreement with the volume fraction of twins measured from microscopy images [5]. Piao et al. [18, 19] extended this study to high temperature and considered twinning-de-twinning under reversed loading; it was found that the de-twinning transition region from compression to tension was suppressed at temperatures higher than 150°C.

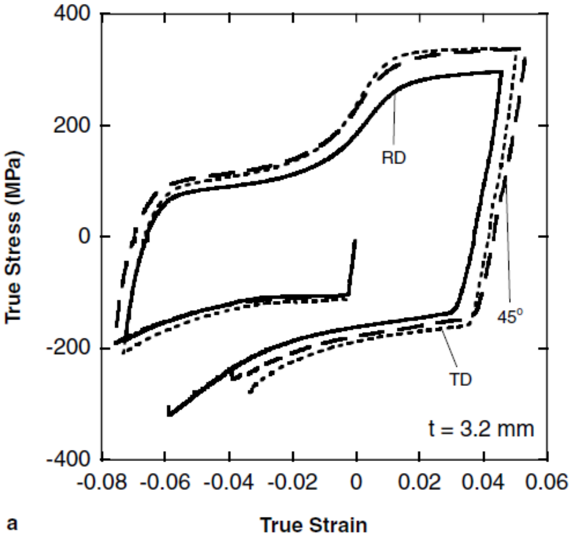

Figure 2. Single-cycle strain hardening cycle C-T-C true strain-true stress curves [5].

In another study by Naka et al. [21] the effect of strain rate, temperature and sheet thickness on the shape and the size of the AZ31B yield surface was investigated using a cruciform sample. In this study three strain rate levels were considered for the test (10^{-2}, 10^{-3}, and 10^{-4} s^{-1}). The size of the yield surface decreases with increasing temperature and increases as higher strain rates were considered. Geiger et al. [22] investigated the effect of temperature on the yielding and hardening behaviour of magnesium alloy AZ31. It was reported that the shape of the yield locus changes due to the temperature variation. The distance between the flow stresses of the subsequent strain levels is also temperature dependent, which demonstrates that this magnesium alloy hardens in an anisotropic manner (Figure 3).

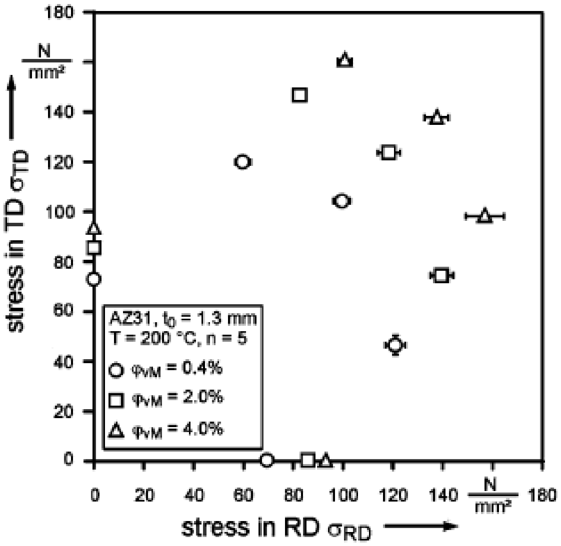

Figure 3. Initial and subsequent yielding of AZ31 magnesium alloy at 200˚C. Circle, rectangle and triangle represent strain at 0.4%, 2.0% and 4.0% correspondingly [22].

The difference between *r*-values in different orientations is a measure of the plastic anisotropy of sheet metals. The *r*-value in the transverse direction is reported to be much higher than along the rolling direction for room temperature measurements. It is observed that both cumulative and instantaneous r-values tend to increase as the plastic strain increases [5]. As temperature increases, pyramidal slip systems are activated which affect the stress anisotropy and resulting *r*-values. The effect of temperature on *r*-value is shown in Figure 4. The difference between the measured *r*-values along different orientations becomes smaller as the temperature increases [14].

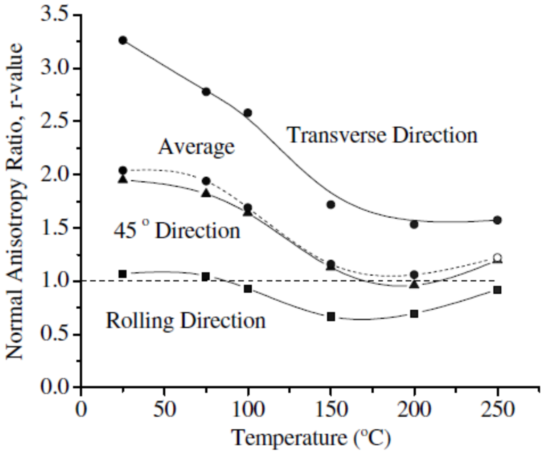

Figure 4. Normal anisotropy as a function of temperature and sample orientation [14].

2.4. Material models

The complicated mechanical response of hexagonal closed packed (HCP) structured materials, including magnesium alloys, has made the development of accurate material models difficult. Different approaches ranging from continuum based models to crystal plasticity models have been proposed to model the anisotropy and asymmetry of HCP materials. In this section, several models proposed for HCP materials and especially magnesium alloys are discussed. However, the focus of this research is mainly on phenomenological material models since this approach is more appealing for sheet metal forming analysis, particularly for large-scale components.

2.4.1. Continuum-based approaches

Continuum-based constitutive models usually consist of a state and an evolution equation. The state equation describes the relationship between the strain, stress, strain rate, temperature and other state variables, whereas the evolution equation represents the development of the microstructure throughout the deformation [23]. A continuum-scale plasticity model, for a multiaxial stress space, is well-described with a yield surface, a flow rule and a hardening law [24]. Due to the complex mechanical response of magnesium alloys, modeling efforts represent a daunting task. Earlier continuum-based models, such as von Mises [25], Hill [26], Barlat et al. [27] and [28], for example, are more appropriate for BCC and FCC material structures for which slip is the primary deformation mechanism. Continuum-level models for HCP materials are less well developed, one noteworthy exception being Cazacu-Plunkett-Barlat-type yield surfaces (CPB) which model the asymmetric response of HCP structured materials. Cazacu and Barlat [29] generalized Drucker's isotropic yield surface model [30] to orthotropy by introducing anisotropy coefficients into the model. Later Cazacu and Barlat [31] generalized this model to orthotropy by replacing J_2 and J_3 by J_2° and J_3° which introduces more flexibility to this yield surface by introducing anisotropy coefficients into the model.

Twinning is a directional deformation mechanism which depends on the sign of the stress. Therefore, in HCP materials a yield asymmetry is observed which is impossible to capture using FCC- and BCC-based material models. Therefore, Cazacu and Barlat [32] modified the constant "c" of Drucker's isotropic yield criterion to create an asymmetric yield surface; "c" is found from the following relation in terms of uniaxial tensile and compression yield stresses. The effect of parameter "c" on the shape of the yield surface is shown in Figure 5.

$$c = \frac{3\sqrt{3}({\sigma_t}^3 - {\sigma_c}^3)}{({\sigma_t}^3 + {\sigma_c}^3)} \tag{2.2}$$

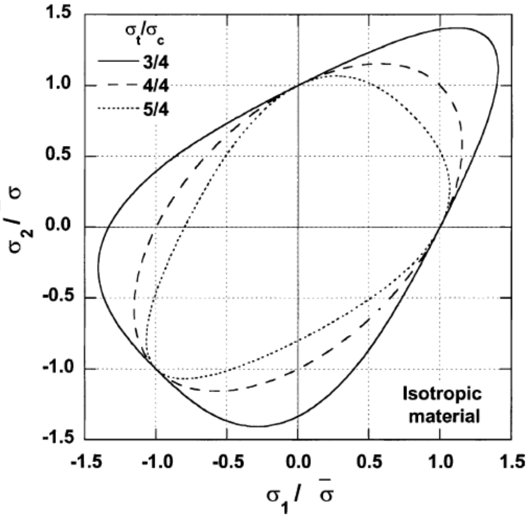

Figure 5. Plane stress yield loci corresponding to σ_t/σ_c =3/4, 4/4 (Von Mises), 5/4 (Cazacu and Barlat [33]).

In order to fit the experimental yield data available for pure magnesium and its alloys, the stress components of the asymmetric yield surface were transformed to generate the anisotropy of the material. The fitting and the corresponding experiments are shown in Figure 6. In order to improve the prediction of strain distribution in sheet metal forming operations, not only shall the experimental flow curves be fitted but also the slope of the yield surface and its evolution should be taken into account (Banabic, [34]).

Cazacu et al. [1] proposed a new non quadratic yield surface to account for the asymmetry of HCP materials. This function is homogeneous of degree "*a*" in stress.

$$(|S_1| - kS_1)^a + (|S_2| - kS_2)^a + (|S_3| - kS_3)^a = F \tag{2.3}$$

where S_i, *i*=1, 2, 3 are the principle values of the stress deviator and "*a*" is a positive integer. *F* gives the size of the yield surface and can change with the accumulated strain. The constant *k* is a parameter that introduces tension-compression yield strength asymmetry in the model and is written based on tension to compression yield strength ratio as follows;

$$\frac{\sigma_T}{\sigma_C} = \left\{ \frac{\left(\frac{2}{3}.(1+k)\right)^a + 2.\left(\frac{1}{3}.(1-k)\right)^a}{\left(\frac{2}{3}.(1-k)\right)^a + 2.\left(\frac{1}{3}.(1+k)\right)^a} \right\}^{\frac{1}{a}} \tag{2.4}$$

This yield function was later extended to orthotropy, using a linear stress transformation on the stress deviator *S*. The test results for pure magnesium at different strain levels were successfully fit using this yield surface as shown in Figure 6.

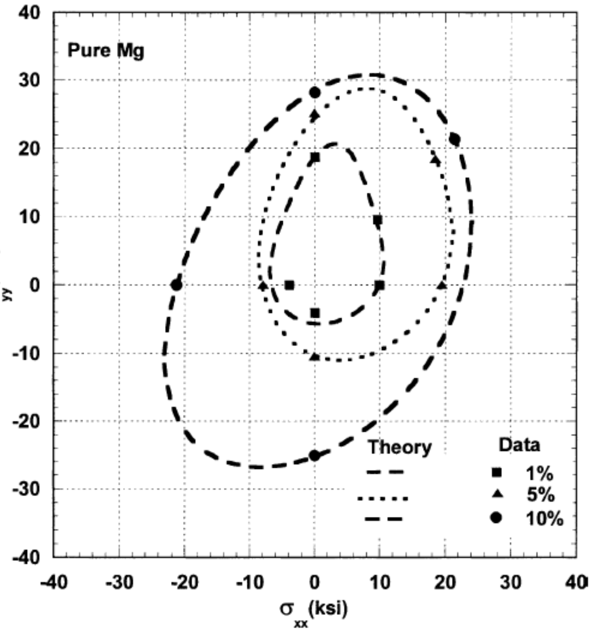

Figure 6. Comparison between the plane stress yield loci for a pure magnesium sheet predicted by Cazacu and Barlat [33] yield surface and experiments (Data after Kelly and Hosford, [6])

The principal values of deviatoric stresses are substituted by the principal values of the transformed stress as found from the following.

$$\Sigma = C[S] \tag{2.5}$$

Where C is a fourth order tensor which includes the anisotropy coefficients; thus, the yield function transforms into

$$(|\Sigma_1| - k\Sigma_1)^a + (|\Sigma_2| - k\Sigma_2)^a + (|\Sigma_3| - k\Sigma_3)^a = F \tag{2.6}$$

In order to satisfy the orthotropy condition and the major and minor symmetries, 9 independent coefficients are needed for a 3D stress state. Plunkett et al. [35] proved that the accuracy in the description of flow stresses and r-values at tension and compression increases if more than one stress transformation is performed on the principle deviatoric stresses. However finding the anisotropic coefficients requires a number of material tests that are not always easy to perform.

Ertürk et al. [38, 39] modified the Cazacu (2004) yield function to account for the evolution of the yield surface based on the plastic strain. The effect of temperature and strain rate was also considered to predict the flow stress. This model was applied to simulate the extrusion of magnesium alloy. Nebebe Metoken et al. [40, 41] modified the same material model to account for the effect of plastic strain on the evolution of *r*-values.

The shape of the yield surface changes with plastic strain due to twinning. This phenomenon cannot be modeled by traditional isotropic hardening models since isotropic hardening is only valid for monotonic loading along a constant strain path under the assumption that every strain path hardens at the same rate. This assumption is valid for FCC and BCC materials; however, Geiger et al. [22] proved that this is not true for HCP materials. Plunkett et al. [36] proposed a macroscopic model to capture the evolution of the anisotropy coefficients due to the texture development under monotonic loading. A combination of the experimental data and simulations with the visco-plastic self-consistent (VPSC) model (Lebensohn and Tome [37]) were used to calibrate the proposed macroscopic model. In this model, anisotropic hardening associated with strain path changes and the Bauschinger effect were neglected. Finding an analytical relation for the evolution of the anisotropy parameters is not a straight forward task, thus a linear interpolation between the independent anisotropic coefficients related to different levels of accumulated strain was considered. A considerable improvement in the predicted strain distribution for a three point bending problem was reported.

A three point bending process was modeled by Kim et al. [38] using the asymmetric Cazacu 2006 yield surface. Two separate isotropic hardening rules were considered for thinning and thickening load paths. The sum of the principal strain increments was used to determine the loading mode between tension and compression. Improvements in the prediction of punch force versus displacement were reported using this anisotropic hardening method [38].

Lee et al. [39] proposed a two-surface plasticity model based on the Cazacu 2004 [33] yield surface to capture the anisotropic and asymmetric hardening behaviour of AZ31 magnesium alloy sheet. The proposed model is in good agreement with the results of uniaxial tension/compression and compression/tension tests. To verify this model under a more complicated loading condition, cylindrical bending and draw bending processes were analysed. The simulation results were compared to the corresponding experiments and a good spring back prediction capability was reported compared to the previous models [40].

A modified non-linear kinematic hardening model was proposed by Li et al. [41] who proposed a texture-dependent movement of the yield surface. To create a strength difference between tension and compression, a constant non-zero back stress was used. Slip, twin and un-twin deformation modes were considered to control the back stress. Although choosing an anisotropic yield surface was recommended for a better representation of the deformation, the scope of this study was limited to an isotropic von Mises yield surface. The adaptation of a more complex anisotropic yield surface along with the general evolution of the yield surface was suggested to be a daunting proposition due to the complexity it may introduce.

2.4.2. Crystal plasticity based approaches

In this review, a brief coverage of literature on the crystal plasticity approach as applied to simulate magnesium alloys is considered. Simulation and analysis of metal forming operations using direct implementation of crystal plasticity approaches is limited due to the higher computational cost of the analysis.

Lévesque et al. [42] proposed a rate-dependent material model for AM30 magnesium alloy assuming primary slip and twin as the active deformation mechanisms during plastic deformation. Stress-strain curves, as well as texture evolution, of AM30 alloy were predicted for a number of loading paths.

A visco-plastic self-consistent anisotropic approach (VPSC) for the simulation of plastic deformation and texture development of polycrystals was proposed by Lebensohn and Tomé [37]. The main assumption of this model is that each grain can be treated as an inhomogeneity embedded in the homogeneous effective medium represented by the polycrystal. The Lankford coefficients and polycrystal yield loci were predicted by this method and compared to the experiments. A crystal plasticity model considering twinning and detwinning deformation mechanisms was proposed by Wang et al. [49, 50].

In an attempt to predict the yield loci for an FCC material using a polycrystal plasticity approach, Kalidindi [43] applied a Taylor averaging scheme for modelling the constitutive behaviour of polycrystal aggregates. A novel assumption considered in this study was the evolution of the slip anisotropy which proved to have a more significant role on the results than was expected.

Tang [44] developed a rate-independent crystal plasticity code for hexagonal closed packed material and incorporated the twinning deformation mechanism. The same model was used to analyse a deep drawing process and compared to the result of simulations using the viscoplastic self-consistent model (VPSC). Izadbakhsh et al. [45] introduced a new rate dependent elastic-viscoplastic crystal plasticity material model for a single crystal of magnesium alloy. In this work, different deformation mechanisms of magnesium alloys including initial, secondary and tertiary slip systems, as well as primary and secondary twin systems, were considered.

2.5. Metal forming and formability

As mentioned in previous sections, the lack of formability is the most important reason for the use of Mg alloys in the automotive industry being mostly limited to parts produced by casting processes [4]; however, warm forming has been proposed as a way to improve the formability of magnesium alloys [46]. Some studies have been conducted on sheet metal forming of magnesium alloy AZ31 at room temperature. The high anisotropy of Mg at room temperature restricts the obtained Limit Draw Ratio (LDR) [47], although optimization of annealing conditions can improve formability [48]. An investigation of the effect of the tooling geometry on formability shows that the corner radius of the tooling exhibits a prominent role on the fracture of magnesium cups at room temperature. In order to improve formability of magnesium, new slip systems should be activated. At elevated temperatures, pyramidal $<c+a>$ slip systems are active, which improve formability to a large extent [5]. The effect of the forming temperature on Limit Drawing Ratio (LDR) of AZ31 alloy was investigated by Zhang et al. [46]. The range of temperature considered in this study was between 105-170˚C. It was reported that at a forming temperature of 40˚C, the maximum LDR recorded could not exceed 2; however, this ratio was increased to 2.7 as the temperature reached 170˚C. Reduced formability was reported in the case of excessive heating periods. The best formability for AZ31 magnesium alloy was reported at temperatures close to 250˚C [49]. It was suggested that dynamic recrystallization at this temperature range improves formability. In contrast, lower formability was observed at temperatures close to 400˚C due to localized necking within the parts (Figure 7). This trend is in agreement with the reported drop of hardening exponent of the material within the 400˚C range of temperature. A brittle fracture occurred at the flat portion of the punch when forming at low temperatures was attempted.

Figure 7. Square cups formed at each forming temperature [49].

Chen et al. [50] obtained forming limit diagrams at three temperature levels and concluded that the optimum forming temperature varies with sheet thickness and forming geometry. The effect of punch and die radius on the drawn depth of the part was investigated and it was concluded that although increase in punch radius always leads to formability improvement, an excessive increase of the die radius could have a reverse effect on it.

The effect of non-isothermal forming of magnesium and aluminum alloys was investigated by Kaya [51]. The experiments were performed to determine the effect of constant and variable punch velocities. Less thickness reduction was reported in case where a variable punch speed was considered for forming. Palumbo et al. [52] investigated the effect of a thermal gradient between the blank centre, in contact with the punch, and the blank flange. It was concluded that a cold punch can improve formability in cases where the flange temperature is kept close to 230˚C. On the contrary, a cold punch reduces formability if the flange region is kept at less than 180˚C. A maximum LDR of 3.37 was obtained when the blank holder was kept at 230˚C. At lower flange temperatures, the process is more sensitive to the punch speed. Similar results were reported by Palaniswamy et al. [53]. This study also modeled the process using a temperature dependent material model which implemented the von Mises yield surface. In comparison to experiments, more thinning at the cup walls and less thickening at the flange region were predicted by the finite element simulation. This suggests that the use of an isotropic yield surface for modeling of magnesium alloys could overestimate the yield stress in the flange region.

Ambrogio et al. [54] characterized the formability of AZ31 magnesium alloy at different temperatures, strain rates and orientations. The formability of magnesium increases as temperature is elevated and reduces as punch speed is increased.

An FLD-based formability criterion was used by Choi [55] in a finite element simulation of a cross-shaped deep drawing process. It was concluded that the prediction of failure by an FLD, in a case where the effect of both temperature and strain path is considered, is more accurate and is in agreement with the experiments.

2.6. Current Deficit in the Literature

In spite of extensive research on magnesium alloys in recent years, there is still limited material characterization data available in the literature, especially that information which is required to model warm forming processes. Due to the asymmetric material behaviour of magnesium alloys, even at elevated temperatures, both tension and compression material characterization should be done; however, performing compression tests on wrought sheet material at elevated temperature is extremely difficult (Kuwabara et al. [17] and Piao et al. [56]) and requires specialized equipment and development of new testing procedures. Cazacu et al. [30, 36] have proposed a material model that captures both asymmetry and anisotropy of HCP material; however, these models have not been implemented for modeling warm forming processes of magnesium alloys. Furthermore, effective strategies to evolve asymmetric yield criteria to account for changes in tension/compression asymmetry and anisotropy with deformation have yet to be developed. Most of the work presented on modeling of magnesium warm forming still uses symmetric yield surfaces and does not use proper hardening models to represent the temperature and strain rate dependency of magnesium at elevated temperatures [40, 38 and 46]. Forming experiments have been performed by different research groups [51, 52 and 53]; however, the effect of temperature gradient on forming behaviour and investigation of different failure modes during warm forming is still to be addressed.

3. Research objectives

The overall objective of this research project is the development of a rate- and temperature-sensitive continuum-level plasticity material model that captures evolving tension/compression asymmetry and anisotropy. A targeted application of this model will be the simulation of the room temperature and warm forming behavior of a magnesium alloy, AZ31B-O. Three primary objectives were defined for this work:

1- Characterize the mechanical behavior of AZ31B magnesium alloy sheet at room and elevated temperatures under different strain rates and loading conditions;
2- Develop a continuum-based material model capturing evolving tension/compression asymmetry and anisotropy and the effect of temperature and strain rate on the material response;
3- Assess the predictive capability of the model through comparison with experiments, including three-point bending, warm limiting dome height tests and warm deep drawing experiments.

An overarching goal of this work is the development of a material model suitable for use in finite element simulation of room temperature and elevated temperature deformation of materials exhibiting tension-compression asymmetry. To this end, the material model has been implemented as a user-defined material subroutine linked to the finite element code, LS-DYNA, which is commonly used in the automotive industry to simulate metal stamping and automotive crash events. The results of the material characterization efforts have been used to develop input parameters and the model has been validated through simulation of a series of metal forming experiments.

4. Research Results

This thesis is organized into several parts. Within this synopsis, an overview of the research results and key findings is provided. Greater detail concerning the research methodology and results is provided Appendices A, B and C, each of which is a separate peer-reviewed article, either published or submitted for publication, as summarized below:

Appendix A	D. Ghaffari Tari, M.J. Worswick, S. Winkler, *Experimental studies of deep drawing of AZ31B magnesium alloy sheet under various thermal conditions,* Journal of Materials processing technology 213, 1337-1347.
Appendix B	D. Ghaffari Tari, M.J. Worswick, U. Ali, M., Gharghouri, *Mechanical response of AZ31B magnesium alloy Experimental characterization and material modeling considering proportional loading at room temperature,* International Journal of Plasticity 55, 247-267.
Appendix C	D. Ghaffari Tari, M.J. Worswick, *Material characterization and metal forming simulations of magnesium alloys at elevated temperatures using an evolving envelope of subsequent yield surfaces approach,* Journal of Materials Processing Technology (submitted).

A number of tasks were undertaken to address the objectives defined for this research. At the start of the research, a series of warm deep drawing experiments were undertaken to characterize the warm drawability of AZ31B under non-isothermal conditions. This work served to establish the thermal conditions under which AZ31B could be deep drawn successfully and identify the temperature range of interest for the material constitutive characterization and model development efforts. In addition, data acquired from the warm deep drawing experiments (load-displacement response and measured strains) served to validate the developed material models. Much of the deep drawing research is summarized in Section 4.1, with additional detail provided in Appendix A.

Detailed mechanical characterization of the subject material, AZ31B, was performed at room and elevated temperatures and over a range of strain rates. This work comprised uniaxial tensile and compressive testing along various in-plane sheet orientations (with respect to material rolling direction) and through-thickness compressive testing. This characterization work was useful to focus the material model development effort, establishing the expected range of material response over conditions ranging from room temperature deformation to warm forming. The room temperature characterization results are Section 4.2 and in Appendix B. Section 4.2 and Appendix B also describe the development of a material model capturing evolving asymmetry, as well as validation of the model through simulation of the three-point bending experiment. The elevated temperature characterization efforts and the extension of the constitutive model to include thermal softening and rate sensitivity are summarized in Section 4.3 and further detailed in Appendix C. This part of the research also includes validation of the model against elevated temperature deep draw experiments (from Section 4.1 and Appendix A), as well as warm limiting dome height experiments performed as part of this research.

In addition to the three papers incorporated as Appendices A, B and C of this thesis, a number of additional peer-reviewed articles further document the outcomes of this research. These are listed in Appendix D.

4.1. Experimental studies of deep drawing of AZ31B magnesium alloy sheet under various thermal conditions

This section summarizes the experiments on the warm forming response of the AZ31B-O sheet; additional detail is provided in Appendix A. Deep drawing experiments were performed on 200 and 225 mm blanks using a 100 mm punch (Figure 8) to characterize the effect of forming temperature on the drawability of this alloy, in particular, considering the benefits of non-isothermal conditions in which the punch temperature is lower than the die temperature. The effects of different process parameters such as forming temperature, temperature difference between the punch and dies, as well as punch speed are investigated.

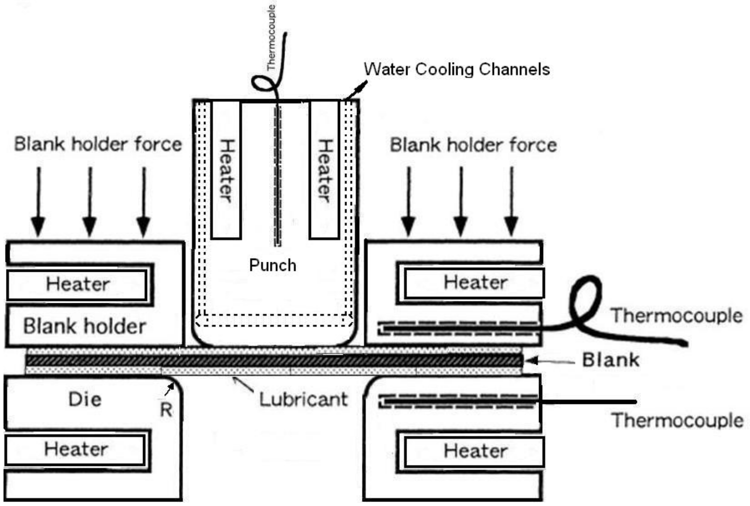

Figure 8. Deep drawing experimental setup schematic.

In order to have an independent control over the temperature within each of the tooling components (punch, die, and blank holder), three separate controllers for the heating system are used. In addition, an optional water cooling system is available for the punch for cases in which lower punch temperatures are required. In contrast to previous research done on warm formability of magnesium [52], the separate heating/cooling system embedded in the punch allows consideration of a wider range of temperature gradient within the blank ranging from near-isothermal conditions to conditions associated with large differences between the punch and die temperatures. This experimental configuration enables determination of the temperature process window for more optimal deep drawing of magnesium alloy sheet. Four different temperature levels (200, 225, 245 and 295˚C) are used for the die and blank holder and the punch temperature was varied in the range 20-295˚C to investigate the effect of temperature difference between the punch and dies. The effect of punch speed on forming forces, strain and thickness distribution within the formed cup is investigated. Finally, the fracture surfaces of the failed cups, formed under isothermal and non-isothermal conditions, are investigated using scanning electron microscopy (SEM) and optical microscopy.

1.57mm thick AZ31B magnesium alloy sheet in the O-temper condition is considered. Of particular interest is the potential for non-isothermal forming to improve the formability of magnesium alloy sheet. In general, non-isothermal processes introduce the benefit of softening the warmer flange region [57] to make flow into the die cavity easier while maintaining a lower temperature at the punch nose to increase the strength of the cup in this region, thereby suppressing fracture. A critical aspect of magnesium formability is to limit the temperature reduction at the punch nose since magnesium becomes brittle if the temperature drops too low. Figure 9a shows an early fracture due to low punch temperature and poor ductility while Figure 9c shows the failure at near-isothermal conditions. The fully drawn cup in the middle is formed at 60˚C temperature difference between the center of the blank (at 160°C) and the flange region (at 225°C), representing a more favorable thermal condition with improved draw depth. Note that the acronym DR in Figure 9 is referring to the draw ratio or the ratio between the cup to the initial blank diameter.

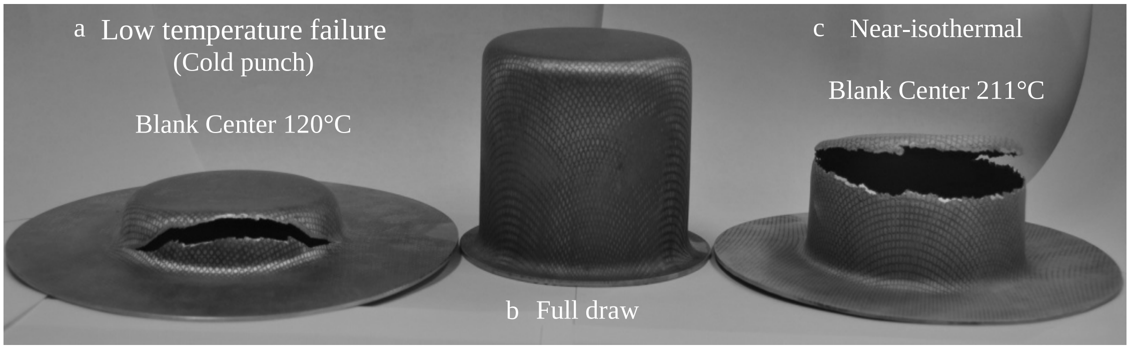

Figure 9. Different failure conditions due to the temperature effects with die and blank holder temperature of 225˚C, punch speed of 4mm/s, blank holder force of 80kN and DR of 2.25. (a) Failure due to low punch temperature and poor ductility. (b) A full draw. (c) Failure due to a low temperature gradient within the cup (Near-isothermal condition).

Figure 10 shows the punch force versus displacement curves for three forming cases with low, medium and high blank center temperature, all formed at a die temperature of 225˚C. Failure occurs in the two experiments with the most extreme thermal conditions, namely the low temperature (cold punch) and the high temperature near-isothermal condition. The intermediate punch temperature case formed fully (see Figure 9b). The failure types corresponding to these thermal conditions are termed “low temperature failure” and “failure at high temperature”.

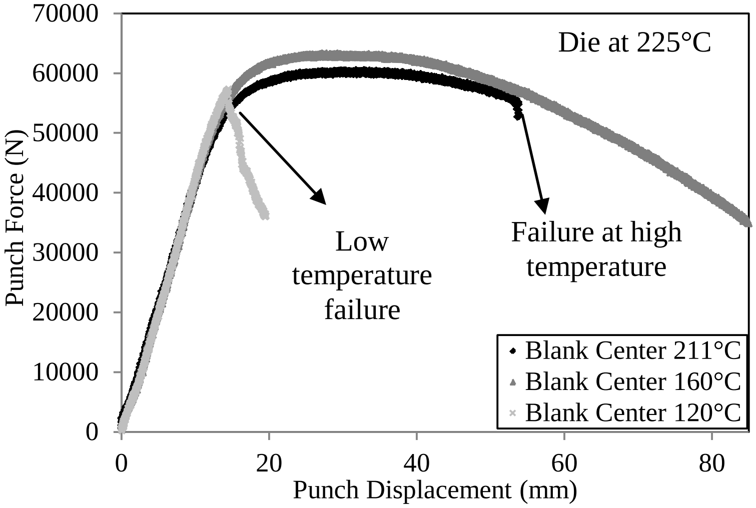

Figure 10. Punch force versus displacement of AZ31B-O at different temperature gradients, die and blank holder kept at 225˚C, with punch speed of 4mm/s, 80kN blank holder force, DR of 2.25 and 2 minutes wait time.

Close examination of the surfaces of the cups formed at conditions close to cold punch and near-isothermal conditions reveals incipient failure for both temperature conditions since both exhibit small surface cracks in the punch radius region (see Figure 11). The figure on the left corresponds to the low temperature case (blank temperature = 120˚C) and incipient cracking is evident, although with relatively low surface strains. For the higher temperature case on the right (blank temperature = 217˚C), the strains are much higher and crack initiation appears to occur at grain boundaries that are manifest on the cup surface. More optimum temperature gradients exist between these two extreme cases which lead to a defect-free, fully drawn cup.

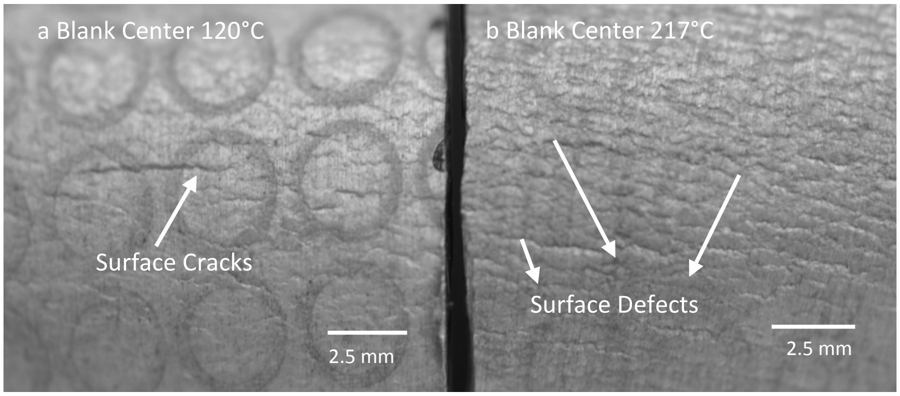

Figure 11. Surface cracks of two successfully drawn cups. Die and blank holder temperature are 245˚C, punch speed is 4mm/s, blank holder force is 80kN, DR is 2.25. Figure on left corresponds to a blank center temperature of 120˚C, on right, 217˚C.

Figure 12 shows the fracture cross section of two isothermally formed samples obtained through optical microscopy. At the fracture surface of the isothermally formed cup at 180˚C, shear bands and crack growth are observed at relatively low strains as evidenced the limited reduction in thickness. The isothermally formed sample at 250˚C (see b) exhibits a dramatic reduction in cross-section to a near-chisel point with void growth and coalescence as the final fracture mechanism. These observations suggest that the local temperature has dramatic effect on the failure mode for this alloy.

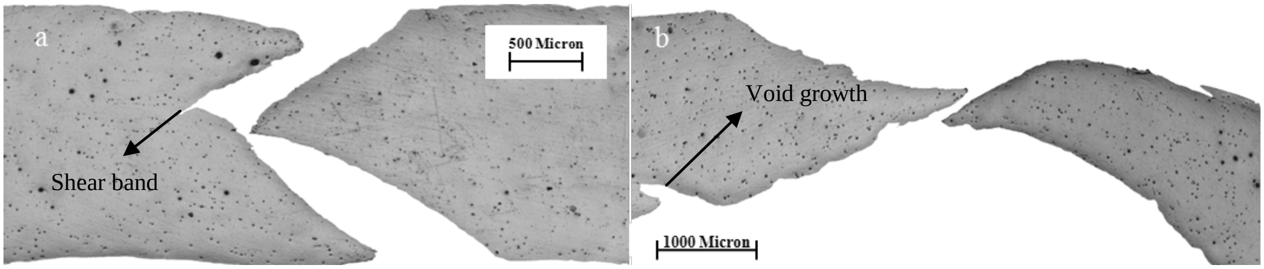

Figure 12**.** (a) Optical microscopy of the fracture surface of two cups formed at isothermal conditions, blank holder force of 80kN and DR of 2.25. (a) Die temperature at 180°C. (b) Die temperature at 250˚C.

These limits imply the existence of a process window which is also investigated herein. Such a process window is explored for the DR=2.25 cups using Figure 13 which illustrates the range of blank center and die temperatures for which the cup either draws successfully or fractures due to either low temperature brittle failure or a high temperature necking mode. From the figure, all the cases for which the die and punch temperature drop below 200°C result in brittle failure at the punch nose.

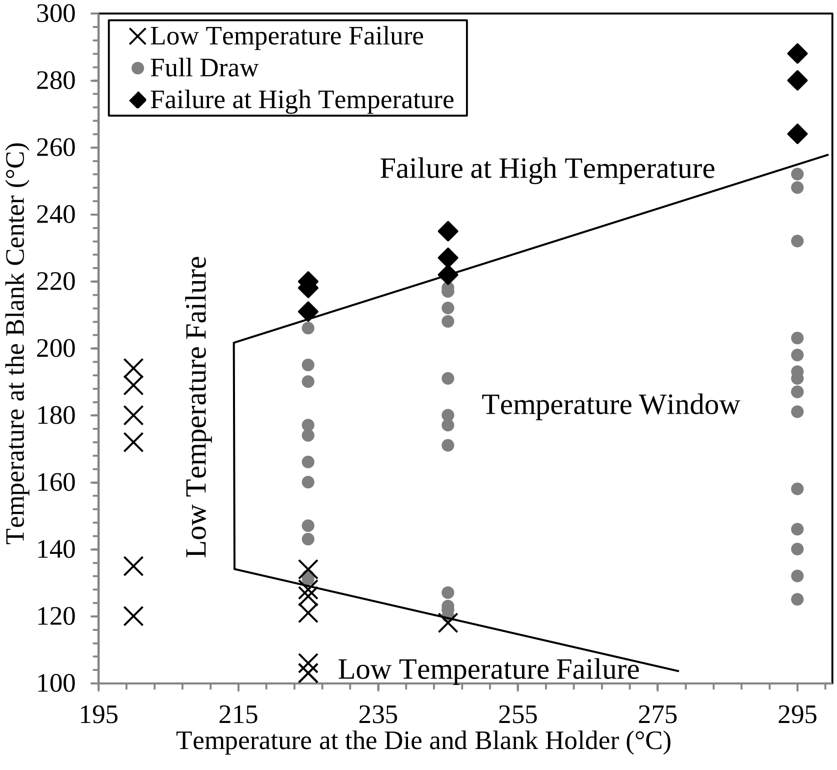

Figure 13. Process temperature window of deep drawing experiments with a punch speed of 4mm/s, blank holder force of 80kN (35kN at 200°C) and DR of 2.25.

The deep drawing experiments demonstrate that warm forming of the AZ31B sheet should be performed at temperatures above 200 ℃ in order to maximize formability. Temperatures above 300 ℃ can also be considered; however, this range goes beyond the conventional "warm" forming regime and invokes superplastic behavior involving extensive dynamic recrystallization response, for example. For this reason the material characterization experiments were limited to below 300 ℃.

4.2. Room temperature mechanical characterization and development of a constitutive model incorporating evolving asymmetry

This section describes the characterization of the constitutive behavior of AZ31B, focusing on the tension-compression asymmetry. In addition, efforts to develop a constitutive model to simulate this behaviour are presented. An important aspect of the model development is to capture the evolution of the asymmetry and anisotropy as a function of plastic strain within a continuum-plasticity material model. Note that a key assumption or limitation in the current model development is to only consider monotonic load paths, such that twinning-de-twinning processes are not considered, for example.

This section focuses primarily on room temperature behavior of AZ31B-O under tension and compression along different sheet orientations. Note that additional description of the room temperature testing and model development is given in Appendix B of this thesis. The elevated temperature response and model extension to elevated temperatures are presented in Section 4.3 and Appendix C.

4.2.1. Material characterization

Material characterization testing is performed on a strongly textured AZ31B-O magnesium alloy sheet. Neutron diffraction was used to characterize the initial texture of the as-received material (Appendix B, Figure 1). Tensile testing is performed using two independent extensometers to measure the stress *versus* strain response as well as the evolution of *r*-values during deformation. Furthermore, compression testing is performed on adhesively bonded cubic specimens made from 1.57mm thick sheet layers. The specimens are bonded using a high performance adhesive to create cubic samples which resist buckling during compression loading. The compression tests are performed using custom-made tooling while the deformation is recorded using a digital image correlation system.

The true stress versus true plastic strain behavior of AZ31B-O at room temperature is shown in Figure 14. A strong asymmetry is observed between the tension and compression data. The initial yield stress in compression is lower than that in tension; however, the rate of hardening under compression is higher. The flow stress in compression overtakes the flow stress in tension at approximately 6% true plastic strain. The initial yield stress under in-plane compression varies little with sheet orientation; beyond yielding, however, the flow curves in compression diverge increasingly from one another with increasing plastic strain. The flow stress for both in-plane tension and compression increases as the loading axis rotates from the rolling direction to the transverse direction. The rate of strain hardening under through-thickness compression is higher than that under in-plane tension.

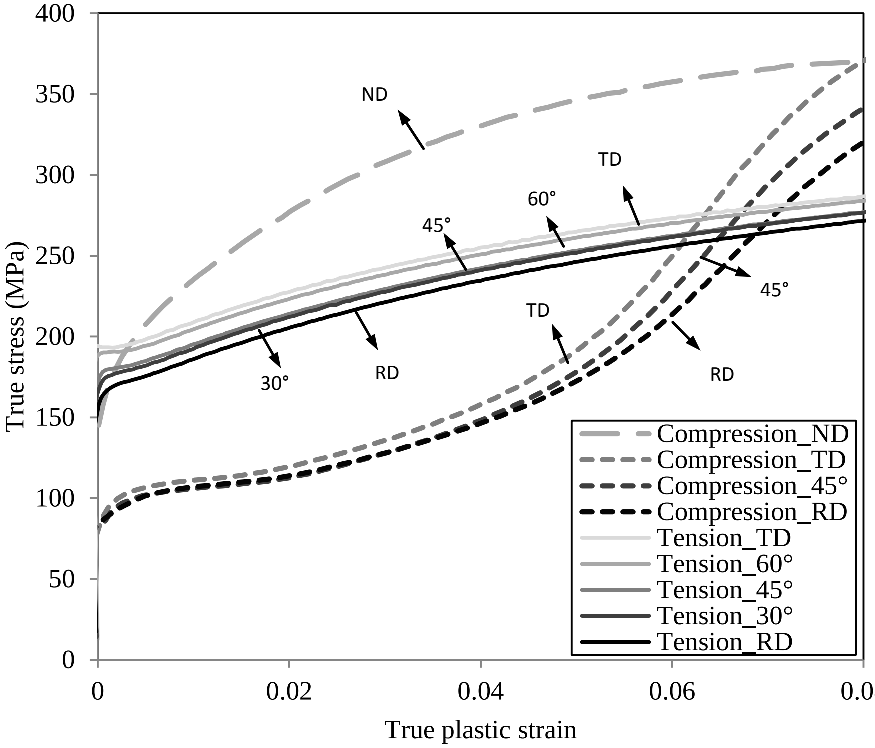

Figure 14. True stress versus true plastic strain under tension and compression (0.001s^{-1} strain rate), along different sheet directions. The compression data are plotted as positive. Error bars are not shown for clarity; however, the average absolute deviation from the mean was approximately 6MPa for the compression curves and 2MPa for the tensile curves.

Figure 15 shows the evolution of the instantaneous *r*-values with plastic strain. The instantaneous *r*-values were calculated from the ratio of strain rate components as follows (neglecting the effect of elastic deformation):

$$r_{Instantaneous} = \frac{\dot{\varepsilon}_w}{\dot{\varepsilon}_t} \quad (1)$$

A large asymmetry is observed when comparing the instantaneous *r*-values in tension and compression. The compressive *r*-values initially start at values close to zero and increase dramatically with plastic strain. The *r*-values increase as the loading axis rotates from the rolling direction towards the transverse direction.

The measured flow stress (Figure 14) indicate an evolving response of flow stress with the plastic strain comparing measurements along different sheet orientations. The rate of hardening differs dramatically between the tensile and compressive stress-strain curves. Moreover, a strong evolving asymmetry is observed in the measured *r*-values.

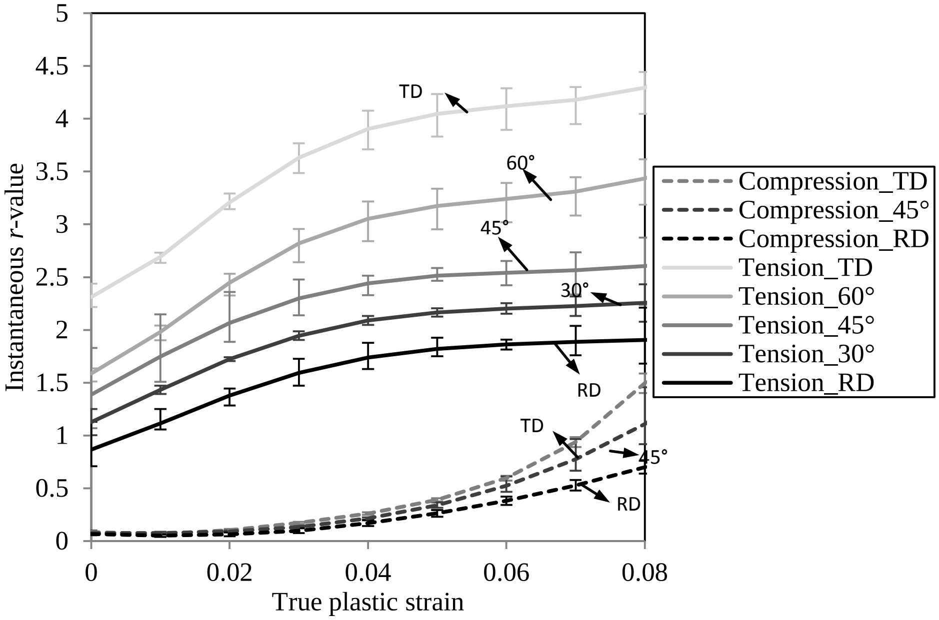

Figure 15. Instantaneous *r*-values versus true plastic strain under tension and compression ($0.001s^{-1}$), along different sheet directions. The error bars indicate the maximum and minimum measured values from the repeat tests.

4.2.2. Evolving yield function

As a starting point in the current research, a CPB06 yield surface formulation [1] is adopted and the anisotropy and asymmetry parameters are modified to evolve with deformation as part of this work. This analytical yield surface due to Cazacu et al. (2006), denoted as CPB06, is described as:

$$F(\boldsymbol{\Sigma}) = (|\Sigma_1| - k\Sigma_1)^a + (|\Sigma_2| - k\Sigma_2)^a + (|\Sigma_3| - k\Sigma_3)^a, \qquad (2)$$

where k is a material parameter that describes the strength difference in tension and compression, a is the degree of homogeneity, and ${\Sigma_i}^{(l)}$, i=1,…,3 are the principal values of the deviatoric stress tensor. $\boldsymbol{\Sigma}$ is given by:

$$\boldsymbol{\Sigma} = \mathbf{C}:\mathbf{S}. \qquad (3)$$

which is an equation to transform the deviatoric stresses. In Equation (3), **C** is the fourth-order anisotropy tensor and **S** is the deviatoric stress tensor. This yield function is fit to the experimental data at different plastic strain intervals to obtain the initial yield surface and evolution of the envelope of subsequent yield surfaces [58] under a monotonic loading assumption. In the current work, a plane stress condition is assumed and the parameters in tensor **C** are rewritten in terms of the plastic strain using a saturation-type interpolation function as follows,

$$C_{ij}^{(l)} = a_{ij}^{(l)} + b_{ij}^{(l)}(1 - exp(-d_{ij}^{(l)} * \bar{\varepsilon}^p)), \tag{4}$$

$$k^{(l)} = e^{(l)} + f^{(l)}(1 - exp(-g^{(l)} * \bar{\varepsilon}^p)), \tag{5}$$

where parameters $a_{ij}^{(l)}$, $b_{ij}^{(l)}$, $d_{ij}^{(l)}$, $e^{(l)}$, $f^{(l)}$ and $g^{(l)}$ are constants corresponding to *l*th linear transformation that are found through optimization methods to capture the material response observed in the experiments, and $\bar{\varepsilon}^p$ is the effective plastic strain. Note that the new model reverts back to a conventional CPB06 type model by setting evolution parameters, $b_{ij}^{(l)}$, $d_{ij}^{(l)}$, $f^{(l)}$ and $g^{(l)}$ equal to zero. During the optimization procedure the difference between the response from the model and the experimental measurements (the error function below) are minimized.

$$E\left(a_{ij}^{(l)}, b_{ij}^{(l)}, d_{ij}^{(l)}, e^{(l)}, f^{(l)}, g^{(l)}\right) = \sum_k \left[\sum_m w_m \left(\frac{\sigma(\bar{\varepsilon}_k^p)_m^{th}}{\sigma(\bar{\varepsilon}_k^p)_m^{exp}} - 1 \right)^2 + \sum_n w_n \left(\frac{r\left(\bar{\varepsilon}_k^p\right)_n^{th}}{r(\bar{\varepsilon}_k^p)_n^{exp}} - 1 \right)^2 \right] \tag{6}$$

In Equation (6) $\sigma(\bar{\varepsilon}_k^p)_m^{th}$ and $r\left(\bar{\varepsilon}_k^p\right)_n^{th}$ represent the material model response for flow stresses and *r*-values, respectively, along a specific loading path while $\sigma(\bar{\varepsilon}_k^p)_m^{exp}$ and $r\left(\bar{\varepsilon}_k^p\right)_n^{exp}$ are the corresponding experimental values. Index *k* corresponds to the number of the plastic strain interval in which the analytical functions are fitted to the experiments. *w* is a weight parameter which introduces more emphasis on an arbitrary experiment. *m* and *n* represent the numbers of stress and *r*-value experiments, respectively, used in the calibration process. The experiments used for the calibration at room and elevated temperatures are discussed in more detail in Appendix B and C of the thesis, respectively. The weighing factors are changed as needed at each stage of the optimization to improve the fit for particular experiments; for instance, the weighting factor corresponding to biaxial tensile and shear flow stresses at room temperature are set to 2 and 5 correspondingly while the rest of the weighting factors are equal to unity.

More linear transformations (equation 3) can be incorporated in this orthotropic yield surface until the desired level of accuracy in the description of the yield locus is obtained [35]. In the current research, different numbers of stress transformations (one to four transformations) were considered to assess the flexibility of the model in capturing the material response. The CPB06ex*l*ev designation is used henceforth to denote the evolving yield function, in which the integer *l* indicates the number of stress transformations performed on the deviatoric stress tensor and “ev” indicates that the anisotropy and asymmetry parameters are evolving with the accumulated plastic strain. In the current work, three transformations were proven to be sufficient to capture the evolving anisotropy and asymmetry observed in the material characterization measurements. More in-depth discussion regarding the effect of number of stress transformations on the quality of the yield function fit can be found in Appendix B.

In contrast to previous research, the developed model captures the evolving asymmetric/anisotropic response of both flow stresses and *r*-values for both tension and compression while also fitting the flow stress under biaxial and shear (experimental data by Khan et al. [19]) conditions. It is noteworthy that the texture and mechanical response from the material used in this work were compared to that used by Khan et al. [19] and it was concluded the two batches of material have reasonably close texture and mechanical response as shown in Appendix E. Figure 16 shows the evolving envelope of subsequent yield surfaces at different effective plastic strain levels using three stress transformations after fitting to the experimental data up to 8% effective plastic strain with the *x*- and *y*- axes parallel to the RD and TD directions, respectively. Total of five plastic strain intervals are used to calibrate the model, namely 0, 2, 4, 6 and 8%. The term "evolving envelope of subsequent yield surfaces" is used herein since kinematic effects associated with de-twinning, for example, are not accounted for; thus, the loci plotted in Figure 16 represent "envelopes" capturing subsequent yield surfaces for given plastic strain intervals valid strictly for monotonic strain paths and for instance reverse bending conditions could not be accurately modeled using the current approach.

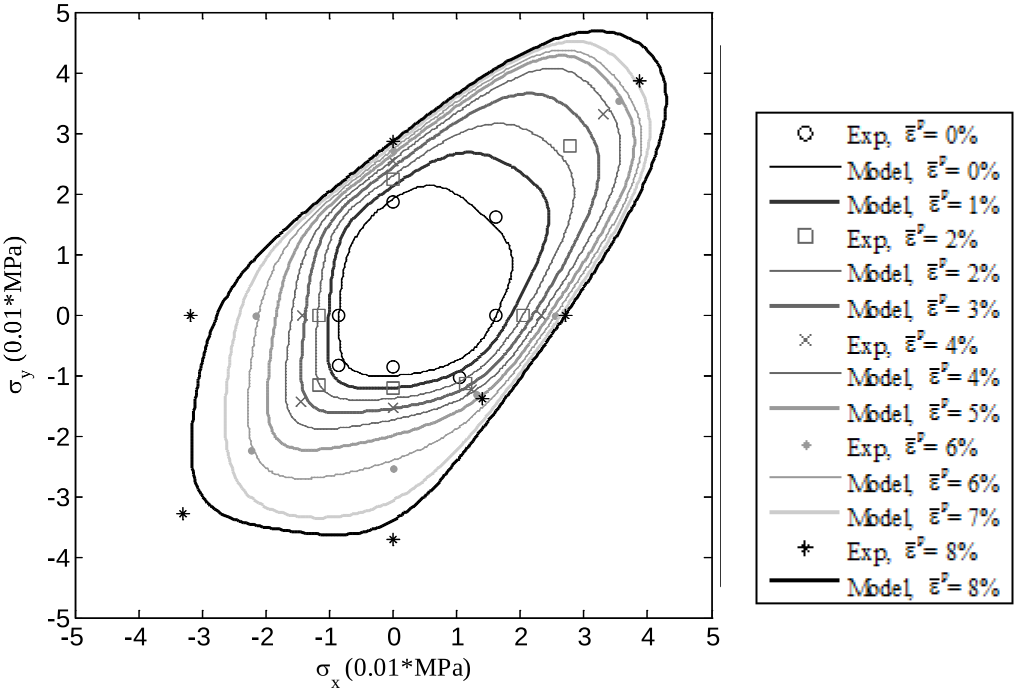

Figure 16. Evolution of the envelope of subsequent yield surfaces with accumulated plastic strain considering three stress transformations.

4.2.3. Finite element implementation and validation

The model utilizing three stress transformations is implemented within a user defined material model (UMAT) linked within the commercial finite element software LS-DYNA. The yield function is referred to in the following as CPB06ex3ev (which denotes a CPB06 yield function utilizing three stress transformations with evolution). The yield formulation, with evolving anisotropy and asymmetry as in Section 4.2.2, is implemented within the framework of rate independent plasticity (Section 4.3 addresses rate effects). A plane stress condition is assumed, corresponding to thin sheet materials. A stress integration algorithm previously proposed by [59] is adopted which uses a return mapping scheme. Appendix B provides further detail concerning the model implementation.

Uniaxial loading cases

As a first validation, the material model was used to predict the stress-strain response under the same loading conditions for which the model is fit to, using single-element finite element model. The measured constitutive data (uniaxial stresses and *r*-values) under different loading conditions are compared to the predicted response in Figure 17 and Figure 18. The model clearly captures the strong anisotropy and tension-compression asymmetry evident in the measured data. Some discrepancy between the predicted response and the measured data under uniaxial in-plane compression is observed near the first yield point and at higher plastic strain levels. The predicted *r*-values agree well with experiment over much of the plastic strain range and loading conditions (Figure 18), although some deviation occurs at plastic strain levels at which the model was not calibrated. This suggests that there may be a tradeoff between the accuracy of different fitted experiments. This is due to the global nature of this model which fits the model for all of the provided experiments at the same time.

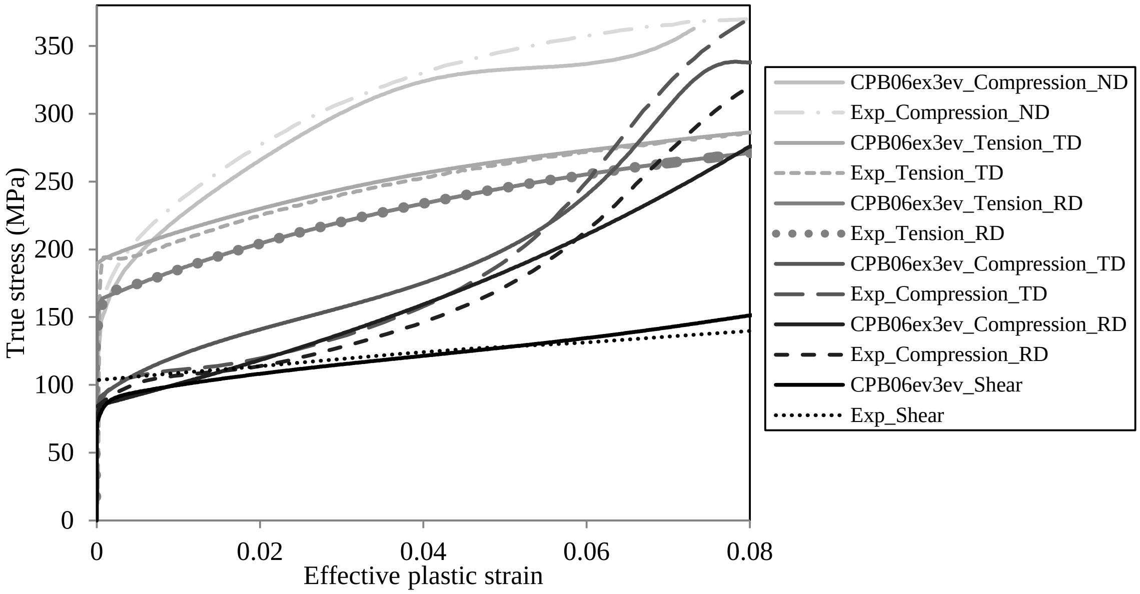

Figure 17. Predicted and measured stress versus plastic strain response (shear experiment data from Khan et al. [19]).

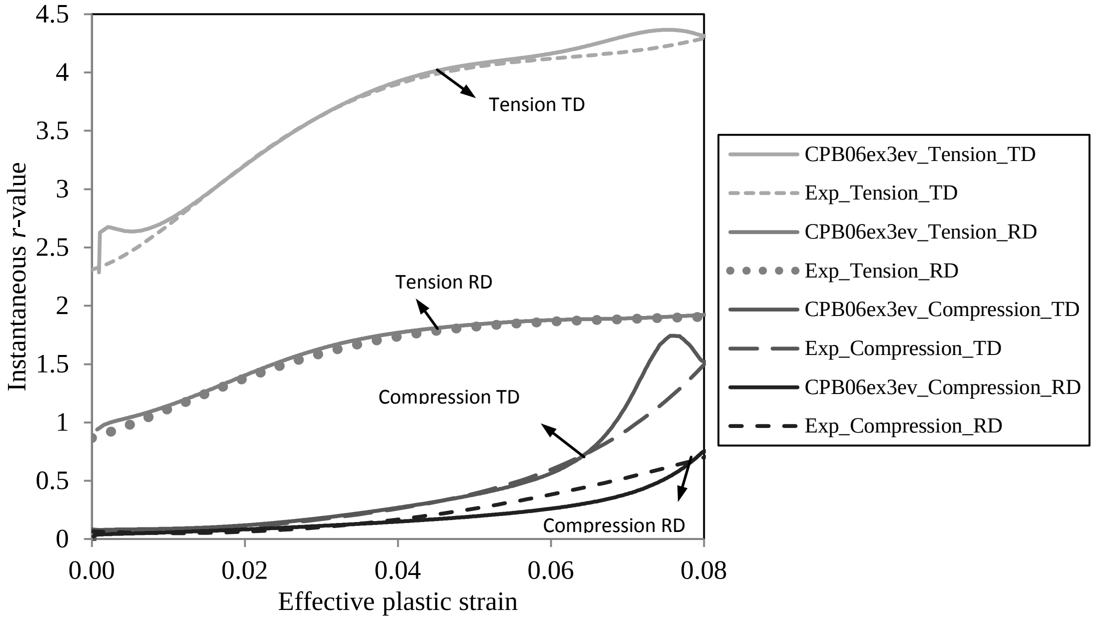

Figure 18. Predicted and measured *r*-values for different loading paths.

Three-point bending case

As a second validation study, a three-point bending experiment (shown in Figure 19) was performed on the AZ31B Mg sheet alloy and then simulated using the new material model. Comparison between the predicted and measured load-displacement response and strain distribution in the bend region is used to assess the model predictions relative to those obtained using non-evolving von Mises and CPB06 models.

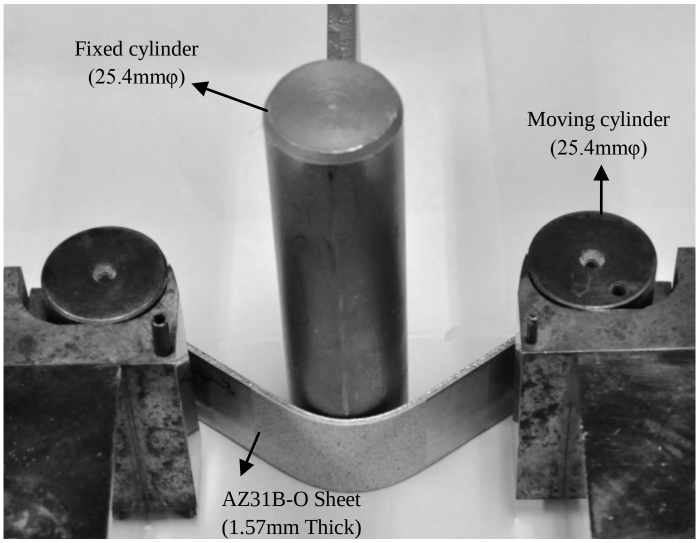

Figure 19. Three-point bending experiment: (a) three-point bending apparatus, (b) ε_{xx} true strain field on the outer surface of the bend region (the rolling direction is aligned with the *x*-axis).

The predicted load versus displacement responses are compared to the experimental results in Figure 20a for the current model (CPB06ex3ev), the von Mises model, and the non-evolving CPB06ex3 model (calibrated at 4% plastic strain). As opposed to the CPB06ex3ev, CPB06ex3 model utilizes constant *C and k* parameters (Equation 2 and 3) which means it only expands in an isotropic manner as deformation progresses (no change in the shape of the yield surface). Both the CPB06ex3 model calibrated at 4% plastic strain and the CPB06ex3ev predictions exhibit good agreement with the measured load-displacement data, with the evolving yield function predictions lying slightly closer to experiment. The von Mises predictions lie above the experimental values and CPB-based predictions. The predicted and measured strains at the center of the bend for the RD oriented samples are compared in Figure 20b. The axial strain component (along the length of the strip) is referred to as ε_{xx}, whereas the lateral strain component is ε_{yy}. The CPB-based predictions agree well with the measured strains, with the lateral strain predictions from the evolving model being slightly closer to the measured data at the specimen edges. The von Mises predictions are offset from the measured strains due to an inability to capture the tension-compression asymmetry of this alloy and the resulting neutral axis shift.

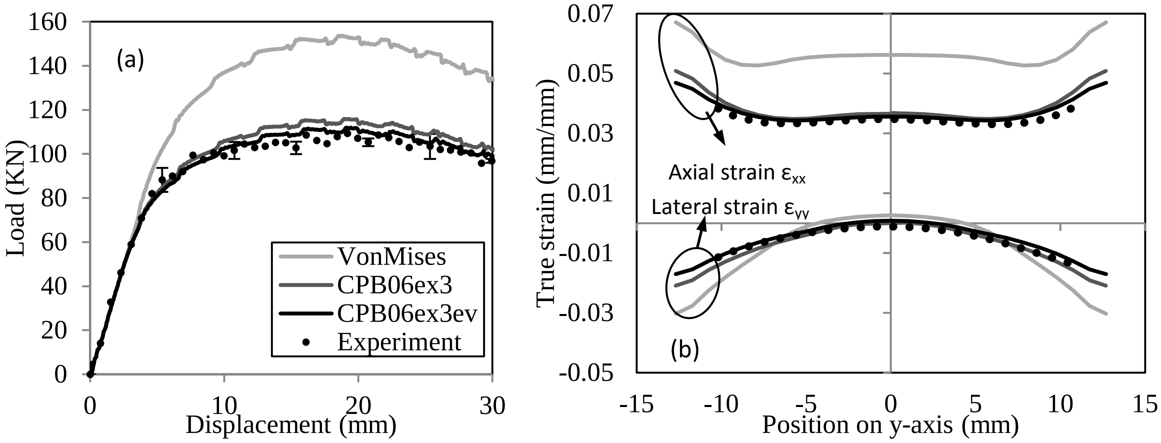

Figure 20. (a) Punch force versus displacement, comparison between the experiment and simulations. The error bars indicate the maximum and minimum measured values from the repeat tests, (b). ε_{xx} and ε_{yy} comparison between the experimental measurements and the simulations.

It is noteworthy that the effective plastic strain predicted in the three-point bending simulation with a cylinder diameter of 25.4mm is limited less than 5%. To compare the CPB06ex3ev and CPB06ex3 predictions for a higher range of effective plastic strain for which the degree of yield surface evolution should be larger, simulations were performed using a smaller cylinder diameter (15.7mm) which corresponds to a nominal bending strain of 10%. Figure 21 shows the bending stress distribution through the sheet thickness corresponding to a load point displacement of 3.8 and 30mm for both the evolving and non-evolving models. The results for the larger cylinder show very little difference between the evolving and non-evolving predictions. The results for the smaller cylinder show stronger evolution of the asymmetry, which can be observed in the difference in the compressive stresses between the two predictions at the higher load point displacement.

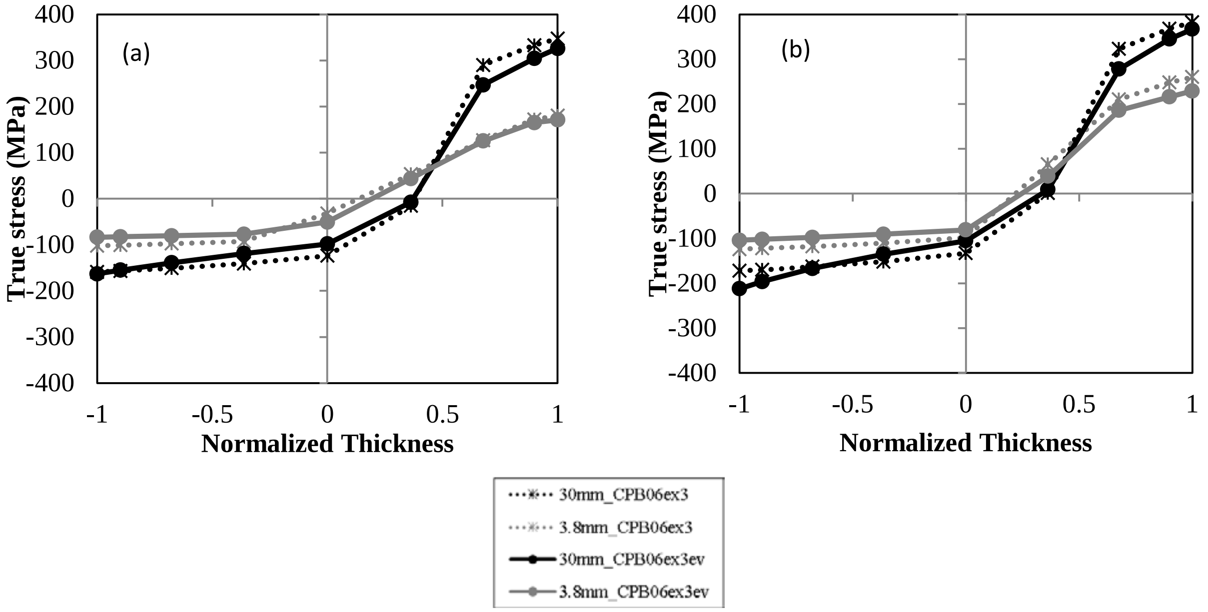

Figure 21. Bending stress (σ_{xx}) distribution through the sheet thickness at the center of the bend. Shown are predictions using the CPB06ex3 and CPB06ex3ev models at two punch displacement levels (3.8 and 30 mm): (a) results for the 25.4mm cylinder diameter used in the experiments and, (b) results for a cylinder diameter of 15.7mm.

4.3. Elevated temperature material characterization and model development

The material characterization and material modeling efforts the previous section were for room temperature conditions. Here, developed material model is extended to include thermal softening effects and strain rate sensitivity of the flow stress. Material characterization (tension and compression) is also conducted at elevated temperatures to ascertain how the anisotropy and asymmetry of AZ31B changes with temperature. Finally, metal forming experiments and simulations are conducted to assess the material model predictive capability under more complex loading conditions. (Additional detail concerning this work on the elevated temperature response experiments and models can be found in Appendix C of this thesis.)

4.3.1. Elevated temperature material characterization

4.3.1.1. Effect of temperature at quasi-static strain rates

The mechanical response of AZ31B-O at elevated temperatures (150-250°C) was characterized under tension and compression loading conditions along different sheet orientations. The tensile testing was performed inside an environmental chamber utilizing two independent high temperature extensometers. A custom-made high temperature compression testing fixture along with a digital image correlation (DIC) strain measurement system was used for compression testing. The tensile and compression testing was performed on 25mm sub-sized ASTM and 6mm cubic specimens, respectively. The true stress *vs.* true plastic strain at different temperatures and a strain rate of 0.001s^{-1} is shown in Figure 22. In comparison to the room temperature data (Figure 22a), as the temperature is increased to 150 °C (Figure 22b), the initial yield strength under tensile loading is reduced which is associated with the activity of additional slip systems [14]. However, the initial yield stress under compression is shown to be temperature independent up to 150 °C. The initial yield stress under both tension and compression is reduced with increasing temperature to 250 °C (Figure 22d). A relatively mild asymmetry is observed comparing the tension *vs*. compression stress-strain curves at 250 °C with the initial yield stress under compression being slightly lower than that of the tensile. Similarly, a reduction in anisotropy is observed as the temperature is increased to 250°C as shown in Figure 22d.

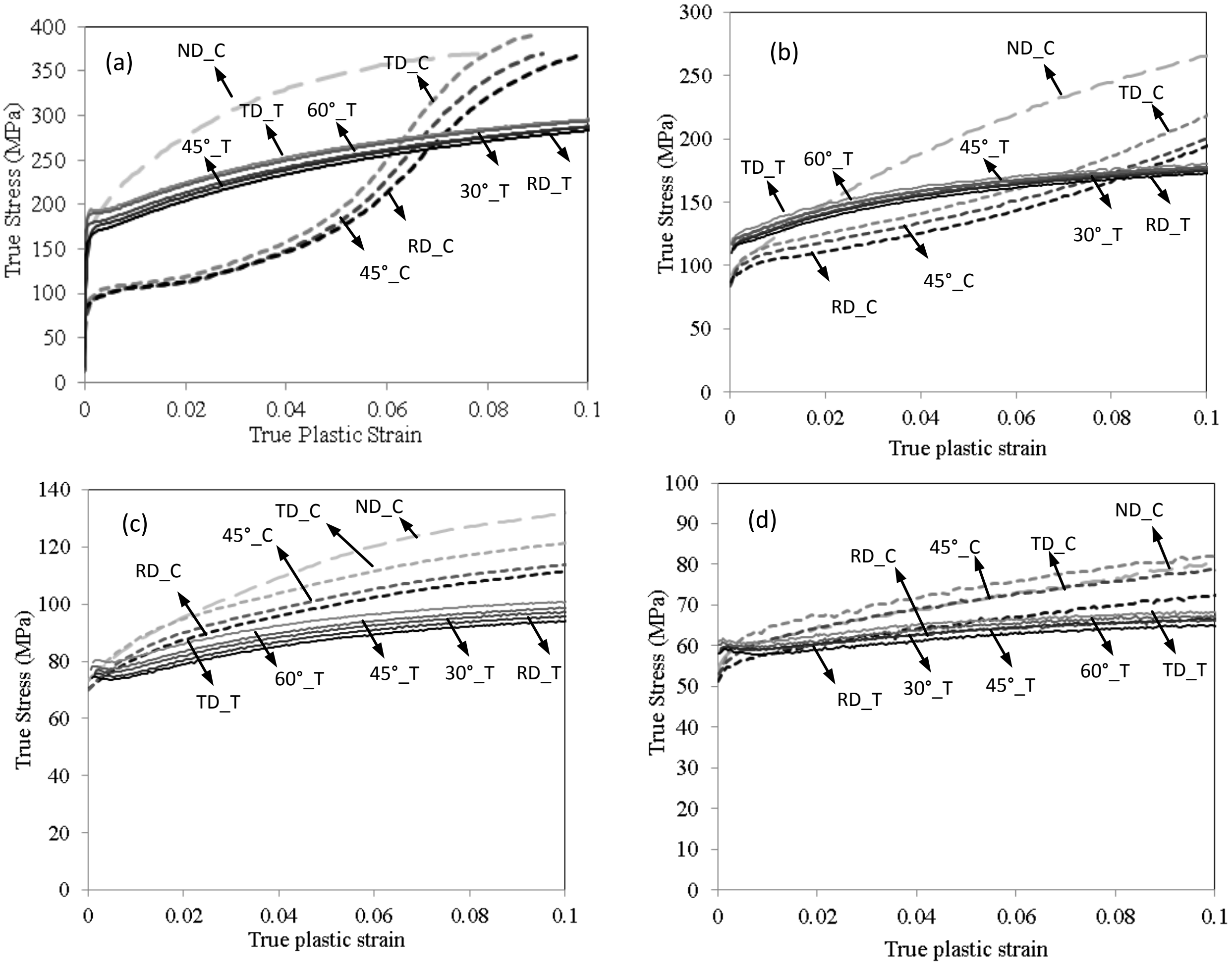

Figure 22. True stress versus true plastic strain under tension and compression loading (0.001 s^{-1} strain rate), along different sheet orientations, (a) Room temperature, (b) 150 °C, (c) 200 °C, (d) 250 °C, The compression data is plotted as positive. The curves corresponding to tensile loading are indicated using the letter "T" and the compression curves using "C".

Figure 23 shows the evolution of the instantaneous *r*-values with plastic strain at room temperature, 150, 200 and 250°C. A large asymmetry is observed when comparing the instantaneous *r*-values in tension and compression at room temperature (Figure 23a) and 150 °C (Figure 23b). The *r*-values increase as the loading axis rotates from the rolling direction towards the transverse direction. As the temperature is increased, the evolution of instantaneous *r*-values with the accumulated plastic strain becomes less significant. Furthermore, the in-plane anisotropy and the tension/compression asymmetry of instantaneous *r*-values is also reduced as the temperature is increased, with the material response at 250°C being the least asymmetric and anisotropic. For instance, the difference in the magnitude of the initial tensile instantaneous *r*-values along the rolling and transverse direction is reduced from 1.5 at room temperature to 0.4 at 250°C.

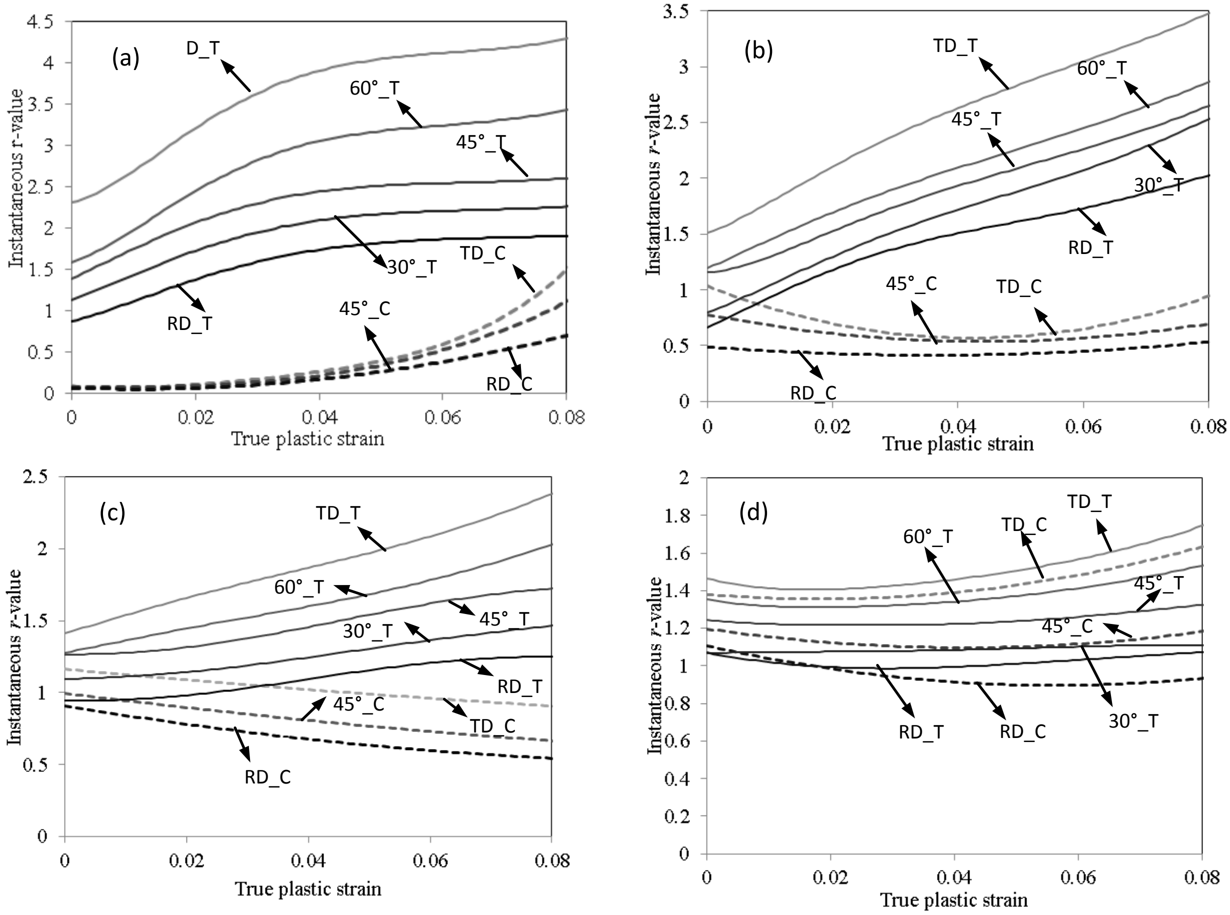

Figure 23. Instantaneous *r*-values versus true plastic strain under tension and compression loading (0.001s^{-1} strain rate), along different sheet orientations, (a) Room temperature (b) 150 °C, (c) 200°C, (d) 250°C, The curves corresponding to tensile loading are indicated using the letter "T" and the compression curves using "C".

4.3.1.2. Strain rate sensitivity

The effect of strain rate on the flow stress of AZ31B-O was characterized at room and elevated temperatures. The dotted curves in Figure 24 represent the experiments performed as part of this research while the solid lines are fits to be discussed in subsequent sections. Four strain rate levels; namely, 0.001, 0.01, 0.1 and 1 s^{-1} are considered for room temperature and 200°C while strain rates of 0.001 and 0.1 s^{-1} are considered for 150 and 250°C. Note that high strain rate data for this alloy at 500s^{-1} and room temperature, 150 and 250°C, due to Hasenpouth et al. [60], has also been plotted for reference. The experiments indicate an increasing effect of strain rate at elevated temperatures, particularly beyond 150°C. A large strain rate sensitivity of the initial yield strength is observed at 200 and 250°C. Furthermore, a reduction in strain hardening rate is observed comparing the slope of the stress-strain curves at room and elevated temperature. A similar strain rate sensitivity trend is also observed in the tensile experiments performed with specimens oriented along 30°, 45°, 60° and TD. (Note that the fits plotted in Figure 24 are discussed in Section 4.3.2.)

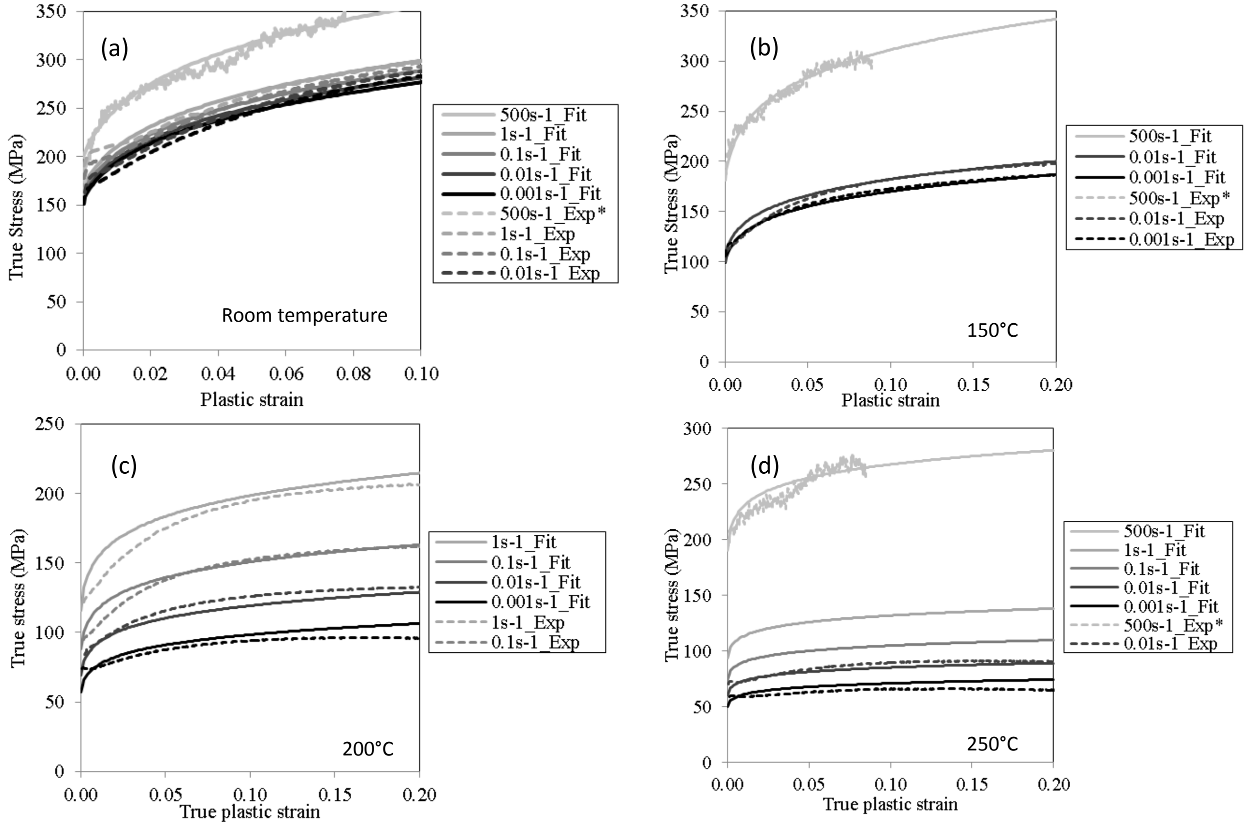

Figure 24. True stress versus true plastic strain under tension loading along the rolling direction at different strain rates, (a) Room Temperature, (b) 150 °C, (c) 200 °C, (d) 250 °C. The solid lines represent the Cowper-Symonds [61] fit.*Stress strain curves at strain rate of 500 s^{-1} are from Hasenpouth et al. [60].

4.3.2. Material modeling

4.3.2.1. Evolving anisotropic/asymmetric yield function

The CPB06ex3ev yield formulation described in Section 4.2.2 is calibrated for the measured mechanical response at elevated temperatures and a strain rate of $0.001s^{-1}$ presented in Section 4.3.1.1. Figure 25shows the evolving yield surface at different effective plastic strain levels up to 250°C. The yield function is calibrated up to 8% effective plastic strain (the limit of the measured data from the experiments) after which the yield function is assumed to work harden in an isotropic manner (Appendix G). In general, the evolving yield criterion is able to capture the experimental data quite well. Comparing the yield surfaces at different temperatures, a significant reduction in the asymmetry of the initial yield surface and its evolution can be observed as the temperature increases.

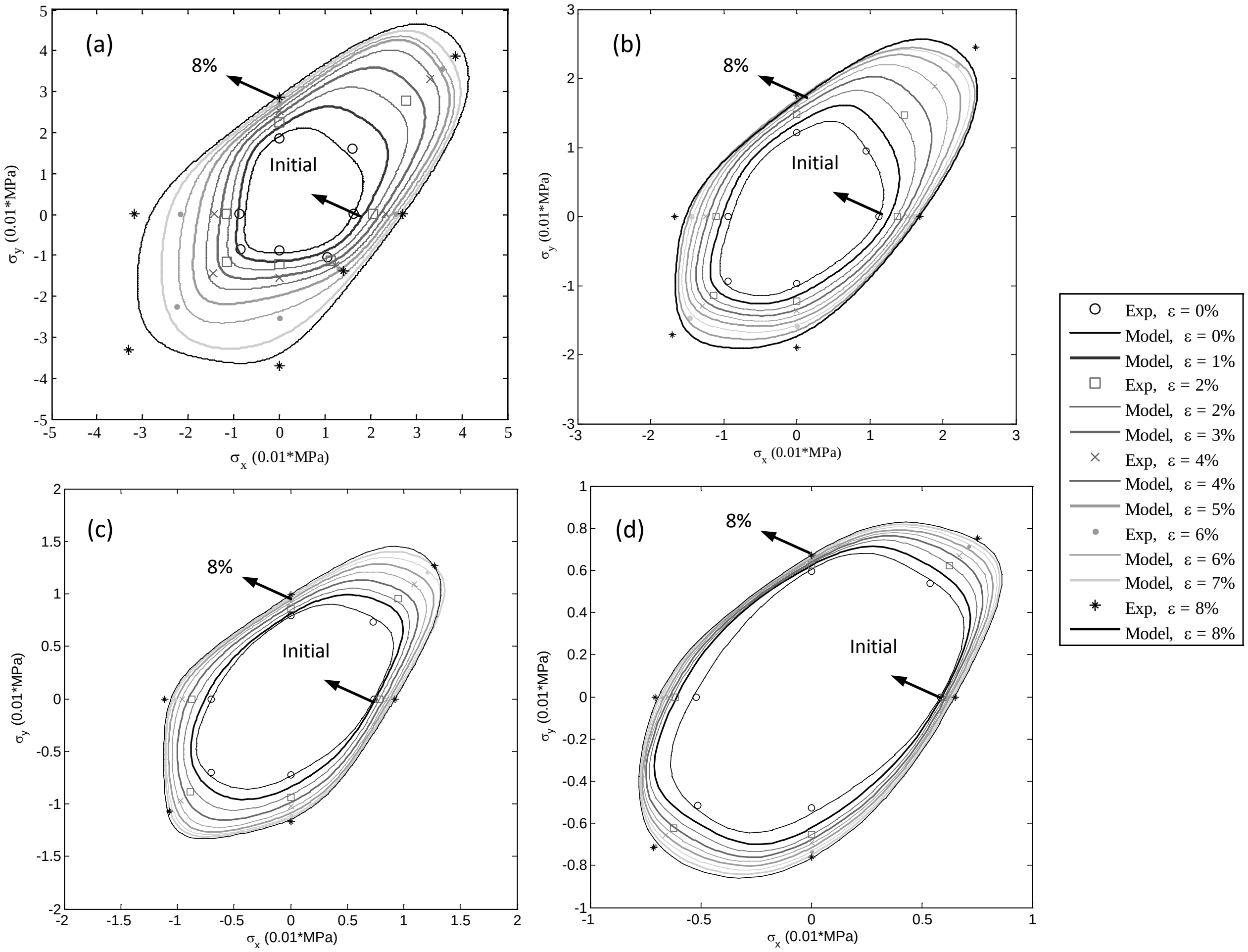

Fig. 1. Yield surface evolution with accumulated plastic s

Figure 25. Yield surface evolution with accumulated plastic strain up to 8% at strain rate of $0.001s^{-1}$, (a) room temperature, (b) 150 °C, (c) 200 °C, (d) 250 °C.

4.3.2.2. Temperature softening effect and strain rate sensitivity modeling

The AZ31B-O sheet considered in this research exhibits significant thermal softening and strain rate sensitivity within the elevated temperature range considered (150-250°C) as seen in Figure 24. Two approaches were considered to introduce these effects into the CPB06ex3ev yield function. The first approximation was developed for isothermal cases in which the temperature of the material is constant (and in this case limited to room temperature, 150, 200 or 250°C). For such an isothermal case, a Cowper-Symonds model [61] as shown in Eq. 7 was fit to the available data to scale the material flow stress, taken here as the rolling direction stress versus effective plastic strain curve, to account for strain rate at each temperature level (room temperature, 150, 200 or 250°C).

$$\mathrm{H}(\bar{\varepsilon}^{p},\dot{\varepsilon})_{T=constant} = \mathrm{K}(\bar{\varepsilon}^{p}+\varepsilon_0)^{n}\left(1.0+\left(\frac{\dot{\varepsilon}}{D}\right)^{\frac{1}{P}}\right) \qquad (7)$$

The parameters K (strength hardening coefficient), n (strain-hardening exponent), D and P (strain rate sensitivity terms) are found at each temperature, while the parameter ε_0 is defined from the following,

$$\varepsilon_0 = (\frac{\mathrm{E}}{\mathrm{K}})^{(\frac{1}{n-1})}, \qquad (8)$$

The second approximation was developed for use in modelling non-isothermal cases in which the temperature and strain rate vary arbitrarily within the material being deformed. In this case, both thermal softening and strain rate sensitivity were accounted for using a modified Nadai model (Van den Boogaard and Huétink, [62]) fit to the material response. The following hardening model is used to fit the experimental tensile data along the rolling direction:

$$\mathrm{H}(\bar{\varepsilon}^{p},\dot{\varepsilon},T) = \mathrm{K}(T)(\bar{\varepsilon}^{p}+\varepsilon_0)^{n(T)}\dot{\varepsilon}^{m(T)}, \qquad (9)$$

where, the functions *K(T)* (strength coefficient), *n(T)* (strain-hardening exponent) and *m(T)* (strain rate-hardening exponent) are found for different temperatures and strain rates as shown in the equations below, while the parameter ε_0 is defined from Eq. (8).

$$\mathrm{K}(T) = A_0 + A_1 * (1 - exp(A_2 * (T - T_r)/T_m)) \qquad (10)$$

$$\mathrm{n}(T) = A_3 + A_4 * (1 - exp(A_5 * (T - T_r)/T_m)) \qquad (11)$$

$$\mathrm{m}(T) = A_6 * (1 - exp(A_7 * (T - T_r)/T_m)) \qquad (12)$$

In the first approximation (isothermal treatment), the yield surface shape treated as strain rate insensitive, while the flow stress is scaled with strain rate. In the second approximation (non-isothermal treatment), the yield surface scales with both strain rate and temperature.

4.3.3. Validation/assessment of the model against warm forming experiments

4.3.3.1. Validation using uniaxial tensile/compression testing

The response of the material model is initially evaluated by simulation of the elevated temperature tensile experiments presented in Section 4.3.1.1. This represents a “closed loop” assessment of the model since the predictions correspond to the same loading conditions for which the model was calibrated, however, it is important to confirm how well the model reproduces the original experiments. The simulations considered a single finite element finite using the Cowper-Symonds [61] hardening model calibrated for isothermal conditions as well as the modified Nadai model for non-isothermal conditions. Note that the material parameters and further detail concerning the calibration process is given in Appendix C.

The comparison between the Cowper-Symonds model fit and the experimental measurements are shown in Figure 24. The comparison between the predicted (modified Nadai model) and measured stress-strain curves and *r*-values at 250°C is shown in Figure 26. The predicted stress-strain curves (Figure 26a) from simulations based on the modified Nadai fit capture the measured trends reasonably well. The predicted *r*-values (Figure 26b) agree well with the experiments over much of the plastic strain range and loading conditions at both temperatures; however, some deviation from the experimental measurements is seen, primarily at the extremes of the plastic intervals over which the model is calibrated. This is due to the global nature of this model which fits the model for all of the experiments at the same time.

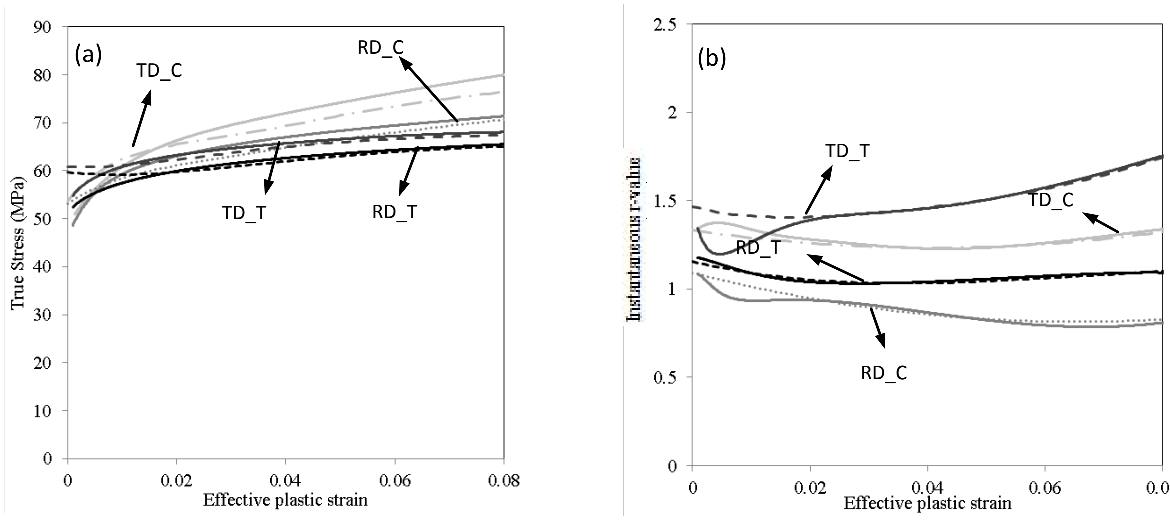

Figure 26. Single-element modified Nadai model response comparison to the experiments using different loading paths at a nominal strain rate of $0.001s^{-1}$ at-250°C, (a) true stress versus plastic strain response, (b) *r*-value response comparison.

4.3.3.2. Assessment of the model using dome height testing

The assessment of the CPB06ex3ev model discussed in Section 4.3.1.1 under isothermal conditions is performed using limited dome height testing (LDH) at 250°C. Details of this elevated temperature forming experiment and the finite element model are provided in Appendix C. The strain rate sensitivity of the flow stress is considered using the Cowper-Symonds model discussed in Section 4.3.1.2. A 100 mm hemispherical dome was utilized to form the samples within a servo controlled hydraulic press. Two different blank geometries, previously proposed by Nakazima et al. [63], were considered to deform the material under different load paths: 203.2 x 203.2 mm square blanks producing near-biaxial stretch conditions and dog-bone samples with widths of 76.2. The 76.2 mm wide sample promotes a near-plane strain condition in which friction limits the lateral strain, while the narrower width sample is closer to a uniaxial stress state. A blank holder force of 40 kN was applied before commencing the experiment. A punch velocity of 0.1 mm/s was used for all experiments. A 3D digital image correlation system (DIC) was used to measure the field of strain throughout the experiment.

The predicted and measured punch force versus displacement response for the two LDH geometries are plotted in Figure 27. The model captures the response of the biaxial sample (203 x 203 mm) quite well, while the agreement between the predictions and measured response for the dog-bone specimen is within 80% of the measured loads. The superior predictions for the biaxial geometry is attributed to the use of a biaxial stress state in the calibration procedure, whereas the plane strain state is not calibrated.

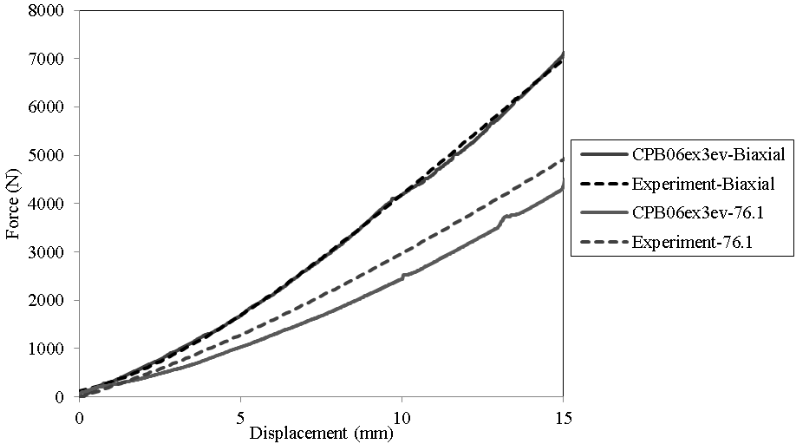

Figure 27. Punch force versus displacement, comparison between the experiment and simulations of biaxial stretch dome height testing (203.2 x 203.2 mm specimen) at 250°C.

Figure 28a serves to compare the predicted and measured strain distributions within the 203 x 203 mm samples at a punch displacement (dome height) of 15 mm. The experimental data indicates that the strain state is not purely biaxial and there is a drop in the strain at the pole region of the specimens. Both trends can be attributed to friction effects. The predictions capture the difference in major versus minor strain, but not the drop in strain over the pole region. The predicted and measured major and minor strain along the rolling direction of 76.1mm wide dog bone specimen are compared in Figure 28b. The strain distributions reflect the near-plane strain condition, as seen in the minor strains across the pole being close to zero. There is a drop in strain at the pole and the numerical model captures this frictional effect for this specimen geometry. However, it still misses the qualitative prediction for some of the compared values, especially for the minor strain.

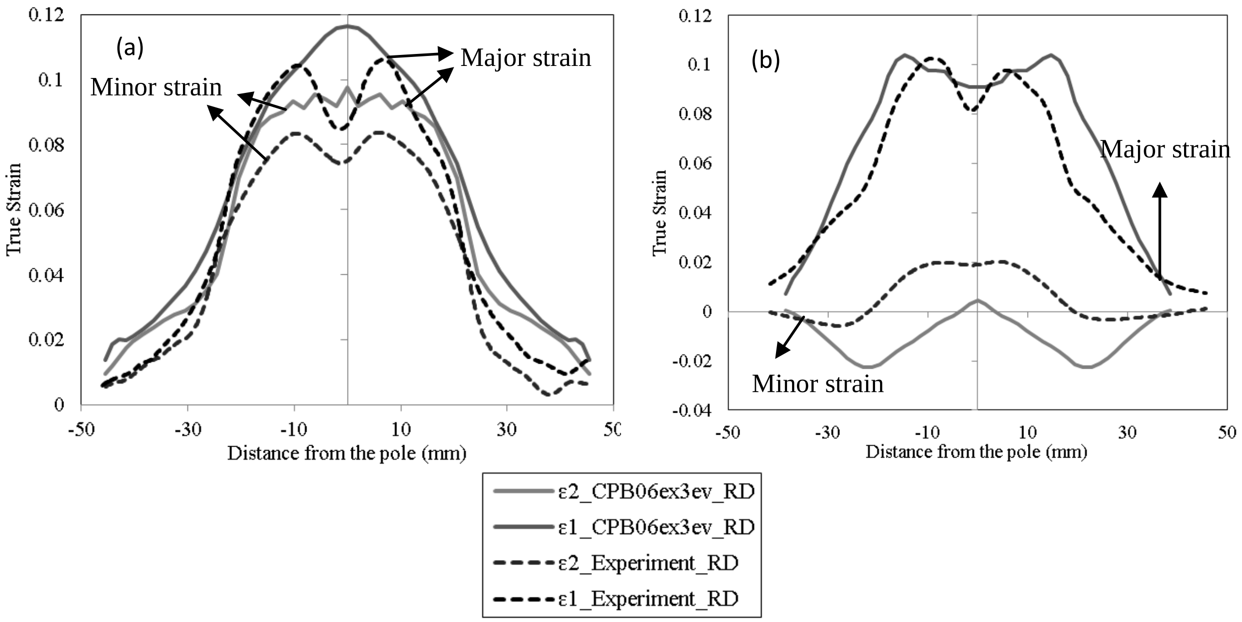

Figure 28. Comparison of predicted and measured major strain (ε_1) and minor strain (ε_2) versus distance from pole along the rolling direction at 250 °C and a dome height of 15 mm: (a) biaxial stretch specimens (203.2 x 203.2 mm) (b) dog-bone sample with widths of 76.2mm).

4.3.3.3. Assessment of the model using warm deep drawing experiments

As a final validation case, the non-isothermal, circular cup deep drawing experiments discussed in Section 4.1 (Appendix A) were simulated. These simulations and comparison to the corresponding experiments allow evaluation of the model under non-isothermal conditions in which the temperature (and strain rate) varies within the workpiece.

The non-isothermal nature of the experiments mandated the use of the temperature- and strain rate-dependent modified-Nadai constitutive treatment described Section 4.3.1.2. This accounts for arbitrary variation of strain rate and temperature within the blank during forming. Furthermore, the yield formulation is made temperature dependent by assigning different evolution parameters based on the current temperature within the simulation. Elements with temperatures in the range 100-175°C are assumed to follow the yield function evolution rule calibrated for 150°C, while elements with temperatures of 175-225°C are assigned the evolution rule calibrated for 200°C. Elements with temperatures above 225°C are considered to obey the evolution rule calibrated for 250°C. The yield surface shape of the CPB06ex3ev model associated with these temperatures was previously discussed in Section 4.3.1.1. Further description of the model is given in Appendix C.

The punch force *versus* displacement response using the CPB06ex3ev model is compared to the experimental measurements in Figure 29. The model over-predicts the measured forces in the drawing operation, but does capture the peak force relatively well.

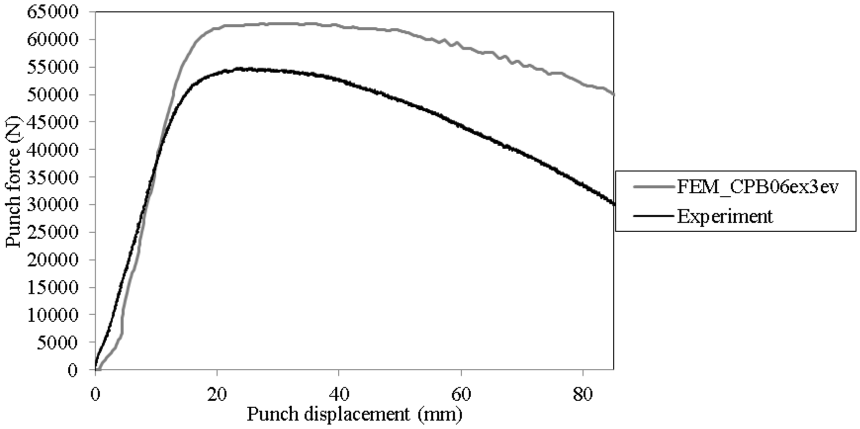

Figure 29. Punch force *vs.* punch displacement curves - comparison between the predictions and the measured loads.

The measured and predicted major and minor strain distribution along the rolling and transverse directions of fully drawn cups are compared in Figure 30. The simulation shows a longer curvilinear length from the pole of the cup (indicated as region “a” in Figure 30) to the flange edge, resulting from a generally a higher predicted major strain in the wall region. The CPB06ex3ev model captures the trends between the rolling and the transverse strain distributions, with larger strains occurring along the sheet rolling direction. The higher strains in the model likely reflect the predicted higher force levels which again may be due to frictional effects, for example. A potentially more significant issue is the fact that the model is only calibrated to 8% effective plastic strain while the deformation experienced during deep drawing of a cup is larger than five times that value. Thus, improvement in the prediction capability of the model is expected if a larger range of effective plastic strain is considered for the calibration.

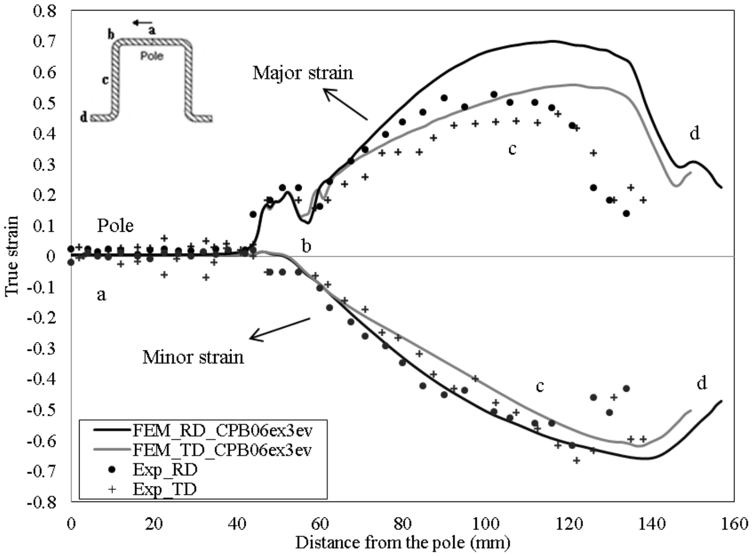

Figure 30. Major and minor strain distribution along the rolling and transverse directions from the simulations and the experiments. Error bars are not shown for clarity; however, the average absolute deviation from the mean was approximately 0.03 and 0.04 for the ε_1 and ε_2 curves along the RD. The average absolute deviation from the mean for the ε_1 and ε_2 curves along the TD was 0.01 and 0.02.

5. DISCUSSION

A detailed characterization of the constitutive response of AZ31B-O has been performed, in particular considering tension/compression asymmetry and the complex temperature and strain rate sensitivity of this material which are of importance during warm forming operations. At room temperature, in addition to the differences in the tensile and compressive strengths, the data reveals significant tension-compression anisotropy/asymmetry in both the measured *r*-values and the evolution of the *r*-values with accumulated plastic strain. A mild strain rate sensitivity of both flow stresses and *r*-values is observed at room temperature, while higher strain rate sensitivity is observed at elevated temperatures. A reduction in the anisotropy and asymmetry of the mechanical behavior is observed as the temperature is elevated. Moreover, a reduction in the evolution of *r*-values with respect to the accumulated plastic strain is seen at elevated temperatures, in agreement with the results from prior work by Agnew and Duygulu [14].

An important achievement of this work is the development of a material model capable of capturing the complex evolving material response considering proportional loading conditions. A saturation-type interpolation function is introduced which enables interpolation between the fitted yield function parameters. The yield function is extended beyond the calibration range by turning interpolation functions into constants at the end of the fitted strain range (in this case, an effective plastic strain of 0.08). In addition, the current approach considers calibration of the yield function parameters to capture both yield stresses and *r*-values over the entire range of the calibration experiments. Furthermore, material asymmetry is captured by fitting evolving yield function coefficients for both tension and compression, thereby capturing evolving asymmetry in strength and *r*-values. A good correlation between the material model response and the measured material characterization data was obtained through this method. Moreover, the current work demonstrates the importance of utilizing higher order stress transformations to fully capture the material behavior. In this case, three transformations were necessary to properly capture the evolving yield asymmetry and mechanical response in the measured response of AZ31B.

A strain rate insensitive material model has been initially developed for room temperature; however, a temperature and strain rate dependent hardening model was later implemented to account for the measured material behavior at elevated temperatures. A Nadai-type hardening model was modified within this work to capture the measured temperature/strain rate sensitivity of AZ31B.

The developed model was utilized within this work to simulate room temperature 3-point bending and elevated temperature forming experiments. Considering the 3-point bending simulations, the current model shows improvement in the prediction of bending stress distribution within the sheet by accounting for the evolving asymmetry; however, the predicted forming forces and strains in the current three-point bending experiment were similar to those predicted using a non-evolving CPB06ex3 approach. To assess the mechanical response along more arbitrary loading conditions and at elevated temperatures, limiting dome height and cup draw forming experiments were simulated. For both experiments, the predicted forming forces and strain distributions along the rolling and the transverse directions are reasonably close to the experimental measurements. It is noteworthy that the current model has the potential to be calibrated along arbitrary loading paths, such as plane strain; however, the calibrations within this work have been limited to the uniaxial tension and compression load paths as well as equi-biaxial loading.

Beyond the constitutive characterization and modelling effort, the formability experiments have provided interesting insight into the effect of temperature and temperature distribution within AZ31B sheet. Two modes of failure have been identified at the process window boundaries in which the cup either fractures due to low temperature (brittle) failure or a high temperature (necking) failure. All of the cases for which the die and punch temperature drop below 200°C result in brittle failure at the punch nose. Low temperature failure is alleviated to some degree as the die temperature is increased, corresponding to the lower limit in the formability window, since the stresses in the cup wall are reduced. So-called high temperature failures represent ductile failure modes that occur when the blank center temperature is too high and excessive softening results in the cup wall being unable to support the stresses required to draw the cup. As the severity of the forming operation increases, for example through increased draw ratio or punch speed, one can anticipate a shift in the process boundaries. The current work has served to show the existence of a process window for magnesium alloy sheet in which the blank center temperature must lie below the die temperature but above the enhanced slip activation temperature of roughly 120°C.

6. CONCLUSION

The following conclusions are drawn from this research:

- A strong, evolving tension/compression asymmetry in both flow stresses and *r*-values of AZ31B was observed. The compressive *r*-values are initially lower than the tensile *r*-values; however, the rate of *r*-value evolution with accumulated plastic strain is higher under compression loading. The anisotropy and asymmetry of *r*-values reduces at higher temperatures while the mechanical response becomes more strain rate dependent.
- The proposed continuum-based plasticity yield function, CPB06ex3ev, has been shown to capture the evolving anisotropic/asymmetric response, in terms flow stress and *r*-values, for proportional loading of HCP metals such as magnesium alloy AZ31B.
- A temperature/strain rate dependent hardening model, when coupled with the CPB06ex3ev model, has been shown to accurately capture rate hardening and thermal softening at elevated temperatures.
- The CPB06ex3ev material model provides improved predictions of bending stress distribution relative to a symmetric yield function such as von Mises; however, the predicted load *versus* displacement response and strain distributions for the current three-point bending tests using the evolving and non-evolving CPB models were similar.
- The CPB06ex3ev material model coupled with temperature/strain rate dependent hardening models provides qualitative predictions of forming forces and strain distributions within height dome test and deep drawing simulations.
- Warm forming of magnesium alloy sheet can be enhanced considerably through the use of elevated forming temperatures, as demonstrated by the isothermal deep draw experiments. Drawability is further enhanced through the introduction of non-isothermal conditions. There exists a process window in terms of the difference in temperature between the punch nose and flange regions within which a successful draw can be made for a given draw ratio.

7. FUTURE WORK

The following future work is proposed as next steps to support the commercial implementation of magnesium alloys:

- The current model has been calibrated for accumulated plastic strain up to 8%. A larger range of calibration has to be considered for the simulation of most metal forming processes.
- The current model does not consider reverse loading conditions and the mechanical response modeling of twinning and un-twinning deformation mechanisms are left to future research.
- The strain rate sensitivity of AZ31B-O under tensile testing is investigated in current research; however, strain rate sensitivity under arbitrary loading paths; such as compression, equibiaxial and shear, needs to be investigated.
- The biaxial tensile flow stress is currently considered for the calibration of CPB06ex3ev model; however, the biaxial tensile *r*-value should also be included in the future work.
- An evolving asymmetric/anisotropic yield surface formulation has been developed considering the evolution of both flow stresses and *r*-values along different sheet orientations in terms of accumulated plastic strain; however, including the strain rate sensitivity of *r*-values in the model is subject of future research.
- The process window defined in the current work is defined at a draw ratio (DR) of 2.25. Investigating the effect of draw ratio on the non-isothermal process window is left for future work.

REFERENCES

[1] O. Cazacu, B. Plunkett and F. Barlat, "Orthotropic yield criterion for hexagonal closed packed metals," *International Journal of Plasticity,* vol. 22, pp. 1171-1194, 2006.

[2] B. Mordike and T. Ebert, "Magnesium Properties-applications-potential," *Materials Science and Engineering A,* vol. 302, pp. 47-45.

[3] C. Bettles and M. Gibson, "Current wrought magnesium alloys: Strengths and Weaknesses," *Journal of Minerals, Metals and Materials,* pp. 46-49, 2005.

[4] M. Easton, A. Beer, M. Barnett, C. Davies, G. Dunlop and Y. Durandet, "Magnesium alloy applications in automotive structures," *JOM,* vol. 60, pp. 57-62, 2008.

[5] X. Lou, M. Li, R. Boger, S. Agnew and R. Wagoner, "Hardening evolution of AZ31B Mg sheet," *International Journal of Plasticity,* vol. 23, pp. 44-86, 2007.

[6] E. Kelley and W. Hosford Jr., "The deformation characteristics of textures magnesium alloys," *Trans TMS-AIME,* vol. 242, pp. 654-661, 1968.

[7] S. Agnew and Ö. Duygulu, "A mechanistic understanding of the formability of magnesium: examining the role of temperature on the deformation mechanisms," *Mater. Sci. Forum,* Vols. 419-422, pp. 177-188, 2003.

[8] S. Agnew, M. Yoo and C. Tome, "Application of texture simulation to understanding mechanical behavior of Mg and solid solution alloys containing Li or Y," *Acta Mater.,* vol. 49, pp. 4277-4289, 2001.

[9] B. Beausir, L. Tóth, F. Qods and K. Neale, "Texture and Mechanical Behavior of Magnesium During Free-End Torsion," *Journal of Material Engineering Technology,* vol. 131, pp. 5061-5077, 2009.

[10] G. Taylor, "Plastic strain in metals," *Journal of institute of Metals,* vol. 62, p. 307, 1938.

[11] U. Knocks and D. Westlake, "The importance of twinning for ductility of CPH polycrystals," *TMS-AIME,* vol. 239, pp. 1107-1109, 1967.

[12] J. Del Valle and O. Ruano, "Effect of anealing treatments on the anisotropy of magnesium alloy sheet processes by severe rolling," *Materials Letters,* vol. 63, pp. 1551-1554, 2009.

[13] J. Kallend, U. Kocks, A. Rollett and H.-R. Wenk, "Operational texture analysis," *Material Science & Engineering: A,* vol. 132, pp. 1-11, 1991.

[14] S. Agnew and Ö. Duygulu, "Plastic anisotropy and the role of non-basal slip in magnesium alloy AZ31B," *International Journal of Plasticity,* vol. 21, pp. 1161-1193, 2005.

[15] J. Jiang, A. Godfreyb and Q. Liu, "Microstructure and texture evolution during warm compression of magnesium alloy AZ31," *Science China,* vol. 52, pp. 186-189, 2009.

[16] A. Jain and S. Agnew, "Modeling the temperature dependent effect of twinning on the behaviour of magnesium alloy AZ31B," *Materials Science & Engineering,* vol. 462, pp. 29-36, 2007.

[17] T. Kuwabara, "Advances in experiments on metal sheets and tubes in support of constitutive modeling and forming simulations," *International Journal of Plasticity,* vol. 23, pp. 385-419, 2007.

[18] T. Cheng Wen, X. Shanna, W. Lu, C. Zhiyoung, W. Fu chi and C. Hong nian, "Effect of temperature on mechanical behavior of AZ31 magnesium alloy," *Transactions of Nonferrous Metals Society of China,* vol. 17, pp. 41-45, 2007.

[19] A. Khan, A. Pandey, T. Gnaupel-Herold and R. Mishra, "Mechanical response and texture evolusion of AZ31 alloy at large strains for different strain rates and temperatures," *International Journal of Plasticity,* vol. 27, no. 5, pp. 688-706, 2011.

[20] R. Boger, R. Wagoner, F. Barlat, M. Lee and K. Chung, "Continuous, large strain, tension/compression testing of sheet material," *International Journal of Plasticity,* vol. 21, pp. 2319-2343, 2005.

[21] T. Naka, T. Uemori, R. Hino, M. Kohzu, K. Higashi and F. Yoshida, "Effects of strain rate, temperature and sheet thickness on yield locus of AZ31 Magnesium alloy sheet," *Journal of Material Processing Technology,* vol. 201, pp. 395-400, 2008.

[22] M. Geiger, M. Merklein, W. Hußnätter and M. Grüner, "Experimental determination of yield loci for magnesium alloy AZ31 under biaxial tensile stress conditions at elevated temperatures," *Computer Aided Engineering,* vol. 2, pp. 303-310, 2008.

[23] F. Barlat, "Material modeling for sheet metal forming simulation," in *Numisheet 2008,* Interlaken, Switzerland, 2008.

[24] F. Barlat, H. Aretz, J. Yoon, M. Karabin, J. Brem and R. Dick, "Linear transfomation-based

anisotropic yield functions," *International Journal of Plasticity,* vol. 21, pp. 1009-1039, 2005.

[25] R. von Mises, "Mechanik der festen Körper im plastisch deformablen zustand," *Göttin. Nachr. Math. Phys.,* vol. 1, pp. 582-592, 1913.

[26] R. Hill, Mathematical theory of plasticity, Clarendon Press, 1950.

[27] F. Barlat, Y. Maeda, K. Chung, M. Yanagawa, J. Brem, Y. Hayashida, D. Lege, K. Matsui, S. Murtha, S. Hattori, R. Becker and S. Makosey, "Yield function development for aluminum alloy sheet," *Journal of Mechanics and Physics of Solids,* vol. 45, pp. 1727-1763, 1997.

[28] F. Barlat, J. Brem, J. Yoon, K. Chung, R. Dick, R. Lege, F. Pourboghrat, S. Choi and E. Chu, "Plane stress yield function for aluminum alloys sheets-part I: Theory," *International Journal of Plasticity,* vol. 19, pp. 1297-1319, 2003.

[29] O. Cazacu and F. Baralat, "Generalization of Drucker's yield criterion to orthotropy," *Mathematics and Mechanics of Solids,* vol. 6, pp. 613-630, 2001.

[30] D. Drucker, "Relation of experiments to mathematical theories of plasticity," *Journal of Applied Mechanics,* vol. 16, pp. 349-357, 1949.

[31] O. Cazacu and F. Barlat, "Application of theory of representation to describe yielding of anisotropic aluminum alloys," *International Journal of Engineering Science,* vol. 41, pp. 1367-1385, 2003.

[32] O. Cazacu and F. Baralat, "A criterion for description of anisotropy and yield differential effects in pressure-insensitive metals," *International Journal of Plasticity,* vol. 20, pp. 2027-2045, 2004.

[33] O. Cazacu and F. Baralat, "A criterion for description of anisotropy and yield differential effects in pressure-insensitive metals," *International Journal of Plasticity,* vol. 20, pp. 2027-2045, 2004.

[34] D. Banabic, D. S. Comsa, M. Sester, M. Selig, K. Kubli, K. Mattiasson and M. Sigvant, "Influence of constitutive equations on the accuracy of prediction in sheet metal forming simulation," in *Numisheet*, Interlaken, Switzerland, 2008.

[35] B. C. O. B. F. Plunkett, "Orthotropic yield criteria for description of the anisotropy in tension and compression of sheet metals," *International Journal of Plasticity,* vol. 24, pp.

847-866, 2008.

[36] B. Plunkett, R. Lebensohn, O. Cazacu and F. Barlat, "Anisotropic yield function of hexagonal materials taking into account texture development and anisotropic hardening," *Acta Materialia,* vol. 54, pp. 4159-4169, 2006.

[37] R. Lebensohn and C. Tome, "A self-consistent anisotropic approach for the simulation of plastic deformation and texture development of the polycrystals: Application to Zirconium alloys," vol. 41, pp. 2611-2624, 1992.

[38] J. Kim, H. Ryou, D. Kim, D. Kim, W. Lee, S. Hong and K. Chung, "Constitutive law for AZ31B Mg alloy sheets and finite element simulation for three-point bending," *International Journal of Mechanical Sciences,* vol. 50, pp. 1510-1518, 2008.

[39] M. Lee, S. Kim, R. Wagoner, K. Chung and H. Kim, "Constitutive modeling for anisotropic/asymmetric hardening behaviour of magnesium alloy sheets," *International Journal of Plasticity,* vol. 24, pp. 545-582, 2008.

[40] M. Lee, S. Kim, R. Wagoner, K. Chung and H. Kim, "Constitutive modeling for anisotropic/asymmetric hardening behaviour of magnesium alloy sheets: Application to sheet springback," *International Journal of Plasticity,* vol. 25, pp. 70-104, 2009.

[41] M. Li, X. Lou, J. Kim and R. Wagoner, "An efficient constitutive model for room-temperature, low-rate plasticity of annealed Mg AZ31B sheet," *International Journal of Plasticity,* vol. 26, pp. 820-858, 2010.

[42] J. Lévesque, K. Inal, K. Neale and R. Mishra, "Numerical modeling of formability of extruded magnesium alloy tubes," *International Journal of Plasticity,* vol. 26, 2010.

[43] S. Kalidindi and S. Schonefeld, "On the prediction of the yield surfaces by crystal plasticity models for fcc polycrystals," *Materials Science & Engineering,* vol. A293, pp. 120-129, 2000.

[44] W. Tang, S. Zhang, Y. Peng and D. Li, "Simulation of magnesium alloy AZ31 sheet during cylindrical cup drawing with rate independent crystal plasticity finite element method," *Computational Materials Science,* vol. 46, pp. 393-399, 2009.

[45] A. Izadbakhsh, K. Inal, R. Mishra and M. Niewczas, "New crystal plasticity constitutive model for large strain deformation in single crystals of magnesium," *Computational Materials Science,* vol. 50, no. 7, 2011.

[46] S. Zhang, K. Zhang, Y. Xu, Z. Wang, Y. Yu and Z. Wang, "Deep-drawing of magnesium alloy sheets at warm temperatures," *Journal of Material Processing Technology,* vol. 185, pp. 147-151, 2007.

[47] Y. Lian-fa, M. Ken-ichiro and T. Hirokazu, "Deformation behaviour of magnesium alloy AZ31 sheet in cold deep drawing," *Transactions of Nonferrous Metals Society of China,* vol. 18, pp. 86-91, 2008.

[48] K. Mori and H. Tsuji, "Cold deep drawing of commercial magnesium alloy sheets," *CIRP Annals-Manufacturing Technology,* vol. 56, pp. 285-288, 2007.

[49] Y. Lee, M. Kim, S. Kim, S. Kwon, S. Choi and S. Lee, "Experimental and analytical studies for forming limit of AZ31 alloy on warm sheet metal forming," *Journal of Material Processing Technology,* Vols. 187-188, pp. 103-107, 2007.

[50] F. Chen, T. Huang and C. Chang, "Deep drawing of square cups with magnesium alloy AZ31 sheets," *International Journal of Machine Tools and Manufature,* vol. 43, pp. 1553-1559, 2003.

[51] S. Kaya, G. Spampinato and T. Altan, "An experimental study on nonisothermal deep drawing process using aluminum and magnesium alloys," *Journal of Manufacturing Science and Engineering,* vol. 130, p. 11, 2008.

[52] G. Palumbo, D. Sorgente, L. Tricarico, S. Zhang and W. Zheng, "Numerical and experimental investigation on the effects of the heating strategy and the punch speed on the warm deep drawing of magnesium alloy AZ31," *Journal of Materials and Processing Technology,* vol. 191, pp. 342-346, 2007.

[53] H. Palaniswamy, G. Ngaile and T. Altan, "Finite element simulation of magnesium alloy sheet forming at elevated temperatures," *Journal of Material Processing Technology,* vol. 146, pp. 52-60, 2004.

[54] G. Amrogio, C. Bruni, S. Bruschi, L. Filice, A. Ghiotti and M. Simoncini, "Charactrisation of AZ31B magnesium alloy formability in warm forming conditions," Lyon, 2007.

[55] S. Choi, H. Kim, S. Hong, Y. Shin, G. Lee and H. Kim, "Evaluation and prediction of forming limit of AZ31B magnesium alloy sheets in a cross-shaped cup deep drawing process," *Metals and Materials International,* vol. 15, pp. 575-584, 2009.

[56] K. Piao, J. Lee, J. Kim, H. Kim, K. Chung and F. Barlat, "A sheet tension/compression test for elevated temperature," *International Journal of Plasticity,* vol. 38, pp. 27-46, 2012.

[57] R. Bagheriasl and M. Worswick, "Formability of AA3003 brazing sheet at elevated temperatures: limiting dome height tests and determination of forming limit diagrams," *International Journal of Material Forming,* 2013.

[58] A. Khan, R. Kazmi, A. Pandey and T. Stoughton, "Evolution of subsequent yield surfaces and elastic constants with finite plastic deformation. Part- A very low work hardening aluminum alloy (Al6061-T6511)," *International Journal of Plasticity,* vol. 25(9), pp. 1611-1625, 2009.

[59] J. Simo and M. Ortiz, "A unified approach to finite deformation elastoplastic anaysis based on the use of hyperelastic constitutive equations," *Computer methods in applied mechanics and engineering,* vol. 49, pp. 221-245, 1985.

[60] D. Hasenpouth, "Tensile High Strain Rate Behavior of AZ31B Magnesium Alloy Sheet," M.Sc. Thesis, University of Waterloo, 2010.

[61] G. Cowper and P. Symonds, "Strain hardening and strain rate effects in the impact loading of cantilever beams," Brown University, 1957.

[62] A. Van den Boogaard and J. Huétink, "Simulation of aluminum sheet forming at elevated temperatures," *Computer Methods in Applied Mechanics and Engineering,* vol. 195, p. 6691–6709, 1996.

[63] K. Nakazima, T. Kikuma and K. Hasuka, "Technical report 264," Yawata Iron & Steel Co., 1968.

[64] E. Canada, "www.ec.gc.ca," 2005. [Online].

[65] M. Nebebe Metoken, "Mechanical charactrisation of Mg alloys and model parameter identification for sheet forming simulations," in *Esaform Conference*, Enschede, Netherlands, 2009.

[66] F. Barlat, D. Lege and J. Brem, "A six component yield function for anisotropic materials," *Int. J. of Plasticity,* pp. 693-712, 1991.

[67] F. Barlat and J. Lian, "Plastic Behavior and Stretchability of Sheet Metals. Part I: Yield Function for Orthotropic Sheets under Plane Stress Conditions," *International Journal of Plasticity,* pp. 51-66, 1989.

[68] O. Cazacu and F. Baralat, "Generalization of Drucker's yield criterion to orthotropy," *Mathematics and Mechanics of Solids,* vol. 6, pp. 613-630, 2001.

[69] T. Kuwabara, Y. Kumano, J. Ziegelheim and I. Kurosaki, "Tension-compression asymmetry of phosphor bronze for electronic parts and its effect on bending behavior," *International Journal of Plasticity,* vol. 25, pp. 1759-1776, 2009.

[70] M. Nebebe Mekonen, D. Steglich, J. Bohlen, L. Stutz, D. Letzig and J. Mosler, "Experimental and numerical investigation of Mg alloy formability," *Materials Science and Engineering A,* vol. 586, pp. 204-214, 2013.

[71] K. Piao, K. Chung, M. Lee and R. Wagoner, "Twinning-Slip Transitions in Mg AZ31B," *Metallurgical and Materials Transactions A,* vol. 43, pp. 3300-3313, 2012.

[72] H. Wang, P. Wu, W. J. and C. Tomé, "A crystal plasticity model for hexagonal close packed (HCP) crystals including twinning and de-twinning mechanisms," *International Journal of Plasticity,* vol. 49, pp. 36-52, 2013.

[73] H. Wang, P. Wu and J. Wang, "Modeling inelastic behavior of magnesium alloys during cyclic loading-unloading," *International Journal of Plasticity,* vol. 47, pp. 49-64, 2013.

[74] N. Abedrabbo, F. Pourboghrat and J. Carsley, "Forming of aluminum alloys at elevated temperatures-Part I: Material charactrization," *International Journal of Plasticity,* vol. 22, pp. 314-341, 2006.

[75] F. Barlat, J. Brem, J. Yoon, K. Chung, R. Dick, R. Lege, F. Pourboghrat, S. Choi and E. Chu, "Plane Stress yield function for aluminum alloys sheets-part I: Theory," *International Journal of Plasticity,* vol. 19, pp. 1297-1319, 2000.

[76] J. Danckert and K. Nielsen, "Determination of the R-Value using automatic tensile test equipment," *Annals of CIRP,* vol. 46, pp. 159-162, 1997.

[77] S. Ertürk, D. Steglich, J. Bohlen, D. Letzig and W. Brocks, "Modelling and simulation of Extrusion of Magnesium Alloys," in *Esaform*, Lyon, 2008.

[78] S. Ertürk, D. Steglich, J. Bohlen, D. Letzig and W. Brocks, "Thermo-mechanical modelling of indirect extrusion process for magnesium alloys," Enschede, Netherlands, 2009.

[79] M. Geiger, M. Merklein, W. Hussnäter and M. Grüner, "Experimental determination of yield loci for magnesium alloy AZ31 under biaxial tensile stress conditions at elevated temperatures," vol. 2, pp. 303-310, 2008.

[80] S. Kaya, T. Altan, P. Groche and C. Klöpsch, "Determination of flow stress of magnesium AZ31-O sheet at elevated temperatures using the hydraulic bulge test," *International*

Journal of Machine Tools and Manufacturing, vol. 48, pp. 550-557, 2008.

[81] Y. Maeda, M. Yanagawa, F. Barlat, K. Chung, Y. Hayashida, S. Hattori, K. Matsui, J. Brem, D. Lege, S. Murtha and T. Ishikawa, "Experimental analysis of aluminum yield surface for binary Al-Mg alloy sheet samples," *International Journal of Plasticity,* vol. 14, pp. 301-318, 1998.

[82] K. Siegert, S. Jäger and M. Vulcan, "Pneumatic bulging of Magnesium AZ31 sheet metals at elevated temperatures," *CIRP Annals - Manufacturing Technology,* vol. 52, pp. 241-244, 2003.

Appendix A: D. Ghaffari Tari, M.J. Worswick, S. Winkler, *Experimental studies of deep drawing of AZ31B magnesium alloy sheet under various thermal conditions,* Journal of Materials processing technology 213, 1337-1347.

Journal of Materials Processing Technology 213 (2013) 1337–1347

Contents lists available at SciVerse ScienceDirect

Journal of Materials Processing Technology

journal homepage: www.elsevier.com/locate/jmatprotec

Experimental studies of deep drawing of AZ31B magnesium alloy sheet under various thermal conditions

D. Ghaffari Tari[a,*], M.J. Worswick[a], S. Winkler[b]

[a] University of Waterloo, 200 University Ave West, Waterloo, Ontario, Canada
[b] Dana Power Technologies, Mississauga, Ontario, Canada

ARTICLE INFO

Article history:
Received 2 July 2012
Received in revised form
22 December 2012
Accepted 5 January 2013
Available online 13 February 2013

Keywords:
Deep drawing
Magnesium alloy sheet
Warm forming
Non-isothermal deep drawing
Thermal gradient

ABSTRACT

The effect of temperature and temperature gradient within the blank on formability of AZ31B-O magnesium alloy is investigated. The effect of blank size on the success of isothermal deep drawing is studied. As blank size increases, forming under isothermal conditions becomes more difficult. To address this issue, non-isothermal forming is investigated and a formability window is identified in which the temperature at the punch nose must lie below the flange temperature to promote enhanced drawability, but above the temperature for activation of non-basal slip systems (to avoid low temperature fracture). The effect of punch speed on the forming forces, thickness and strain distribution within the formed cup is also investigated. At higher punch speeds, small cracks initiate at the punch radius region which increases the possibility of failure. Finally, the fracture surfaces from each thermal condition are observed using scanning electron microscopy. It is demonstrated that the fracture mechanism during deep drawing of magnesium alloy AZ31B is dependent on the forming temperature which controls the active deformation mechanisms.

1. Introduction

Increasingly stringent goals set by governments to limit the emission of greenhouse gases and the demand by customers for fuel efficient vehicles, motivate the automotive industry to research approaches to reduce fuel consumption and associated emissions. One method to reduce fuel consumption is to introduce lightweight materials within the vehicle body. Magnesium alloys offer a high strength-to-density ratio and are considered as a potential replacement material for commonly used metals in automotive applications, such as aluminum and mild steel. At present, most magnesium components used in cars are produced by die-casting (Easton et al., 2008). Therefore, increased use of wrought magnesium can significantly reduce both vehicle weight and fuel consumption (Environment Defense Fund, 2008). However, magnesium alloys exhibit low formability at room temperature (Lou et al., 2007). Khan et al. (2011) presented comprehensive stress–strain responses and texture measurements for an AZ31 magnesium alloy sheet, at different strain rates, temperatures and load paths. Positive strain rate sensitivity at room temperature was reported and the strain rate sensitivity increased with increase in temperature. Ghaffari Tari and Worswick (2011) investigated the effect of temperature on anisotropy and strain rate sensitivity of AZ31B-O magnesium alloy at room temperature and 200 °C. At elevated temperatures, lower *R*-values were measured and the measurements were more sensitive to the strain rate. A significant improvement in the formability of magnesium alloys at elevated temperatures has been reported (Zhang et al., 2007). Lee et al. (2007) considered three forming temperatures for deep drawing of square cups; namely, room temperature, 250 °C and 400 °C. A better formability was reported at 250 °C. Ambrogio et al. (2008) investigated the formability of magnesium at different temperatures and punch speeds. The formability of magnesium increases as temperature is elevated and reduces as the punch speed is increased. Drawability improvements have been reported under non-isothermal forming conditions for magnesium and aluminum alloys. Yoshihara et al. (2003) applied non-isothermal forming conditions for magnesium alloys along with variable blank holder force to increase the limit drawing ratio (LDR) up to 5. Kaya et al. (2008) investigated the effect of constant and variable punch velocities using non-isothermal forming conditions. Less thickness reduction was reported in cases where a variable punch speed was considered for forming. Palumbo et al. (2007) investigated the effect of a thermal gradient between the blank center and the flange by using a heated blank holder and a cooled punch. It was concluded that a cooled punch can improve the formability in cases when the die set is above a certain temperature. Palaniswamy et al. (2004) conducted a non-isothermal finite element simulation for

---

[*] Corresponding author. Tel.: +1 (519)7290919.
E-mail addresses: dghaffar@uwaterloo.ca (D. Ghaffari Tari), worswick@lagavulin.uwaterloo.ca (M.J. Worswick), sooky.winkler@dana.com (S. Winkler).

0924-0136/$ – see front matter © 2013 Elsevier B.V. All rights reserved.
http://dx.doi.org/10.1016/j.jmatprotec.2013.01.028

forming of round cups and rectangular pans at elevated temperatures. The simulation results were compared to experiments; an increase in limiting draw ratio (LDR) was reported with increase in temperature. Although prior research reported improvements by using non-isothermal forming conditions, the mechanisms of this improvement was not investigated.

In this paper, the effects of different process parameters such as forming temperature, temperature difference between the punch and dies, as well as punch speed are investigated. AZ31B magnesium alloy sheet in the O-temper condition is considered for this study. Of particular interest is the potential for non-isothermal forming to improve the formability of magnesium alloy sheet. In general, non-isothermal processes introduce the benefit of softening the warmer flange region to make flow into the die cavity easier while maintaining a lower temperature at the punch nose to increase the strength of the cup in this region, thereby suppressing fracture. A critical aspect of magnesium formability is to limit the temperature reduction at the punch nose since magnesium becomes brittle if the temperature drops too low. These limits imply the existence of a process window which is also investigated herein.

In the current research, in order to have an independent control over the temperature within each of the tooling components (punch, die, and blank holder), three separate controllers for the heating system are used. In addition, an optional water cooling system is available for the punch for cases in which lower punch temperatures are required. In contrast to previous research done on warm formability of magnesium, the separate heating/cooling system embedded in the punch allows consideration of a wider range of temperature gradient within the blank ranging from near-isothermal conditions to conditions associated with large differences between the punch and die temperatures. This experimental configuration enables determination of the temperature process window for more optimal deep drawing of magnesium alloy sheet. Four different temperature levels (200 °C, 225 °C, 245 °C and 295 °C) are used for the die and blank holder and the punch temperature was varied in the range 20–295 °C to investigate the effect of temperature difference between the punch and dies. The effect of punch speed on forming forces, strain and thickness distribution within the formed cup is investigated. Finally, the fracture surfaces of the failed cups, formed under isothermal and non-isothermal conditions, are investigated using scanning electron microscopy (SEM) and optical microscopy.

2. Experimental procedure

Deep drawing experiments are performed using an instrumented double-action hydraulic press. Fig. 1a shows a schematic of the experimental setup. The press used for the experiments is shown in Fig. 1b. The blank holder force and punch displacement are controlled by MTS servo-hydraulic controllers with a programmed data acquisition system using Labview. One actuator applies the blank holder force while another actuator imposes the punch movement. A constant blank holder force is applied for these experiments. The experimental setup consists of the die, blank holder and punch. Each tooling component is heated using embedded electrical heating elements. The temperature of each heating element is controlled independently. Thermocouples are used in each component to record and monitor the temperature. Note that the punch incorporated optional water cooling channels which were used to prescribe large difference in punch temperature relative to die temperature.

The blank is sandwiched between two layers of PTFE (Teflon) film to reduce friction. The Teflon film used is temperature resistant up to 300 °C. The PTFE film deforms with the blank and maintains a low coefficient of friction during deformation. McKinley (2010) conducted room temperature twist compression testing on Teflon

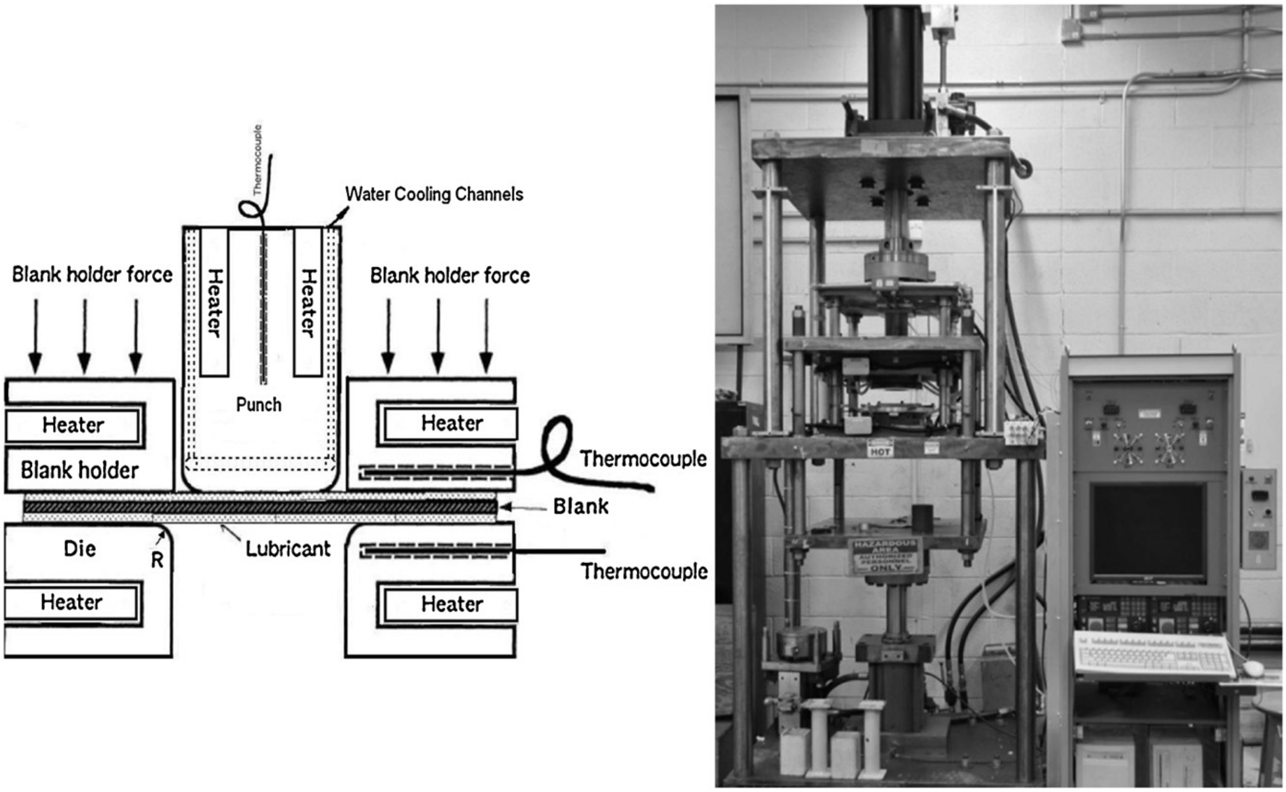

Fig. 1. (a) Deep drawing experimental setup schematic. (b) Double action hydraulic press and warm deep drawing tooling.

Table 1
Summary of the test conditions at near-isothermal conditions using different draw ratios.

Blank holder force (kN)	Drawing ratio	Die temperature (°C)	Punch temperature (°C)	Blank center temperature (°C)	Punch speed (mm/s)	Failure (Y/N)
29	1.75	225	215	205	4	N
48	2	225	215	207	4	N
80	2.25	225	217	211	4	Y
29	1.75	245	220	210	4	N
48	2	245	220	213	4	N
80	2.25	245	220	216	4	Y
29	1.75	295	262	255	4	N
48	2	295	264	260	4	N
80	2.25	295	267	269	4	Y

film. The coefficient of friction, independent of the applied pressure or sliding distance, was reported to be 0.043.

Two repeat experiments were performed for most conditions in the test matrix. For cases shown to lie near critical conditions (such as the draw limit for a particular blank size), three repeats were usually performed. A drawing ratio (DR) of 2.25 is adopted for most of the experiments, with the focus being the effect of the temperature distribution in the blank on draw depth. The outer diameter of the punch is 101.6 mm. The sequence of the experiments is as follows. Initially, the blank is positioned and centered on the die, after which the blank holder is closed. To control the temperature gradient within the blank, the punch is positioned within 1 mm of the blank surface and held in this position during a period referred to as the wait time or dwell time during which heating of the blank occurs. Forming begins at the end of the wait time.

2.1. Blank temperature

The temperature of the center of the blank (under the punch) prior to testing is determined by the punch temperature, the die temperature, the dwell time, and the nature of the heat conduction between the tooling and blank. It was not possible to measure the temperature of the blank within the tooling, although numerical prediction of the variation in temperature distribution during forming will be considered in future work. Note that a dwell time of 2 min was used for most of the experiments reported herein and the blank temperature was recorded prior to the start of each forming experiment. This data, along with the punch and die temperatures, is summarized in Tables 1–3, for the near-isothermal and non-isothermal experiments, respectively. There was some variation in the blank center temperature during forming, however, this was limited to 20 °C for a punch speed of 2 mm/s and only 5 °C at the highest punch speed of 32 mm/s. It is recognized that a dwell time of several minutes is not suitable for high volume production implementation; techniques to rapidly impose temperature gradients within blanks for non-isothermal forming are the focus of on-going research.

2.2. Blank holder force

Different blank holder forces are applied, ranging from 35,500 to 89,600 N. Fig. 2 illustrates the reduction of wrinkling at the flange region as the blank holder force is increased. The balance of the experiments is conducted using a blank holder force for which a wrinkle free cup is formed.

Only minor punch force variations were observed due to changes in the blank holder force from 35.5 kN to 89.6 kN. Consequently, a blank holder force of 80 kN was selected for all of the subsequent experiments with a drawing ratio of 2.25. For smaller blank sizes, the blank holder force was scaled accordingly to maintain the same initial pressure on the blank surface. Thus, blank holder forces of 28, 44 and 80 kN are used for 177.8, 203.2 and 228.6 mm blanks, respectively.

3. Results

Here, the effect of forming parameters on warm forming of AZ31B-O magnesium alloy sheet is presented. In Section 3.1, the effect of drawing ratio (DR) at three levels, 1.75, 2.0 and 2.25, on near-isothermal and isothermal forming of O-temper material is presented. The effect of non-isothermal forming on drawability is presented in Section 3.2. The effect of temperature gradient on forming forces and on the strain and thickness distribution within the formed cup is shown in Section 3.3. The effect of punch speed is investigated in Section 3.4. Finally, fractography observations to characterize the difference between fracture surfaces of

Table 2
Summary of the test conditions at difference temperature gradients within the blank (F = failed, S = safe).

Blank holder force (kN)	Drawing ratio	Die temperature (°C)	Punch temperature (°C)	Blank center temperature (°C)	Punch speed (mm/s)	Outcome (F/S)
35.5	2.25	200	197	195	4	2F
35.5	2.25	200	184	189	4	2F
35.5	2.25	200	170	180	4	2F
35.5	2.25	200	155	172	4	2F
35.5	2.25	200	93	135	4	2F
80	2.25	225	217	211	4	3F
80	2.25	225	133	160	4	2S
80	2.25	225	80	133	4	1F/2S
80	2.25	225	61	120	4	2F
80	2.25	245	241	227	4	2F
80	2.25	245	223	217	4	2S
80	2.25	245	160	191	4	2S
80	2.25	245	41	120	4	1F/1S
80	2.25	295	267	269	4	2F
80	2.25	295	136	206	4	4S
80	2.25	295	18	145	4	4S

Table 3
Summary of the test conditions at different punch speeds.

Blank holder force (KN)	Drawing ratio	Die temperature (°C)	Punch temperature (°C)	Blank center temperature (°C)	Punch speed (mm/s)	Failure (Y/N)
80	2.25	245	138	183	32	Y
80	2.25	245	135	185	32	N
80	2.25	245	135	186	16	N
80	2.25	245	136	185	8	N
80	2.25	245	134	182	4	N
80	2.25	245	135	188	2	N

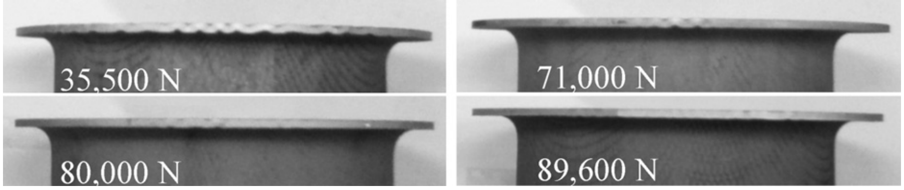

Fig. 2. Wrinkling at the flange of AZ31B-O cup using different blank holder forces, die and blank holder temperature at 250 °C, punch temperature at 135 °C and punch speed of 4 mm/s, using DR of 2.25.

near-isothermal and isothermal versus non-isothermal samples are given in Section 3.5.

3.1. Isothermal and near-isothermal forming

To investigate the effect of blank size on failure during near-isothermal conditions, three blank sizes 177.8, 203.2 and 228.6 mm were considered; representing drawing ratios (DRs) of 1.75, 2.0 and 2.25, respectively. At lower DRs, lower forming punch forces are needed (Fig. 3). To compensate for the effect of smaller area under the blank holder for lower DRs, the blank holder force is scaled down accordingly. The summary of test conditions is shown in Table 1. The punch force versus displacement curves for each drawing ratio under the same thermal condition and die temperature of 225 °C and 295 °C are shown in Fig. 3. The blank with highest size fails at a punch depth of 52 mm while the other two draw ratios are drawn fully. The comparison between the attainable draw depths from the experiments in Fig. 3 suggests that the limit drawing ratio (LDR) for the applied thermal condition is between 2.0 and 2.25.

Fig. 4 illustrates the cups drawn at 225 °C die temperature and 215 °C punch temperature using DRs of 2.25, 2.0 and 1.75. The cup with the DR of 2.25 failed while the other two cups were drawn fully. The drawing ratio (DR) has an important effect on obtaining a successful draw under critical thermal conditions such as near-isothermal forming conditions because it has a direct correlation to the stress levels within the cup as previously reported by Takuda et al. (2002). An improvement of the limiting drawing ratio (LDR) for magnesium alloys with a localized heating and cooling technique was reported by Yoshihara et al. (2003).

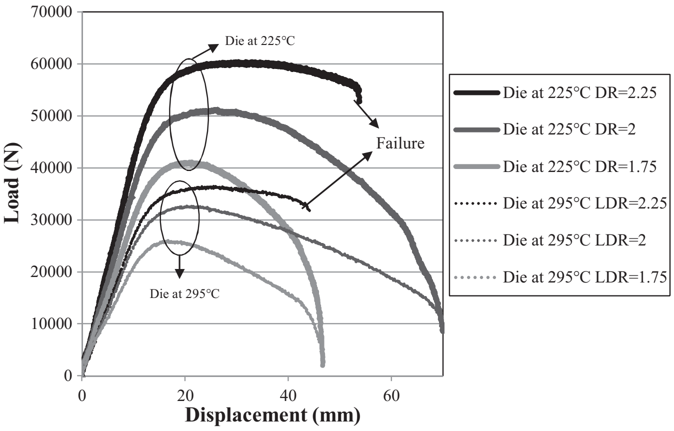

Fig. 3. Punch force versus displacement of AZ31B-O at die temperature of 225 and 295 °C, near-isothermal condition at punch temperature of 215 and 265 °C, 2 min wait time, using 2.25, 2.0 and 1.75 DR with blank holder force of 29 kN, 48 kN and 80 kN, respectively.

In an effort to form cups with DR exceeding 2.0 under near-isothermal conditions, experiments were performed with elevated die temperatures of 245 °C and 295 °C. However, no improvement in the draw performance was obtained for the samples with DR = 2.25. In addition, the punch force versus displacement curves for each blank size and temperature condition showed trends similar to those in Fig. 3, although a large drop in punch force is observed from forming at 225 °C to 295 °C. The results of the experiment with a die temperature of 245 °C are not shown for brevity.

To investigate the effect of blank holder force on failure under isothermal forming conditions, a smaller range of blank holding force from 4.45 to 35.5 kN was considered for a die temperature of 295 °C. In general, the cup failed at a draw depth of approximately 26–29 mm for all blank holder forces. Failure occurrence under isothermal and near-isothermal conditions appears difficult to avoid for a DR of 2.25.

3.2. Non-isothermal forming

In order to capture the effect of temperature distribution within the blank during the deep drawing process, a set of non-isothermal experiments at four die temperature levels are performed, namely 200 °C, 225 °C, 245 °C and 295 °C. Table 2 shows the summary of the critical experiments performed in this section. A number of 2–4 repetitions have been performed for each experimental case. The outcome of each case (failed/safe) is also shown in Table 2. The die and the blank holder are set to one of these four temperatures while the punch is varied from 10 °C to the die set temperature; the highest temperature corresponds to the isothermal case. Note that initial attempts to form the 2.25 DR cups with a die temperature of 200 °C resulted in failure of the cup. Consequently, the blank holder force for this die temperature was reduced to 35.5 kN in an attempt to produce formable cups, however, all of these cups also failed as reported in Table 2.

Fig. 5 shows force versus displacement curves for parts formed at a die and blank holder temperature of 200 °C. The achievable punch force and displacement to failure increases as the blank center temperature is reduced. Despite a lower blank holder force (35 kN) is applied at experiments with a die temperature of 200 °C, no cups could be formed at this draw ratio. The fracture surfaces of

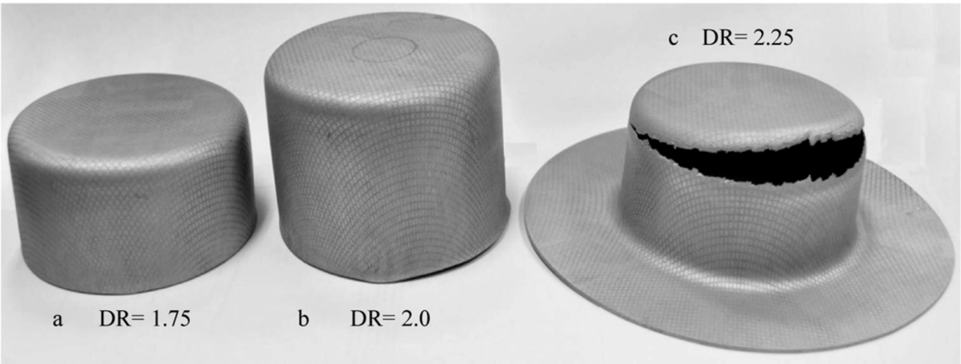

Fig. 4. AZ31B-O cups drawn at near-isothermal conditions and a die and blank holder temperature of 225 °C, a punch temperature of 215 °C and 2 min wait time. (a) LDR = 1.75. (b) LDR = 2.0. (c) LDR = 2.25.

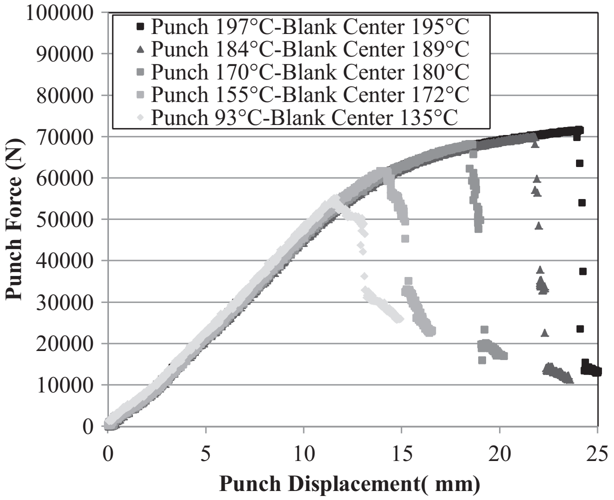

Fig. 5. Punch force versus displacement for deep drawing of AZ31B-O with different punch temperatures and a die temperature of 200 °C, punch speed of 4 mm/s, blank holder force of 35.5 kN, DR of 2.25 and 6 min wait time prior to forming.

cups formed at 200 °C are similar for all punch temperatures and are characteristic of a low temperature failure case.

Fig. 6 shows the punch force versus displacement curves for three forming cases with low, medium and high blank center temperature, all formed at a die temperature of 225 °C. Failure occurs in the two experiments with the most critical thermal conditions, namely the low temperature (cold punch) and the near-isothermal condition. The intermediate punch temperature case formed fully (see Figs. 6 and 7). The failure types corresponding to these thermal conditions are termed "low temperature" and "failure at high temperature". The fracture surfaces of each failure type formed at 225 °C are different and are compared in Section 3.5.

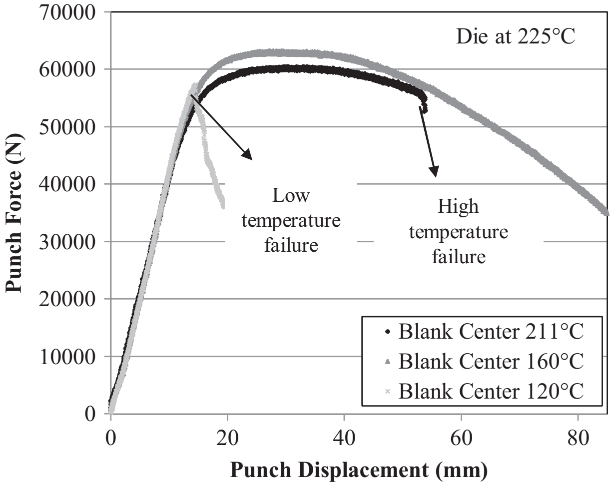

Fig. 6. Punch force versus displacement of AZ31B-O at different temperature gradients, die and blank holder kept at 225 °C, with punch speed of 4 mm/s, 80 kN blank holder force, DR of 2.25 and 2 min wait time.

Fig. 7 shows the three cups formed at thermal conditions presented in Fig. 6. Fig. 7a shows an early fracture due to low punch temperature and poor ductility while Fig. 7c shows the failure at near-isothermal conditions. The fully drawn cup in the middle is formed at 60 °C temperature difference between the center of the blank (at 160 °C) and the flange region (at 225 °C). Enhancements in the formability of aluminum alloys were reported by Li and Ghosh (2004) as a temperature difference between the punch and the dies was introduced. A similar trend was later observed in forming of magnesium alloys (Palumbo and Tricarico, 2007) in which a water cooled punch was used; however, the use of a heated punch with temperature control in the current research novel and enables a better understanding of the thermal process window for forming of magnesium alloys as seen in Fig. 7 and further discussed in Section 4.

The punch force versus displacement curves for experiments performed at 245 °C show similar trends of failure compared to Fig. 6. Note that for the 245 °C die temperature, 41–43 °C punch temperature condition, one sample drew fully whereas the second sample failed (Table 2). This mixed outcome suggests that this low blank temperature condition (120 °C) is very close to the process limit for a successful deep draw. A similar transition region was observed for a die temperature of 225 °C (blank center at 133 °C) in which one repetition out of 4 failed. All repetitions of the experiment with the blank center temperature of 120 °C and die temperature of 225 °C failed. This is actually a more severe case than the case with a die temperature of 245 °C since the flow stress of the flange region is higher at the die temperature of 225 °C, making forming more difficult compared to the case with 245 °C die temperature.

Fig. 8 shows the punch force versus displacement curves for three forming cases with low, medium and high blank center temperature, all formed at a die temperature of 295 °C, respectively. At a die temperature of 295 °C, low temperature failure does not occur (see Fig. 8) since it is hard to reduce the temperature of the punch region low enough to cause failure. At this temperature, the heat flux from the flange region to the blank center is so high that even a water-cooled punch could not reduce the temperature to levels at which ductility is poor. In addition, high temperature at the flange region reduces the flow stress which leads to a lower stresses within the blank and less likelihood of failure. It is interesting to note that

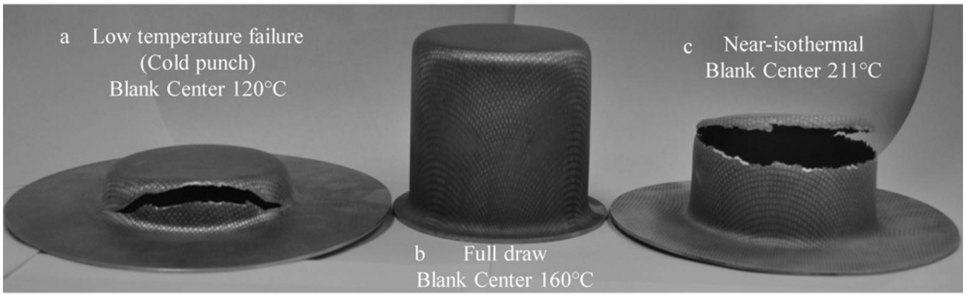

Fig. 7. Different failure conditions due to the temperature effects with die and blank holder temperature of 225 °C, punch speed of 4 mm/s, blank holder force of 80 kN and DR of 2.25. (a) Failure due to low punch temperature and poor ductility. (b) A full draw. (c) Failure due to a low temperature gradient within the cup (near-isothermal condition).

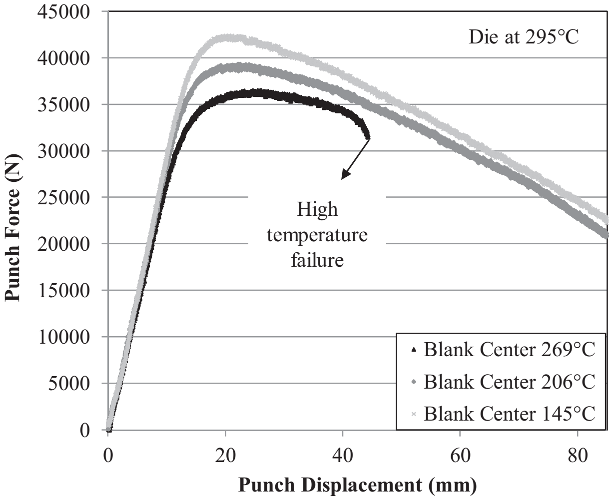

Fig. 8. Punch force versus displacement of AZ31B-O at different temperature gradients, die and blank holder kept at 295 °C, with punch speed of 4 mm/s, 80 kN blank holder force, DR of 2.25 and 2 min wait time.

failure occurs for the highest punch temperature since the difference in temperature (and strength) between the blank center and the flange was insufficient to allow the flange to be drawn into the die without failure at the punch nose.

Fig. 9 illustrates the draw depth at different blank center temperatures, for die temperatures of 200, 225, 245 and 295 °C. Fracture during deformation is used as a failure criterion and surface cracks are not considered as failure. Two modes of failure are indicated in this figure, namely low-temperature failure for cold punch conditions and failure at high temperature. Low-temperature failure occurs when the temperature within the blank is insufficient to impart adequate material ductility (activate higher temperature deformation systems). Failure at high temperature refers to failure cases in which the deformation mechanisms are active but the thermal difference between the flange region and the blank center is comparatively small (or no difference). The near-isothermal cases failed at a higher draw depth compared to the low temperature cases for which failure occurred during the early stages of deformation.

At a die temperature of 200 °C, an increase in draw depth was observed from 10 mm to 25 mm when the punch temperature was increased to near-isothermal conditions; however, a fully drawn cup was not obtained in any of the experiments performed at this die temperature. This mild increase of draw depth is attributed to an increase in material formability as the punch temperature approaches 200 °C. At die temperatures of 225, 245 and 295 °C, failure occurs at near-isothermal conditions. At all experiments using a cold punch and a die temperature of 295 °C, low temperature failure does not occur; however, surface cracks along the rolling direction at the punch radius are observed. This may indicate that failure occurrence at low temperature cases is due to a combination of limited active deformation systems at lower temperatures and higher forming forces required for forming the material at the flange region. In Fig. 9, at higher die temperatures a larger temperature difference between the blank center and the die is required for a successful draw. This is due to a strength drop in the material from 225 °C to 295 °C.

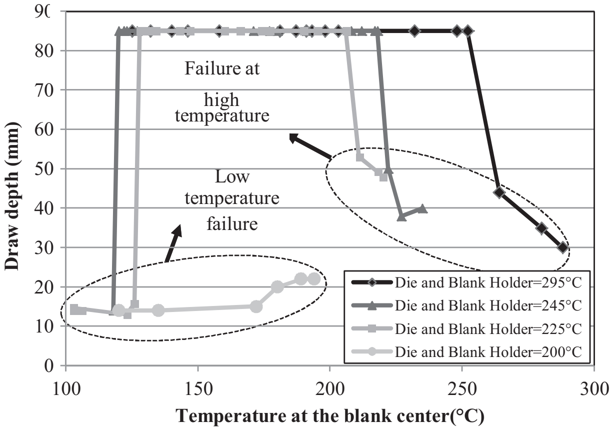

Fig. 9. Draw depth acquired under different temperatures gradients for 225, 245 and 295 °C die and blank holder temperature, punch speed of 4 mm/s, blank holder force of 80 kN (35 kN at 200 °C) and DR of 2.25. An 85 mm draw depth indicates a fully drawn cup.

3.3. *Effect of temperature gradient on strain*

To further understand the effect of temperature difference between the blank center and the flange region, two cups were formed at a die temperature of 245 °C, but with blank temperatures of either 217 °C or 120 °C, corresponding to near-isothermal and cold punch conditions, respectively. The major and minor strain distributions for these two temperature conditions, measured using a circle grid technique, are shown in Fig. 10a. The major strain in the near-isothermal experiment is generally higher in the wall region and is much higher around the punch radius (see Fig. 10a, region b). This trend is an indication of higher potential for necking and instability as conditions become more isothermal. The curvilinear length of the cup formed under near-isothermal conditions is longer compared to the other case. This is due to thinning at the wall region which leaves a larger flange region (see Fig. 10a and b, region d) for a given draw depth.

Fig. 10b shows the thickness distribution along the rolling direction of the same cups. The thickness distribution along the rolling direction is consistent with the strain measurements. The

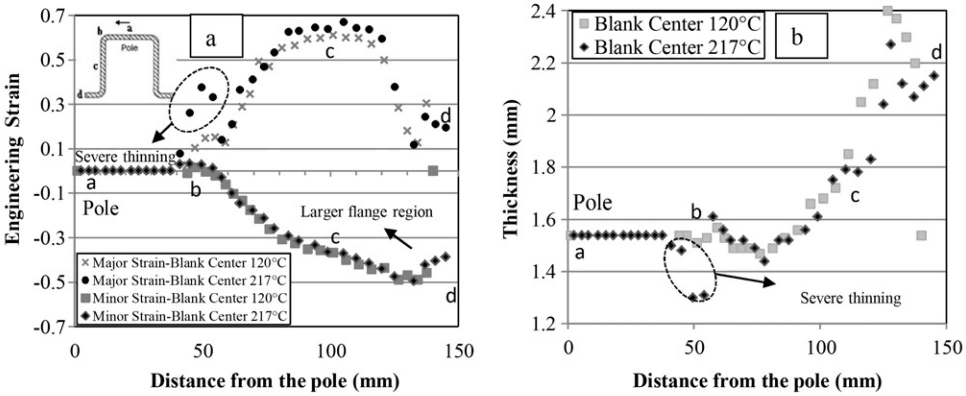

Fig. 10. (a) The major and minor strain distributions, (b) the thickness distribution along the rolling direction of two successfully draw cups. Die and binder temperature are 245 °C, punch speed is 4 mm/s, blank holder force is 80 kN, DR is 2.25.

maximum thinning occurs at the punch radius and is greatest for the near-isothermal case.

Close examination of the surfaces of these two cups reveals incipient failure for both temperature conditions since both exhibit small surface cracks in the punch radius region (Fig. 11). The figure on the left corresponds to the low temperature case (blank temperature = 120 °C) and incipient cracking is evident, although with relatively low surface strains. For the higher temperature case on the right (blank temperature = 217 °C), the strains are much higher (Fig. 10a) and crack initiation appears to occur at grain boundaries that are manifest on the cup surface. More optimum temperature gradients exist between these two extreme cases which lead to a defect-free, fully drawn cup.

3.4. Effect of punch speed on strain and forming forces

The effect of punch speed on non-isothermal deep drawing of AZ31B-O is investigated. The variation in punch force, strain and thickness distribution within the cup is studied at different punch speeds. The blank holder and die are kept at 245 °C while the punch temperature is close to 135 °C (blank center at 182–188 °C). A summary of the test conditions is shown in Table 3.

These die and punch temperatures lead to a defect-free cup for a punch speed of 4 mm/s and lower, as discussed in Section 3.2 (see Figs. 7b and 9). All experiments performed to examine the effect of punch speed are conducted using an 80 kN blank holder force and 6 min of wait time before each experiment. Five punch speeds are considered; 2, 4, 8, 16, and 32 mm/s. The forming forces are significantly influenced by the punch speed as shown in Fig. 12, and increase with punch speed. A similar response of forming forces to the punch speed in aluminum alloys has been reported in the work of Bagherias1 (2012), where the positive strain rate sensitivity of aluminum at elevated temperatures was reported to be the source of this behavior. Kaya et al. (2008) investigated the effect of constant

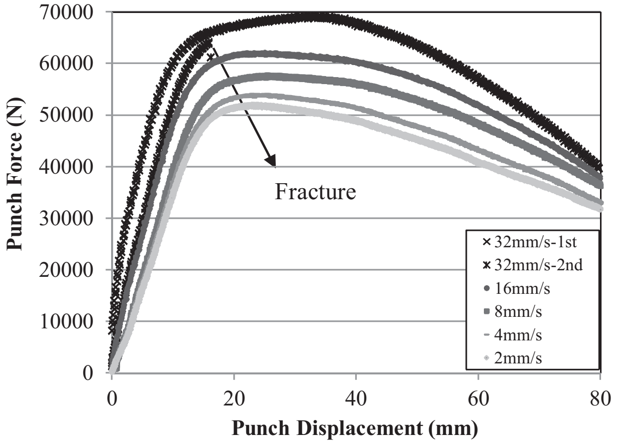

Fig. 12. Punch force versus displacement of AZ31B-O at different punch speeds, at non-isothermal condition with die and blank holder at 245 °C, punch at 135 °C using blank holder force of 80 kN, DR of 2.25 and 6 min wait time.

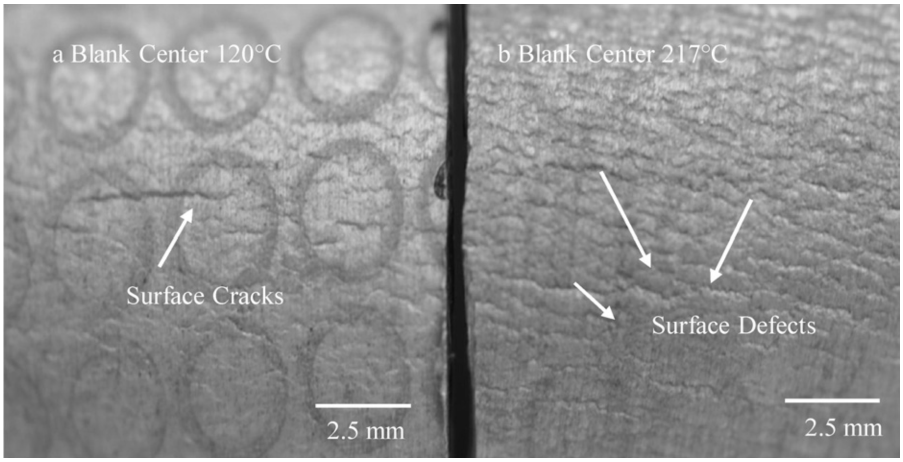

Fig. 11. Surface cracks of two successfully drawn cups. Die and blank holder temperature are 245 °C, punch speed is 4 mm/s, blank holder force is 80 kN, DR is 2.25. Figure on the left corresponds to a blank center temperature of 120 °C, on the right, 217 °C.

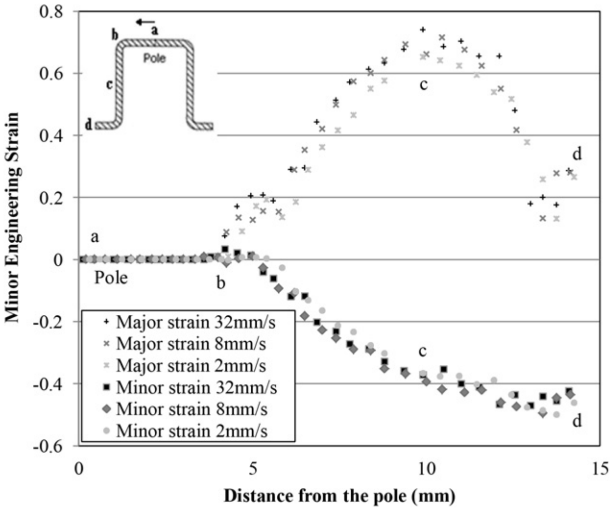

Fig. 13. Major and minor true strain versus distance from the outer edge of the AZ31B-O cup flange to the pole, at non-isothermal condition with die and blank holder at 245 °C and punch at 135 °C using blank holder force of 80 kN, DR of 2.25 and 6 min wait time.

and variable punch speed on forming of AZ31B-O alloy and proposed that there exist a maximum punch speed for each drawing ratio above which forming is not possible. One source of the elevated punch loads with increasing punch speed is material strain rate sensitivity. Magnesium is known to have relatively strong strain rate sensitivity as reported by Ghaffari Tari and Worswick (2011). Their result is consistent with the strain rate sensitivity of AZ31B reported by Hasenpouth et al. (2009). Tensile experiments performed by Ulacia et al. (2011) also show a strong strain rate sensitivity of AZ31B material at elevated temperatures. Kurukuri et al. (2012) investigated the strain rate sensitivity of AZ31B under compressive loading using adhesively bonded stacked sheet specimens and reported strain rate sensitivity of the work hardening behavior.

It is also noted that at the punch speed of 32 mm/s, some repetitions of the deep drawing experiment fractured, before a full draw was achieved. The onset of fracture at this forming speed is attributed to the higher stresses in the cup wall.

The distributions of the major and minor true strain along the rolling direction of AZ31B-O cups formed using the punch speed of 32, 8 and 2 mm/s are shown in Fig. 13. Considering the major strain distribution, at higher punch speeds a larger major strain is observed in the wall region. (See Fig. 13, region c). The larger strains are associated with the high punch loads and stresses in the cup wall. The increased stresses are in part attributed to the strain rate sensitivity of the actively deforming high temperature flange region, but could also be due to rate sensitivity of the lubricant. These effects are left for future work.

As the punch speed is increased, small cracks begin to grow close to the punch radius region of the cup. These cracks are shown for the cup formed at 32 mm/s in Fig. 14. This may be related to texture evolution and formation of cracks at twin intersections as described by Ando and Kitahara (2010); however, this is beyond the scope of the current research. Punch speed is an important parameter that influences the process window of AZ31B deep drawing, as described by Kaya et al. (2008).

3.5. Fracture modes

The fracture surface of formed cups that failed during forming under various thermal conditions is investigated using electron scanning microscopy (SEM). Figs. 15 and 16 show 20× and 400× magnification of the fracture surfaces. An example of a low temperature failure is shown in Figs. 15a and 16a. This fracture surface reveals a more brittle character with relatively little reduction in cross-section prior to onset of failure.

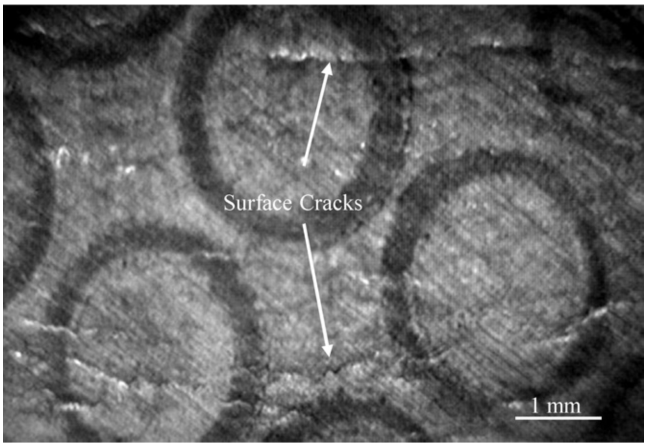

Fig. 14. Cracks on the punch radius of AZ31B-O cup formed at 32 mm/s punch speed, with die and blank holder temperature of 245 °C and punch at 135 °C using blank holder force of 80 kN, DR of 2.25 and 6 min wait time.

Figs. 15b–d and 16b–d show fracture surfaces from parts formed under near-isothermal conditions (failure at high temperature) which display severe thinning and high levels of plastic deformation. The failure mechanism is ductile fracture through void growth and coalescence. As the temperature levels increases, the voids grow larger. Void coalescence is seen on the fracture tip in Fig. 16d.

To investigate the effect of temperature within the cup on the failure, without any temperature gradient effects, isothermal forming deep drawing experiments were conducted at two temperature levels. The first deep draw was performed at 250 °C while the other experiment was performed at 180 °C. Fig. 17 shows the fracture cross-section of two isothermally formed samples obtained through optical microscopy. At the fracture surface of the isothermally formed cup at 180 °C, shear bands and crack growth are observed at relatively low strains as evidenced the limited reduction in thickness. The isothermally formed sample at 250 °C (see Fig. 17b) exhibits a dramatic reduction in cross-section to a near-chisel point with void growth and coalescence as the final fracture mechanism. These observations suggest that the local temperature has dramatic effect on the failure mode for this alloy.

4. Discussion

The data and metallographic observations presented above suggest the existence of a process window for successful warm forming of this sheet material. Such a process window is explored for the DR = 2.25 cups using Fig. 18 which illustrates the range of blank center and die temperatures for which the cup either draws successfully or fractures due to either low temperature failure or high temperature failure. From the figure, all the cases for which the die and punch temperature drop below 200 °C result in brittle failure at the punch nose. These cases correspond to the fracture mode shown in Figs. 7a, 15a and 17a. Low temperature failure is alleviated to some degree as the die temperature is increased, corresponding to the lower limit in the formability window, since the stresses in the cup wall are reduced. The so-called high temperature failures represent ductile failure modes that occur when the blank center temperature is too high and excessive softening results in the cup wall being unable to support the stresses required to draw the cup. This mode is shown in Figs. 7c, 15b and 17b. Clearly, a “safe” cup will lie between these boundaries. Note that temperatures above

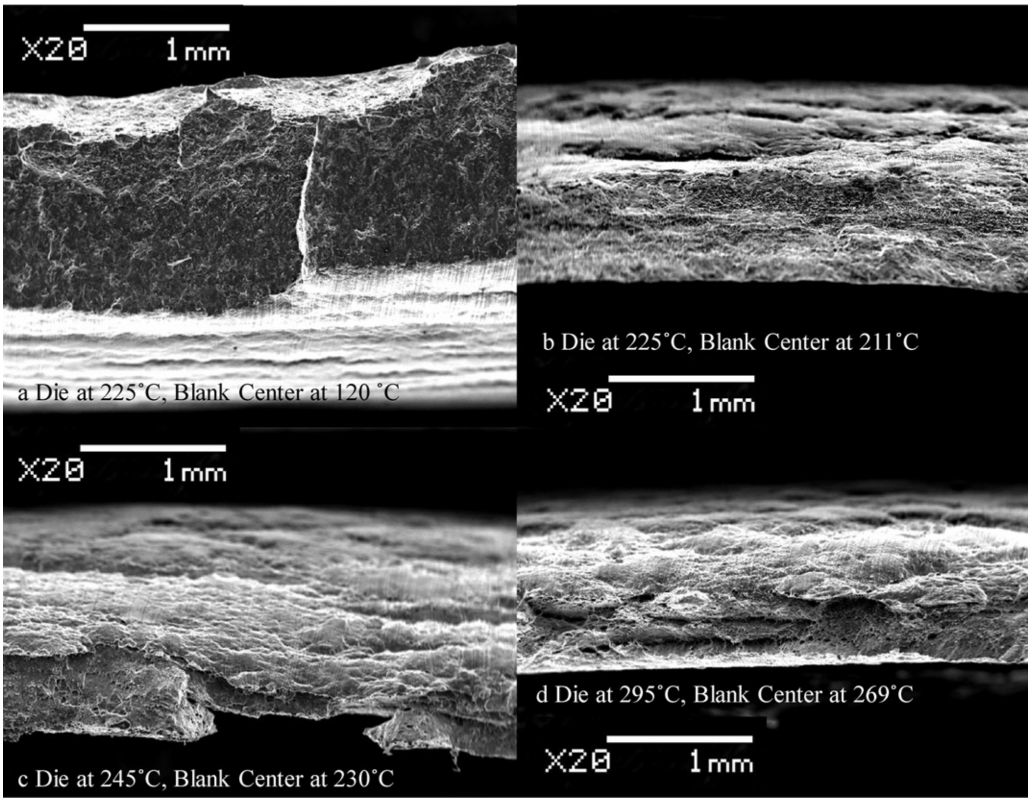

Fig. 15. Scanning electron microscopy of the fractured surfaces (20× magnification) of AZ31B-O cups drawn with punch speed of 4 mm/s, blank holder force of 80 kN and DR of 2.25. (a) Non-isothermal forming at 225 °C (Blank center at 120 °C). (b) Near-isothermal forming at 225 °C (Blank center at 211 °C). (c) Near-isothermal forming at 245 °C (Blank center at 230 °C). (d) Near-isothermal forming at 295 °C (Blank center at 269 °C).

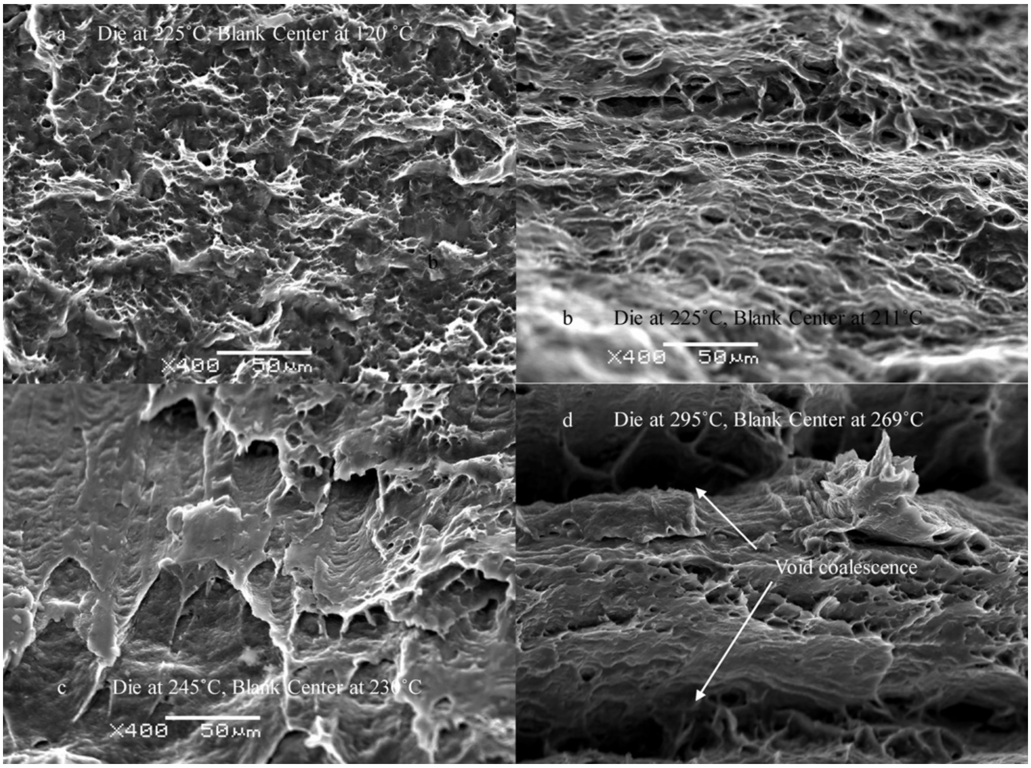

Fig. 16. Scanning electron microscopy of the fractured surfaces (400× magnification) of AZ31B-O cups drawn with punch speed of 4 mm/s, blank holder force of 80 kN and DR of 2.25. (a) Non-isothermal forming at 225 °C (blank center at 120 °C). (b) Near-isothermal forming at 225 °C (blank center at 211 °C). (c) Near-isothermal forming at 245 °C (blank center at 230 °C). (d) Near-isothermal forming at 295 °C (blank center at 269 °C).

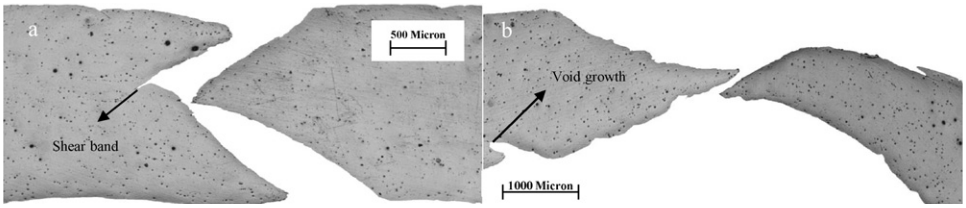

Fig. 17. Optical microscopy of the fracture surface of two cups formed at isothermal conditions, blank holder force of 80 kN and DR of 2.25. (a) Die temperature at 180 °C. (b) Die temperature at 250 °C.

300 °C were not addressed in the current work which focuses on the so-called warm forming conditions.

The current results are consistent with a number of previous studies of non-isothermal forming of magnesium alloy sheet, such that of Palumbo et al. (2007) who used a punch without heating which enabled investigation of low punch temperatures. In that work two heating strategies were considered in which the punch was either kept away from the blank center (cold punch) or was heated through direct contact with the blank during the heating phase prior to forming. Yoshihara et al. (2003) considered much higher die temperatures than in the current work in conjunction with a direct water chill on the blank and variable blank holder pressure during forming. That work reported drawing ratios as high as 5.0; however, the higher die temperatures correspond to a temperature regime for which dynamic recrystallization is expected to be more active than in the current work which focuses on so-called warm conditions. In addition, the current work has considered both heating and cooling systems embedded inside the punch which has allowed a broader range of temperature gradients, ranging from isothermal to non-isothermal, within the blanks and the identification of the process window in Fig. 18.

Note that the process window in Fig. 18 corresponds to a DR of 2.25 and punch speed of 4 mm/s. As the severity of the forming operation increases, for example through increased DR or punch speed, for example, one can anticipate a shift in the process boundaries. Examination of such trends was beyond the scope of the current investigation. Nonetheless, the work has served to show the existence of a process window for magnesium alloy sheet in which the blank center temperature must lie below the die temperature but above the enhanced slip activation temperature of roughly 200 °C. This lower limit is not commonly observed in other candidate materials for warm forming such as aluminum alloy sheet (McKinley et al., 2008) which remains ductile at room temperature.

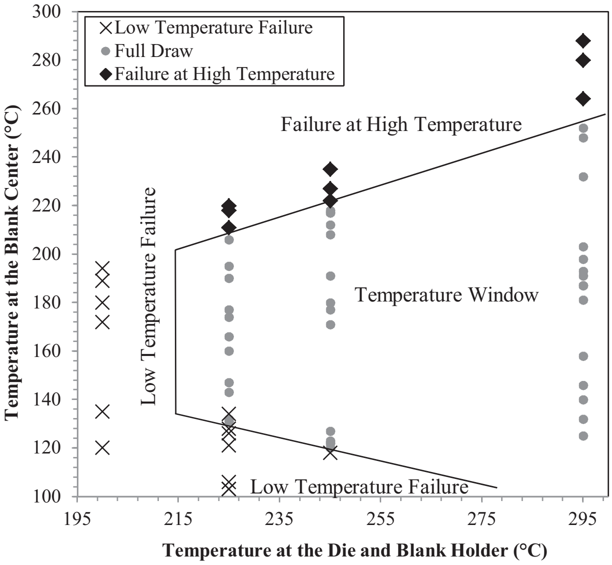

Fig. 18. Process temperature window of deep drawing experiments with a punch speed of 4 mm/s, blank holder force of 80 kN (35 kN at 200 °C) and DR of 2.25.

5. Conclusion

Warm forming of magnesium alloy sheet can be enhanced considerably through the use of elevated forming temperatures, as demonstrated by the isothermal deep draw experiments in which punch depth to failure is enhanced with increased forming temperature. Drawability is further enhanced through the introduction of non-isothermal conditions. There exists a process window in terms of the difference in temperature between the punch nose and flange regions within which a successful draw can be made for a given draw ratio. Elevated temperature in the flange region up to the maximum considered in this research (295 °C) is clearly beneficial and the lowest flange region temperature (die temperature) to obtain a successful draw was 225 °C, for a draw ratio of 2.25. A lower temperature limit also applies to the punch nose region of the blank. Depending upon the draw ratio and flange temperature (draw severity), the lower limit of the blank center temperature for a successful non-isothermal draw was roughly 130 °C for a 225 °C die temperature. Below these temperatures, the benefits of enhanced slip activity associated with warm forming are lost and cracking and fracture is observed at the punch nose. The fractography observations support this conclusion revealing a ductile fracture behavior at high temperatures transitioning to punch nose region cracking and brittle failure modes as punch temperature is reduced. Punch speed has the opposite effect to temperature in that elevated punch speed tends to increase punch loads due to material rate sensitivity which in turn increases stress in the cup side-wall promoting an earlier fracture. The results of this research suggest that viable process windows exist to support industrial warm forming of light weight components using magnesium alloy sheet, particularly through the use of non-isothermal processes.

Acknowledgments

This research was carried out under the framework of the Research Program of the Magnesium Network (MagNET), Canada. Financial support from MagNET is gratefully acknowledged. The authors would like to thank Tom Gawel, Andy Barber, Yaquan Ding and Eckhard Budziarek at the University of Waterloo for their experimental support.

References

Ambrogio, G., Bruni, C., Bruschi, S., Filice, L., Ghiotti, S., Simoncini, M., 2008. Characterization of AZ31B magnesium alloy formability in warm forming conditions. In: Proceedings of the Esaform 2008, Lyon, France.

Ando, S., Kitahara, H., 2010. Fatigue properties in magnesium single crystals. In: MagNET Research Network Workshop 2010, Waterloo, Ontario, Canada.

Bagheriasl, R., 2012. Formability of aluminum alloy sheet at elevated temperature. Ph.D. Thesis. University of Waterloo, Ontario, Canada.

Easton, M., Beer, A., Barnett, M., Davies, C., Dunlop, G., Durandet, Y., 2008. Magnesium alloy applications in automotive structures. JOM-Journal of the Minerals Metals & Materials Society 60, 57–62.

Environment Defense Fund, 2008, U.S. EPA Greenhouse Gas Inventory: 2006. Washington, DC, U.S.A.

Ghaffari Tari, D., Worswick, M.J., 2011. Experimental investigation of anisotropy evolution of AZ31 magnesium alloy sheets under tensile loading. In: Proceedings of the Esaform 2011, Belfast, Ireland.

Hasenpouth, D., Salisbury, C., Bardelcik, A., Worswick, M.J., 2009. Constitutive behavior of magnesium alloy sheet at high strain rates. In: Proceedings of DYMAT 2009 9th International Conference on the Mechanical and Physical Behavior of Materials under Dynamic Loading, Brussels, Belgium.

Kaya, S., Spampinato, G., Altan, T., 2008. An experimental study on nonisothermal deep drawing process using aluminum and magnesium alloys. Journal of Manufacturing Science and Engineering 130, 11.

Khan, A.S., Pandey, A., Gnäupel-Harold, T., Mishra, R.K., 2011. Mechanical response and texture evolution of AZ31 alloy at large strains for different strain rates and temperatures. International Journal of Plasticity 27, 688–706.

Kurukuri, S., Ghaffari Tari, D., Worswick, M.J., Mishra, R.K., Carter, J.T., 2012. Dynamic characterization of AZ31B and ZEK100 magnesium alloy sheets. In: Proceedings of Magnesium Conference 2012, Vancouver, Canada.

Lee, Y.S., Kim, M.C., Kim, S.W., Kwon, Y.N., Choi, S.W., Lee, J.H., 2007. Experimental and analytical studies for forming limit of AZ31 alloy on warm sheet metal forming. Journal of Materials Processing Technology 187, 103–107.

Li, D., Ghosh, A., 2004. Biaxial warm forming behavior of aluminum sheet alloys. Journal of Materials Processing Technology 145, 281–293.

Lou, X.Y., Li, M., Boger, R.K., Agnew, S.R., Wagoner, R.H., 2007. Hardening evolution of AZ31B Mg sheet. International Journal of Plasticity 23, 44–86.

McKinley, J.J., 2010. Warm forming of aluminum brazing sheet experiments and numerical Simulations. M.Sc. Thesis. University of Waterloo, Ontario, Canada.

McKinley, J.J., Abedrabbo, N., Worswick, M.J., Kozdras, M., 2008. Effect of independent die and punch temperature control on the formability of 3003 aluminum alloy in warm deep drawing. In: Proceedings of the Numisheet 2008, Interlaken, Switzerland.

Palaniswamy, H., Ngaile, G., Altan, T., 2004. Finite element simulation of magnesium alloy sheet forming at elevated temperatures. Journal of Materials Processing Technology 146, 52–60.

Palumbo, G., Sorgente, L., Tricarico, S., Zhang, S.H., Zheng, W.T., 2007. Numerical and experimental investigation on the effects of the heating strategy and the punch speed on the warm deep drawing of magnesium alloy AZ31. Journal of Materials Processing Technology 191, 342–346.

Palumbo, G., Tricarico, S., 2007. Numerical and experimental investigation on the warm deep drawing process of circular aluminium alloy specimens. Journal of Materials Processing Technology 184, 115–123.

Takuda, H., Mori, K., Masuda, I., Abe, Y., Matsuo, M., 2002. Finite element simulation of warm deep drawing of aluminum alloy sheet when accounting for heat conduction. Journal of Materials Processing Technology 120, 412–418.

Ulacia, I., Salisbury, C.P., Hurtado, I., Worswick, M.J., 2011. Tensile characterization and constitutive modeling of AZ31B magnesium alloy sheet over wide range of strain rates and temperatures. Journal of Materials Processing Technology 211, 830–839.

Yoshihara, S., Nishimura, H., Yamamoto, H., Ken-ichi, M., 2003. Formability enhancement in magnesium alloy stamping using a local heating and cooling technique: circular cup deep drawing process. Journal of Materials Processing Technology 142, 609–613.

Zhang, S.H., Zhang, K., Xu, Y.C., Wang, Z.T., Yu, Z.G., 2007. Deep-drawing of magnesium alloy sheets at warm temperatures. Journal of Materials Processing Technology 185, 147–151.

Appendix B: **D. Ghaffari Tari, M.J. Worswick, U. Ali, M., Gharghouri,** ***Mechanical response of AZ31B magnesium alloy Experimental characterization and material modeling considering proportional loading at room temperature,*** **International Journal of Plasticity, 55, pp. 247-267, 2014**

International Journal of Plasticity 55 (2014) 247–267

Contents lists available at ScienceDirect

International Journal of Plasticity

journal homepage: www.elsevier.com/locate/ijplas

Mechanical response of AZ31B magnesium alloy: Experimental characterization and material modeling considering proportional loading at room temperature

D. Ghaffari Tari [a,*], M.J. Worswick [a], U. Ali [a], M.A. Gharghouri [b]

[a] *University of Waterloo, 200 University Ave West, Waterloo, Ontario, Canada*
[b] *Canadian Neutron Beam Centre, Chalk River Laboratories, Chalk River, Ontario, Canada*

A R T I C L E I N F O

Article history:
Received 2 May 2013
Received in final revised form 21 October 2013
Available online 11 November 2013

Keywords:
The evolution of the envelope of subsequent yield surfaces
Anisotropic hardening
Magnesium alloys
Continuum-based plasticity

A B S T R A C T

Tension and compression experiments have been performed to characterize the mechanical response of 1.57 mm AZ31B-O sheet at room temperature. Five different sheet orientations were used to characterize the in-plane anisotropy under tensile loading conditions while cubic samples consisting of adhesively-bonded layers of sheet samples were used for compression testing along four sheet directions. During uniaxial tensile testing, the axial and transverse strain components were measured using two independent extensometers. A digital image correlation system was used to measure the strain components during compression testing. Both instantaneous and cumulative *r*-values were measured as they evolved with plastic strain. A strong, evolving asymmetry is observed. An evolving anisotropic/asymmetric continuum-based material model based on a Cazacu–Plunkett–Barlat (CPB)-type yield function is proposed to fit the material behavior as a continuous function of plastic strain. Considerable improvement in the representation of the material behavior is achieved as the number of stress transformations used in the CPB yield surface formulation is increased. To capture the evolution of the envelope of the subsequent yield surfaces, the anisotropy and asymmetry parameters are replaced with functions expressed in terms of plastic strain. The evolution parameters are found by minimizing the difference between the model predictions and the experiments at discrete plastic strain levels, using gradient search methods. A strain rate-independent elastic–plastic material model incorporating the evolving envelope of subsequent yield surface formulation has been developed and implemented within a commercial finite element package. The model reproduces the experiments initially used for fitting. The predictions of the developed material model are compared with the measured load–displacement and strain distributions from a three-point bending experiment. Improvement in the prediction of strain and forming forces is observed compared to the previously available non-evolving material models.

1. Introduction

A limited number of slip systems are active in hexagonal-close-packed (HCP) magnesium alloys at room temperature. Twinning is another deformation mechanism which can contribute significantly to plastic deformation, depending on the initial texture and loading path. Texture measurements reveal strong basal or near-basal crystallographic texture in sheet

---

* Corresponding author.
E-mail address: dghaffar@uwaterloo.ca (D. Ghaffari Tari).

0749-6419/$ - see front matter © 2013 Elsevier Ltd. All rights reserved.
http://dx.doi.org/10.1016/j.ijplas.2013.10.006

magnesium alloys (see Kelley and Hosford, 1968) which results in strong tension–compression asymmetry. Cumulative and instantaneous *r*-values under uniaxial tension were measured in prior research by Lou et al. (2007) and Khan et al. (2011) and *r*-values were found to evolve with accumulated plastic strain. Piao et al. (2012a,b) considered twinning–de-twinning under reversed loading and found that the de-twinning transition region from compression to tension was suppressed at temperatures higher than 150 °C. Khosravani et al. (2013) investigated the formation of compression twin shear bands under biaxial tension conditions at room and moderately elevated temperatures of 75 and 125 °C. They reported less formation of shear bands at higher temperature conditions which is due to higher activity of $\langle c + a \rangle$ type slip systems, which accommodates through-thickness thinning. A reduction in the anisotropy of the mechanical behavior is observed with increasing temperature (Agnew and Duygulu, 2005). The onset of yielding was reported to be insensitive to temperature which suggests that a temperature-independent deformation mechanism is active during yielding under compression (Jiang et al., 2007). In addition, a very low compressive *r*-value was measured which is known to be indicative of twinning (Jain and Agnew, 2007). The strain rate sensitivity of magnesium alloys was investigated by Kurukuri et al. (2012) and Hasenpouth et al. (2009). Yield stress is reported to be strain rate-insensitive, while the work hardening rate is strongly strain rate-sensitive. At elevated temperatures (200 °C), the flow stress and *r*-values are strongly rate-sensitive (Ghaffari Tari and Worswick, 2011).

Due to the complex mechanical response of magnesium alloys, modeling efforts represent a daunting task. Earlier continuum-based models, such as those of Von Mises (1913), Hill (1948, 1950), and Barlat et al. (1997, 2003), for example, are more appropriate for BCC and FCC lattice structures for which slip is the primary deformation mechanism. Continuum-level models for HCP materials are less well developed, one noteworthy exception being Cazacu–Plunkett–Barlat (CPB) family of yield surfaces which model the asymmetric response of materials with HCP lattice structure. Cazacu and Barlat (2001) generalized Drucker's isotropic yield surface model (Drucker, 1949) to the orthotropic case by introducing anisotropy coefficients into the model. This model was later used to describe the anisotropic response of aluminum alloys (Cazacu and Barlat, 2003). The same yield surface was modified to account for tension/compression asymmetry (Cazacu and Barlat, 2004). Barlat et al. (2005) proposed that by performing linear transformations on the Cauchy stress tensor, anisotropic parameters can be introduced into a yield surface. To improve the accuracy of the description of the anisotropic behavior of aluminum alloys, Barlat et al. (2003) performed two independent stress transformations on the deviatoric stress tensor and formulated the yield surface (YLD2000-2d) based on the sum of the two functions. A more flexible yield surface was obtained by increasing the number of anisotropy parameters to 18 (YLD2011-18p) and 27 (YLD2011-27p) as proposed by Aretz and Barlat (2013). A non-quadratic yield surface (CPB06) to account for asymmetry was proposed by Cazacu et al. (2006). This yield surface formulation is homogeneous of arbitrary degree. An asymmetry parameter is included in this formulation which is controlled by the ratio of the strengths in tension and compression. The accuracy of the description of flow stresses and *r*-values in tension and compression increases if more than one stress transformation is performed on the principal deviatoric stresses (Plunkett et al., 2008).

Due to texture evolution during plastic deformation in HCP metals, the shape of the yield surface changes and traditional isotropic hardening models cannot capture this material response. Kim et al. (2008) divided the deformation modes into tension and compression and assumed two independent hardening laws for each case. In the same study, to account for the asymmetric and anisotropic response of AZ31B magnesium alloy, a CPB06 yield surface was fit to the initial yield stress and *r*-values. The results showed improvement in the displacement vs. load predictions for a three-point bending test. Plunkett et al. (2006) proposed a methodology to account for anisotropic hardening in HCP metals by linearly interpolating between two previously calibrated yield surfaces. To model the initial yielding of high-purity zirconium alloys at room temperature, an asymmetric/anisotropic CPB06 type yield surface was used. This material model was later used to simulate 4-point bending and Taylor cylinder impact experiments (Plunkett et al., 2007) and proved to be more capable in the prediction of strain distributions compared with the non-evolving material models. A similar modeling approach was also used by Yoon et al. (2013), Nixon et al. (2010), and Gilles et al. (2011). A different approach was used by Lou et al. (2013) to introduce evolving asymmetry in the yield surface by introducing a pressure sensitive term into the yield formulation as proposed by Spitzig (1975) and Stoughton and Yoon (2004). Nebebe Mekonen et al. (2012) calibrated a Cazacu-2004 (Cazacu and Barlat, 2004) yield function with evolving anisotropy parameters in terms of accumulated plastic strain using tensile experiments performed on AZ31B and ZE10 at 200 °C. Steglich et al. (2011) used a genetic algorithm approach to fit a similar model for evolving flow stresses along different load paths obtained through crystal plasticity simulations.

In this paper, the mechanical response of AZ31B-O is characterized under tension and compression along different sheet orientations. Tensile testing is performed using two independent extensometers to measure the *r*-values as the deformation proceeds. Sheet layers are stacked and bonded using a high performance adhesive to create cubic samples which resist buckling during compression loading. The compression tests are performed using custom-made tooling while the deformation is recorded using a digital image correlation system. A CPB06 yield surface formulation (Cazacu et al., 2006) is adopted and the anisotropy and asymmetry parameters are modified to evolve with deformation as part of this work. This yield function is fit to the experimental data at different plastic strain intervals to obtain the initial yield surface and evolution of the envelope of subsequent yield surfaces (Khan et al., 2009, 2010a,b) under a monotonic loading assumption. In contrast to previous research, the developed model captures the evolving asymmetric/anisotropic response of both flow stresses and *r*-values for both tension and compression while also fitting the flow stress at biaxial and shear (Khan et al., 2011) locations on the yield locus. The model, which uses three stress transformations, is implemented within a user defined material model (UMAT) linked within the commercial finite element software LS-DYNA. A three-point bending experiment is performed using the DIC system and simulated using the new material model. Comparison between the predicted and measured load–displacement response and strain distribution in the bend region is used to assess the model predictions relative to those obtained using non-evolving von Mises and CPB06 models.

2. Material characterization

2.1. Experimental procedure

The material used in this research was 1.57 mm AZ31B-O sheet supplied by Magnesium Elektron North America, Inc. in an annealed (O temper) condition. The chemical composition and the initial mechanical properties of the alloy provided by the manufacturer are shown in Tables 1 and 2, respectively.

Neutron diffraction was used to characterize the initial texture of the as-received material. Fig. 1 shows the measured pole figures obtained on the E3 spectrometer of the Canadian Neutron Beam Centre (CNBC). A strong basal texture is evident, in which most grains have the basal poles closely aligned with the sheet normal direction (ND) (Fig. 1a).

Mechanical testing was performed using an Instron 1331 tension/compression servo-hydraulic load frame. All of the experiments were performed at ambient temperature (23 °C) and a strain rate of 0.001 s^{-1}. Tensile testing was performed on dog-bone shaped sub-size ASTM E8M standard specimens with 25 mm gage length. Tensile testing was conducted along five sheet orientations namely the RD, 30°, 45°, 60° and TD directions. Two independent extensometers were used to measure the axial and transverse strains.

To avoid buckling during compression testing, sheet layers were stacked together to form a solid cube 8 mm on a side, similar to the method used by Tozawa (1978) and further studied by Maeda et al. (1998). A high performance adhesive, Master bond SUP10HT®, was used to bond the layers. The shear strength of the adhesive exceeds 24 MPa, compressive strength 66 MPa and tensile strength 86 MPa. To improve the performance of the adhesive, the smooth surface of the sheet was roughened using an abrasive tool mounted on a milling machine. This process resulted in a uniform crosshatched pattern on the surfaces to which the adhesive was applied. The external surfaces of the cube were machined and polished to produce a smooth finish (Fig. 2b). Krytox® lubricant was used between the contact surfaces. Maeda et al. (1998) and Klepaczko and Malinowski (1977) investigated the error in compression testing for which the friction coefficient is below 0.1 and both reported errors in the uniaxial compressive stress to be less than 5%. To improve the alignment of the compression testing apparatus, a custom compression fixture was used (Fig. 2a) which incorporates a die set to align the compression platens.

A digital image correlation system (DIC) from Correlated Solution Inc. was used to measure the distribution of strain components throughout the experiment. The DIC system also recorded load–displacement data, allowing synchronization of the load and DIC images. Fig. 2b shows a typical speckle pattern used in this work. The analysis utilized a subset size of 39–47 pixels and a step size of 7 pixels. The subset size is selected based upon the range of speckle size encountered in the images; a subset size of 39 pixels corresponds to 0.6 mm on the surface and the speckle size ranged from 3 to 15 pixels. Note that while DIC measurements were not used in the tensile experiments, subsequent comparison between extensometer- and DIC-based measurements of axial and transverse strain revealed good agreement.

2.2. Experimental results

The true stress vs. true plastic strain behavior of AZ31B-O at room temperature is shown in Fig. 3. The curves shown in the figure are the average of three test repetitions. The repeatability of the experiments was reasonably good, with an average absolute deviation from the mean of approximately 6 MPa for the compression curves and 2 MPa for the tensile curves. A strong asymmetry is observed between the tension and compression data. The initial yield stress in compression is lower than that in tension; however, the rate of hardening under compression is higher. The flow stress in compression overtakes the flow stress in tension at approximately 6% true plastic strain. The initial yield stress under in-plane compression varies little with sheet orientation; beyond yielding, however, the flow curves in compression diverge increasingly from one another with increasing plastic strain. The flow stress for both in-plane tension and compression increases as the loading

Table 1
Chemical composition limits of AZ31B-O provided by Magnesium Elektron North America (MENA).

Al	Zn	Mn	Ca	Cu	Fe	Ni	Si	Mg
2.9	0.25	0.94	–	0.001	0.004	0.005	0.005	Bal

Table 2
As-received mechanical properties of AZ31B-O.

Thickness (mm)	UTS (MPa)	Yield strength (MPa)	Total elongation (%)
1.57	255	160	16.5

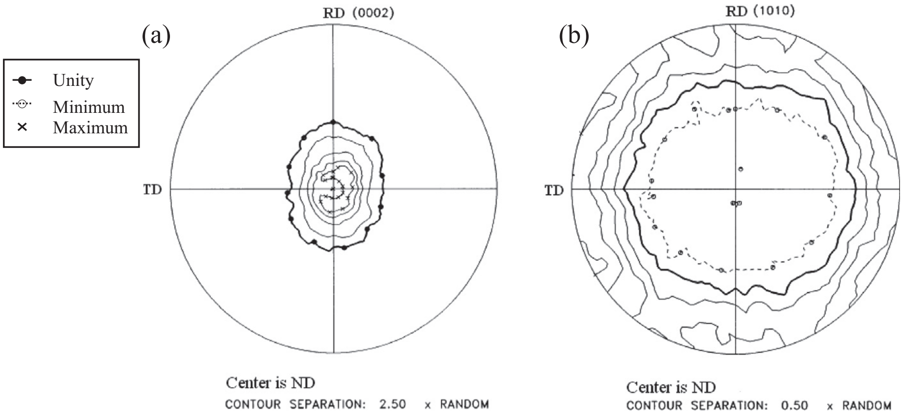

Fig. 1. Pole figures showing the initial texture, measured by neutron diffraction. The rolling direction (RD) and the transverse direction (TD) are in the plane and the normal direction (ND) is normal to the plane. (a) (0002) pole figure, (b) {10–10} pole figure. Contours drawn in solid bold lines correspond to the intensity expected from a uniform texture (i.e. 1 × uniform). Contours corresponding to intensities greater/lower than expected in a uniform texture are indicated by solid/dashed lines. The maximum intensity contours are labeled with crosses, while the minimum intensity contours are labeled with closed circles.

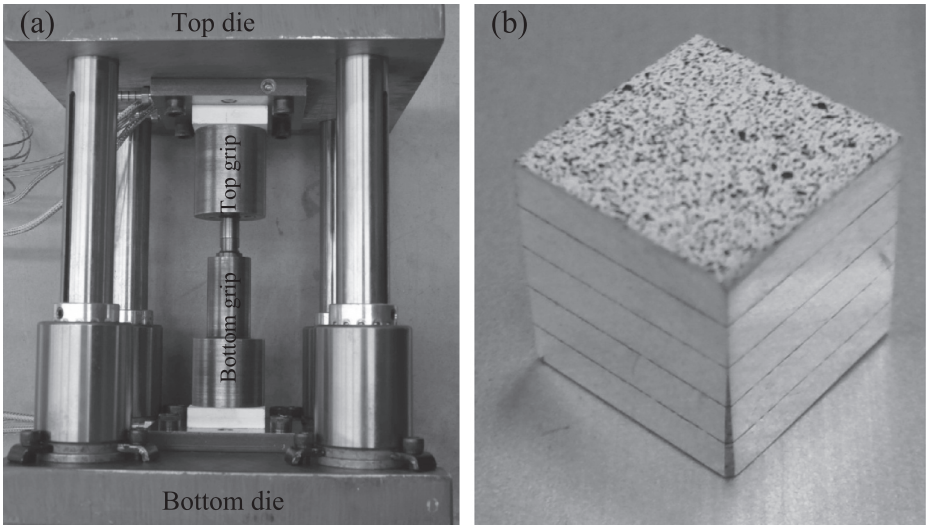

Fig. 2. (a) The custom-made compression fixture, (b) adhesively stacked 8 mm cubic sample speckled for DIC measurements.

axis rotates from the rolling direction to the transverse direction. The rate of strain hardening under through-thickness compression is higher than under in-plane tension.

The instantaneous *r*-values were calculated from the ratio of strain rate components as follows (neglecting the effect of elastic deformation):

$$r_{Instantaneous} = \frac{\dot{\varepsilon}_w}{\dot{\varepsilon}_t} \tag{1}$$

Fig. 4 shows the evolution of the instantaneous *r*-values with plastic strain. A large asymmetry is observed when comparing the instantaneous *r*-values in tension and compression. Both components of strain rate used in this calculation are small numbers; thus, small oscillations in the measured strain rates can strongly influence the computed *r*-values. Therefore, the measured displacement curves were initially smoothed after which the *r*-values were calculated. The compressive *r*-values initially start at values close to zero and increase dramatically with plastic strain. The *r*-values increase as the loading axis rotates from the rolling direction towards the transverse direction.

The cumulative *r*-values are calculated from the following,

$$r_{Cumulative} = \frac{\varepsilon_w^p}{\varepsilon_t^p} \tag{2}$$

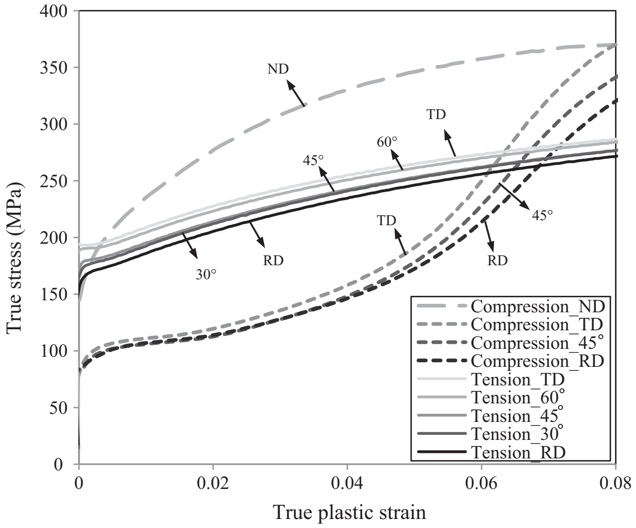

Fig. 3. True stress vs. true plastic strain under tension and compression (0.001 s^{-1} strain rate), along different sheet directions. The compression data are plotted as positive. Error bars are not shown for clarity, however, the average absolute deviation from the mean was approximately 6 MPa for the compression curves and 2 MPa for the tensile curves.

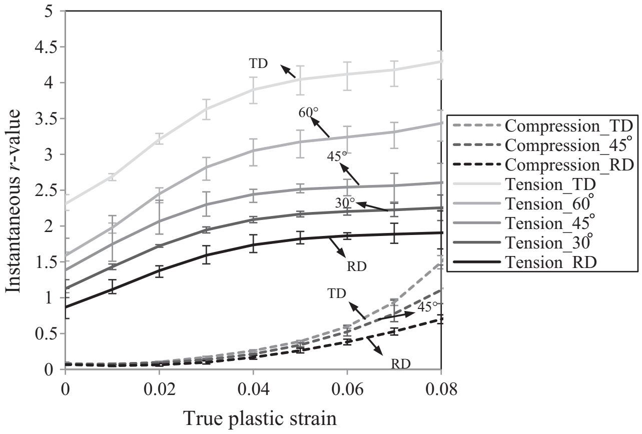

Fig. 4. Instantaneous *r*-values vs. true plastic strain under tension and compression (0.001 s^{-1}), along different sheet directions. The error bars indicate the maximum and minimum measured values from the repeat tests.

where the axial and transverse plastic strains were obtained from the corresponding total strains by subtracting the elastic strains, as follows:

$$\varepsilon_l^p = \varepsilon_l - \frac{\sigma_l}{E} \tag{3}$$

$$\varepsilon_w^p = \varepsilon_w + \upsilon\frac{\sigma_l}{E} \tag{4}$$

In Eqs. (3) and (4), E is Young's modulus, υ is Poisson's ratio and σ_l is the axial stress. The through-thickness plastic strain component is calculated assuming plastic incompressibility. An effective Young's modulus was calculated for each experiment as the slope of the linear fit to the elastic part of the strain vs. stress curve. This value was typically approximately 39 GPa which is somewhat lower than handbook values (45 GPa) which are generally determined based upon acoustic measurements and do not account for non-linear elastic response prior to yielding (Powel and Skove, 1982; Wong and Johnson, 1988; Sun and Wagoner, 2011). The yield point was taken as the stress at which point Eq. (3) becomes zero using the effective modulus. The measured cumulative *r*-values under both tension and compression are shown in Fig. 5. Under both tension and compression, the *r*-values increase as the loading axis rotates from the rolling direction to the transverse

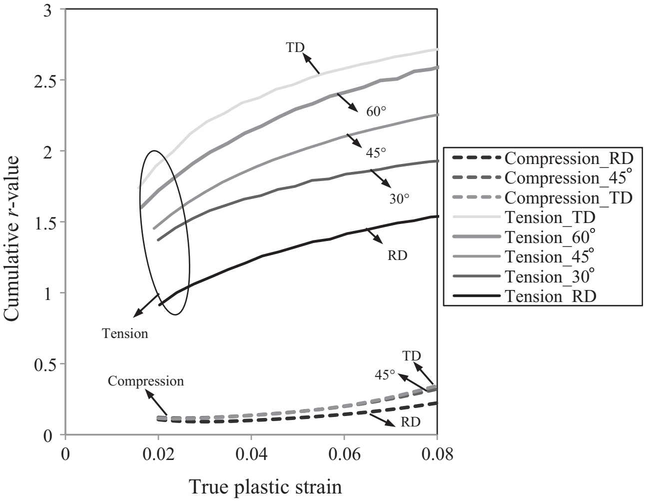

Fig. 5. Cumulative *r*-value vs. true plastic strain under tension and compression (0.001 s^{-1} strain rate), for different sheet directions. Error bars are not shown for clarity; however, the average absolute deviation from the mean was approximately 0.07 for the compression curves and 0.05 for the tensile curves.

direction. The measurement of the cumulative *r*-values at low plastic strain levels (0–2%) is difficult due to elastic effects; therefore the tensile cumulative *r*-values for plastic strain lower than 2% are not presented in Fig. 5.

3. Anisotropic hardening

3.1. Theoretical background of the yield function

One of the goals of this research is to develop a plastic strain-dependent, evolving anisotropic/asymmetric material model for monotonic loading conditions. To achieve this, the anisotropic yield criterion proposed by Cazacu et al. (2006) is modified to capture the initial yield surface and evolution of the envelope of subsequent yield surfaces due to variations in both strength and *r*-value with plastic strain. The evolved yield function determined herein represents a contour constant plastic work under monotonic loading and does not capture the exact yield function for non-monotonic loading as elucidated by Khan et al. (2009, 2010a,b).

This analytical yield surface due to Cazacu et al. (2006), denoted as CPB06 is described as:

$$F(\mathbf{\Sigma}) = (|\Sigma_1| - k\Sigma_1)^a + (|\Sigma_2| - k\Sigma_2)^a + (|\Sigma_3| - k\Sigma_3)^a \tag{5}$$

where k is a material parameter that describes the strength difference in tension and compression, a is the degree of homogeneity, and $\Sigma_i^{(l)}$, $i = 1,\ldots,3$ are the principal values of the deviatoric stress tensor. $\mathbf{\Sigma}$ is given by:

$$\mathbf{\Sigma} = \mathbf{C} : \mathbf{S} \tag{6}$$

In Eq. (6), **C** is the fourth-order anisotropy tensor (below) and **S** is the deviatoric stress tensor. Considering orthotropy with respect to the Cartesian coordinate system in the x_i directions, the anisotropy matrix acting on the stress deviator can be represented in matrix form as:

$$\mathbf{C} = \begin{bmatrix} C_{11} & C_{12} & C_{13} & 0 & 0 & 0 \\ C_{12} & C_{22} & C_{23} & 0 & 0 & 0 \\ C_{13} & C_{23} & C_{33} & 0 & 0 & 0 \\ 0 & 0 & 0 & C_{44} & 0 & 0 \\ 0 & 0 & 0 & 0 & C_{55} & 0 \\ 0 & 0 & 0 & 0 & 0 & C_{66} \end{bmatrix} \tag{7}$$

It is also noteworthy that although the transformed tensors are not deviatoric, the orthotropic criterion is insensitive to hydrostatic pressure; therefore, the plastic incompressibility condition is satisfied. Furthermore, this anisotropic yield criterion is convex if $k \in [-1,1]$ for any integer $a \geqslant 1$ as proven by Cazacu et al., 2006.

Plunkett et al. (2008) proposed that more linear transformations can be incorporated in this orthotropic yield surface until the desired level of accuracy in the description of the yield locus is obtained. Thus, the following general yield description is proposed,

$$F(\mathbf{S}) = f^{(1)} + f^{(2)} + f^{(3)} + \cdots + f^{(l)} + f^{(n)}, \quad \text{with } 1 \le l \le n \tag{8}$$

where

$$f^{(l)} = \left(\left|\Sigma_1^{(l)}\right| - k^{(l)}\Sigma_1^{(l)}\right)^a + \left(\left|\Sigma_2^{(l)}\right| - k^{(l)}\Sigma_2^{(l)}\right)^a + \left(\left|\Sigma_3^{(l)}\right| - k^{(l)}\Sigma_3^{(l)}\right)^a \tag{9}$$

In Eq. (9), $\Sigma_i^{(l)}$, $i = 1,\ldots,3$ are the principal values of the transformed deviatoric stress calculated from $\boldsymbol{\Sigma}^{(l)} = \mathbf{C}^{(l)} : \mathbf{S}$ with $\mathbf{C}^{(l)}$ being a fourth order orthotropic tensor associated with the lth linear transformation and $k^{(l)}$ are the material parameters corresponding to the asymmetry of the yield stress.

3.2. Evolution of yield function parameters

In the simplest form of work hardening, the yield surface expands isotropically. However, due to load path dependency of the activity of different deformation mechanisms in HCP metals, not only the position of the yield surface and its size but also its shape changes with the accumulated plastic strain. Recent work by Ghaffari Tari and Worswick (2011) showed that the strain rate sensitivity of the r-values and flow stresses at room temperature and under quasi-static loading is mild; therefore, the yield surface in the current work is assumed to be strain rate insensitive. To capture evolving plastic anisotropy and asymmetry, the yield surface described in Section 3.1 is modified to account for anisotropic hardening with the accumulated plastic strain. A saturation-type function is used to describe the change in the anisotropy and asymmetry parameters; this function has the important advantage that it is well-behaved (continuous, differentiable and bounded) for the range of plastic strain considered here. A similar approach was used by Steglich et al. (2011) to calibrate a pressure insensitive yield formulation by Cazacu and Barlat (2004) using the flow stress responses obtained through crystal plasticity simulations to create an evolving yield locus in terms of the accumulated plastic strain. However, in the current work, both flow stress and plastic strain ratio (r-value) variations with accumulated plastic strain, obtained from the material characterization experiments, are used to control the evolution and shape change of the yield locus. Thus the parameters are rewritten in terms of the plastic strain as follows,

$$C_{ij}^{(l)} = a_{ij}^{(l)} + b_{ij}^{(l)}\left(1 - exp\left(-d_{ij}^{(l)} * \bar{\varepsilon}^p\right)\right) \tag{10}$$

$$k^{(l)} = e^{(l)} + f^{(l)}\left(1 - exp\left(-g^{(l)} * \bar{\varepsilon}^p\right)\right) \tag{11}$$

where parameters $a_{ij}^{(l)}, b_{ij}^{(l)}, d_{ij}^{(l)}, e^{(l)}, f^{(l)}$ and $g^{(l)}$ are constants corresponding to lth linear transformation that are found through optimization methods to capture the material response observed in the experiments, and $\bar{\varepsilon}^p$ is the effective plastic strain.

3.3. Model calibration

The independent anisotropy and asymmetry constants in Eqs. (10) and (11) are determined by minimizing the difference between the model response and the experimental data. A numerical error minimization method similar to that proposed by Plunkett et al. (2008) has been used. A code was developed using the commercial software MathCAD to minimize the difference between the yield surface and the experimental data. Based on this approach, flow stresses and r-values under tension and compression along arbitrary directions are described in terms of the effective plastic strain-dependent anisotropy coefficients. The following relation describes the uniaxial tensile stress at an arbitrary orientation θ. The index l corresponds to the lth stress transformation, n is the total number of transformations, $\bar{\varepsilon}^p$ and $X^T(\bar{\varepsilon}^p)$ represent the effective plastic strain and the flow stress along the rolling direction, respectively.

$$\sigma^T(\theta, \bar{\varepsilon}^p) = X^T(\bar{\varepsilon}^p)\left\{\frac{1}{\sum_{l=1}^{n}\left[\left(\left|A_1^{(l)}(\bar{\varepsilon}^p)\right| - k^{(l)}(\bar{\varepsilon}^p)A_1^{(l)}(\bar{\varepsilon}^p)\right)^a + \left(\left|A_2^{(l)}(\bar{\varepsilon}^p)\right| - k^{(l)}(\bar{\varepsilon}^p)A_2^{(l)}(\bar{\varepsilon}^p)\right)^a + \left(\left|A_3^{(l)}(\bar{\varepsilon}^p)\right| - k^{(l)}(\bar{\varepsilon}^p)A_3^{(l)}(\bar{\varepsilon}^p)\right)^a\right]}\right\}^{1/a} \tag{12}$$

where,

$$A_1^{(l)}(\bar{\varepsilon}^p) = \frac{1}{2}\left(A_{xx}^{(l)}(\bar{\varepsilon}^p) + A_{yy}^{(l)}(\bar{\varepsilon}^p) + \sqrt{\left(A_{xx}^{(l)}(\bar{\varepsilon}^p) - A_{yy}^{(l)}(\bar{\varepsilon}^p)\right)^2 + 4A_{xy}^{(l)}(\bar{\varepsilon}^p)^2}\right) \tag{13}$$

$$A_2^{(l)}(\bar{\varepsilon}^p) = \frac{1}{2}\left(A_{xx}^{(l)}(\bar{\varepsilon}^p) + A_{yy}^{(l)}(\bar{\varepsilon}^p) - \sqrt{\left(A_{xx}^{(l)}(\bar{\varepsilon}^p) - A_{yy}^{(l)}(\bar{\varepsilon}^p)\right)^2 + 4A_{xy}^{(l)}(\bar{\varepsilon}^p)^2}\right) \tag{14}$$

$$A_3^{(l)}(\bar{\varepsilon}^p) = A_{zz}^{(l)}(\bar{\varepsilon}^p) \tag{15}$$

$$A_{xx}^{(l)}(\bar{\varepsilon}^p) = \phi_1^{(l)}\cos^2\theta + \psi_1^{(l)}\sin^2\theta \tag{16}$$

$$A_{yy}^{(l)}(\bar{\varepsilon}^p) = \phi_2^{(l)}\cos^2\theta + \psi_2^{(l)}\sin^2\theta \tag{17}$$

$$A_{zz}^{(l)}(\bar{\varepsilon}^p) = \phi_3^{(l)}\cos^2\theta + \psi_3^{(l)}\sin^2\theta \tag{18}$$

$$A_{xy}^{(l)}(\bar{\varepsilon}^p) = C_{66}^{(l)}(\bar{\varepsilon}^p)\sin\theta cos\theta \tag{19}$$

$$\psi_1^{(l)}(\bar{\varepsilon}^p) = \frac{2}{3}C_{12}^{(l)}(\bar{\varepsilon}^p) - \frac{1}{3}C_{11}^{(l)}(\bar{\varepsilon}^p) - \frac{1}{3}C_{13}^{(l)}(\bar{\varepsilon}^p) \tag{20}$$

$$\psi_2^{(l)}(\bar{\varepsilon}^p) = \frac{2}{3}C_{22}^{(l)}(\bar{\varepsilon}^p) - \frac{1}{3}C_{12}^{(l)}(\bar{\varepsilon}^p) - \frac{1}{3}C_{23}^{(l)}(\bar{\varepsilon}^p) \tag{21}$$

$$\psi_3^{(l)}(\bar{\varepsilon}^p) = \frac{2}{3}C_{23}^{(l)}(\bar{\varepsilon}^p) - \frac{1}{3}C_{13}^{(l)}(\bar{\varepsilon}^p) - \frac{1}{3}C_{33}^{(l)}(\bar{\varepsilon}^p) \tag{22}$$

$$\phi_1^{(l)}(\bar{\varepsilon}^p) = \frac{2}{3}C_{11}^{(l)}(\bar{\varepsilon}^p) - \frac{1}{3}C_{12}^{(l)}(\bar{\varepsilon}^p) - \frac{1}{3}C_{23}^{(l)}(\bar{\varepsilon}^p) \tag{23}$$

$$\phi_2^{(l)}(\bar{\varepsilon}^p) = \frac{2}{3}C_{12}^{(l)}(\bar{\varepsilon}^p) - \frac{1}{3}C_{22}^{(l)}(\bar{\varepsilon}^p) - \frac{1}{3}C_{23}^{(l)}(\bar{\varepsilon}^p) \tag{24}$$

$$\phi_3^{(l)}(\bar{\varepsilon}^p) = \frac{2}{3}C_{13}^{(l)}(\bar{\varepsilon}^p) - \frac{1}{3}C_{23}^{(l)}(\bar{\varepsilon}^p) - \frac{1}{3}C_{33}^{(l)}(\bar{\varepsilon}^p) \tag{25}$$

Similar relations can be written for the compressive stress and the shear stress, while equi-biaxial conditions are satisfied by considering σ_{xx} and σ_{yy} to be equal (see Plunkett et al., 2008). r-values at any arbitrary orientation are calculated using,

$$r_\theta = -\frac{sin^2\theta\,\frac{\delta F(\bar{\varepsilon}^p)}{\delta\sigma_{xx}} - \sin(2\theta)\,\frac{\delta F(\bar{\varepsilon}^p)}{\delta\sigma_{xy}} + cos^2\theta\,\frac{\delta F(\bar{\varepsilon}^p)}{\delta\sigma_{yy}}}{\frac{\delta F(\bar{\varepsilon}^p)}{\delta\sigma_{xx}} + \frac{\delta F(\bar{\varepsilon}^p)}{\delta\sigma_{yy}}} \tag{26}$$

where $\frac{\delta F}{\delta\sigma_{xx}}$, $\frac{\delta F}{\delta\sigma_{yy}}$ and $\frac{\delta F}{\delta\sigma_{xy}}$ are the derivatives of the yield surface in terms of the Cauchy stress, considering the plane stress assumption in which $C_{44} = C_{55}$. Finally, the yield surface anisotropy parameters are found such that the following error function (Eq. (27)) is minimized.

$$E\left(a_{ij}^{(l)}, b_{ij}^{(l)}, d_{ij}^{(l)}, e^{(l)}, f^{(l)}, g^{(l)}\right) = \sum_k\left[\sum_m w_m\left(\frac{\sigma(\bar{\varepsilon}_k^p)_m^{th}}{\sigma(\bar{\varepsilon}_k^p)_m^{exp}} - 1\right)^2 + \sum_n w_n\left(\frac{r(\bar{\varepsilon}_k^p)_n^{th}}{r(\bar{\varepsilon}_k^p)_n^{exp}} - 1\right)^2\right] \tag{27}$$

In Eq. (27) $\sigma(\bar{\varepsilon}_k^p)_m^{th}$ and $r(\bar{\varepsilon}_k^p)_n^{th}$ represent the material model response for flow stresses and r-values, respectively, along a specific loading path while $\sigma(\bar{\varepsilon}_k^p)_m^{exp}$ and $r(\bar{\varepsilon}_k^p)_n^{exp}$ are the corresponding experimental values. Index k corresponds to the number of the plastic strain interval in which the analytical functions are fitted to the experiments. w is a weight parameter which introduces more emphasis on an arbitrary experiment. m and n represent the numbers of stress and r-value experiments, respectively, used in the calibration process. The flow stresses along different loading paths and sheet directions are normalized against the flow stress from the uniaxial tensile test along the rolling direction at each corresponding effective plastic strain level. The number of parameters found through this optimization procedure depends on the number of stress transformations (l).

A non-linear conjugate gradient method with a central difference scheme within the commercial software Mathcad® is used to minimize the error function (Eq. (27)). The minimization process is performed several times until the fit parameters converge and further reduction of the error magnitude is not possible. The weight parameter w is modified manually to improve the fit at those experimental points where the error in the model prediction is comparatively large. A smaller value for the error function E (Eq. (27)) represents higher regression accuracy. Since the gradient optimization method leads to a local extremum of the objective function, the choice of the initial guess of the parameters may influence the optimum. A variety of initial guesses are used to improve the final regression accuracy.

3.4. Stress integration for evolving anisotropic/asymmetric yield function

The yield formulation with evolving anisotropy and asymmetry described in Sections 3.1 and 3.2 is implemented within the framework of rate independent plasticity. A plane stress condition is assumed, corresponding to thin sheet materials. A stress integration algorithm previously proposed by Simo and Ortiz (1985), Ortiz and Simo (1986) is used which uses a return mapping scheme. A similar approach was previously used by Abedrabbo et al. (2006, 2007) to develop material models for warm forming operations of aluminum alloys, in their case adopting YLD96 (Barlat et al., 1996) and YLD2000-2d (Barlat et al., 2003) type yield functions. In the current work, the incremental theory of plasticity by Chung and Richmond (1993) is adopted in which a coordinate system embedded in the material is considered; thus, the objectivity of the Cauchy stress tensor is assured. The strain increments in the flow formulation are true (logarithmic) strains. In this material model, additive decomposition is assumed. In the commercial finite element package LS-DYNA, in each step of an explicit solution, the current total strain increment, the previous stress state and the effective plastic strain from the past step are provided.

The term $\frac{\partial\bar{\sigma}(\boldsymbol{\sigma})}{\partial\boldsymbol{\sigma}}$ is required for the following calculations which are explicitly provided by Plunkett et al. (2008) or can be calculated numerically as proposed by Barlat et al. (2005). At the start of a time step, the total strain increment is assumed to be fully elastic and then a trial stress state is calculated using the previous stress state as,

$$\boldsymbol{\sigma}_{(n+1)}^{(Trial)} = \boldsymbol{\sigma}_{(n)} + \mathbf{C} : \dot{\boldsymbol{\varepsilon}}_{(n+1)} \tag{28}$$

If the trial stress state lies inside or on the yield surface, this stress state is accepted and the history variables are updated; however, if it is outside the yield locus, it should be returned to the surface. This is indicated by checking the following term.

$$\emptyset\left(\bar{\sigma}_{(n+1)}^{(Trial)}, \bar{\varepsilon}_{(n+1)}^{p}\right) = \bar{\sigma}\left(\boldsymbol{\sigma}_{(n+1)}^{(Trial)}, \bar{\varepsilon}_{(n+1)}^{p}\right) - H\left(\bar{\varepsilon}_{(n+1)}^{p}\right) \leqslant 0 \tag{29}$$

In Eq. (29) $H\left(\bar{\varepsilon}_{(n+1)}^{p}\right)$ indicates the size of the yield surface and is calculated using the hardening rule, while $\bar{\sigma}(\boldsymbol{\sigma}_{(n+1)}^{(Trial)}, \bar{\varepsilon}_{(n+1)}^{p})$ refers to the yield function (the effective stress) which depends on the effective plastic strain. If the trial stress state is not on the yield surface, $\dot{\lambda}$ should be found so that the condition in Eq. (29) holds. The residual of $\emptyset(\bar{\sigma}_{(n+1)}^{(Trial)}, \bar{\varepsilon}_{(n+1)}^{p})$ or δ should be a small number, taken as 10^{-6} MPa in the current work, and i is the iteration number. The normality parameter $\Delta\lambda$ is found using

$$\Delta\lambda = \frac{\phi\left(\bar{\sigma}_{(n+1)}^{(i)}, \bar{\varepsilon}_{(n+1)}^{p(i)}\right)}{\frac{\partial\bar{\sigma}_{(n+1)}^{(i)}}{\partial\boldsymbol{\sigma}} : \mathbf{C} : \frac{\partial\bar{\sigma}_{(n+1)}^{(i)}}{\partial\boldsymbol{\sigma}} + \frac{\delta H^{(i)}}{\partial\bar{\varepsilon}^{p}} - \frac{\delta\bar{\sigma}^{(i)}}{\partial\bar{\varepsilon}^{p}}} \tag{30}$$

$\Delta\lambda$ represents the effective plastic strain increment which is integrated (summed) as the deformation proceeds. For plane stress calculations, the through-thickness component of the strain has to be calculated and reported back to the solver as described by Abedrabbo et al. (2006).

4. Results

4.1. Yield surface predictions

The model discussed in Sections 3.1 and 3.2 is calibrated using the experimental results shown in Section 2.2 and shear data from Khan et al. (2011). The stress values and instantaneous *r*-values at each effective plastic strain are obtained from the measured data shown in Figs. 3 and 4. In the analysis of the experimental data, the effective plastic strain was calculated using a von Mises yield assumption with associated flow. This approach is similar to that used by Steglich et al. (2011). A yield surface exponent $a = 6.0$ is assumed. Five effective plastic strain intervals (Eq. (27), $k = 5$) were used for the calibration of the evolving model, namely 0, 0.02, 0.04 0.06 and 0.08 effective plastic strain. A total of 19 experimental values at each effective plastic strain level are used in the calibration including the following: five flow stress and instantaneous *r*-values under tensile loading (0°, 30°, 45°, 60° and 90° (TD) orientations), three flow stress and instantaneous *r*-values for compressive loading (0, 45, TD orientation), the equi-biaxial tension and compression flow stresses, and a pure shear flow stress. The through-thickness compression experiment is used to fit the equibiaxial tension point on the yield surface, assuming the plastic deformation is independent of the hydrostatic stress. This assumption was judged reasonable since extension twinning, the primary source of tension–compression asymmetry, is only activated during tensile straining along the crystallographic *c*-axis which should not occur given the strong basal texture (Fig. 1) and compressive through-thickness straining experienced during both in-plane biaxial tension and through-thickness compression. As previously discussed in Fig. 3 the rate of strain hardening under through-thickness compression is higher than under uniaxial tension. A similar trend has been reported by Steglich et al. (2012) and Andar et al. (2012), comparing the equibiaxial tension and uniaxial tension flow stress responses of AZ31B magnesium alloy. Results from equibiaxial compressive experiments are not available for this material, so to avoid a non-physical response of the model in the equibiaxial compression regime, the equibiaxial compression stress is assumed to be equal to the average of the rolling and 45° compression tests in fitting the model. It is noted that the measured shear stress–strain data from Khan et al. (2011) is from a different lot of material; however, similar data for the current material lot was not available and it was judged important to constrain the shear response within the model calibration. The shear data from Khan et al. (2011) actually corresponds to simple shear, however, the difference between simple and pure shear should be small for the plastic strain levels (<0.2) considered in the calibration process (van den Boogaard, 2002).

Fig. 6 shows the evolving envelope of subsequent yield surfaces at different effective plastic strain levels after fitting to the experimental data up to 8% effective plastic strain with the *x*- and *y*-axes parallel to the RD and TD directions, respectively. Different numbers of stress transformations (one to four transformations, shown in Fig. 6a–d, respectively)

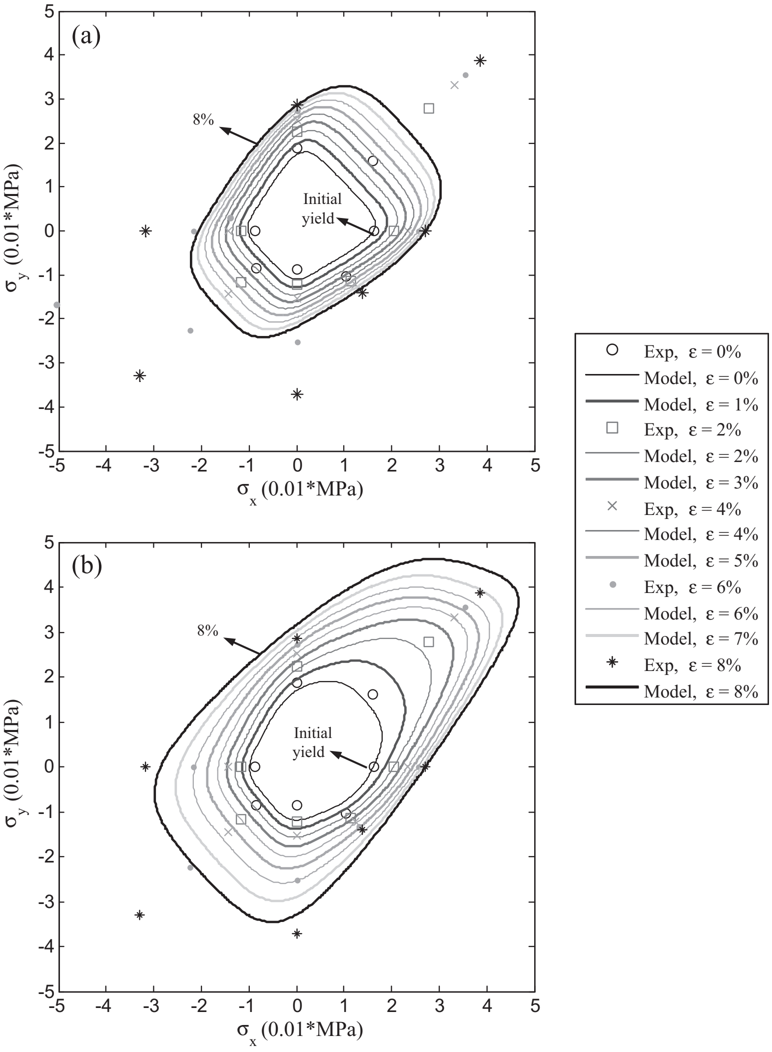

Fig. 6. Evolution of the envelope of subsequent yield surfaces considering different number of stress transformations, (a) one stress transformation (CPB06ex1ev), (b) two stress transformations (CPB06ex2ev), (c) three stress transformations (CPB06ex3ev), (d) four stress transformations (CPB06ex4ev).

were considered to assess the flexibility of the model in capturing the material response. The experimental data used for calibrating the model was the same for all four cases. The CPB06exlev designation is used henceforth to denote the evolving yield function, in which the integer *l* indicates the number of stress transformations performed on the deviatoric stress tensor and "ev" indicates that the anisotropy and asymmetry parameters are evolving with the accumulated plastic strain. In general, the use of higher numbers of stress transformations will increase the flexibility of the yield surface to more accurately fit the measured yield strength and *r*-values; however, an increased number of stress transformations will require use of additional mathematical operations and consequently more simulation time. The single stress transformation yield locus (Fig. 6a) does not capture the experimental yield stresses well. Similar mismatch is observed between the two-transformation yield locus and experiment (Fig. 6b), although the locus itself has a more reasonable shape. The best fit is seen for the three- and four-transformation yield loci and very little difference in yield locus shape is seen between Fig. 6c and d. This comparison favors adoption of the three-transformation yield locus, simply due to lower computational cost. It is noted that a single transformation fit to the measured stresses without consideration of the measured *r*-values should provide a yield surface in closer accord to the measurements in stress space; however, the predicted *r*-values (local normal) using such a fit would be in error.

To evaluate the response of the material model under the same loading conditions for which the model is fit to, a single-element finite element model is used. The measured material model responses (flow stresses and *r*-values) under different loading conditions are compared to the three-transformation fit in Figs. 7 and 8. The response of the model to different loading conditions indicates that this model is both anisotropic and asymmetric with an anisotropic hardening response

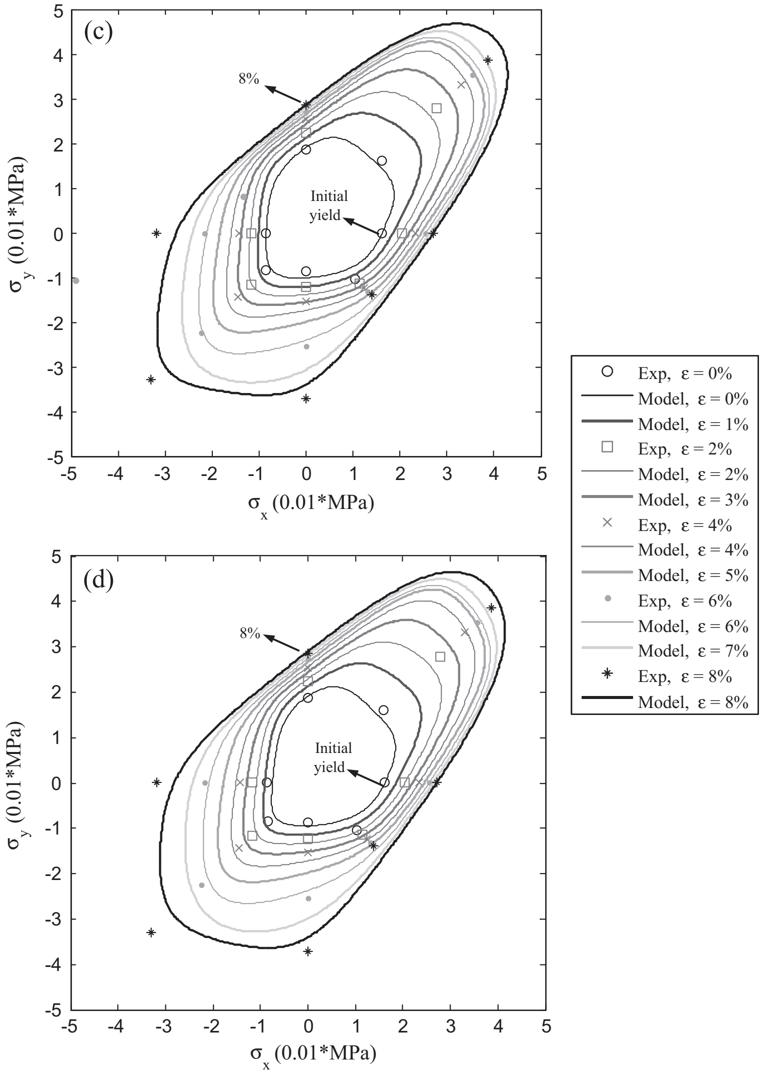

Fig. 6 (*continued*)

capturing that of the HCP metal. The tensile response is captured quite well by the model. Some discrepancy between the predicted response and the measured data under uniaxial in-plane compression is observed near the first yield point and at higher plastic strain levels. The predicted *r*-values agree well with experiment over much of the plastic strain range and loading conditions (Fig. 8), although some deviation occurs at plastic strain levels at which the model was not calibrated. This suggests that there may be a tradeoff between the accuracy of different fitted experiments. This is due to the global nature of this model which fits the model for all of the provided experiments at the same time.

Due to the rapidly evolving anisotropy and asymmetry of both flow stresses and *r*-values of AZ31B at room temperature, obtaining a fit with a high accuracy for a wide range of plastic strain is difficult. To examine this behavior, a second calibration or fitting exercise was performed for a limited plastic strain range up to only 4% effective plastic strain. Fig. 9 shows the resulting evolving envelope of subsequent yield surfaces for which only the mechanical response up to 4% effective plastic strain was used. The magnitude of the error function *E* (Eq. (27)) is improved from 0.3 to 0.01 as a lower range of plastic strain, only up to 4%, is used. In addition, a CPB06ex3 (non-evolving) model was calibrated using flow stresses and cumulative *r*-values (Fig. 4) at 4% effective plastic strain. The yield surface corresponding to this model is shown in Fig. 9.

Fig. 10 shows how the predictions of the calibrated material model compare with the experimental data. The comparison is for different directions and plastic strain intervals (up to 4%). The current model captures the trends observed in the variation in the flow stress with increased strain and orientation relative to RD under both tension and compression (Fig. 10a). The maximum error between the predicted and measured flow stress is less than 4%. Moreover, the model shows good agreement with the measured tensile and compressive instantaneous *r*-values within the plastic strain levels used for the model calibration (Fig. 10b).

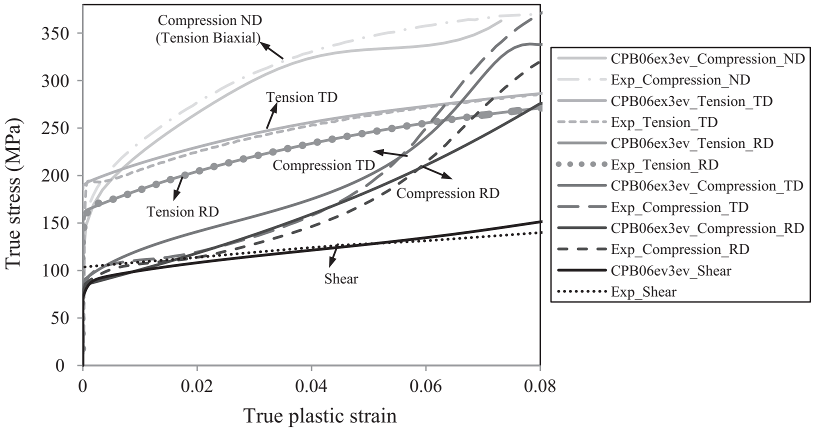

Fig. 7. Single-element stress vs. plastic strain response comparison to the experiments using different loading paths (shear experiment data from Khan et al. (2011)).

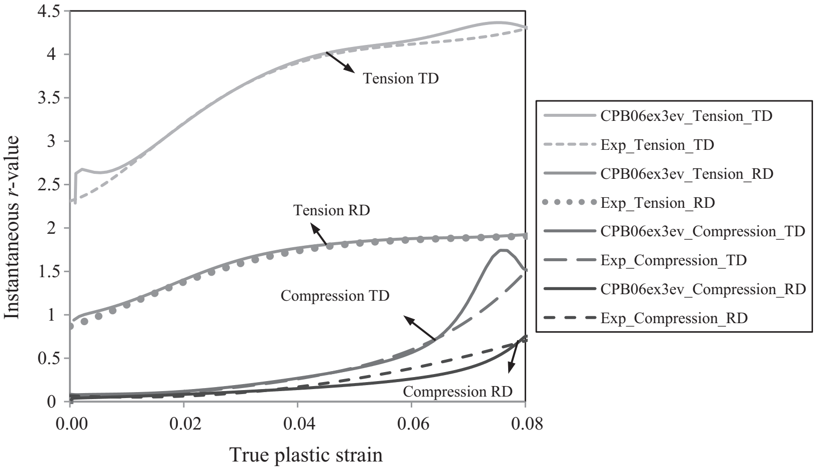

Fig. 8. Single-element instantaneous *r*-value response comparison to the experiments using different loading paths.

4.2. Three-point bending experiments

The comparison between model and experiment in the previous section is limited to essentially comparing a fit to the data used to generate the fit. In this section, the constitutive model with fitted material parameters is used to simulate an independent experiment, namely three-point bending of the AZ31B sheet. The three-point bending experiment was performed on an Instron model 1331 servo-hydraulic load frame (Fig. 11a). The samples are cut in a rectangular shape with dimensions 140 mm × 25 mm. The diameter of the cylindrical supports was 25.4 mm and the centers of the two outer cylinders were 93 mm apart. The central cylinder was fixed while the two side cylinders were actuated hydraulically. PTFE Teflon film is used between the contact surfaces to reduce friction. The distribution of strain components on the outer surface of the bend was measured using a digital image correlation system (DIC). The global coordinate system used to describe the components of strain is illustrated in Fig. 11b. Samples were cut along two sheet orientations, namely the rolling and transverse directions. The distribution of strain (ε_{xx}) in the bend region is also shown in Fig. 11b.

4.3. Model description

The commercial finite element code Ls-Dyna is used to model the three-point bending experiment. Due to symmetry, only one-fourth of the geometry is modeled and symmetry boundary conditions are applied on the central nodes of the strip. All components of the model are meshed using 4-node shell elements. A fully integrated shell element formulation with nine through thickness integration points (900 elements) is used for the deformable sheet. A Lobatto quadrature integration scheme is used to obtain the values of strain on the outer surfaces. The cylinders are modeled as rigid bodies and penalty

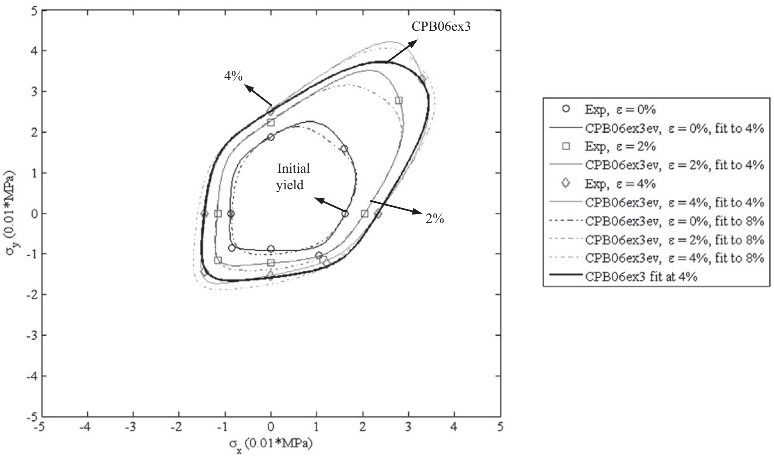

Fig. 9. Comparison of the evolution of the envelope of subsequent yield surfaces with the corresponding experimental points using 3 stress transformations (CPB06ex3ev) fit for 4% and 8% effective plastic strain. The non-evolving CPB06ex3 model at 4% effective plastic strain is also shown (bold curve).

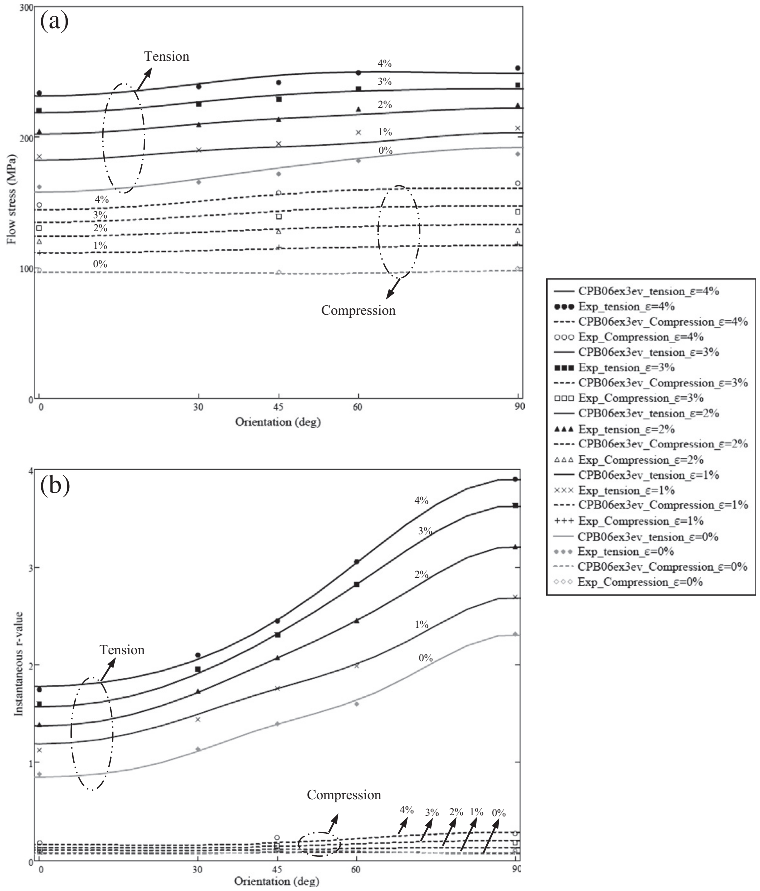

Fig. 10. Comparison of the evolution of the envelope of subsequent yield surfaces with the experimental points using 3 stress transformations (CPB06ex3ev), fit for 4% plastic strain. (a) Tensile and compressive flow stress, (b) Tensile and compressive instantaneous *r*-value.

function-based contact boundary conditions, with a constant coulomb friction coefficient of 0.048 (McKinley, 2010), are enforced between the contacting surfaces. A constant velocity of 0.76 mm/s is applied on the moving cylinders while all rotations and displacements of the fixed cylinders are constrained. A total displacement of 30 mm is applied on the moving cylinders for this simulation. To reduce the simulation time, the time step is increased to 4.5×10^{-5} s using the mass scaling

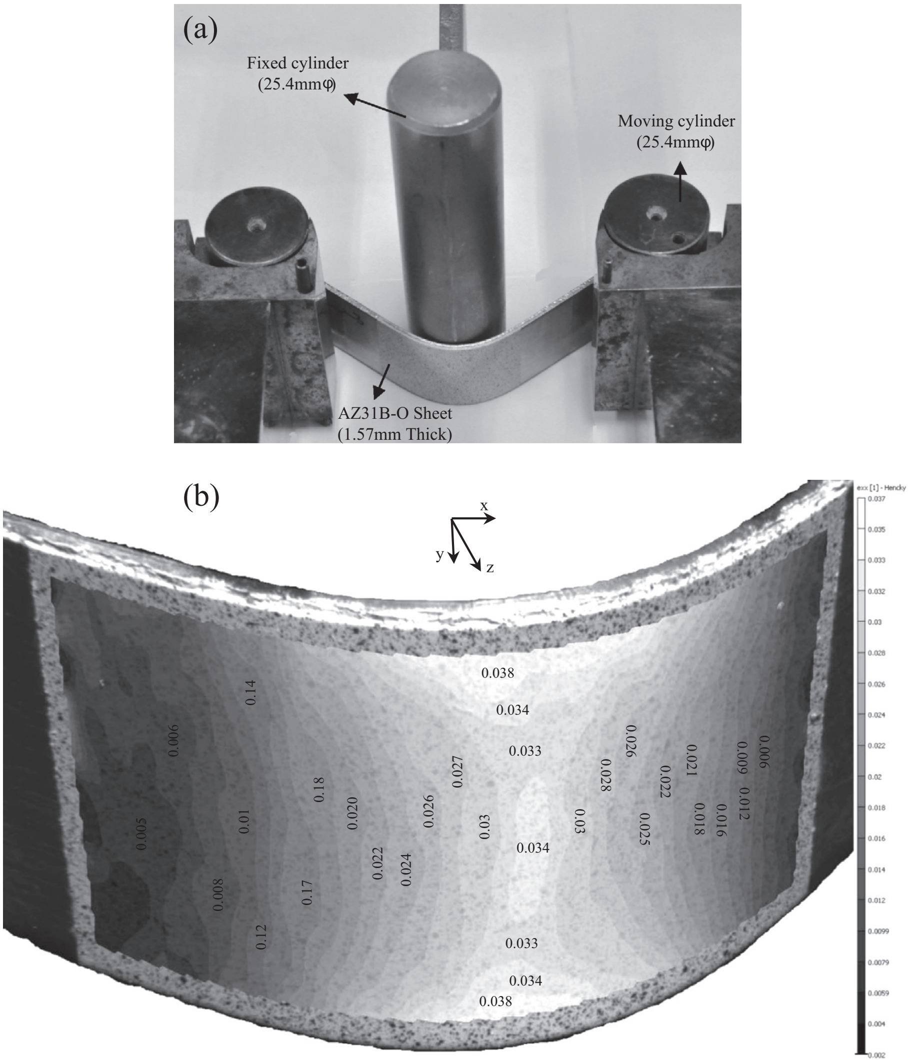

Fig. 11. Three-point bending experiment: (a) three-point bending apparatus, (b) ε_{xx} true strain field on the outer surface of the bend region (the rolling direction is aligned with the *x*-axis).

method. A constant global damping is applied to the model to reduce the oscillations caused by contact forces. The geometry and meshing of the three-point bending model is shown in Fig. 12. The major axis of the material model is either aligned along the length of the sheet (representing the RD sample) or perpendicular to it (TD sample), matching the experimental cases considered.

In order to assess the current evolving constitutive model, simulations were performed using the three-transformation evolving formulation of the Cazacu–Plunkett–Barlat yield surface (referred to here as CPB06ex3ev) and the non-evolving formulation (CPB06ex3) seen in Fig. 9 Simulations were also performed using a von Mises constitutive model. Note that the non-evolving von Mises and CPB models utilized only the tensile stress–strain response along the rolling direction to describe the material hardening response. Note that an *r*-value of unity is inherent within a von Mises yield criterion using an associated flow rule assumption. The von Mises simulation is added primarily to enable comparison between the asymmetric and symmetric (Mises) constitutive behaviors. The simulation time depends on the complexity of the yield surface formulation. The von Mises-based simulation required 276 min for the simulation on a single core of an 8-core Intel Xeon 7500 CPU, whereas the CPB06ex3 (non-evolving) and CPB06ex3ev (evolving) models needed 829 and 3057 min to run, respectively. The results corresponding to these simulations are presented in Section 4.4.

4.4. Comparison between numerical vs. experimental results

The stress vs. effective plastic strain responses obtained using the baseline von Mises and CPB06ex3ev models are compared in Fig. 13. The data are from integration points located at the center of the bend region. The integration points

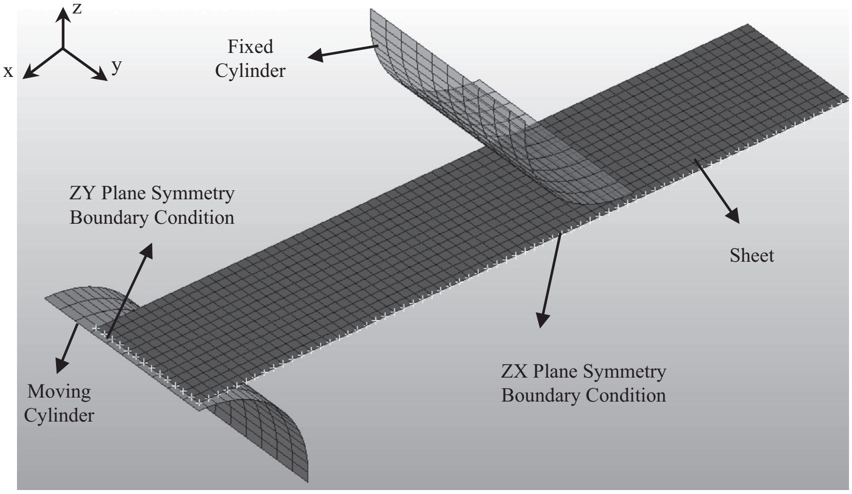

Fig. 12. Finite element model of the three-point bending experiment.

illustrated in Fig. 13 are on the top, middle and bottom surface of the shell element. The von Mises predictions exhibit the classical tension–compression bending symmetry. In contrast, the CPB06ex3ev model exhibits an evolving asymmetry of stress vs. plastic response at the different integration points through the element thickness. The middle integration point in the von Mises case is located close to the neutral axis of the bend; thus, it did not undergo plastic deformation. The neutral axis of the CPB06ex3ev model is shifted toward the outer surface of the bend which results in larger strains on the compression side including the middle integration point.

The neutral axis shift associated with the asymmetric constitutive behavior of this alloy can also be seen in the predicted strain and stress distribution through the sheet thickness, shown in Fig. 14 for the CPB06ex3ev, CPB06ex3 and von Mises models. The strain distribution is linear which is consistent for the shell element used and the relatively small thickness to bending radius ratio, $t/R = 0.121$. The nominal bending strain is 0.06 and is reflected in the von Mises predictions for which no neutral axis shift is observed (Fig. 14a). The CPB-based model predictions exhibit a shift in the neutral axis towards the compressive side of the bending distribution. A corresponding shift in the predicted stress distribution is observed in Fig. 14b.

The predicted load vs. displacement responses are compared to the experimental results in Fig. 15 for the current model (CPB06ex3ev), the von Mises model, and the non-evolving CPB06ex3 model (calibrated at 4% plastic strain). Fig. 15a shows results for RD oriented samples while Fig. 15b shows TD results. A higher load level is observed for the samples oriented along the TD direction in both the experiments and simulations. The effect of elastic anisotropy is neglected in the current material model; therefore this observed difference is the result of plastic anisotropy only. Recent research by Chung et al. (2011) suggests that elastic anisotropy might be an influential parameter influencing the load response of three point bending simulations along different orientations; however, this was not examined in the current research. Both the

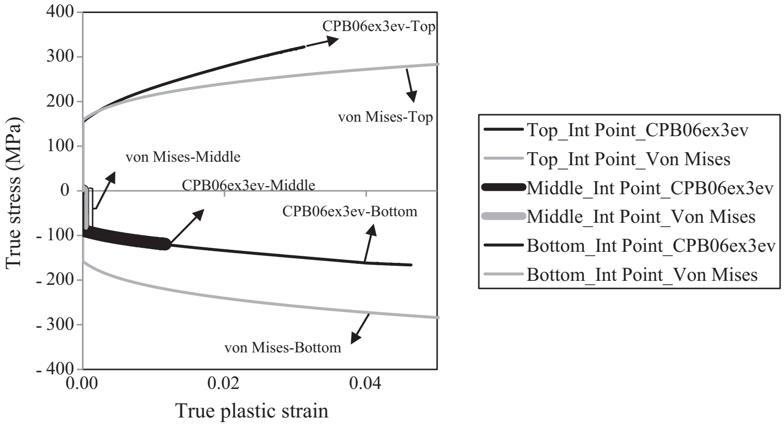

Fig. 13. Stress vs. effective plastic strain at different integration points in an element in the bending region.

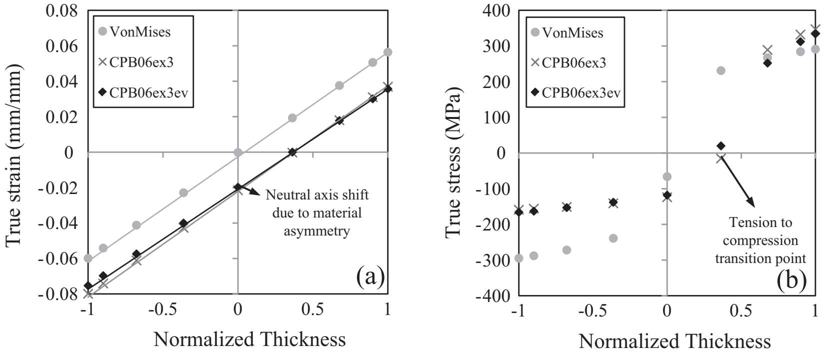

Fig. 14. Through-thickness integration point result comparison between von Mises, CPB06ex3 and CPB06ex3ev models, (a) ε_{xx} distribution, (b) σ_{xx} distribution.

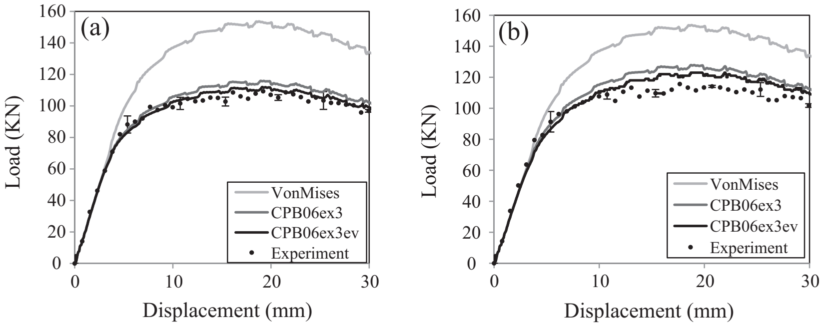

Fig. 15. Punch force vs. displacement, comparison between the experiment and simulations, (a) RD oriented sample, (b) TD oriented sample. The error bars indicate the maximum and minimum measured values from the repeat tests.

CPB06ex3 model calibrated at 4% plastic strain and the CPB06ex3ev predictions exhibit good agreement with the measured load–displacement data, with the evolving yield function predictions lying slightly closer to experiment. The von Mises predictions lie above the experimental values and CPB-based predictions.

Predicted and measured strains at the center of the bend for (a) the RD oriented samples and (b) the TD oriented samples are compared in Fig. 16. The distributions are plotted along the axis of the bend (parallel to the cylinder support axis, the y-direction in Fig. 12 with the origin corresponding to the center of the strip) and the axial strain component is referred to as ε_{xx}, whereas the lateral strain component is ε_{yy}. Both CPB-based predictions agree well with the measured strains, with the lateral strain predictions from the evolving model being slightly closer to the measured data at the specimen edges. Again, the von Mises predictions are offset from the measured strains due to an inability to capture the tension–compression asymmetry of this alloy and the resulting neutral axis shift.

The comparison between the predictions from the three-point bending simulations using CPB06ex3ev and CPB06ex3 models, illustrated in Figs. 15 and 16, indicates only a minor difference between the two models. It is noteworthy that the effective plastic strain predicted in the three-point bending simulation with a cylinder diameter of 25.4 mm is limited less than 5% (Fig. 13). To compare the CPB06ex3ev and CPB06ex3 predictions for a higher range of effective plastic strain for which the degree of yield surface evolution should be larger, simulations were performed using a smaller cylinder diameter (15.7 mm) which is corresponds to a nominal bending strain of 10%. Fig. 17 shows the bending stress distribution through the sheet thickness corresponding to a load point displacement of 3.8 and 30 mm for both the evolving and non-evolving models. These predictions utilized the yield function coefficients fit to an effective plastic strain range of 8%. Fig. 17a and b show the predictions for a cylinder diameter of 25.4 and 15.7 mm, respectively. The results for the larger cylinder show very little difference between the evolving and non-evolving predictions. The results for the smaller cylinder show stronger evolution of the asymmetry, which can be observed in the difference in the compressive stresses between the two predictions at the higher load point displacement.

5. Discussion

The room temperature mechanical response of AZ31B-O at a quasi-static strain rate (0.001 s^{-1}) has been characterized along a broad range of loading paths in both tension and compression. In addition to differences in the tensile and

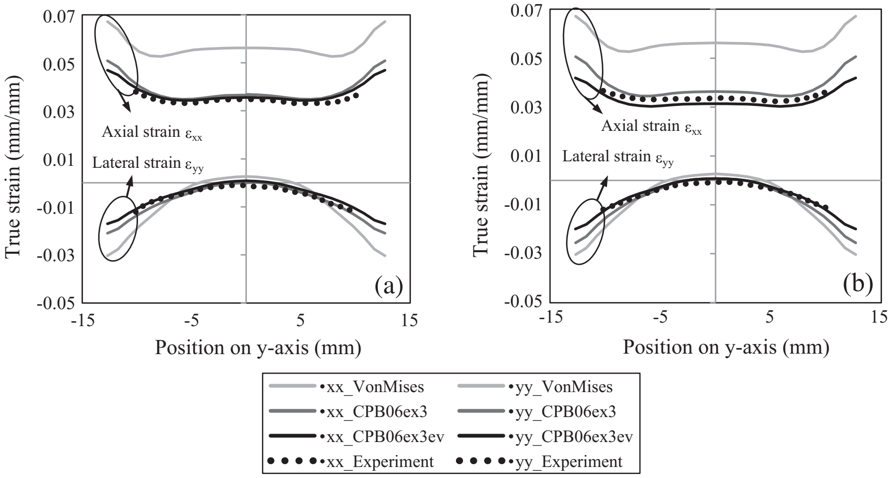

Fig. 16. ε_{xx} and ε_{yy} comparison between the experimental measurements and the simulations, (a) RD oriented sample, (b) TD oriented sample. Error bars are not shown for clarity; however, the average absolute deviation from the mean was approximately 0.003 and 0.004 for the ε_{xx} and ε_{yy} curves of the RD oriented samples. The average absolute deviation from the mean for the ε_{xx} and ε_{yy} curves of the TD oriented samples was 0.002 and 0.001.

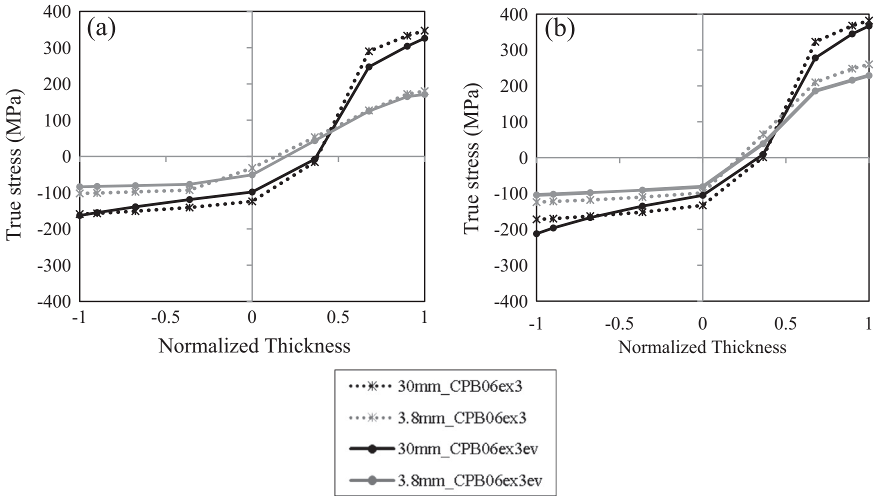

Fig. 17. Bending stress (σ_{xx}) distribution through the sheet thickness at the center of the bend. Shown are predictions using the CPB06ex3 and CPB06ex3ev models at two punch displacement levels (3.8 and 30 mm): (a) results for the 25.4 mm cylinder diameter used in the experiments and, (b) results for a cylinder diameter of 15.7 mm.

compressive strengths, the data reveals significant tension–compression anisotropy in both the measured *r*-values and the evolution of the *r*-values with accumulated plastic strain. The (0002) pole figure in Fig. 1 shows a slight off-basal shift of the *c*-axis towards the rolling direction which leads to the in-plane anisotropic behavior of AZ31B (Kallend and Rollet, 1991). This tilt of the basal planes towards the rolling direction favors basal slip over non-basal prismatic slip which leads to lower *r*-values along the rolling direction, as indicated by Del Valle and Ruano (2009).

The yield criteria developed by Cazacu et al. (2006) and Plunkett et al. (2008) was adopted in the current research as a starting point to develop a phenomenological constitutive model capable of capturing the complex evolving measured material response. In the work by Plunkett et al. (2006, 2007) and Nixon et al. (2010) a linear interpolation approach between two sequential yield surfaces was proposed. In the current work, a saturation-type interpolation function is introduced which enables interpolation between fitted yield function parameters and extension of the yielding response beyond the calibrated response. In addition, the current approach considers calibration of the yield function parameters to capture both yield stresses and *r*-values over the entire range of the calibration experiments. Previous work by Nebebe Mekonen et al. (2012) has undertaken calibration of yield strength and *r*-values in the tensile quadrant of the yield surface; in the current work, material asymmetry is also captured by fitting evolving yield function coefficients for both tension and compression, thereby capturing evolving asymmetry in strength and *r*-values. This broad calibration is enabled by the flexibility of the CPB yield function (Cazacu et al., 2006; Plunkett et al., 2008) and the current work demonstrates the importance of utilizing higher order stress transformations to fully capture the material behavior. In this case, three transformations were necessary to properly capture the evolving yield asymmetry and mechanical response in the measured response of AZ31B.

Note that the effective plastic strain was approximated in the analysis of the experimental data (before calibrating the CPB06 model) using a von Mises yield assumption with associated flow, following the approach of Steglich et al. (2011) whereas in the model, the effective plastic strain is calculated by direct integration of equation (30). This difference arises since no explicit term for calculation of effective plastic strain using the CPB06 model is available. To estimate the resulting difference in the plastic strain calculation between the experiments and model, each experiment was simulated using the UMAT using the calibrated CPB06 coefficients. In most cases, the difference between the effective plastic strain calculated using the CPB06 and von Mises assumptions was small, with the largest difference being 11.6% for the tensile, TD loading case. In principle, the experimental data could be reanalyzed using the CPB06 equations to improve the estimate of effective plastic strain after which the yield function fits could be improved; however, this was not attempted in the current work.

An important limitation of the current yield formulation is that it is strictly valid for proportional loading only. Non-proportional loading paths, in particular reversed loading, results in de-twinning (Lou et al., 2007) in magnesium alloys and the current formulation does not account for such behavior. Modeling such behavior is difficult within phenomenological formulations, although significant progress has been made by Li et al. (2010) and Lee et al. (2010), and crystal plasticity approaches have made significant gains in modeling de-twinning behavior (Proust et al., 2009; Hama and Takuda, 2011; Hama et al., 2013; Wang et al., 2013a,b). The effect of reversed loading and the treatment of de-twining and Bauschinger phenomena are left for future work.

As the solution for the anisotropy and asymmetry parameters is found through minimization procedures (a deterministic solution is not available), depending on the complexity of the material characterization data a residual error may remain after the optimization has reached the final solution. This may cause some deviation from the actual material response which should be carefully investigated and understood before using the calibrated model in computer simulations.

The current model shows improvement in the prediction of bending stress distribution within the sheet by accounting for the evolving asymmetry; however, the predicted forming forces and strains in the current three-point bending experiment were similar to those predicted using a non-evolving approach. The assessment of the proposed model for larger bending strains and for more complex forming processes, such as non-isothermal deep drawing of AZ31B (Ghaffari Tari et al., 2013), is the subject of current work. This on-going effort includes inclusion of the effect of temperature and strain rate, building upon the efforts of Khan et al. (2011), Kurukuri et al. (2012), Ghaffari Tari and Worswick (2011),.

6. Conclusion

- A strong, evolving tension/compression asymmetry in both flow stress and *r*-value response of AZ31B was observed. The compressive *r*-values are initially lower than the tensile *r*-values; however, the rate of *r*-value evolution with accumulated plastic strain is higher under compression loading.
- A continuum-based plasticity approach, considering proportional loading, has been proposed to capture the evolving anisotropic/asymmetric response of HCP metals such as magnesium alloy AZ31B which not only captures the evolution of the flow stress response under different loading conditions but also the evolution of *r*-values under both tension and compression.
- The CPB06ex3ev material model provides improved predictions of bending stress distribution by capturing evolving yield asymmetry; however, the predicted load vs. displacement response and strain distributions for the current three-point bending tests using the evolving and non-evolving CPB models were similar.

Acknowledgments

This research was carried out under the framework of the Research Program of the Magnesium Network (MagNET), Canada. Financial support from MagNET, the Natural Sciences and Engineering Research Council (NSERC), the Canada Research Chairs Secretariat and the Ontario Research Fund is gratefully acknowledged. The advice and helpful comments from Kamyar Ghavam, Srihari Kurukuri and Reza Bagheriasl are highly appreciated. The authors would like to thank Mark Kuntz, Eckhard Budziarek, Richard Forgett, Andy Barber and Mark Griffet at the University of Waterloo for their experimental support.

Appendix A

Anisotropy/asymmetry parameters for CPB06ex3ev and CPB06ex3 models.

Up to 4% plastic strain																				
a_{11}	b_{11}	d_{11}	a_{12}	b_{12}	d_{12}	a_{13}	b_{13}	d_{13}	a_{22}	b_{22}	d_{22}	a_{23}	b_{23}	d_{23}	a_{33}	b_{33}	d_{33}	a_{66}	b_{66}	d_{66}
−0.46500	19.53100	−0.28900	−1.14900	−9.69300	1.61200	−1.63400	0.07500	0.01900	0.02000	−3.83800	2.42700	−1.57000	0.18800	426.76000	−0.22000	−23.98500	0.81100	1.25200	0.11600	0.09000
a'_{11}	b'_{11}	d'_{11}	a'_{12}	b'_{12}	d'_{12}	a'_{13}	b'_{13}	d'_{13}	a'_{22}	b'_{22}	d'_{22}	a'_{23}	b'_{23}	d'_{23}	a'_{33}	b'_{33}	d'_{33}	a'_{66}	b'_{66}	d'_{66}
0.08000	−0.06400	0.05800	−1.12000	1.46400	−0.08800	−0.53600	13.23500	0.37100	0.07300	−0.00005	0.06000	−0.09900	1.10100	0.07200	0.54100	−0.51800	0.07100	1.16300	6.11700	−0.00040
a''_{11}	b''_{11}	d''_{11}	a''_{12}	b''_{12}	d''_{12}	a''_{13}	b''_{13}	d''_{13}	a''_{22}	b''_{22}	d''_{22}	a''_{23}	b''_{23}	d''_{23}	a''_{33}	b''_{23}	d''_{33}	a''_{66}	b''_{66}	d''_{66}
0.10100	−238.49500	0.03200	−0.75700	−28.00500	0.31300	−1.54000	270.99200	−0.01700	0.04900	−76.36600	0.09900	−1.56000	0.00250	2.75200	−1.41400	−7.49900	−0.63200	0.83700	−0.64100	−0.00089
e	f	g																		
0.32300	−0.26800	475.68000																		
e'	f'	g'																		
0.35000	4.88800	−0.12300																		
e''	f''	g''																		
1.00000	−1.17600	0.00009																		
Up to 8% plastic strain																				
a_{11}	b_{11}	d_{11}	a_{12}	b_{12}	d_{12}	a_{13}	b_{13}	d_{13}	a_{22}	b_{22}	d_{22}	a_{23}	b_{23}	d_{23}	a_{33}	b_{33}	d_{33}	a_{66}	b_{66}	d_{66}
−1.26300	58.36200	0.19300	0.25900	−1.70700	11.52300	0.47700	0.07100	0.01800	0.00263	−1.93900	3.97700	0.58300	0.00001	−141.90600	2.52300	−2.60600	33.43600	0.51300	−0.09200	−0.42600
a'_{11}	b'_{11}	d'_{11}	a'_{12}	b'_{12}	d'_{12}	a'_{13}	b'_{13}	d'_{13}	a'_{22}	b'_{22}	d'_{22}	a'_{233}	b'_{23}	d'_{23}	a'_{33}	b'_{33}	d'_{33}	a'_{66}	b'_{66}	d'_{66}
−0.03300	−0.07000	0.06300	−1.21300	0.21200	−0.03800	−0.39900	−4.42000	0.17900	−0.05600	−0.05400	3.97400	−0.11500	3.59700	−0.77400	−2.30900	19.43800	0.85800	1.20800	−102.11200	0.00585
a''_{11}	b''_{11}	d''_{11}	a''_{12}	b''_{12}	d''_{12}	a''_{13}	b''_{11}	d''_{13}	a''_{22}	b''_{22}	d''_{22}	a''_{23}	b''_{23}	d''_{23}	a''_{33}	b''_{33}	d''_{33}	a''_{66}	b''_{66}	d''_{66}
0.21900	−257.76700	0.07800	−0.78600	−5.77700	3.62700	−1.80900	421.84700	−0.02900	0.21400	−135.04700	0.17400	-1.13900	0.03300	−42.88000	−2.74700	2.48900	−0.28200	0.99800	−0.47900	−0.00066
e	f	g																		
−0.20000	0.05600	12.91800																		
e'	f'	g'																		
0.31200	−2.61600	−0.32000																		
e''	f''	g''																		
1.00000	−220.50000	0.04800																		
At 4% plastic strain																				
C_{11}	C_{12}	C_{13}	C_{22}	C_{23}	C_{33}	C_{66}														
−0.00507	−0.78100	−0.68700	0.01200	−0.58600	0.40700	0.79500														
C'_{11}	C'_{12}	C'_{13}	C'_{22}	C'_{23}	C'_{33}	C'_{66}														
0.81400	−0.00016	−0.47300	0.81300	−0.55900	0.00016	0.82200														
C'_{11}	C'_{12}	C'_{13}	C'_{22}	C'_{23}	C'_{33}	C'_{66}														
0.76700	−0.00016	−0.63300	0.63600	−0.15800	0.00016	0.74100														
k	k'	k''																		
−1.00000	1.00000	1.00000																		

References

Abedrabbo, N., Pourboghrat, F., Carsley, J., 2006. Forming of aluminum alloys at elevated temperatures – Part I: material characterization. International Journal of Plasticity 22, 314–341.

Abedrabbo, N., Pourboghrat, F., Carsley, J., 2007. Forming of AA5182-O and AA5754-O at elevated temperatures using coupled thermo-mechanical finite element models. International Journal of Plasticity 23, 841–875.

Agnew, S.R., Duygulu, Ö., 2005. Plastic anisotropy and the role of non-basal slip in magnesium alloy AZ31B. International Journal of Plasticity 21, 1161–1193.

Andar, M.O., Kuwabara, T., Steglich, D., 2012. Material modeling of AZ31 Mg sheet considering variation of *r*-values and asymmetry of the yield locus. Materials Science and Engineering A 549, 82–92.

Aretz, H., Barlat, F., 2013. New convex yield functions for orthotropic metal plasticity. International Journal of Non-Linear Mechanics 51, 97–111.

Barlat, F., Maeda, Y., Chung, K., Yanagawa, M., Brem, J.C., Hayashida, Y., Lege, D.J., Matsui, K., Murtha, S.J., Hattori, S., Becker, R.C., Makosey, S., 1997. Yield function development for aluminum alloy sheet. Journal of Mechanics and Physics of Solids 45, 1727–1763.

Barlat, F., Brem, J.C., Yoon, J.W., Chung, K., Dick, R.E., Lege, R.E., Pourboghrat, F., Choi, S.H., Chu, E., 2003. Plane stress yield function for aluminum alloys sheets – Part I: theory. International Journal of Plasticity 19, 1297–1319.

Barlat, F., Aretz, H., Yoon, J.W., Karabin, M.E., Brem, J.C., Dick, R.E., 2005. Linear transformation-based anisotropic yield functions. International Journal of Plasticity 21, 1009–1039.

Cazacu, O., Barlat, F., 2001. Generalization of Drucker's yield criterion to orthotropy. Mathematics and Mechanics of Solids 6, 613–630.

Cazacu, O., Barlat, F., 2003. Application of theory of representation to describe yielding of anisotropic aluminum alloys. International Journal of Engineering Science 41, 1367–1385.

Cazacu, O., Barlat, F., 2004. A criterion for description of anisotropy and yield differential effects in pressure-insensitive metals. International Journal of Plasticity 20, 2027–2045.

Cazacu, O., Plunkett, B., Barlat, F., 2006. Orthotropic yield criterion for hexagonal closed packed metals. International Journal of Plasticity 22, 1171–1194.

Chung, K., Richmond, O., 1993. A deformation theory of plasticity based on minimum work paths. International Journal of Plasticity 9 (8), 907–920.

Chung, K., Ahn, K., Yoo, D., Chung, K., Seo, M., Park, S., 2011. Formability of TWIP (twinning induced plasticity) automotive sheets. International Journal of Plasticity 27, 52–81.

Del Valle, J.A., Ruano, O.A., 2009. Effect of annealing treatments on the anisotropy of magnesium alloy sheet processes by severe rolling. Materials Letters 63, 1551–1554.

Drucker, D.C., 1949. Relation of experiments to mathematical theories of plasticity. Journal of Applied Mechanics 16, 349–357.

Ghaffari Tari, D., Worswick, M.J., 2011. Experimental investigation of anisotropy evolution of AZ31 magnesium alloy sheets under tensile loading. In: Proceedings of the Esaform 2011, Belfast, Ireland.

Ghaffari Tari, D., Worswick, M.J., Winkler, S., 2013. Experimental studies of deep drawing of AZ31B magnesium alloy sheet under various thermal conditions. Journal of Materials Processing Technology 213, 1337–1347.

Gilles, G., Hammami, W., Libertiaux, V., Cazacu, O., Yoon, J.H., Kuwabara, T., Habraken, A.M., Duchêne, 2011. Experimental characterization and elasto-plastic modeling of the quasi-static mechanical response of TA-6 V at room temperature. International Journal of Solids and Structures 48, 1277–1289.

Hama, T., Takuda, H., 2011. Crystal-plasticity finite-element analysis of inelastic behavior during unloading in a magnesium alloy sheet. International Journal of Plasticity 27, 1072–1092.

Hama, T., Kitamura, N., Takuda, H., 2013. Effect of twinning and detwinning on inelastic behavior during unloading in a magnesium alloy sheet. Materials Science and Engineering A 583, 232–241.

Hasenpouth, D., Salisbury, C., Bardelcik, A., Worswick, M.J., 2009. Constitutive behavior of magnesium alloy sheet at high strain rates. In: Proceedings of DYMAT 2009 9th International Conference on the Mechanical and Physical Behavior of Materials under Dynamic Loading, Brussels, Belgium.

Hill, R., 1948. A theory of the yielding and plastic flow of anisotropic metals. Proceedings of the Royal Society of London 193, 281–297.

Hill, R., 1950. Mathematical Theory of Plasticity. Clarendon Press.

Jain, A., Agnew, S.R., 2007. Modeling the temperature dependent effect of twinning on the behavior of magnesium alloy AZ31B sheet. Materials Science and Engineering A 462, 29–36.

Jiang, L., Jonas, J.J., Mishra, R.K., Luo, A.A., Sachdev, A.K., Godet, S., 2007. Twinning and texture development in two Mg alloys subjected to loading along three different strain paths. Acta Materialia 55, 3899–3910.

Kallend, J.S., Rollet, U.F., 1991. Operational texture analysis. Material Science and Engineering 132, 1–11.

Kelley, E.W., Hosford Jr., W.F., 1968. The deformation characteristics of textured magnesium. Transactions of TMS-AIME 242, 654–661.

Khan, A.S., Kazmi, R., Pandey, A., Stoughton, T., 2009. Evolution of subsequent yield surfaces and elastic constants with finite plastic deformation. Part-A very low work hardening aluminum alloy (Al6061-T6511). International Journal of Plasticity 25 (9), 1611–1625.

Khan, A.S., Pandey, A., Stoughton, T., 2010a. Evolution of subsequent yield surfaces and elastic constants with finite plastic deformation. Part II: a very high work hardening aluminum alloy (annealed 1100 Al). International Journal of Plasticity 26 (10), 1421–1431.

Khan, A.S., Pandey, A., Stoughton, T., 2010b. Evolution of subsequent yield surfaces and elastic constants with finite plastic deformation. Part III: yield surface in tension–tension stress space (Al 6061-T 6511 and annealed 1100 Al). International Journal of Plasticity 26 (10), 1432–1441.

Khan, A.S., Pandey, A., Gnaupel-Herold, T., Mishra, R.K., 2011. Mechanical response and texture evolution of AZ31 alloy at large strains for different strain rates and temperatures. International Journal of Plasticity 27, 688–706.

Khosravani, A., Scott, J., Miles, M.P., Fullwood, D., Adams, B.L., Mishra, R.K., 2013. Twinning in magnesium alloy AZ31B under different load paths at moderately elevated temperatures. International Journal of Plasticity 45, 160–173.

Kim, J., Ryou, H., Kim, D., Kim, D., Lee, W., Hong, Seung-Hyun, Chung, K., 2008. Constitutive law for AZ31B Mg alloy sheets and finite element simulation for three-point bending. International Journal of Mechanical Sciences 50, 1510–1518.

Klepaczko, J.R., Malinowski, J.Z., 1977. Dynamic frictional effects as measured from the split Hopkinson pressure bar. In: IUTAM Symposium on High: Velocity Deformation of Solids, Tokyo, Japan. Springer-Verlag, Berlin, p. 403.

Kurukuri, S., Ghaffari Tari, D., Worswick, M.J., Mishra, R.K., Carter, J.T., 2012. Dynamic characterization of AZ31B and ZEK100 magnesium alloy sheets. In: Proceedings of Magnesium Conference 2012. Vancouver, Canada.

Lee, M.G., Kim, S.J., Wagoner, R.H., Chung, K., Kim, H.Y., 2010. Constitutive modeling for anisotropic/asymmetric hardening behavior of magnesium alloy sheets: application to sheet springback. International Journal of Plasticity 25, 70–104.

Li, M., Lou, X.Y., Kim, J.H., Wagoner, R.H., 2010. An efficient constitutive model for room-temperature, low-rate plasticity of annealed Mg AZ31B sheet. International Journal of Plasticity 26, 820–858.

Lou, X.Y., Li, M., Boger, R.K., Agnew, S.R., Wagoner, R.H., 2007. Hardening evolution of AZ31B Mg sheet. International Journal of Plasticity 23, 44–86.

Lou, Y., Huh, H., Yoon, J.W., 2013. Consideration of strength differential effect in sheet metals with symmetric yield functions. International Journal of Mechanical Sciences 66, 214–223.

Maeda, Y., Yanagawa, M., Barlat, F., Chung, K., Hayashida, Y., Hattori, S., Matsui, K., Brem, J.C., Lege, D.J., Murtha, S.J., Ishikawa, T., 1998. Experimental analysis of aluminum yield surface for binary Al–Mg alloy sheet samples. International Journal of Plasticity 14, 301–318.

McKinley, J.J., 2010. Warm forming of aluminum brazing sheet experiments and numerical Simulations. M.Sc. Thesis, University of Waterloo; Ontario, Canada.

Nebebe Mekonen, M., Steglich, D., Bohlen, J., Letzig, D., Mosler, J., 2012. Mechanical characterization and constitutive modeling of Mg alloy sheets. Materials Science and Engineering A 540, 174–186.

Nixon, M.E., Cazacu, O., Lebensohn, R.A., 2010. Anisotropic response of high-purity α-titanium: experimental charactrization and constitutive modeling. International Journal of Plasticity 26, 516–532.

Ortiz, M., Simo, J.C., 1986. An analysis of a new class of integration algorithms for elastoplastic constitutive relations. International Journal for Numerical Methods in Engineering 23, 353–366.

Piao, K., Lee, J.K., Kim, J.H., Kim, H.Y., Chung, K., Barlat, F., 2012a. A sheet tension/compression test for elevated temperature. International Journal of Plasticity 38, 27–46.

Piao, K., Chung, K., Lee, M.G., Wagoner, R.H., 2012b. Twinning-slip transitions in Mg AZ31B. Metallurgical and Materials Transactions A 43, 3300–3313.

Plunkett, B., Lebensohn, R.A., Cazacu, O., Barlat, F., 2006. Anisotropic yield function of hexagonal materials taking into account texture development and anisotropic hardening. Acta Materialia 54, 4159–4169.

Plunkett, B., Cazacu, O., Lebensohn, R.A., Barlat, F., 2007. Elastic-viscoplastic anisotropic modeling of textured metals and validation using the Taylor cylinder impact test. International Journal of Plasticity 23, 1001–1021.

Plunkett, B., Cazacu, O., Barlat, F., 2008. Orthotropic yield criteria for description of the anisotropy in tension and compression of sheet metals. International Journal of Plasticity 24, 847–866.

Powel, B.E., Skove, M.J., 1982. A combination of third-order elastic constants of aluminum. Journal of Applied Physics 53, 764–765.

Simo, J.C., Ortiz, M., 1985. A unified approach to finite deformation elastoplastic anaysis based on the use of hyperelastic constitutive equations. Computer Methods in Applied Mechanics and Engineering 49, 221–245.

Spitzig, W.A., Sober, R.J., Richmond, O., 1975. Pressure dependence of yielding and associated volume expansion in tempered martensite. Acta Metallurgica 23, 885–893.

Steglich, D., Brocks, W., Bohlen, J., Barlat, F., 2011. Modelling direction-dependent hardening in magnesium sheet forming simulations. International Journal of Material Forming 4, 243–253.

Steglich, D., Jeong, Y., Andar, M.O., Kuwabara, T., 2012. Biaxial deformation of AZ31 magnesium alloy: crystal-plasticity-based prediction and experimental validation. International Journal of Solid and Structures 49, 3551–3561.

Stoughton, T.B., Yoon, J., 2004. A pressure-sensitive yield criterion under a non-associated flow rule for sheet metal forming. International Journal of Plasticity 20, 705–731.

Sun, L., Wagoner, R.H., 2011. Complex unloading behavior: nature of the deformation and its consistent representation. International Journal of Plasticity 27, 1126–1144.

Tozawa, N., 1978. Plastic deformation behavior under the conditions of combined stress. In: Koistinen, D.P., Wang, N.-M. (Eds.), Mechanics of Sheet Metal Forming. Plenum Press, New York, pp. 81–110.

Van den Boogaard, A.H., 2002. Thermally enhanced forming of aluminum alloy sheet modelling and experiments, Ph.D. Thesis, University of Twente, the Netherlands.

Von Mises, R., 1913. Mechanik der festen Körper im plastisch- deformablen Zustand. Nachrichten von der Gesellschaft der Wissenschaften zu Göttingen, Mathematisch-Physikalische Klasse 1, 582–592.

Wang, H., Wu, P.D., Wang, J., Tomé, C.N., 2013a. A crystal plasticity model for hexagonal close packed (HCP) crystals including twinning and de-twinning mechanisms. International Journal of Plasticity 49, 36–52.

Wang, H., Wu, P.D., Wang, J., 2013b. Modeling inelastic behavior of magnesium alloys during cyclic loading–unloading. International Journal of Plasticity 47, 49–64.

Wong, T.E., Johnson, G.C., 1988. On the Effects of Elastic Nonlinearity in Metals. J. Eng. Mater. Technol. 110 (4), 332–337.

Yoon, J., Cazacu, O., Mishra, R.K., 2013. Constitutive modeling of AZ31 magnesium alloy with application to axial crushing. Materials Science and Engineering A 565, 203–212.

Appendix C: D. Ghaffari Tari, M.J. Worswick, *Material characterization and metal forming simulations of magnesium alloys at elevated temperatures using an evolving envelope of subsequent yield surfaces approach*, Journal of Materials Processing Technology, submitted March 19, 2014

Elevated Temperature Constitutive Behavior and Simulation of Warm Forming of AZ31B

D. Ghaffari Tari[a],*, M. J. Worswick[a]

a. University of Waterloo, 200 University Ave West, Waterloo, Ontario, Canada

Abstract

Tension and compression testing has been performed over a wide range of temperatures (23-250°C), strain rates (0.001-1 s^{-1}) and material orientations to characterize the mechanical response of AZ31B-O. Instantaneous *r*-values were measured and their evolution with plastic strain. A strong evolving asymmetry/anisotropy is observed comparing the tension and compression flow stresses and *r*-values at room temperature, while weaker anisotropy/asymmetry is seen at higher temperatures. Higher strain rate sensitivity is measured at elevated temperatures. An evolving anisotropic/asymmetric continuum level material model based on a CPB-type yield function (Cazacu et al., 2006), as modified by Ghaffari Tari et al. (2014), was used to fit the material behavior at different temperatures. Two approaches are considered to introduce thermal softening and strain rate sensitivity. For isothermal conditions, a rate-sensitive Cowper-Symonds strain hardening model, fit at individual temperatures, captured the material behavior well. For non-isothermal conditions, a strain rate and temperature dependent hardening response based on a modified Nadai model was used. Both approaches have been coded into a user material subroutine within the commercial finite element package, LS-DYNA and used to simulate limiting dome height experiments performed at 250°C and non-isothermal deep drawing experiments in which the temperature distribution within the blank ranged between 170°C to 250°C.

Keywords: Magnesium alloys, yield function, anisotropic hardening, yield asymmetry, thermal softening, strain rate sensitivity, continuum-based plasticity, metal forming.

1. INTRODUCTION

Magnesium alloys have a high strength-to-density ratio which makes them a good alternative to the steel and aluminum alloys currently used in the automotive industry (Mordike and Ebert, 2001). However, at present the application of magnesium alloys is mostly limited to extruded parts and castings (Kulekci, 2008). Magnesium alloys generally have limited formability at room temperature due to the limited number of active slip systems in their hexagonal closed packed crystal (HCP) structure (Zhang et al., 2011). Twinning is an additional deformation mechanism which is only active for certain loading paths. Furthermore, a basal or a near-basal crystallographic texture is found in conventional magnesium alloy sheet as a result of rolling (Kelley and Hosford, 1968). Consequently, the mechanical response of magnesium at room temperature under tension and compression is highly asymmetric and anisotropic (Lou et al., 2007). However, as temperature is increased, the observed anisotropy and asymmetry decreases (Agnew et al., 2005). Piao et al. (2012) considered twinning-de-twinning under reversed loading and found that the de-twinning transition region from compression to tension was suppressed at temperatures higher than 150 °C. Khan et al. (2011) investigated the mechanical response of magnesium alloys at room and elevated temperatures (up to 150°C) and reported a reduction in the tension/compression asymmetry at elevated temperatures. In another study by Jain and Agnew (2007), compression tests were performed under a wide range of temperatures varying from 22-250˚C. The onset of yield was reported to be insensitive to temperature up to 200°C which suggests that a temperature independent deformation mechanism is active during yielding. In addition, a very low compressive *r*-value was measured at room temperature which is known to be indicative of twining (Jain et al., 2007). Kurukuri et al. (2013) investigated the compression response of AZ31 at different strain rates at room temperature using adhesively bonded stacked sheet specimens. Strain rate insensitivity of the compressive yield stress was reported, while a strong strain rate sensitivity of the work hardening behavior beyond the twinning plateau was observed. A strong strain rate sensitivity of the *r*-values at 200°C was also reported by Ghaffari Tari and Worswick (2011).

Due to the complex mechanical response of magnesium alloys, the earlier continuum-based yield functions, such as those of Hill (1948), and Barlat et al. (1997), for example, are not appropriate for modeling materials with HCP lattice structures. Therefore, asymmetric yield surface formulations have been proposed for materials with HCP structure. In these models, the general frame work of performing linear transformations on the Cauchy stress tensor, proposed by Barlat et al. (2005), is used to introduce anisotropic parameters into the yield function formulation. One notable example of this type of yield function formulation is the non-quadratic yield surface (CPB06) proposed by Cazacu et al. (2006). This yield surface formulation is homogeneous of degree *a*. An asymmetry parameter is included in this formulation which is controlled by the strength ratio between tension and compression. Plunkett et al. (2008) proposed that the accuracy in the description of flow stresses and *r*-values at tension and compression increases if more than one stress transformation is performed on the principal deviatoric stresses. The anisotropic/asymmetric evolution of the yield locus has been modeled in the previous research by Plunkett et al. (2006). Ghaffari Tari et al. (2014) replaced the anisotropy and asymmetry parameters of a CPB06 yield surface with functions expressed in terms of plastic strain to capture the evolution of the yield surfaces. The modified model with three stress transformations reproduced tension/compression experiments on AZ31B at room temperature and a strain rate of $0.001s^{-1}$ which was initially used for fitting purposes. The capability of the proposed model was later assessed by comparing the load *vs.* displacement curves and strain predictions from a three point bending simulation to the corresponding experiments at room temperature.

Simulation of forming processes at elevated temperatures requires consideration of thermal softening and strain rate effects (Kurukuri et al., 2009). Abedrabbo et al. (2006) developed a material model based on YLD96 (Barlat et al., 1996) for aluminum alloys adopting the cutting-plane algorithm (Simo and Ortiz, 1985) for the integration of the elastoplastic constitutive model. Due to texture evolution in hexagonal close-packed (HCP) materials, with the accumulation of plastic strain the shape of the yield surface associated with these materials changes (Choi et al., 2009). Therefore, the traditional isotropic hardening models cannot capture this material response (Nebebe Mekonen et al., 2012). Several continuum based material models have been previously proposed to account for anisotropic hardening in HCP metals including the work by Steglich et al., 2011. The simulation of forming processes for magnesium alloys is a challenge due to thermal softening and strain rate sensitivity exhibited within the mechanical response (Ghaffari Tari et al., 2010). Prior research on warm forming of magnesium alloys is mainly limited to the use of material models developed for FCC and BCC materials (Palaniswamy et al., 2004). For instance, Palumbo et al. (2007) simulated the circular deep drawing of AZ31 using a von Mises yield function (von Mises, 1913) assumption and reported an increase in the limiting drawing ratios when a non-isothermal heating strategy was used. In contrast, Nebebe Metoken (2013) used an evolving anisotropic yield formulation based on a yield function previously proposed by Cazacu and Barlat (2004) to simulation Nakazima type dome height testing and reported a reasonably good agreement between the responses of the model and the respective experiments.

In this paper the mechanical response of AZ31B-O at room and elevated temperatures (23-250°C) and strain rates of 0.001–1 s^{-1} is characterized under tensile and compressive loading conditions along different sheet orientations. A CPB06-type (Cazacu et al., 2006) yield surface formulation with modified anisotropy and asymmetry parameters proposed by Ghaffari Tari et al. (2014) is extended to consider thermal softening and rate sensitivity effects. This model is used to fit the experimental data at different temperatures and plastic strain intervals up to 8% effective plastic strain while simultaneously satisfying the convexity of the yield surface and capturing the evolving asymmetry and anisotropy of both flow stresses and *r*-values. This constitutive model is implemented within a user defined material subroutine (UMAT) and linked to the commercial finite element code LS-DYNA. To assess the developed material model under more complex warm sheet forming conditions, isothermal limiting dome height experiments are performed on AZ31B sheet at 250°C and the results are compared to corresponding simulations. In addition, the non-isothermal deep drawing of AZ31B by Ghaffari Tari et al. (2013) is simulated to assess the material model under complex loading and thermal conditions. The predictions of load-displacement and strain distribution within the formed cup are compared to the experiments.

2. MATERIAL CHARACTERIZATION

2.1. Experimental procedure

The material used in this research was 1.57 and 6 mm AZ31B-O sheet supplied by Magnesium Elektron North America, Inc. in an annealed (O temper) condition. The chemical composition of the AZ31B-O alloy provided by the manufacturer is shown in Table 1.

Table 1
Chemical composition limits of AZ31B-O provided by Magnesium Elektron North Amercia (MENA).

Al	Zn	Mn	Ca	Cu	Fe	Si	Ni	Mg
2.9	0.25	0.94	-	0.001	0.004	0.005	0.005	bal

Neutron diffraction was used to characterize the initial texture of the as-received material for both sheet thicknesses. Figure 1 shows the measured pole figures obtained on the E3 spectrometer of the Canadian Neutron Beam Centre (CNBC). A strong basal texture is observed, in which most grains have the basal poles closely aligned with the sheet normal direction (ND) (Figs. 1-a and c). Only minor difference in the texture is observed between the two batches of the material with different thicknesses; thus, it seems reasonable to assume the compressive behavior of both batches of material will be similar. To validate this assumption further some experiments using adhesively bonded stacked sheet samples, as described by Ghaffari Tari et al. (2014), were performed. The stress-strain response of the stacked sheet samples matches that of the 6 mm thick monolithic samples within the low plastic strain range before de-bonding of the layers initiates (Kurukuri et al., 2013). As a result, the 6 mm samples were utilized in the current work to characterize the compressive response since a high level of plastic strain could be reached before specimen failure (usually by shear localization).

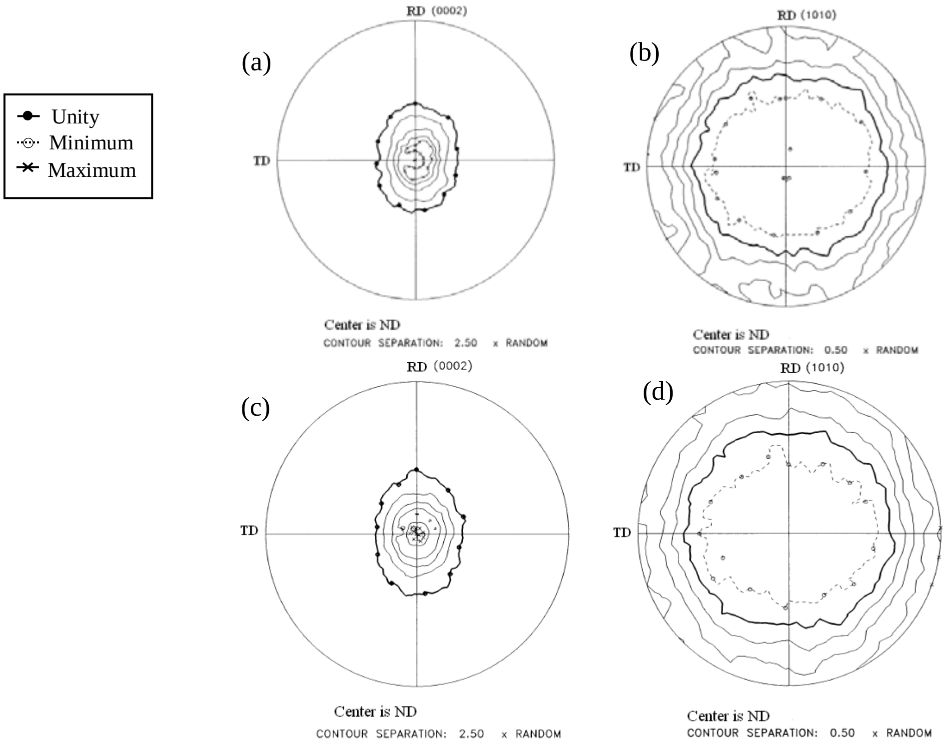

Fig. 1. Pole figures showing the initial texture, measured by neutron diffraction. The rolling direction (RD) and the transverse direction (TD) are in the plane and the normal direction (ND) is normal to the plane. (a) (0 0 0 2) pole figure for 1.57 mm thick sheet, (b) {1 0 -1 0} pole figure for 1.57 mm thick sheet, (c) (0 0 0 2) pole figure for 6 mm thick sheet, (d) {1 0 -1 0} pole figure for 6 mm thick sheet Contours drawn in solid bold lines correspond to the intensity expected from a uniform texture (i.e. 1×uniform). Contours corresponding to intensities greater/lower than expected in a uniform texture are indicated by solid/dashed lines. The maximum intensity contours are labeled with crosses, while the minimum intensity contours are labeled with closed circles.

Mechanical testing was performed using an Instron 1331 tension/compression servo-hydraulic load frame. Tensile testing was performed on dog-bone shaped sub-size ASTM E8M standard specimens with a 25 mm gage length. Tensile testing was conducted along five sheet orientations, namely the rolling (RD) and transverse directions (TD) and at 30°, 45°, and 60° with respect to the sheet rolling direction. The tensile testing was performed inside an environment chamber which heats up the sample to the desired temperatures. Two independent high temperature extensometers were used to capture the axial and transverse strains. Table 2 summarizes the mechanical testing conditions. Note that room temperature experiments were not performed as part of this work; instead, the room temperature results of Ghaffari Tari et al. (2014) were incorporated within this characterization effort.

Table 2
Mechanical testing conditions: an asterisk (*) is used to indicate the conditions at which experiments were performed.

	Tension				compression
Temperature(°C)\Strain rate (s^{-1})	0.001	0.01	0.1	1	0.001
23	*	*	*	*	*
150	*	*	-	-	*
200	*	*	*	*	*
250	*	*	-	-	*

Compression testing was performed using 6 mm cubic samples. The external surfaces of the cube were machined and polished to produce a smooth finish. Krytox® lubricant was used between the contact surfaces. To improve the alignment of the compression testing apparatus, a custom compression fixture with heated compression platens and a die set to align the compression platens was utilized. A detailed description of the compression testing arrangement is provided by Ghaffari Tari et al. (2014). A digital image correlation system (DIC) from Correlated Solution Inc. was used to measure the distribution of strain components throughout the experiment. The DIC system also recorded load-displacement data, allowing synchronization of the load measurements and DIC images.

2.2. Material characterization at quasi-static strain rate

The true plastic strain versus true stress behavior of AZ31B-O at room temperature, 150, 200 and 250 °C is shown in Fig. 2. Note that the room temperature results were reported earlier by Ghaffari Tari et al. (2014). The curves shown in Fig. 2 are the average of three test repetitions. The repeatability of the experiments was reasonably good, with the average deviation from mean being 6, 1.2, 3 and 1 MPa for the compression curves and 2, 0.8, 1.8 and 2 MPa for the tensile curves at room temperature, 150, 200 and 250°C, respectively. A strong asymmetry is observed between the tension and compression flow stress curves at room temperature which persists in the data at 150°C. At lower temperatures, the initial yield strength under in-plane compression is lower than that in tension as expected for twinning dominated compressive loading; however, the subsequent rate of hardening under compression is higher. The initial yield stress under in-plane compression loading is independent of the sheet orientation while a larger orientation dependency is observed as the plastic strain accumulates. The flow stress for both in-plane tension and compression increases as the loading axis rotates from the rolling direction to the transverse direction. The rate of strain hardening under through-thickness compression is higher than under in-plane tension.

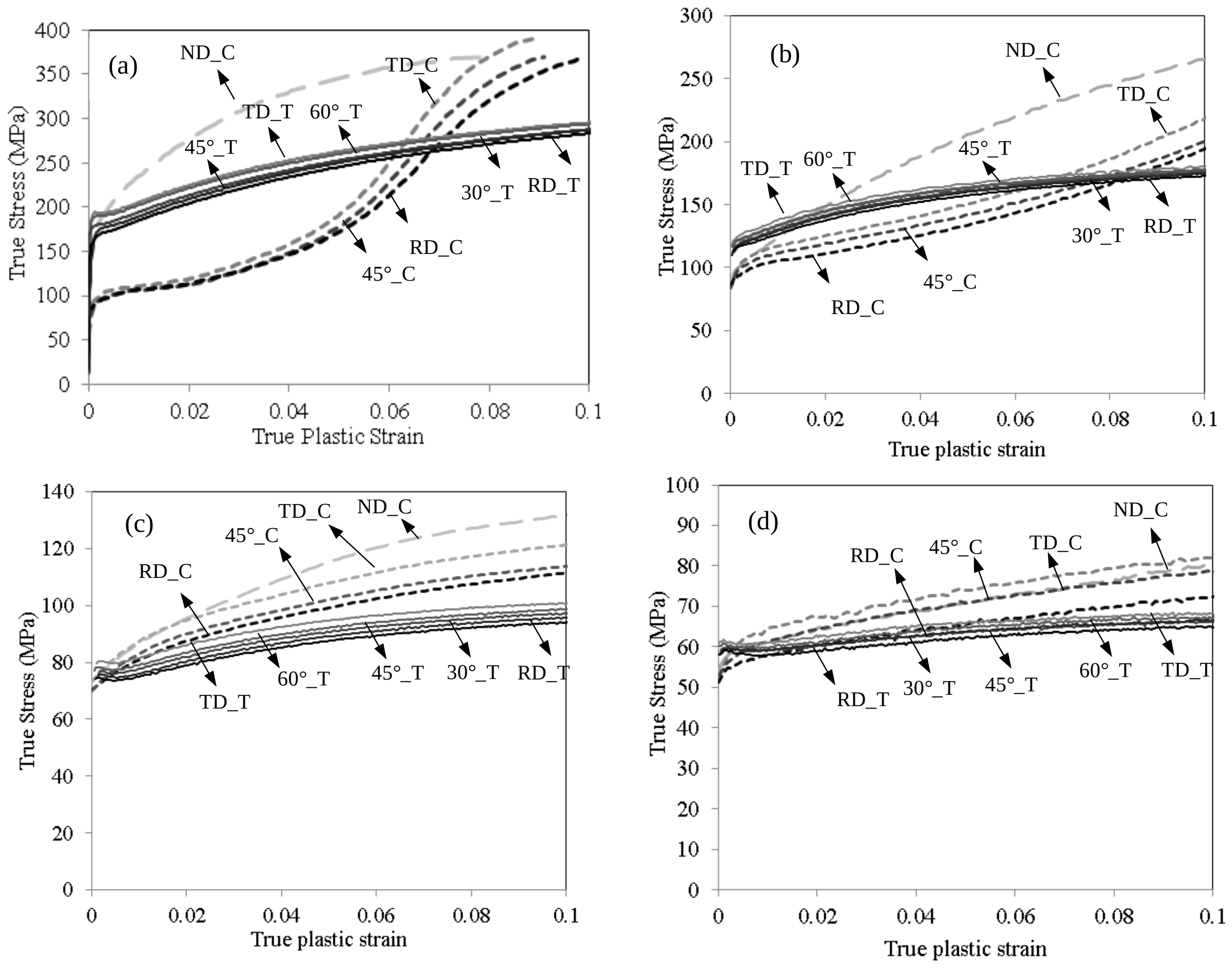

Fig. 2. True stress versus true plastic strain under tension and compression loading (0.001 s^{-1} strain rate), along different sheet orientations, (a) Room temperature, (b) 150 °C, (c) 200 °C, (d) 250 °C, The compression data is plotted as positive. The curves corresponding to tensile loading are indicated using the letter "T" and the compression curves using "C".

As the temperature is increased to 150°C the initial yield under tensile loading is reduced which is associated with the activation of additional slip systems (Agnew et al. 2005). The initial yield stress under in-plane compression is shown to be temperature independent up to 150°C, although the work hardening rate is reduced in comparison to room temperature resulting in curves with a milder concave upwards shape.

At temperatures beyond 150°C (ie. at 200 and 250°C) the initial yield stress and work hardening rates in all directions are reduced due largely to the activation of non-basal slip systems at higher temperatures (Jain and Agnew, 2007). The shape of the compression curves at 200 and 250°C becomes concave downwards which is similar to the tensile curves and indicative of slip-dominated flow (rather than twinning followed by slip). The through-thickness compression curves at 250°C exhibit a response similar to in-plane compression hardening. Only a mild asymmetry is observed comparing the tension *vs.* compression stress-strain curves at 250°C, with the initial yield stress under compression being slightly lower than that under tension. The in-plane flow stress anisotropy reduces at elevated temperatures; for instance, the difference between the flow stress along the rolling and transverse direction at 0.04 true plastic strain is reduced from 18 MPa at room temperature to 4 MPa at 250°C. Note that some of the tension-compression asymmetry can be attributed to friction in the compression testing and the current results have not been corrected for friction. However, Maeda et al. (1998) and Klepaczko and Malinowski (1977) investigated the error in compression testing for conditions where the friction coefficient is below 0.1 and both reported an error of less than 5% in the uniaxial compressive stress.

The instantaneous *r*-values are calculated from the ratio of strain rate (or plastic strain increment) components as described in Eq. 1 (neglecting the effect of elastic deformation).

$$r_{Instantaneous} = \frac{\dot{\varepsilon}_w}{\dot{\varepsilon}_t} \tag{1}$$

Fig. 3 shows the evolution of the instantaneous *r*-values with plastic strain at three different temperatures, namely room temperature (from Ghaffari Tari et al., 2014), 150, 200, 250°C. The average deviation from mean was 0.12, 0.05, 0.02 and 0.09 for the compression curves and 0.02, 0.09, 0.14 and 0.13 for the tensile curves at room temperature, 150, 200 and 250°C, respectively. A large asymmetry is observed when comparing instantaneous *r*-values in tension and compression at room temperature and 150 °C. Both components of strain rate used in this calculation are small numbers; thus, small errors in the measured strain rates can significantly influence the computed *r*-values. Therefore, the measured displacement curves were initially smoothened after which the *r*-values were calculated. The measured *r*-values under compression at 150 °C (Fig. 3b) show higher initial values compared to the room temperature measurements (Fig. 3a) by Ghaffari Tari et al. (2014). The *r*-values increase as the loading axis rotates from the rolling direction towards the transverse direction. As the temperature is increased, the evolution of instantaneous *r*-values with the accumulated plastic strain becomes less significant. Furthermore, the in-plane anisotropy and the tension/compression asymmetry of instantaneous *r*-values is also reduced as the temperature is increased; with the material response at 250°C being the least asymmetric and anisotropic. For instance, the difference in the magnitude of the initial tensile instantaneous *r*-values along the rolling and transverse direction is reduced from 1.5 at room temperature to 0.4 at 250°C.

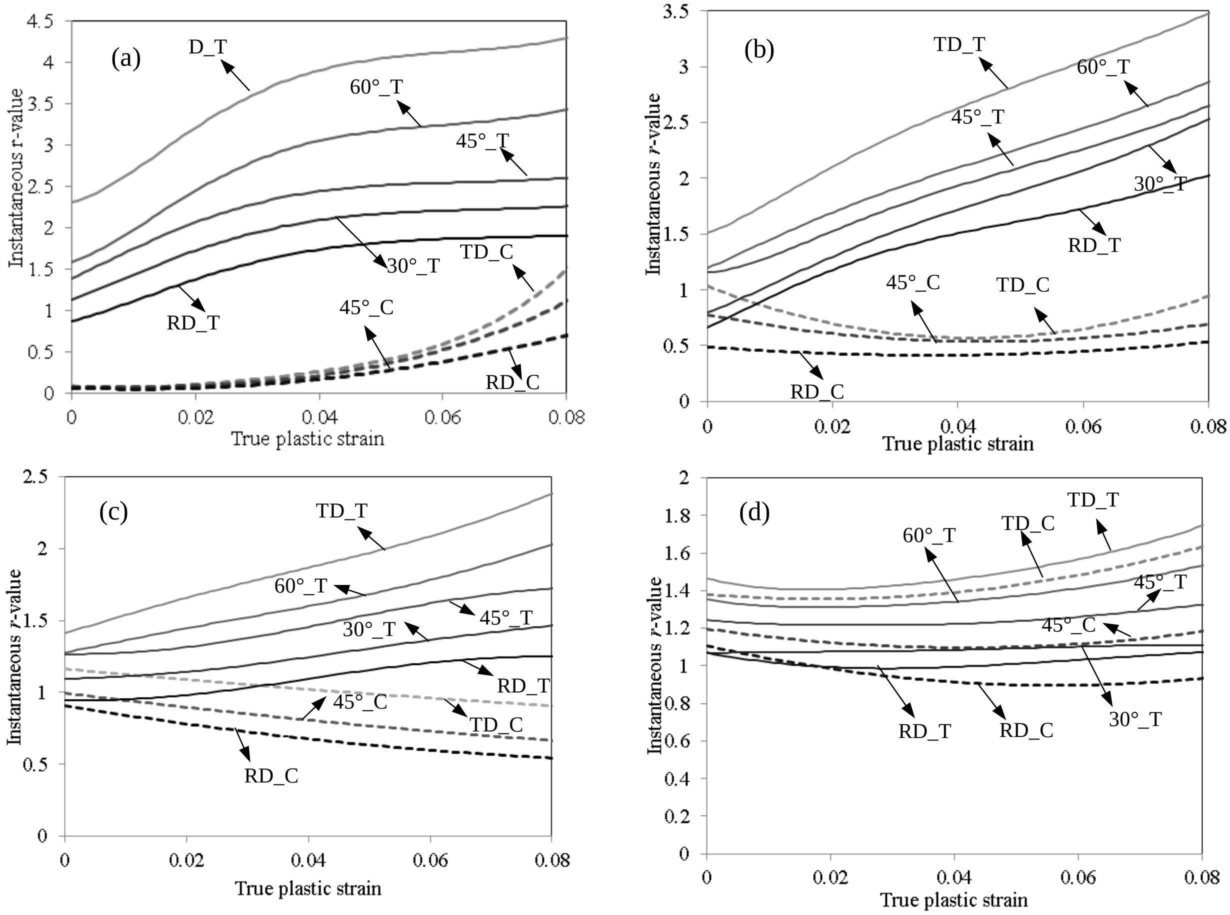

Fig. 3. Instantaneous *r*-values versus true plastic strain under tension and compression loading (0.001s^{-1} strain rate), along different sheet orientations, (a) Room temperature (b) 150 °C, (c) 200°C, (d) 250°C, The curves corresponding to tensile loading are indicated using the letter "T" and the compression curves using "C".

2.3. Strain rate sensitivity

The effect of strain rate on the flow stress of AZ31B-O was characterized at room and elevated temperatures. The dotted curves in Fig. 4 represent the measured data, while the solid lines are fits to be discussed in subsequent sections. Experiments were performed at four strain rate levels, namely 0.001, 0.01, 0.1 and 1s^{-1}, at room temperature and 200°C, while strain rates of 0.001 and 0.01s^{-1} were considered at 150 and 250°C. Note that high strain rate data for this alloy at 500s^{-1} and 150 and 250°C, due to Hasenpouth et al. (2010), has also been plotted for reference and was considered in some of the fits, as described below. (Unfortunately, high rate data at 200°C was not available.). The experiments indicate an increasing effect of strain rate at elevated temperatures, particularly beyond 150°C. A large strain rate sensitivity of the initial yield strength is observed at 200 and 250°C. Furthermore, a reduction in strain hardening rate is observed comparing the slope of the stress-strain curves at room and elevated temperature. A similar strain rate sensitivity trend is also observed in the tensile experiments performed with specimens oriented along 30°, 45°, 60° and TD which has not been shown here for brevity.

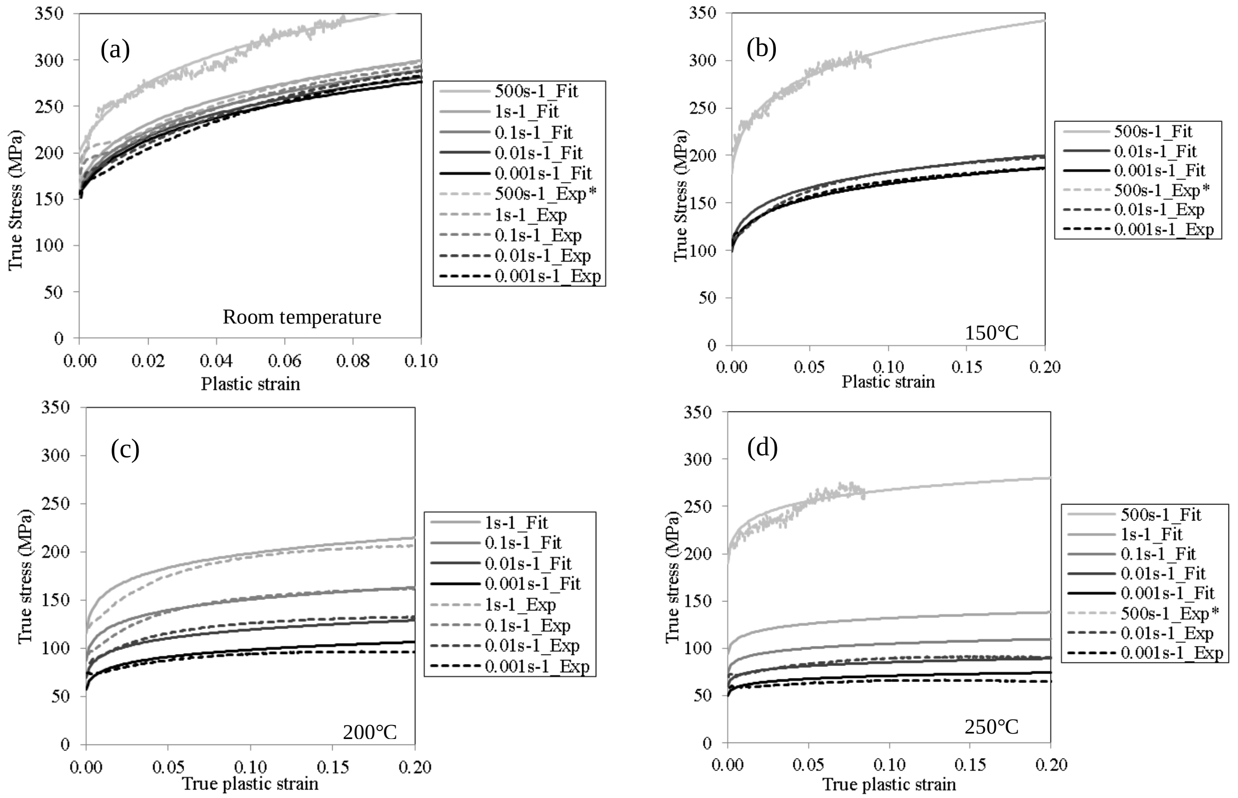

Fig. 4. True stress versus true plastic strain under tension loading along the rolling direction at different strain rates, (a) Room Temperature, (b) 150 °C, (c) 200 °C, (d) 250 °C. The solid lines represent the Cowper-Symonds fit. *Stress strain curves at strain rate of 500 s^{-1} are from Hasenpouth et al. (2010).

3. MATERIAL MODELING

3.1 *Evolving anisotropic/asymmetric yield function and calibration*

A precise description of the material behavior, including flow stress and plastic strain anisotropy, is a requirement to accurately simulate sheet metal forming processes (Banabic et al., 2008). Due to complex response of magnesium alloy sheet at different temperatures, a flexible material model with tension and compression asymmetry is also required, and it is also important to accurately capture thermal softening and material rate sensitivity at elevated temperature in order to simulate warm forming operations. This section describes the yield surface formulation adopted in the current work, while the following section details the two approaches considered to introduce thermal softening and material rate sensitivity into the material model.

A modified form of the CPB06 yield criterion proposed by Cazacu (2006) was adopted since it captures anisotropy and asymmetry of the flow stress as well as r-values. This analytical yield surface, denoted as CPB06, is described as,

$$\mathrm{F}(\Sigma) = (|\Sigma_1| - k\Sigma_1)^{\mathrm{a}} + (|\Sigma_2| - k\Sigma_2)^{\mathrm{a}} + (|\Sigma_3| - k\Sigma_3)^{\mathrm{a}}, \tag{2}$$

where, k is a material parameter that describe the strength difference in tension and compression and a is the degree of homogeneity. Σ_1 to Σ_3 are the principal (Eigen) values of the following transformed stress tensor;

$$\Sigma = \mathrm{C} : \mathrm{S}. \tag{3}$$

In the case of a plane stress condition, the anisotropy matrix *C* contains seven independent parameters. *S* represents the deviatoric stress tensor.

In most material models which are developed for FCC and BCC structured materials the yield surface hardens uniformly in all directions as the material deforms. However, due to load path dependency of the activity of different deformation mechanisms in hcp materials, the shape of the yield surface changes with accumulated plastic strain (Plunkett et al., 2007). To capture such effects, the method proposed by Ghaffari Tari et al. (2014) is adopted in which the anisotropy and asymmetry parameters in Eq. (2) are replaced with functions written in terms of accumulated plastic strain; the resulting evolving yield function utilizes three stress transformations and is denoted “CPB06ex3ev”. The evolved yield function determined in this manner represents a contour of constant plastic work under monotonic loading, but does not capture the exact yield function for non-monotonic loading, as elucidated by Khan et al. (2010). This yield function has been implemented as a user material subroutine within LS-DYNA; details of the stress integration procedure are provided by Ghaffari Tari et al. (2014).

The CPB06ex3ev yield function was calibrated to the experimental results presented in Section 2.2 (Figures 2 and 3) at a strain rate of 0.001s^{-1} at each temperature using the calibration procedure developed by Ghaffari Tari et al. (2014). A yield surface exponent $a=6.0$ is assumed. Five effective plastic strain intervals were used for the calibration of the evolving model, namely 0, 0.02, 0.04 0.06 and 0.08 effective plastic strain. A total of 18 experimental values at each effective plastic strain level are used in the calibration including the following: five flow stress and instantaneous *r*-values under tensile loading (0°, 30°, 45°, 60° and 90° orientations), three flow stress and instantaneous *r*-values for compressive loading (0°, 45°, 90° orientations), and the equi-biaxial tension and compression flow stresses. The through-thickness compression experiment is used to fit the equibiaxial tension point on the yield surface, assuming the plastic deformation is independent of the hydrostatic stress. The equibiaxial compressive stress is taken as the average of the uniaxial stress from RD and 45° compression experiments, so as to avoid a non-physical response of the model since results from equibiaxial compressive experiments are not available

Fig. 5 shows the evolving yield surface at different effective plastic strain levels at room and elevated temperatures (the CPB06ex3ev parameters fit at each temperature level are provided in Appendix 1). The yield function is calibrated up to 8% effective plastic strain (the limit of the measured data from the experiments) after which the yield function is assumed to work harden in an isotropic manner. In general, the evolving yield criterion is able to capture the experimental data quite well. Comparing the yield surfaces at different temperatures, a significant reduction in the asymmetry of the initial yield surface and its evolution can be observed as the temperature increases. The magnitude of the calibration R-squared error reduces from 0.3 at room temperature to 0.065, 0.037 and 0.011 at 150, 200 and 250 °C, respectively. This reduction in the error values is due to the reduction of both anisotropy and asymmetry in the experimental data which makes the fitting easier.

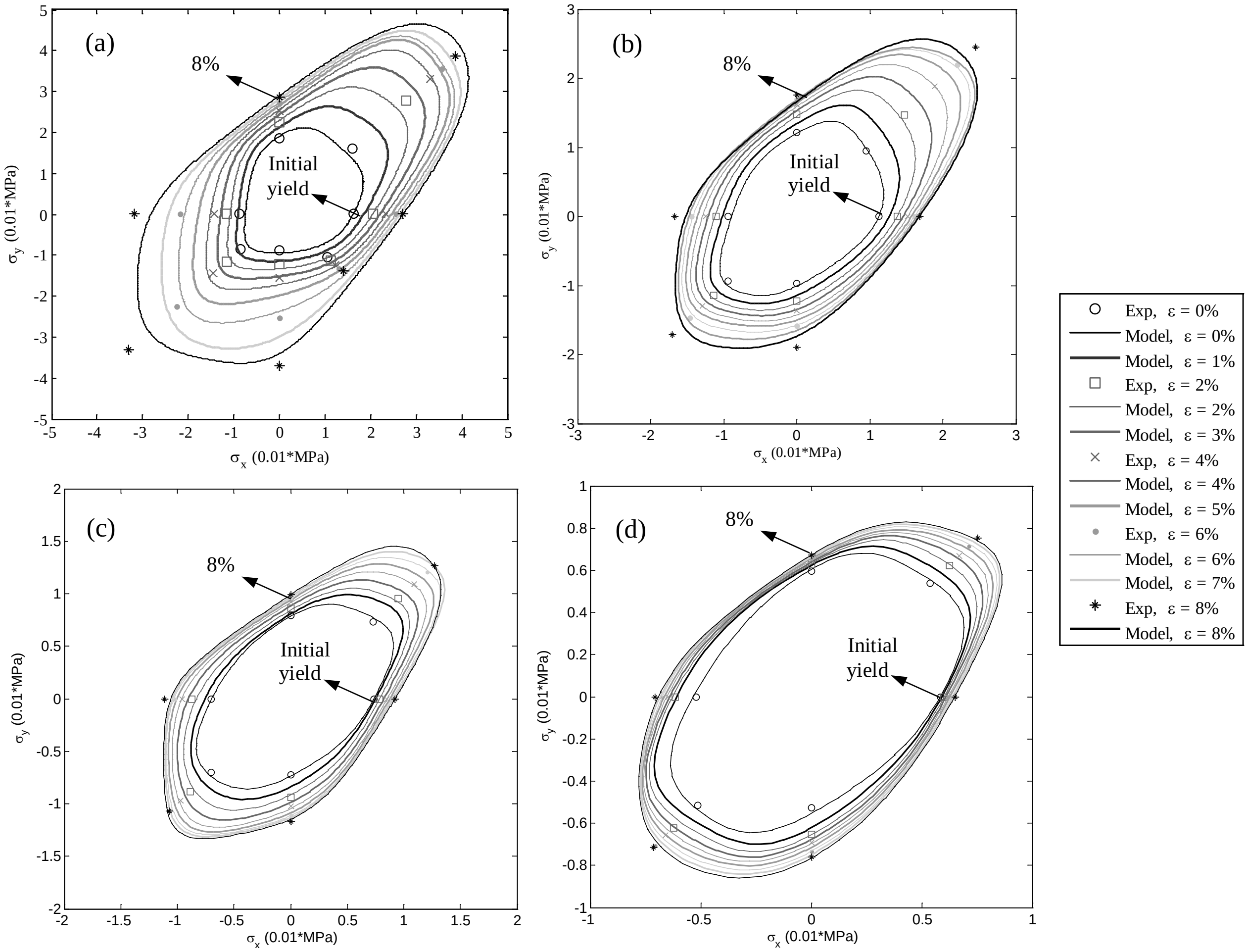

Fig. 5. Yield surface evolution with accumulated plastic strain up to 8% at strain rate of 0.001s^{-1}, (a) room temperature, (b) 150 °C, (c) 200 °C, (d) 250 °C. Room temperature measured data from (Ghaffari Tari et al., 2014).

3.2. Rate sensitivity and thermal softening models

The AZ31B-O sheet considered in this research exhibits significant thermal softening and strain rate sensitivity within the elevated temperature range considered (150-250°C) as seen in Fig. 4. Two approaches were considered to introduce these effects into the CPB06ex3ev yield function. The first approximation was developed for isothermal cases in which the temperature of the material is constant (and in this case limited to room temperature, 150, 200 or 250°C). For such an isothermal case, a Cowper-Symonds (1957) model was fit to the available data to scale the material flow stress, taken here as the rolling direction stress versus effective plastic strain curve, to account for strain rate at each temperature level (room temperature, 150, 200 or 250°C).

The second approximation was developed for use in modelling non-isothermal cases in which the temperature and strain rate vary arbitrarily within the material being deformed. In this case, both thermal softening and strain rate sensitivity were accounted for using a modified Nadai model (Van den Boogaard and Huétink, 2006) fit to the material response. In the first approximation (isothermal treatment), the yield surface shape was treated as strain rate insensitive, while the flow stress is scaled with strain rate. In the second approximation (non-isothermal treatment), the yield surface scales isotropically with both strain rate and temperature. The fits, limitations and merits of these two approaches are discussed in the following.

3.2.1.Cowper-Symonds isothermal strain rate dependent hardening model

A strain rate dependent Cowper-Symonds (1957) type isotropic hardening model is used to fit the tensile experiments along the rolling direction at room temperature, 150, 200 and 250°C (Section 2.3, Fig. 4). In addition to the low strain rate experiments performed in this work, the tensile stress *vs.* strain response of AZ31B-O measured by Hasenpouth et al. (2010) at a strain rate of 500s^{-1} at room temperatures and 150 and 250°C is also used to fit the material rate sensitivity. Incorporation of this elevated strain rate data within the fits provided higher quality fits that proved important during simulation of the sheet forming operations, presented in Section 4, for which the strain rates exceeded that of the uniaxial tests in Section 2. Unfortunately, higher strain rate data (at 500s^{-1}) at 200°C was not available for use in the fits at this temperature; however, material testing data at four strain rate levels (0.001-1s^{-1}) was available from the current work to facilitate calibration of the model at this temperature.

The Cowper-Symonds (1957) model describes the true stress in terms of effective plastic strain and strain rate:

$$\mathrm{H}(\bar{\varepsilon}^p, \dot{\varepsilon}\,)\big|_{T=constant} = \mathrm{K}(\bar{\varepsilon}^p + \varepsilon_0)^n \left(1.0 + \left(\frac{\dot{\varepsilon}}{D}\right)^{\frac{1}{P}}\right) \tag{2}$$

The parameters *K* (strength hardening coefficient), *n* (strain-hardening exponent), *D* and *P* (strain rate sensitivity terms) are found at each temperature, while the parameter ε_0 is defined from the following,

$$\varepsilon_0 = \left(\frac{\mathrm{E}}{\mathrm{K}}\right)^{\left(\frac{1}{n-1}\right)}, \tag{3}$$

where, *E* represents the Young's modulus. The Cowper-Symonds parameters fit to the rolling direction tensile data using a non-linear regression procedure are presented in Table 3. For reference, Cowper-Symonds fits have also been performed without the high rate data of Hasenpouth et al. (2010) and are provided in Table 4. The comparison between the model response and the experimental curves along the rolling direction is shown in Fig. 4.

Table 3
Cowper-Symonds parameters at 150, 200 and 250°C.

Temp(°C)	K (MPa)	N	D	P	R-square
RT	395.198	0.176	4.33E5	6.317	0.98
150	177.355	0.137	26.557	8.719	0.98
200	60.317	0.111	7.339E-4	6.346	0.99
250	32.218	0.065	0.0039	7.607	0.97

Table 4
Cowper-Symonds parameters at 150, 200 and 250°C excluding testing data at 500s^{-1} from Hasenpouth et al. (2010)

Temp(°C)	K (MPa)	N	D	P	R-square
RT	399.252	0.176	3.33E5	5.966	0.99
150	183.012	0.126	572.56	9.239	0.99
200	75.663	0.108	0.008	6.068	0.99
250	75.093	0.055	0.015	0.371	0.99

3.2.2. Modified Nadai strain rate and temperature dependent power law hardening model

To develop a constitutive model for non-isothermal cases (or for temperatures other than those used to develop the isothermal fits in the previous section), a phenomenological Nadai type power law hardening model (Van den Boogaard and Huétink, 2006) was modified to incorporate the effect of strain rate and temperature on the constitutive response of AZ31B-O. The following hardening model is used to fit the experimental tensile data along the rolling direction:

$$\mathrm{H}(\bar{\varepsilon}^p, \dot{\varepsilon}, T) = \mathrm{K}(T)(\bar{\varepsilon}^p + \varepsilon_0)^{n(T)}\dot{\varepsilon}^{m(T)}, \tag{4}$$

where, the functions *K(T)* (strength coefficient), *n(T)* (strain-hardening exponent) and *m(T)* (strain rate-hardening exponent) are found for different temperatures and strain rates as shown in the equations below, while the parameter ε_0 is defined from Eq. (3).

$$\mathrm{K}(T) = A_0 + A_1 * (1 - exp(A_2 * (T - T_r)/T_m)) \tag{5}$$

$$\mathrm{n}(T) = A_3 + A_4 * (1 - exp(A_5 * (T - T_r)/T_m)) \tag{6}$$

$$\mathrm{m}(T) = A_6 * (1 - exp(A_7 * (T - T_r)/T_m)) \tag{7}$$

In Eqs. (5) to (7), T_r and T_m are 273 and 923° Kelvin which represent the room temperature and melting temperature of magnesium. To calibrate the hardening model in Eq (4), the RD tensile data at 150, 200 and 250°C, at strain rates of 0.001-0.1 s^{-1} is used (Fig. 6). The high strain rate data of Hansenpouth et al. (2010) was not utilized since the exponential form of eqn. (4) extrapolated well over the strain rate regime considered. The fitting parameters A_i, *i=1 to 7* shown in Table 5 are found through a nonlinear regression. An R-squared value of 0.98 is obtained from the regression.

Table 5
Temperature and strain rate dependent power law hardening model parameters.

A_0	A_1	A_2	A_3	A_4	A_5	A_6	A_7
2550	-2435	-13.998	0.288	-3.13	-0.261	10.196	-0.04

The comparison between the fitted curves and the experimental curves along the rolling direction is shown in Fig. 6. The current model does not capture the low strain rate sensitivity of AZ31B-O at 150°C particularly well; however the model does reproduce the rate sensitivity observed at 200 and 250°C.

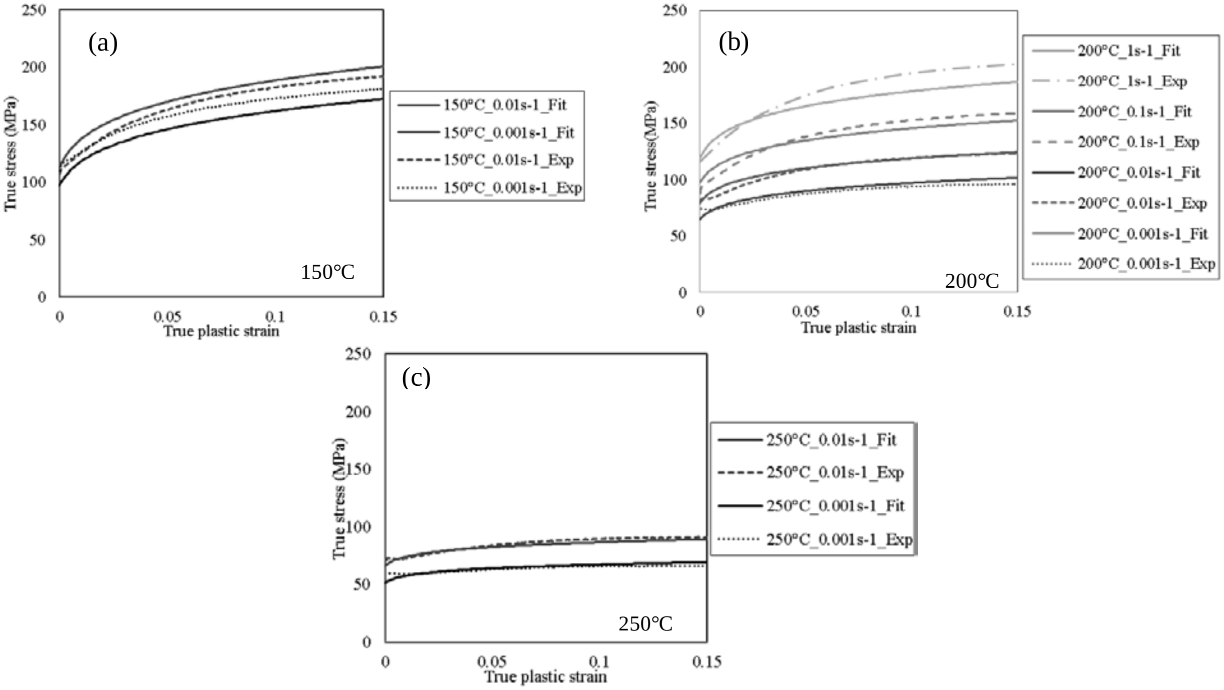

Fig. 6. True stress versus true plastic strain under tension loading along the rolling direction at different temperatures and strain rates: (a) 150 °C, (b) 200 °C, (c) 250 °C.

4. MODEL ASSESSMENT

4.1. Simulation of uniaxial experiments

As a first evaluation of the the material model, simulations of the elevated temperature tensile experiments presented in Section 2 were performed. This represents a "closed loop" assessment of the model since the predictions correspond to the same loading conditions for which the model was calibrated, however, it is important to confirm how well the model reproduces the original experiments. The simulations considered a single finite element finite using the Cowper-Symonds hardening model calibrated for isothermal conditions (Section 3.2.1). The measured material response (flow stresses and *r*-values) under different loading conditions at 200 and 250 °C is compared to the CPB06ex3ev model predictions in Fig. 7(a) and (b). The comparison between the rolling direction response of the model to the corresponding experiment at 200 °C (Fig. 7a) shows somewhat larger deviation at low effective plastic strains, which can be attributed to the algebraic form of the Cowper-Symonds equation. However, at larger strains, the quality of the fit improves and good agreement is obtained in all orientations. A larger difference observed in the prediction of the. true stress *versus* effective plastic strain response at 250°C is due to the overall deviation of the hardening model compared to the experiments in the rolling orientation (Fig. 7b) and not in the calibration of the CPB06ex3ev model (Fig. 5c) which has the total calibration error of 0.011. In a similar fashion, the response of the model using the strain rate and temperature dependent power law (modified Nadai model) has been validated as shown in Fig. 7(c) and (d). The simulations based on the modified Nadai fit also capture the measured trends reasonably well.

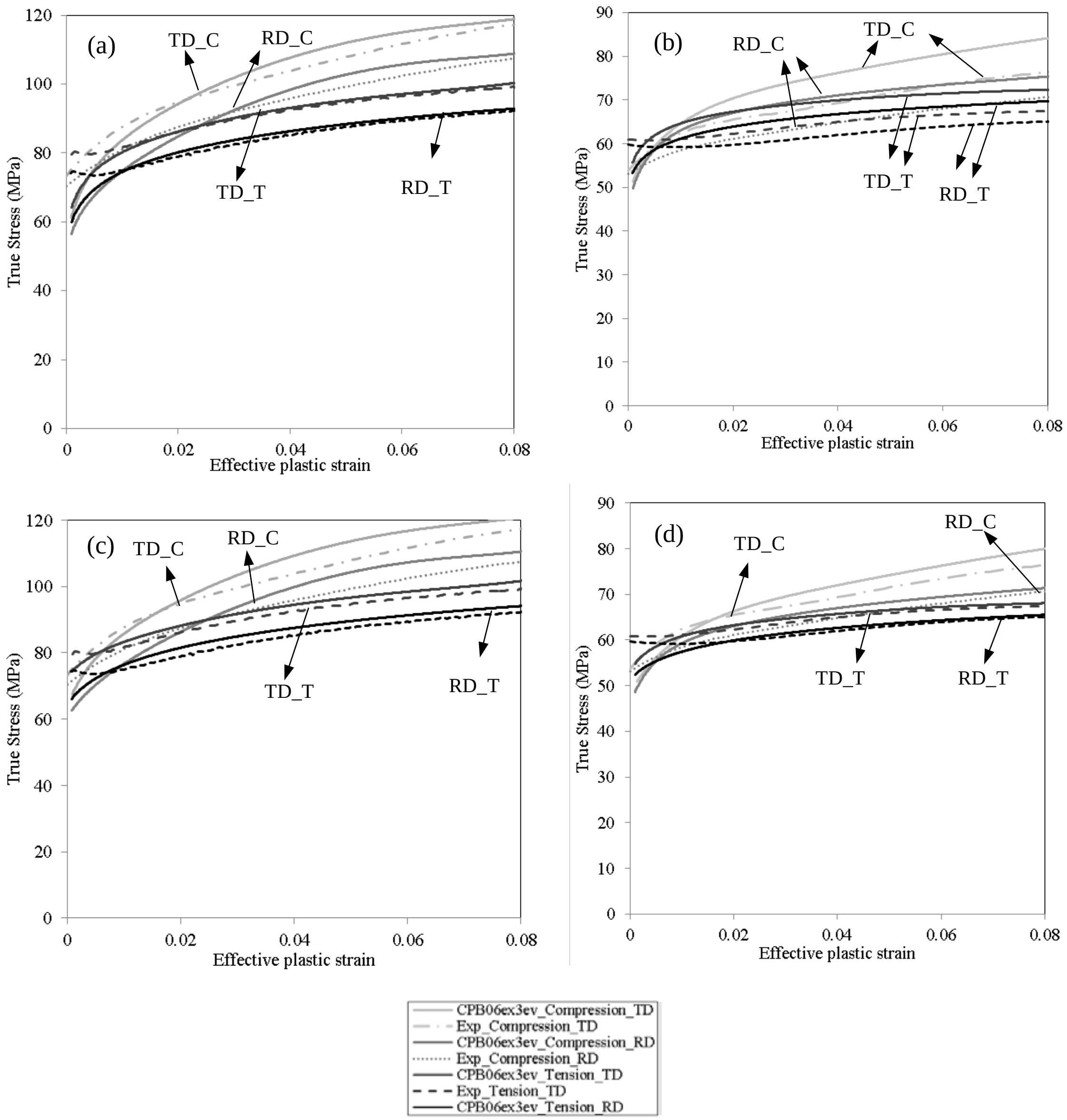

Fig. 7. Single-element true stress versus plastic strain response comparison to the experiments using different loading paths at a nominal strain rate of 0.001s^{-1} (a) Cowper-Symonds at 200°C, (b) Cowper-Symonds at 250°C, (c) Modified Nadai at 200°C, (d) Modified Nadai at 250°C.

The instantaneous *r*-value *vs.* effective plastic strain curves from single element simulations (using the Cowper-Symonds hardening response) along the RD and TD directions at 200 and 250°C are compared to the corresponding experiments in Fig. 8a and b. The predicted *r*-values agree well with the experiments over much of the plastic strain range and loading conditions at both temperatures; however, some deviation from the experimental measurements is seen, primarily at the extremes of the plastic intervals over which the model is calibrated. This is due to the global nature of this model which fits the model for all of the experiments at the same time. This effect has been discussed in detail by Ghaffari Tari et al. (2014).

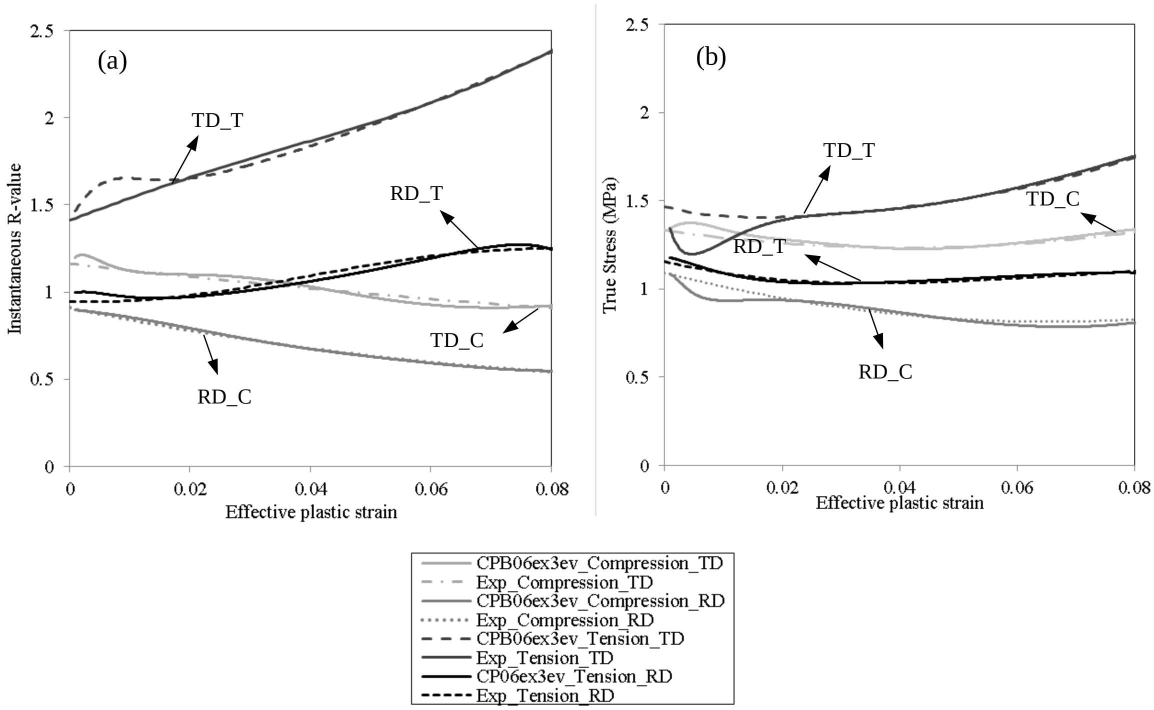

Fig. 8. Single-element instantaneous *r*-value response - comparison to the experiments using different loading paths at a nominal strain rate of 0.001s^{-1} (a) 200 °C, (b) 250 °C.

4.2. Limiting Dome Height Validation Case

Elevated temperature limiting dome height (LDH) experiments were conducted and corresponding numerical simulations were performed to assess the predictive capability of the constitutive model for complex loading cases. The following sections describe the experiments and finite element model and provide a comparison between the predicted and measured load-displacement and strain distributions.

4.2.1.LDH Experiments

The LDH experiments were isothermal and considered a blank and tooling temperature of 250°C. A 100 mm hemispherical dome was utilized to form the samples within a servo controlled hydraulic press. The experimental procedure and tooling arrangement corresponds to that utilized by Bagheriasl and Worswick (2012, 2013) for formability characterization of aluminum alloys. Two different blank geometries, previously proposed by Nakazima et al. (1968), were considered to deform the material under different load paths: 203.2 x 203.2 mm square blanks, producing near-biaxial stretch conditions, and a dog-bone sample with a width of 76.2mm, producing a near-plane strain condition. PTFE (Teflon) film is used between the punch and the blank to reduce friction. A blank holder force of 40 kN was applied before commencing the experiment. A punch velocity of 0.1 mm/s was used for all experiments. A 3D digital image correlation system (DIC) was used to measure the strain field throughout the experiment. The sample preparation procedures and DIC system parameters have been thoroughly discussed by Bagheriasl and Worswick (2012, 2013).

4.2.2. LDH Simulations

The geometry and meshing of the LDH model is shown in Fig. 9. Due to symmetry, only one-fourth of the geometry is modeled and symmetry boundary conditions are applied on the central nodes of the blank along two directions. All components of the model are meshed using 4-node shell elements. A fully integrated shell element formulation with five through thickness integration points is used for the blank. A Gauss-Lobatto quadrature scheme is used to obtain the values of strain on the outer surfaces. The tooling (punch, blank holder and die) are modeled as rigid bodies and penalty function-based contact boundary conditions, with a constant Coulomb friction coefficient of 0.04 (McKinley, 2010), are enforced between the contacting surfaces. A constant velocity of 0.1 mm/s is applied on the moving punch while the die is constrained in all rotations and displacements. A constant blank holder force of 40 kN is applied to the binder and a total displacement of 30 mm is applied on the punch. The simulations were performed using the explicit dynamic formulation within LS-DYNA; to reduce the simulation time, the time step is increased to 4.5×10^{-5} s using mass scaling method. A contact viscous damping of 20% is applied to the model to reduce the oscillations caused by the penalty function contact treatment. The rolling direction is taken as the *x*-axis (Fig. 9) and the dog-bone samples considered the rolling direction to lie along the major axis of the sample. The CPB06ex3ev material model, with yield function coefficients calibrated for 250°C (Fig. 5d) along with the Cowper-Symonds hardening model Eq. (2) (Section 3.2.1), is used for the simulations.

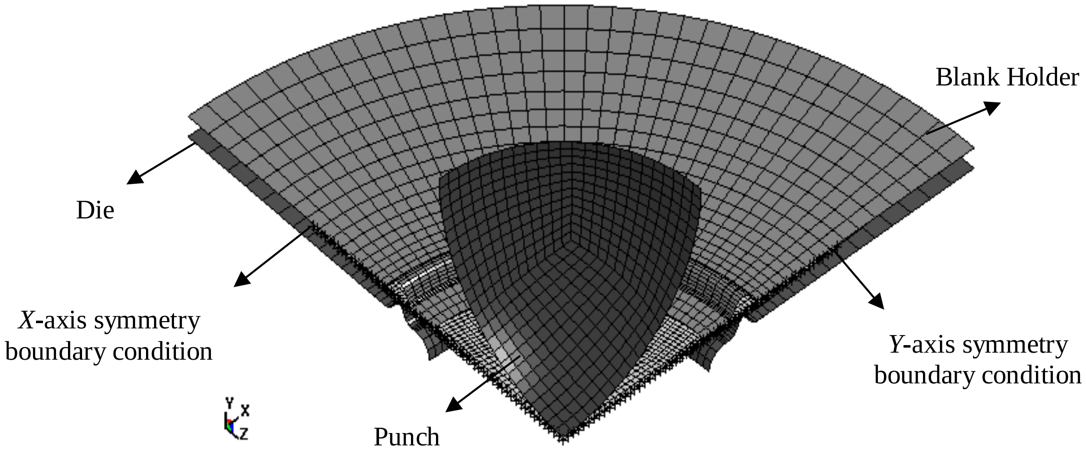

Fig. 9. Finite element mesh used to simulate the limiting dome height (LDH) experiment.

4.2.3 Comparison between LDH predictions and measured results

The predicted and measured punch force versus displacement response for the two LDH geometries are plotted Fig. 10. The model captures the response of the biaxial sample (203 x 203 mm) quite well, while the predicted load for the dog-bone specimen is within 80% of the measured data. The superior predictions for the biaxial geometry may be attributed to the use of a biaxial stress state in the calibration procedure; whereas the plane strain state is not calibrated (plane strain calibrations are planned for future work).

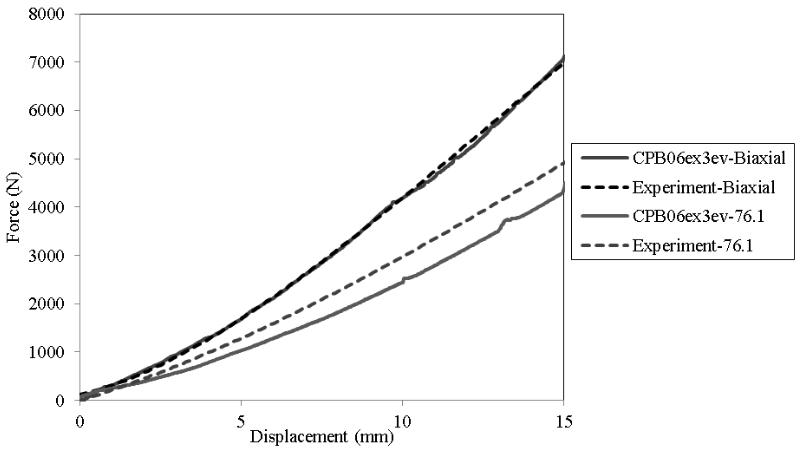

Fig. 10. Punch force versus displacement, comparison between the experiment and simulations of LDH specimens at 250°C.

Figure 11a serves to compare the predicted and measured strain distributions within the 203 x 203 mm samples at a punch displacement (dome height) of 15 mm. The experimental data indicates that the strain state is not purely biaxial and there is a drop in the strain at the pole region of the specimens. Both trends can be attributed to friction effects. The predictions capture the difference in major versus minor strain, but not the drop in strain over the pole region, suggesting that the friction level at the punch-work piece interface is underestimated using the adopted Coulomb coefficient of 0.04. The predicted and measured strains along the rolling direction of the 76.1mm wide dog bone specimen are compared in Fig. 11b. The strain distributions reflect the near-plane strain condition, as seen in the minor strains across the pole being close to zero. There is a drop in strain at the pole and the numerical model captures this frictional effect for this specimen geometry.

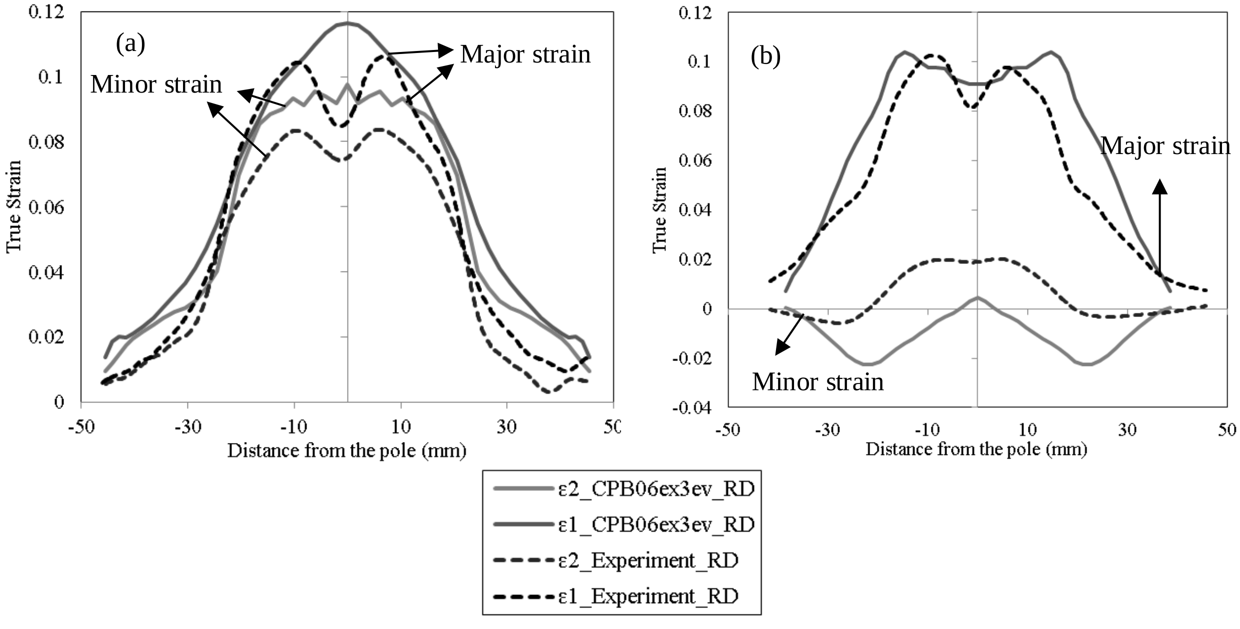

Fig. 11. Comparison of predicted and measured major strain (ε_1) and minor strain (ε_2) versus distance from pole along the rolling direction at 250 °C and a dome height of 15 mm: (a) biaxial stretch specimens (203.2 x 203.2 mm) (b) plane strain dog-bone sample with width of 76.2mm).

4.3. Non-Isothermal deep drawing validation case

As a final validation case, the non-isothermal, circular cup deep drawing experiments performed by Ghaffari Tari et al. (2013) were simulated. These simulations and comparison to the corresponding experiments allow evaluation of the model under non-isothermal conditions in which the temperature (and strain rate) varies within the workpiece. The following sections describe the experiments, finite element model and comparison between the predicted and measured load-displacement and strain distributions.

4.3.1. Non-isothermal cup draw experiments

A detailed description of the non-isothermal cup drawing experiments (100 mm diameter punch) can be found in Ghaffari Tari et al. (2013). In the current paper, one experimental case is simulated which considers a draw ratio (ratio of blank diameter to punch diameter) of 2.25. The die and blank holder tooling temperature was 245°C and the punch was cooled such that the temperature of the sheet at the center of the punch was 171°C. The punch speed was 4 mm/s, the total punch displacement was 85 mm, and the blank holder force was 80 kN. As in the LDH experiments, Teflon film was used as a lubricant.

4.3.2. Non-isothermal cup draw simulations

Figure 12 shows the quarter-symmetry finite element mesh adopted for the deep draw simulation. The element formulations and contact treatment are identical to that used for the LDH model.

The non-isothermal nature of the experiments mandated the use of the temperature- and strain rate-dependent modified-Nadai constitutive treatment described by Eqs. (4)-(7) (Section 3.2.2). This accounts for arbitrary variation of strain rate and temperature within the blank during forming. Furthermore, the yield formulation is made temperature dependent by assigning different evolution parameters (Appendix A) based on the current temperature within the simulation. Elements with temperatures in the range 100-175°C are assumed to follow the yield function evolution rule calibrated for 150°C, while elements with temperatures of 175-225°C are assigned the evolution rule calibrated for 200°C. Elements with temperatures above 225°C are considered to obey the evolution rule calibrated for 250°C. An alternative approach might be to interpolate the yield function shape based on element temperature, however, this was not considered in the current work.

A coupled thermo-mechanical formulation is utilized to account for heat transfer between the blank and tooling as the blank slides along the tooling surface. The thermal properties of AZ31 at 200°C reported by Lee et al. (2012) were used to model heat transfer in the current deep drawing simulation. Table 6 describes the adopted thermal parameters. To initialize the temperature distribution prior to forming, the punch is kept in thermal contact with the blank while the blank holder is closed until the temperature distribution within the blank matches the 247°C temperature in the flange region and the measured temperature (171°C) at the punch center.

Table 6
Heat transfer parameters used in the simulation

Thermal properties	
Thermal conductivity (sheet), (W/m °K)	95.8
Heat Capacity (sheet), (J/kg °K)	1049.3
Interface heat transfer coefficient (N/s mm °C)	4.5
Factor to convert plastic deformation energy to heat	0.95

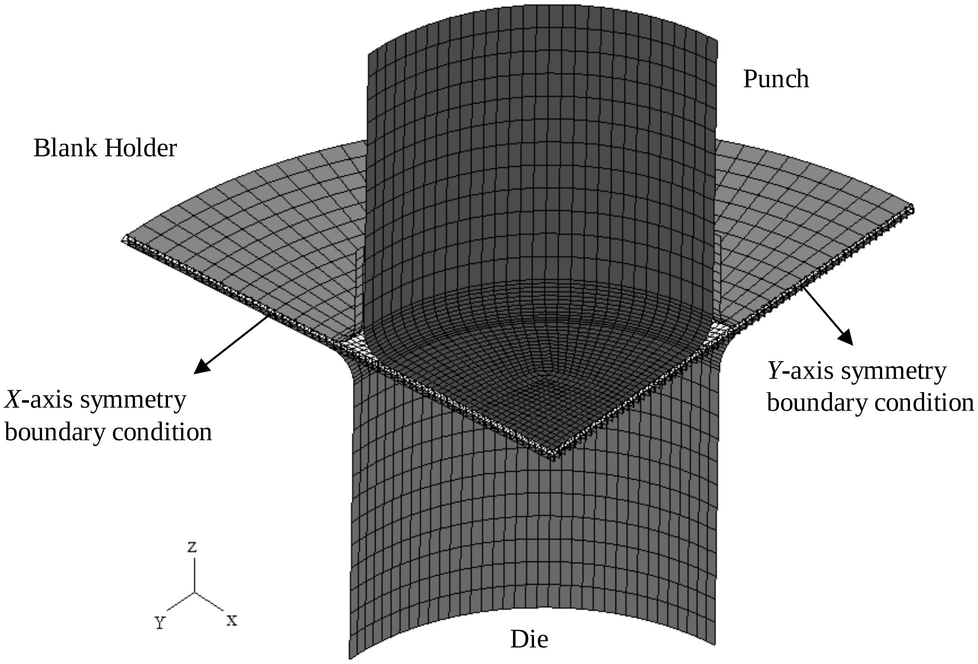

Fig. 12. The finite element mesh used to simulate the deep drawing process.

4.3.1 Comparison between deep draw predictions and measured results

The punch force *versus* displacement response using the CPB06ex3ev model is compared to the experimental measurements in Fig. 13. The model over-predicts the measured forces in the drawing operation, but does capture the peak force relatively well. The higher predicted value from the simulations may be due to a weak representation of the frictional forces at the interface between the sheet and the die/blank holder. The friction coefficients used for the PTFE Teflon film were measured at room temperature conditions (McKinley et al., 2010) and the actual response at 245°C may well be well different.

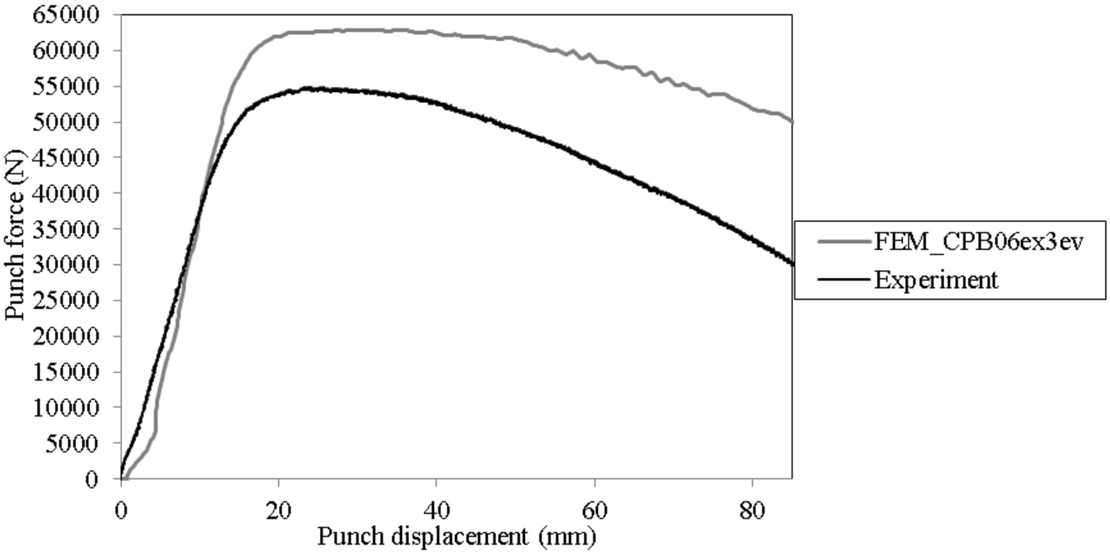

Fig. 13. Punch force *vs.* punch displacement curves - comparison between the predictions and the measured loads.

The measured and predicted major and minor strain distributions along the rolling and transverse directions of a fully drawn cup are compared in Fig. 14. The simulation shows a longer curvilinear length from the pole of the cup (indicated as region “a” in Fig. 14) to the flange edge (region “d”), resulting from a generally a higher predicted major strain in the wall region. The CPB06ex3ev model captures the trends between the rolling and the transverse strain distributions, with larger strains occurring along the sheet rolling direction. The higher strains in the model likely reflect the predicted higher force levels which again may be due to frictional effects, for example. A potentially more significant issue is the fact that the model is only calibrated to 8% effective plastic strain while the deformation experienced during deep drawing of a cup is larger than five times that value. Thus, improvement in the prediction capability of the model is expected if a larger range of effective plastic strain is considered for the calibration. Furthermore, the *r*-values used to calibrate the model are measured at strain rate of 0.001 s^{-1} whereas the actual strain rate varies considerably within the cup during the deformation.

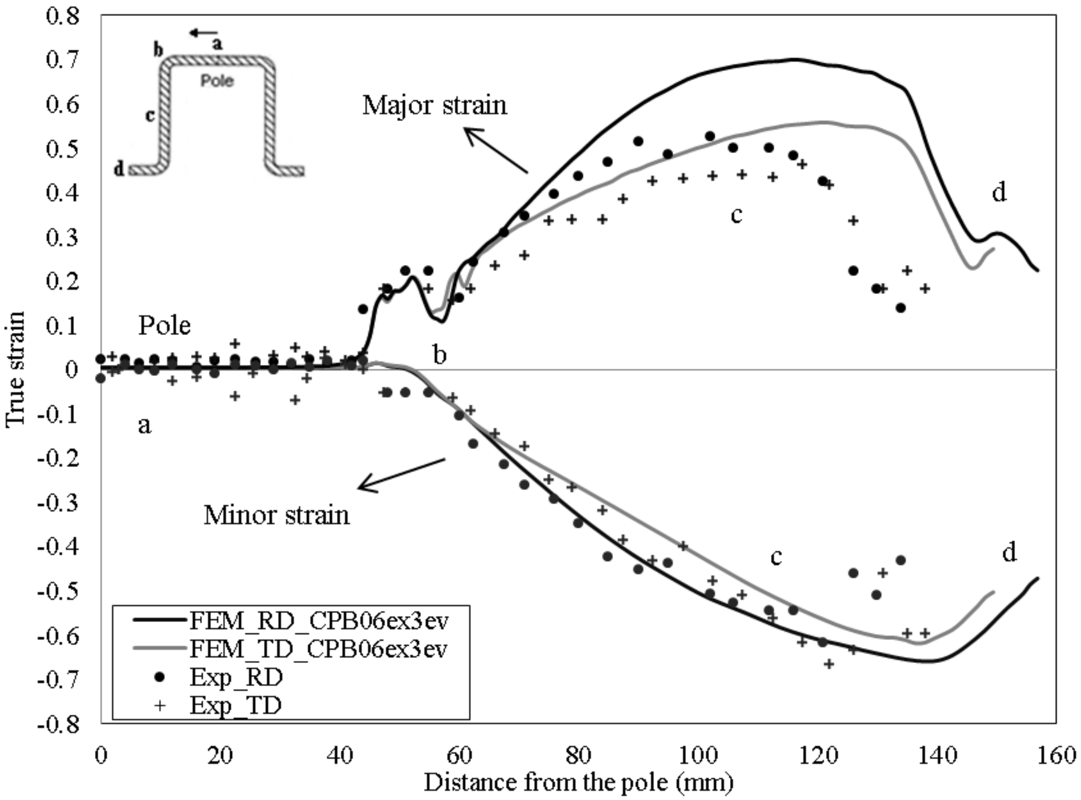

Fig. 14. Major and minor strain distribution along the rolling and transverse directions from the simulations and the experiments. Error bars are not shown for clarity; however, the average absolute deviation from the mean was approximately 0.03 and 0.04 for the ε_1 and ε_2 curves along the RD. The average absolute deviation from the mean for the ε_1 and ε_2 curves along the TD was 0.01 and 0.02.

5. DISCUSSION

The mechanical response of AZ31B-O in the quasi-static strain rate range (0.001-1 s^{-1}) has been characterized for a broad range of loading orientations in both tension and compression at room and elevated temperatures (150, 200 and 250˚C). A reduction in the anisotropy and asymmetry of the mechanical behavior is observed as the temperature is elevated. Moreover, a reduction in the evolution of *r*-values with respect to the accumulated plastic strain is seen at elevated temperatures, which is in agreement with the results from prior work by Agnew and Duygulu (2005). This effect can be explained by the activation of non-basal slip as the temperature is increased (Jain and Agnew, 2007) which improves the ductility of magnesium alloys at elevated temperature.

Increased strain rate sensitivity is observed at elevated temperatures which is important to consider for modeling warm forming simulations such as deep drawing. The positive strain rate sensitivity of magnesium alloys at elevated temperatures improves the drawability of AZ31B since positive rate sensitivity is known to stabilize deformation within the diffuse necking regime. Accurate description of thermal softening effects within simulations of non-isothermal deep drawing is critical as previously shown in the experiments by Ghaffari Tari et al. (2013). Although the current work includes the evolution of *r*-values with strain at elevated temperature, the effect of strain rate on the evolution of *r*-values, as reported by Ghaffari Tari et al. (2011), has not been considered in the current work and is left for future work.

The material model developed by Ghaffari Tari et al. (2014) which uses an evolving yield surface formulation is adopted as a starting point to capture the mechanical response of AZ31B-O at elevated temperatures. In addition, the current approach considers either a strain rate dependent Cowper-Symonds model for isothermal simulations or a temperature and strain rate dependent power law (modified Nadai) hardening model for non-isothermal conditions. Previous work by Nebebe Mekonen et al. (2012) has undertaken calibration of yield strength and *r*-values in the tensile quadrant of the yield surface; in the current work, material asymmetry is also captured by fitting evolving yield function coefficients for tension and compression, thereby capturing evolving asymmetry in strength and *r*-values. The evolving CPB06ex3ev model (Ghaffari Tari et al., 2014) used in this work is calibrated independently at 150, 200 and 250˚C. In the case of non-isothermal conditions the appropriate yield evolution parameters are used in the finite element code depending on the range of temperature in which an integration point is located.

An important limitation of the current yield formulation is that it is strictly valid for proportional loading only. Non-proportional load paths, in particular reversed loading, will result in de-twinning response (Lou et al., 2007) in magnesium alloys, although the de-twinning transition region under reverse loading from compression to tension is suppressed at temperatures higher than 150˚C (Piao et al., 2012). The effect of reverse loading and the treatment of de-twining and Bauschinger phenomena are left for future work. Moreover, the strain rate dependency of the evolution of *r*-values with accumulated plastic strain (Ghaffari Tari and Worswick, 2011) has not been considered in the current work which is of importance at elevated temperatures. However, considering the evolution of the of the yield surfaces as a function of both accumulated plastic strain and strain rate using the current approach requires a much larger number of model parameters which increases the computation costs required for the calibration of the model. Crystal plasticity approaches have made significant gains in modeling the deformation mechanisms and mechanical behavior of magnesium alloys (Proust et al., 2009); however, crystal plasticity approaches tend to be prohibitively expensive for simulation of large scale industrial problems. Thus, a combination of physically-based and phenomenological models are an alternative approach that combines the strength of these two simulation methods, such as in prior work by Li et al. (2010).

To assess the mechanical response along arbitrary loading conditions for which the model has not been calibrated, the LDH and cup draw experiments were simulated. In contrast to the prior work by Nebebe Metoken (2013) the current work considers evolving anisotropy and asymmetry by adopting an evolving CPB06 yield surface. Moreover, an isotropic strain rate sensitivity is also introduced. The predicted forming forces and strains for the LDH models are reasonably close to the experimental measurements. It is noteworthy that the current model has the potential to be calibrated along arbitrary loading conditions such as plane strain; however, the calibrations presented herein are limited to uniaxial tension and compression load paths as well as equi-biaxial tension conditions.

The deep drawing simulations show similar trends to that observed in the measurement of forming forces and major/minor strain distribution within the formed cup. Nevertheless, the predicted results consistently show lower resistance of the material to stretch in the wall region resulting in a longer curvilinear length of cup from the pole to the outer rim and consequently a comparatively higher predicted major strain. The predicted forming forces exceed the experimental measurements. A more accurate description of the frictional conditions between the PTFE Teflon film and the AZ31B-O sheet at elevated temperatures may improve the predicted results. Furthermore, considering a larger range of accumulated plastic strain during the calibration (currently up to 8% strain) is to be considered in future work since the major strains in the deep drawing experiments exceed 50%. Moreover, considering the strain rate dependency of *r*-values, as reported by Ghaffari Tari and Worswick (2011) and Kurukuri et al. (2013), may improve the predictions of major and minor strain distribution within the cup. Finally, development of a model for the prediction of actual failure (necking) in this magnesium alloy is left for future work.

6. CONCLUSION

- A strong, evolving tension/compression asymmetry in both measured flow stress and *r*-values for AZ31B was observed at room temperature as well as at 150°C. The anisotropy and asymmetry reduces dramatically at higher temperatures, while the mechanical response becomes more strain rate dependent.
- The evolving anisotropic and asymmetric response of AZ31B is captured at room and elevated temperatures utilizing a CPB06ex3ev yield surface formulation. It is shown that a strain rate/temperature dependent hardening rule can be coupled with the current yield function to incorporate the strain rate sensitivity and thermal softening of the flow stress.
- The CPB06ex3ev material model coupled with temperature and strain rate dependent hardening models provides qualitative predictions of forming force and strain distribution within elevated temperature limiting dome height and deep drawing experiments.

7. ACKNOWLEDGEMENTS

This research was carried out under the framework of the Research Program of the Magnesium Network (MagNET), Canada. Financial support from MagNET, the Natural Sciences and

Engineering Research Council (NSERC), the Canada Research Chairs Secretariat and the Ontario Research Fund is gratefully acknowledged.

REFERENCES

Abedrabbo, N., Pourboghrat, F., Carsley, J., 2006. Forming of aluminum alloys at elevated temperatures-Part I: Material charactrization. International Journal of Plasticity 22, 314-341.

Agnew, S.R., Duygulu, Ö., 2005. Plastic anisotropy and the role of non-basal slip in magnesium alloy AZ31B. International Journal of Plasticity 21, 1161-1193.

Bagheriasl, R., 2012. Formability of Aluminum Alloy Sheet at Elevated Temperature, Ph.D. Thesis, University of Waterloo.

Bagheriasl, R., Worswick, M.J., Formability of AA3003 brazing sheet at elevated temperatures: limiting dome height tests and determination of forming limit diagrams, accepted for publication in the International Journal of Material Forming, December 27, 2013.

Banabic, D., Comsa, D.S., Sester, M., Selig, M., Kublin, W., Mattiasson, K., Sigvant, M., 2008. Influence of constitutive equations on the accuracy of prediction in sheet metal forming simulations. In: Proceedings of the Esaform 2008, Interlaken, Switzerland.

Barlat, F., Maeda, Y., Chung, K., Yanagawa, M., Brem, J.C., Hayashida, Y., Lege, D.J., Matsui, K., Murtha, S.J., Hattori, S., Becker, R.C., Makosey, S., 1997. Yield function development for aluminum alloy sheet. J. Mech. Phys. Solids 45, 1727.

Barlat, F., Aretz, H., Yoon, J.W., Karabin, M.E., Brem, J.C., Dick, R.E., 2005. Linear transfomation-based anisotropic yield functions. International Journal of Plasticity 21, 1009-1039.

Cazacu, O., Baralat, F., 2004. A criterion for description of anisotropy and yield differential effects in pressure-insensitive metals. International Journal Of Plasticity 20, 2027-2045.

Cazacu, O., Plunkett, B., Barlat, F., 2006. Orthotropic yield criterion for hexagonal closed packed metals. International Journal of Plasticity 22, 1171-1194.

Chung, K., Richmond, O., 1993. A deformation theory of plasticity based on minimum work paths. International Journal of Plasticity 9 (8), 907–920.

Choi, S.-H, Kim, D.H., Lee, H.W., Seong B.S., Piao, K., Wagoner, R., 2009. Evolution of the deformation texture and yield locus shape in an AZ31 Mg alloy sheet under uniaxial loading, Materials Science and Engineering: A 526, 38–49.

Cowper, G.R., Symonds, P.S., Strain hardening and strain rate effects in the impact loading of cantilever beams, Technical report, Brown University 1957

Ghaffari Tari, D., Worswick, M.J., McKinley, J., Bagheriasl, R., 2010. AZ31 magnesium deep drawing experiments and finite element simulation. International Journal of Material Forming, Vol. 3, Suppl l, 159-162.

Ghaffari Tari, D., Worswick, M.J., 2011. Experimental investigation of anisotropy evolution of AZ31 magnesium alloy sheets under tensile loading. In: Proceedings of the Esaform 2011, Belfast, Ireland.

Ghaffari Tari, D., Worswick, M.J., 2012. Deep drawing simulations of AZ31B magnesium alloy sheet considering asymmetry in tension and compression. In: Proceedings of the 9th International Conference on Magnesium Alloys and Their Applications, Vancouver, Canada.

Ghaffari Tari, D., Worswick, M.J., Ali, U., Gharghouri, M., 2014. Mechanical response of AZ31B magnesium alloy: Experimental characterization and constitutive modeling considering proportional loading. International Journal of Plasticity 55, 247-267.

Ghaffari Tari, D., Worswick, M.J., Winkler, S., 2013. Experimental studies of deep drawing of AZ31B magnesium alloy sheet under various thermal conditions. Journal of Materials Processing and Technology 213, 1337-1347.

Hasenpouth, D., 2010. Tensile High Strain Rate Behavior of AZ31B Magnesium Alloy Sheet, M.Sc. Thesis, University of Waterloo.

Hill, R., 1948.A theory of the yielding and plastic flow of anisotropic metals. Proc. Roy. Soc. London 193, 281–297.

Jain, A., Agnew, S.R., 2007. Modeling the temperature dependent effect of twinning on the behavior of magnesium alloy AZ31B sheet. Materials Science and Engineering A 462, 29-36.

Jiang, L., Jonas, J.J., Mishra, R.K., Luo, A.A., Sachdev, A.K., Godet, S., 2007. Twinning and texture development in two Mg alloys subjected to loading along three different strain paths. Acta Materialia 55, 3899-3910.

Khan, A.S., Pandey, A., Gnaupel-Herold, T., Mishra, R.K., 2011. Mechanical response and texture evolusion of AZ31 alloy at large strains for different strain rates and temperatures. International Journal of Plasticity 27, 688-706.

Khan, A.S, Pandey, A., Stoughton, T., 2010, Evolution of subsequent yield surfaces and elastic constants with finite plastic deformation. Part II: A very high work hardening aluminum alloy (annealed 1100 Al), International Journal of Plasticity, 26(10), 1421-1431.

Klepaczko, J.R., Malinowski, J.Z., Dynamic frictional effects as measured from the split Hopkinson pressure bar, in: High: Velocity Deformation of Solids. IUTAM Symposium, Tokyo, Japan. Springer-Verlag, Berlin, 1977, p. 403.

Lee, S., Ham, H.J., Kwon, S.Y., Kim, S.W., Suh, C.M., 2012. Thermal condictivity of magnesium alloys in the temperature range from -125 °C to 400 °C. International Journal of Thermophysics, DOI 10.1007/s10765-011-1145-1.

Li, M., Lou, X.Y., Kim, J.H., Wagoner, R.H., 2010. An efficient constitutive model for room-temperature, low-rate plasticity of annealed Mg AZ31B sheet. International Journal of Plasticity 26, 820-858.

Lou, X.Y., Li, M., Boger, R.K., Agnew, S.R., Wagoner, R.H., 2007. Hardening evolution of AZ31B Mg sheet. International Journal of Plasticity 23, 44-86.

Maeda, Y., Yanagawa, M., Barlat, F., Chung, K., Hayashida, Y., Hattori, S., Matsui, K., Brem, J.C., Lege, D.J., Murtha, S.J., Ishikawa, T., 1998. Experimental analysis of aluminum yield surface for binary Al-Mg alloy sheet samples. International Journal of Plasticity 14, 301-318.

Mordike, B.L., Ebert, T., 2001. Magnesium Properties-applications-potential, Materials Science and Engineering A 302, 37-45.

Nebebe Mekonen, M., Steglich, D., Bohlen, J., Letzig, D., Mosler, J., 2012. Mechanical charactrization and constitutive modeling of Mg alloy sheets, Materials Science and Engineering A 540, 174-186.

Nebebe Mekonen, M., Steglich, D., Bohlen, J., Stutz, L., Letzig, D., Mosler, J., 2013. Experimental and numerical investigation of Mg alloy formability. Materials Science and Engineering A 586, 204-214.

Ortiz, M., Simo, J.C., 1986. An analysis of a new class of integration algorithms for elastoplastic constitutive relations, International journal for numerical methods in engineering 23, 353-366.

Palaniswamy, H., Ngaile, G., Altan, T., 2004. Finite element simulation of magnesium alloy sheet forming at elevated temperatures. Journal of Material Processing Technology 146, 52-60.

Palumbo, G., Sorgente, L., Tricarico, S., Zhang, S.H., Zheng, W.T., 2007. Numerical and experimental investigation on the effects of the heating strategy and the punch speed on the warm deep drawing of magnesium alloy AZ31. Journal of Materials Processing Technology 191, 342-346.

Piao, K., Lee, J.K., Kim, J.H., Kim, H.Y., Chung, K., Barlat, F. 2012. A sheet tension/compression test for elevated temperature. International Journal of Plasticity 38, 27-46.

Plunkett, B., Cazacu, O., Barlat, F., 2008. Orthotropic yield criteria for description of the anisotropy in tension and compression of sheet metals, International Journal of Plasticity 24, 847-866.

Plunkett, B., Cazacu, O., Lebensohn, R.A., Barlat, F., 2007. Elastic-viscoplastic anisotropic modeling of textured metals and validation using the Taylor cylinder impact test. International Journal of Plasticity 23, 1001–1021.

Plunkett, B., Lebensohn, R.A., Cazacu, O., Barlat, F., 2006. Anisotropic yield function of hexagonal materials taking into account texture development and anisotropic hardening. Acta Materialia 54, 4159-4169.

Proust, G., Tomé, C., Jain, A., Agnew, S.R., 2009. Modeling the effect of twinning and detwinning during strain-path changes of magnesium alloy AZ31. International Journal of Plasticity 25, 861-880.

Kelley, E.W., Hosford Jr., W.F., 1968. The deformation characteristics of textured magnesium. Trans.TMS-AIME 242, 654–661.

Kulekci, M.K., 2008. Magnesium and its alloys applications in automotive industry. International Journal of Advanced Manufacturing Technology 39, 851-865.

Kurukuri, S., Van den Boogaard, A.H., Miroux, A., Holmedal, B., 2009. Warm forming simulation of Al-Mg sheet. Journal of Materials Processing Technology 209, 5636-5645.

Kurukuri, S., Worswick, M.J., Ghaffari Tari, D., Mishra, R.K., Carter, J.T., 2013. Material characterization and constitutive modeling of commercial grade AZ31B Mg alloy sheet over wide range of strain rates, accepted for publication in Philosophical Transactions A of the Royal Society, October 17, 2013.

Simo, J.C., Ortiz, M., 1985. A unified approach to finite deformation elastoplastic anaysis based on the use of hyperelastic constitutive equations. Computer methods in applied mechanics and engineering 49, 221-245.

Steglich, D., Brocks, W., Bohlen, J., Barlat, F., 2011. Modelling direction-dependent hardening in magnesium sheet forming simulations. International Journal of Material Forming 4, 243-253.

Steglich, D., Jeong Y., Andar M.O., Kuwabara, T., 2012. Biaxial deformation of AZ31 magnesium alloy: Crystal-Plasticity-based prediction and experimental validation. International Journal of Solid and Structures 49, 3551-3561.

Van den Boogaard, A.H., J. Huétink, 2006, Simulation of aluminum sheet forming at elevated temperatures. Computer Methods in Applied Mechanics and Engineering 195, 6691–6709.

von Mises, R., 1913. Mechanik der festen Körper im plastisch deformablen zustand. Göttin. Nachr. Math. Phys., vol. 1, 582–592.

Zhang, L., Huang, G., Zhang, H., Song, B., 2011. Cold stamping formability of AZ31B magnesium alloy sheet undergoing repeated unidirectional bending process. Journal of Materials Processing Technology 211, 644-649.

Appendix

CPB06ex3ev parameters

At 23°C used if Temperature<100°C

a_{11}	b_{11}	d_{11}	a_{12}	b_{12}	d_{12}	a_{13}	b_{13}	d_{13}	a_{22}	b_{22}	d_{22}	a_{23}	b_{23}	d_{23}	a_{33}	b_{33}	d_{33}	a_{66}	b_{66}	d_{66}
-1.263	58.362	0.193	0.259	-1.707	11.523	0.477	0.071	0.018	0.003	-1.939	3.977	0.583	0.000	-141.906	2.523	-2.606	33.436	0.513	-0.092	-0.426
a'_{11}	b'_{11}	d'_{11}	a'_{12}	b'_{12}	d'_{12}	a'_{13}	b'_{13}	d'_{13}	a'_{22}	b'_{22}	d'_{22}	a'_{23}	b'_{23}	d'_{23}	a'_{33}	b'_{33}	d'_{33}	a'_{66}	b'_{66}	d'_{66}
-0.033	-0.070	0.063	-1.213	0.212	-0.038	-0.399	-4.420	0.179	-0.056	-0.054	3.974	-0.115	3.597	-0.774	-2.309	19.438	0.858	1.208	-102.112	0.006
a''_{11}	b''_{11}	d''_{11}	a''_{12}	b''_{12}	d''_{12}	a''_{13}	b''_{13}	d''_{13}	a''_{22}	b''_{22}	d''_{22}	a''_{23}	b''_{23}	d''_{23}	a''_{33}	b''_{33}	d''_{33}	a''_{66}	b''_{66}	d''_{66}
0.219	-257.767	0.078	-0.786	-5.777	3.627	-1.809	421.847	-0.029	0.214	-135.047	0.174	-1.139	0.033	-42.880	-2.747	2.489	-0.282	0.998	-0.479	-0.001
e	f	g																		
-0.200	0.056	12.918																		
e'	f'	g'																		
0.312	-2.616	-0.320																		
e"	f"	g"																		
1.000	-220.500	0.048																		

At 150°C used if 100°C<Temperature<175°C

a_{11}	b_{11}	d_{11}	a_{12}	b_{12}	d_{12}	a_{13}	b_{13}	d_{13}	a_{22}	b_{22}	d_{22}	a_{23}	b_{23}	d_{23}	a_{33}	b_{33}	d_{33}	a_{66}	b_{66}	d_{66}
-1.948	0.138	0.013	-1.010	-0.493	3.769	-0.540	-2.575	-0.612	-1.384	-0.642	10.012	-0.070	0.050	-25.911	-0.748	2.203	6.433	0.491	24.471	0.137
a'_{11}	b'_{11}	d'_{11}	a'_{12}	b'_{12}	d'_{12}	a'_{13}	b'_{13}	d'_{13}	a'_{22}	b'_{22}	d'_{22}	a'_{23}	b'_{23}	d'_{23}	a'_{33}	b'_{33}	d'_{33}	a'_{66}	b'_{66}	d'_{66}
-0.042	-0.369	0.340	-1.753	2.318	0.827	-0.365	-9.728	0.266	-0.265	-1.630	-0.762	-0.051	2.215	-1.886	-1.270	6.806	-0.344	1.525	-34.863	-0.014
a''_{11}	b''_{11}	d''_{11}	a''_{12}	b''_{12}	d''_{12}	a''_{13}	b''_{13}	d''_{13}	a''_{22}	b''_{22}	d''_{22}	a''_{23}	b''_{23}	d''_{23}	a''_{33}	b''_{33}	d''_{33}	a''_{66}	b''_{66}	d''_{66}
-0.165	-29.294	0.258	-0.179	5.071	1.296	-0.587	89.104	0.017	0.018	13.206	0.796	-0.435	0.000	-89.303	0.380	-3.953	0.646	0.842	-0.605	-0.001
e	f	g																		
-0.488	11.293	0.277																		
e'	f'	g'																		
-0.081	1.003	1.762																		
e"	f"	g"																		
1.000	-13.600	1.163																		

At 200°C used if 175°C<Temperature<225°C

a_{11}	b_{11}	d_{11}	a_{12}	b_{12}	d_{12}	a_{13}	b_{13}	d_{13}	a_{22}	b_{22}	d_{22}	a_{23}	b_{23}	d_{23}	a_{33}	b_{33}	d_{33}	a_{66}	b_{66}	d_{66}
-1.181	-0.857	0.012	-0.660	-0.308	-4.708	0.297	-0.646	-0.095	-1.525	1.089	1.982	-0.223	0.018	5.857	0.249	1.309	5.792	0.711	-2.998	0.155
a'_{11}	b'_{11}	d'_{11}	a'_{12}	b'_{12}	d'_{12}	a'_{13}	b'_{13}	d'_{13}	a'_{22}	b'_{22}	d'_{22}	a'_{23}	b'_{23}	d'_{23}	a'_{33}	b'_{33}	d'_{33}	a'_{66}	b'_{66}	d'_{66}
-0.077	-0.087	0.082	-1.351	-1.116	0.522	-0.350	-5.513	0.213	-0.065	-0.119	0.245	-0.135	1.004	-1.243	-1.571	10.158	2.517	1.303	-35.756	-0.016
a''_{11}	b''_{11}	d''_{11}	a''_{12}	b''_{12}	d''_{12}	a''_{13}	b''_{13}	d''_{13}	a''_{22}	b''_{22}	d''_{22}	a''_{23}	b''_{23}	d''_{23}	a''_{33}	b''_{33}	d''_{33}	a''_{66}	b''_{66}	d''_{66}
-0.008	-98.093	0.005	-0.759	-2.244	-1.049	-0.778	-13.649	-0.005	0.057	-1.846	1.373	-0.557	0.000	6.952	0.009	11.277	-0.399	0.767	-0.576	-0.001
e	f	g																		
0.008	-8.398	0.167																		
e'	f'	g'																		
0.177	0.022	-0.035																		
e"	f"	g"																		
1.000	-16.033	1.039																		

At 250°C used if 225°C<Temperature

a_{11}	b_{11}	d_{11}	a_{12}	b_{12}	d_{12}	a_{13}	b_{13}	d_{13}	a_{22}	b_{22}	d_{22}	a_{23}	b_{23}	d_{23}	a_{33}	b_{33}	d_{33}	a_{66}	b_{66}	d_{66}
-0.820	-0.062	0.090	-0.717	-0.641	17.540	0.098	0.070	0.018	0.003	-1.390	2.570	0.228	0.000	-108.174	1.247	-2.266	148.886	0.671	-0.149	-0.700
a'_{11}	b'_{11}	d'_{11}	a'_{12}	b'_{12}	d'_{12}	a'_{13}	b'_{13}	d'_{13}	a'_{22}	b'_{22}	d'_{22}	a'_{23}	b'_{23}	d'_{23}	a'_{33}	b'_{33}	d'_{33}	a'_{66}	b'_{66}	d'_{66}
-0.082	-0.084	0.076	-1.521	0.132	-0.024	-0.239	-6.000	0.262	-0.109	-0.119	6.792	0.035	5.038	-0.825	-1.666	8.873	0.949	1.483	-140.667	0.008
a''_{11}	b''_{11}	d''_{11}	a''_{12}	b''_{12}	d''_{12}	a''_{13}	b''_{13}	d''_{13}	a''_{22}	b''_{22}	d''_{22}	a''_{23}	b''_{23}	d''_{23}	a''_{33}	b''_{33}	d''_{33}	a''_{66}	b''_{66}	d''_{66}
0.167	-214.094	0.063	-0.622	-3.043	4.430	-0.296	560.937	-0.032	0.190	-105.678	0.147	-0.444	0.030	-43.784	-0.834	2.479	-0.281	0.745	-0.476	-0.001
e	f	g																		
-0.134	0.104	27.887																		
e'	f'	g'																		
0.003	-3.376	-0.345																		
e"	f"	g"																		
1.000	-214.124	0.086																		

Appendix D: Additional publications stemming from this research

(Note that this list does not include the publications comprising Appendices A, B and C)

- D. Ghaffari Tari, M.J. Worswick, U. Ali, *Asymmetric yield locus evolution for HCP materials: a continuum constitutive modeling approach*, Key Engineering Materials 554-557, 1184-1188.
- D. Ghaffari Tari, M.J. Worswick, J. Mckinley, R., Bagheriasl, *AZ31 magnesium deep drawing experiments and finite element simulation*, International Journal of Material Forming 3, 159-162.
- R., Bagheriasl, D. Ghaffari Tari, S. Kurukuri, M.J. Worswick, *Material properties for numerical calculations, Book chapter in:* Comprehensive Material Processing Technology, Elsevier Publication 2014.
- Kurukuri, S., Worswick, M.J., Ghaffari Tari, D., Mishra, R.K., Carter, J.T., 2013. Material characterization and constitutive modeling of commercial grade AZ31B Mg alloy sheet over wide range of strain rates, Philosophical Transactions of the Royal Society 2013.
- D. Ghaffari Tari, M.J. Worswick, *Deep drawing simulations of AZ31 magnesium alloy sheet considering asymmetry in tension and compression*, 9th International Magnesium Conference on Magnesium Alloys and their Applications, Vancouver, Canada, July 2012.
- D. Ghaffari Tari, M.J. Worswick, *Deep drawing experiments of AZ31 magnesium alloy*, International Deep Drawing Research Group (IDDRG) Conference, Bilbao, Spain, June 2011.
- D. Ghaffari Tari, M.J. Worswick, *Experimental investigation of anisotropy evolution of AZ31 magnesium alloy sheets under tensile loading*, European Scientific Association for Metal Forming (Esaform) Conference, Belfast, United Kingdom, April 2011.

Appendix E: Comparison between the AZ31B-O used in this work to that used by Khan et al. [19]

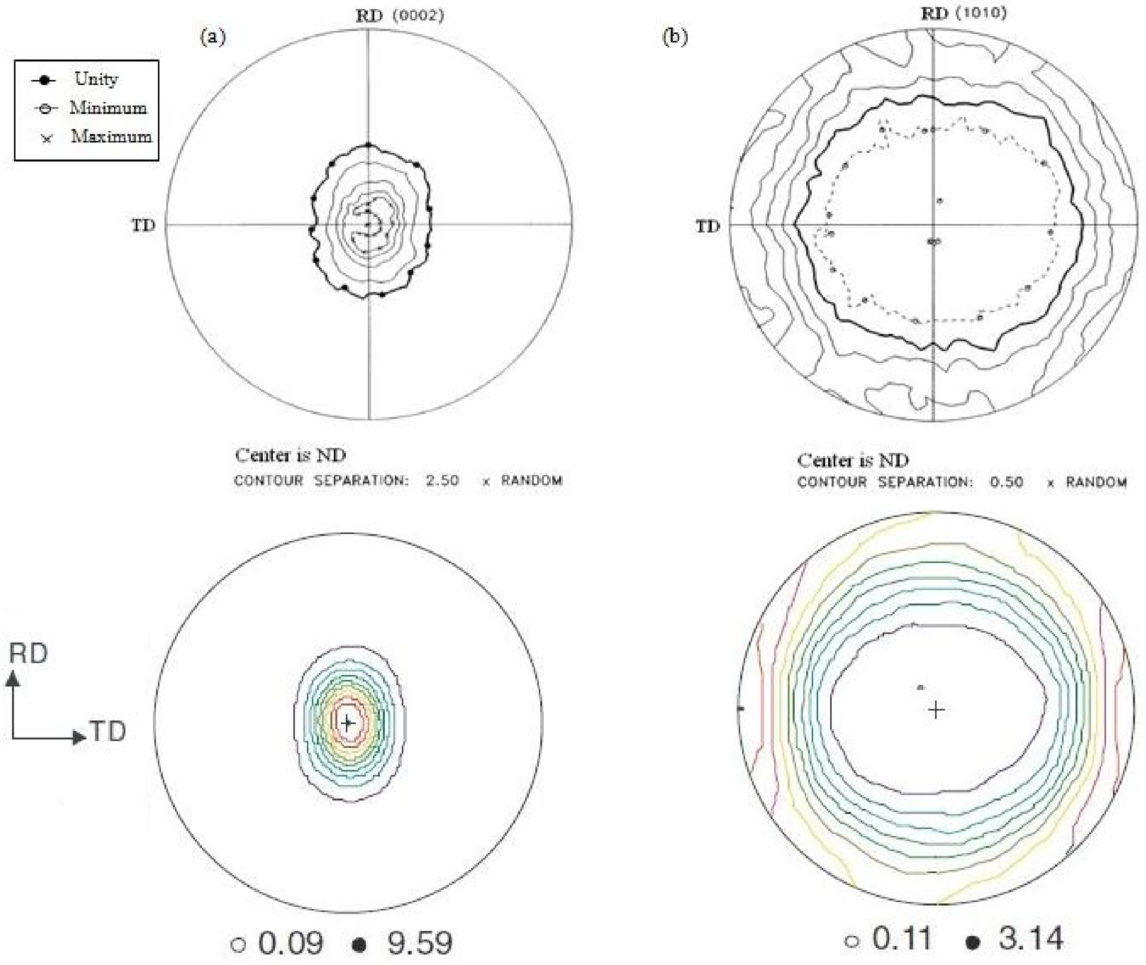

Figure 31. Comparison between poles figure from AZ31B-O material used in this research (top) and the material used by Khan et al. [19] (bottom).

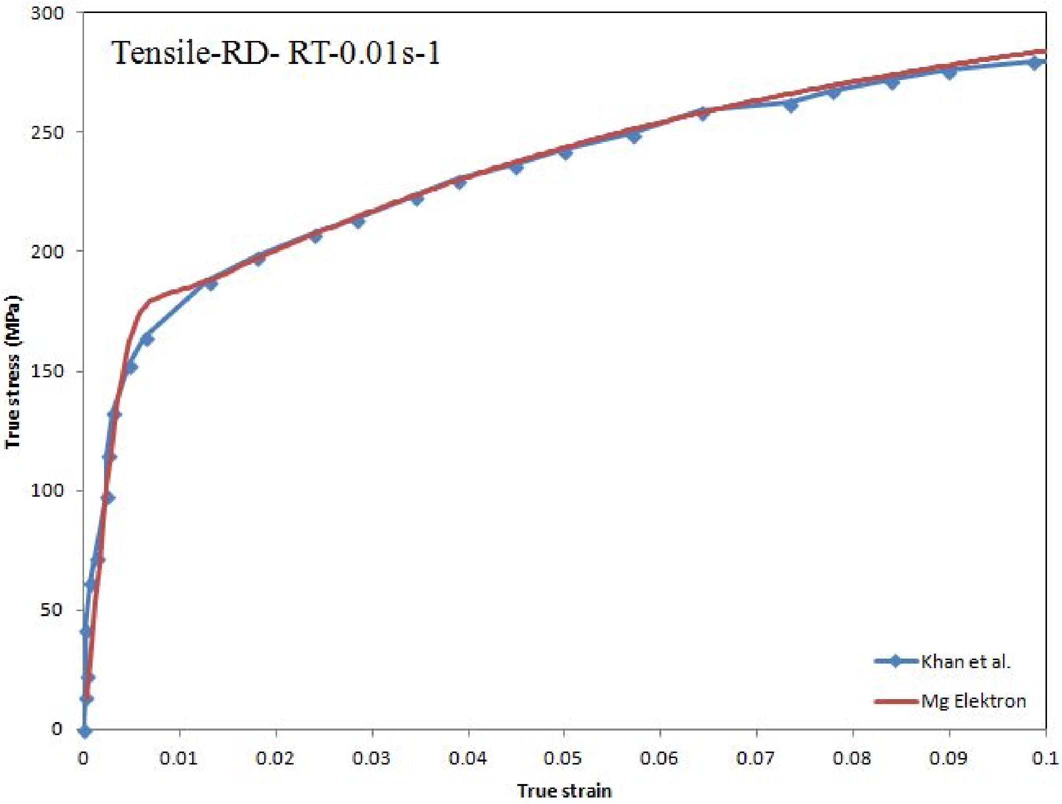

Figure 31. Comparison between uniaxial tensile response along the rolling direction from AZ31B-O material used in this research and the material used by Khan et al. [19].

Appendix F: Calculating instantaneous *r*-values from the tensile tests.

Initially the axial and transverse displacements are measured using two independent extensometers as shown in Figure 32 and a polynomial is fit to the associated displacement curve to smoothen the measurements.

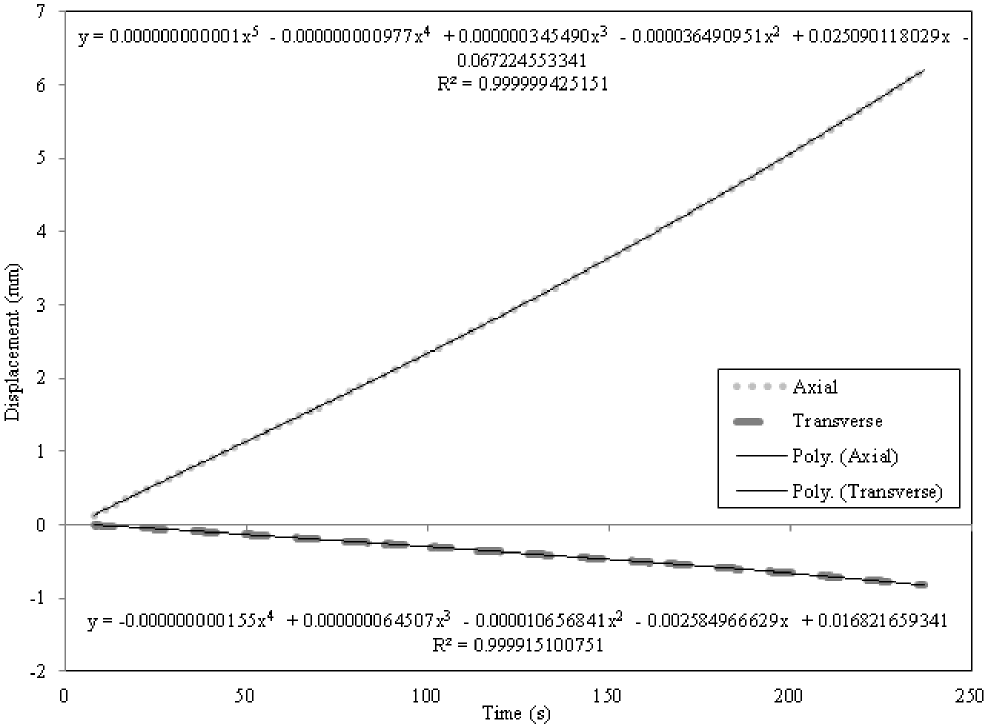

Figure 32. Axial and transverse displacement measurements from the extensometers and the corresponding polynomial fits.

The true strain components along the axial and transverse directions are calculated from the polynomial fits. The calculated true strain is then corrected as described in Appendix B. The through-thickness true plastic strain is obtained assuming volume conservation during plastic deformation. Figure 33 shows a plot of the true plastic strain component along width of the specimen *vs.* true plastic strain component along the through-thickness direction.

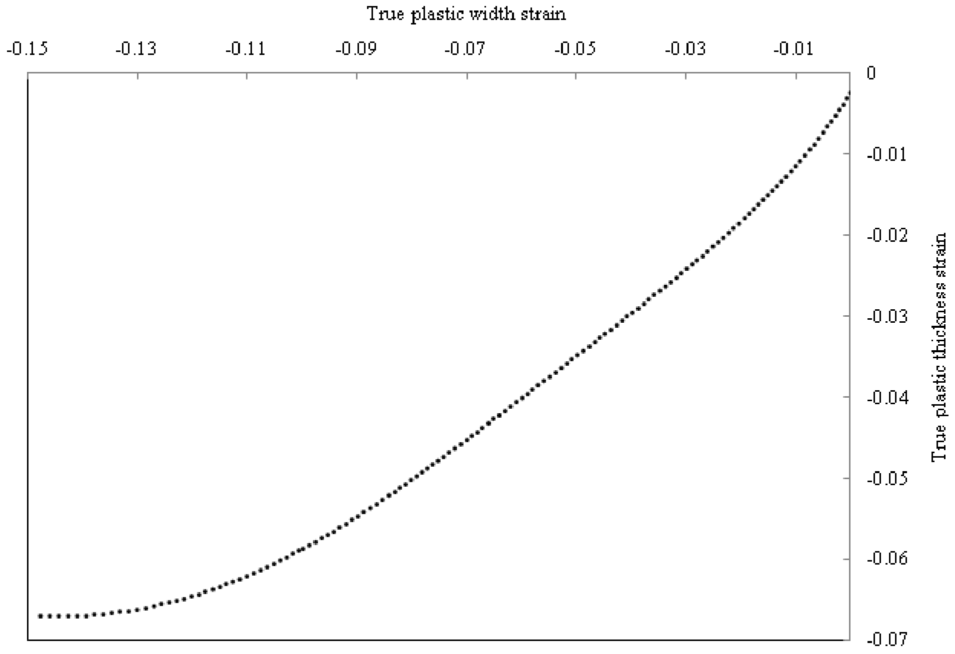

Figure 33. Axial and transverse displacement measurements from the extensometers and the corresponding polynomial fits.

True plastic strain increments along the width and through-thickness directions are calculated by subtracting two subsequent strain readings. Figure 34 shows the true plastic strain increment along the width of the specimen as a function of the true plastic strain increment along the through-thickness direction. The instantaneous *r*-value is found from equation (1), as described in Appendix B and plotted in Figure 35.

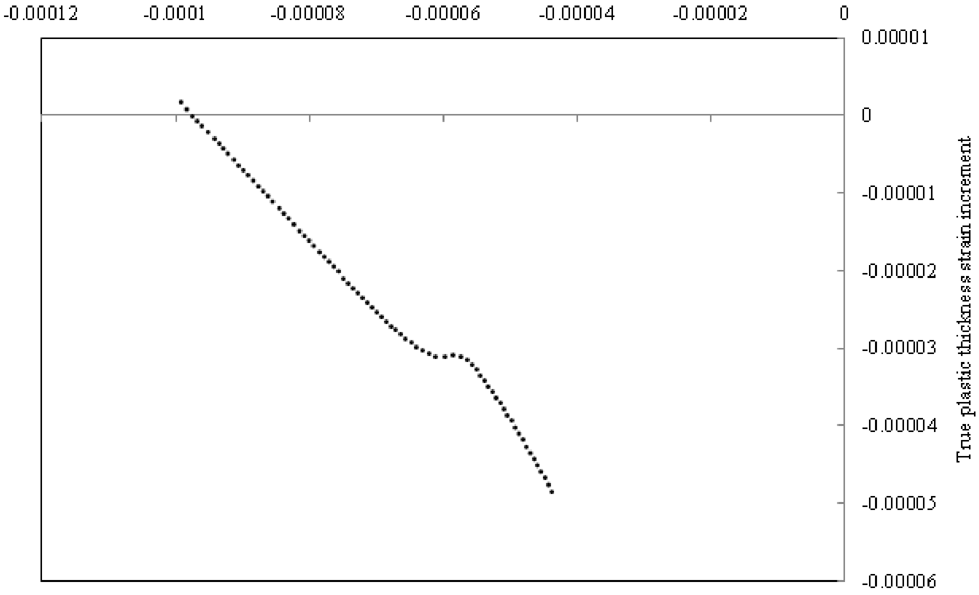

Figure 34. Axial and transverse displacement measurements from the extensometers and the corresponding polynomial fits.

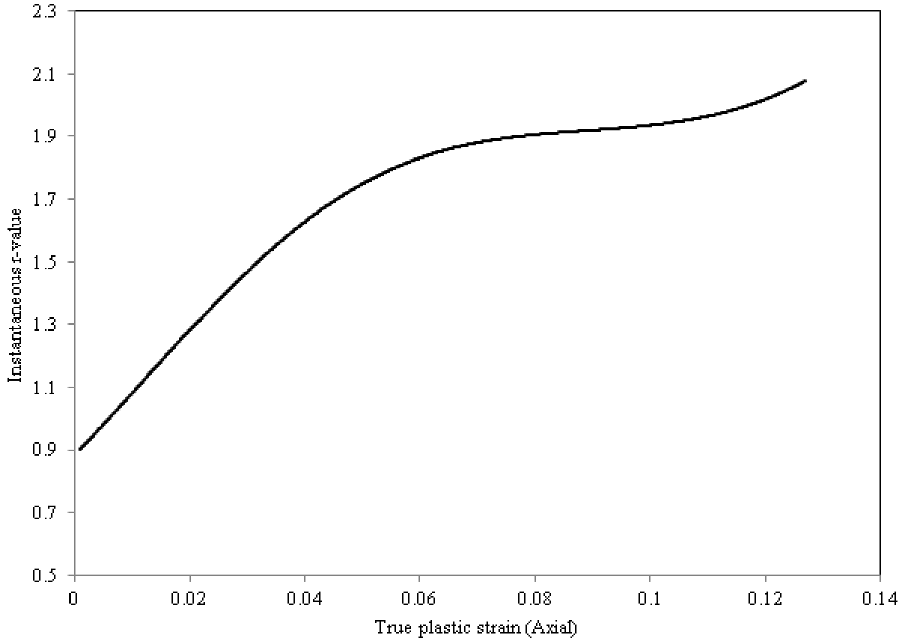

Figure 35. Instantaneous *r*-value *vs.* true plastic strain along axial direction.

Appendix G: Isotropic hardening beyond calibration limit.

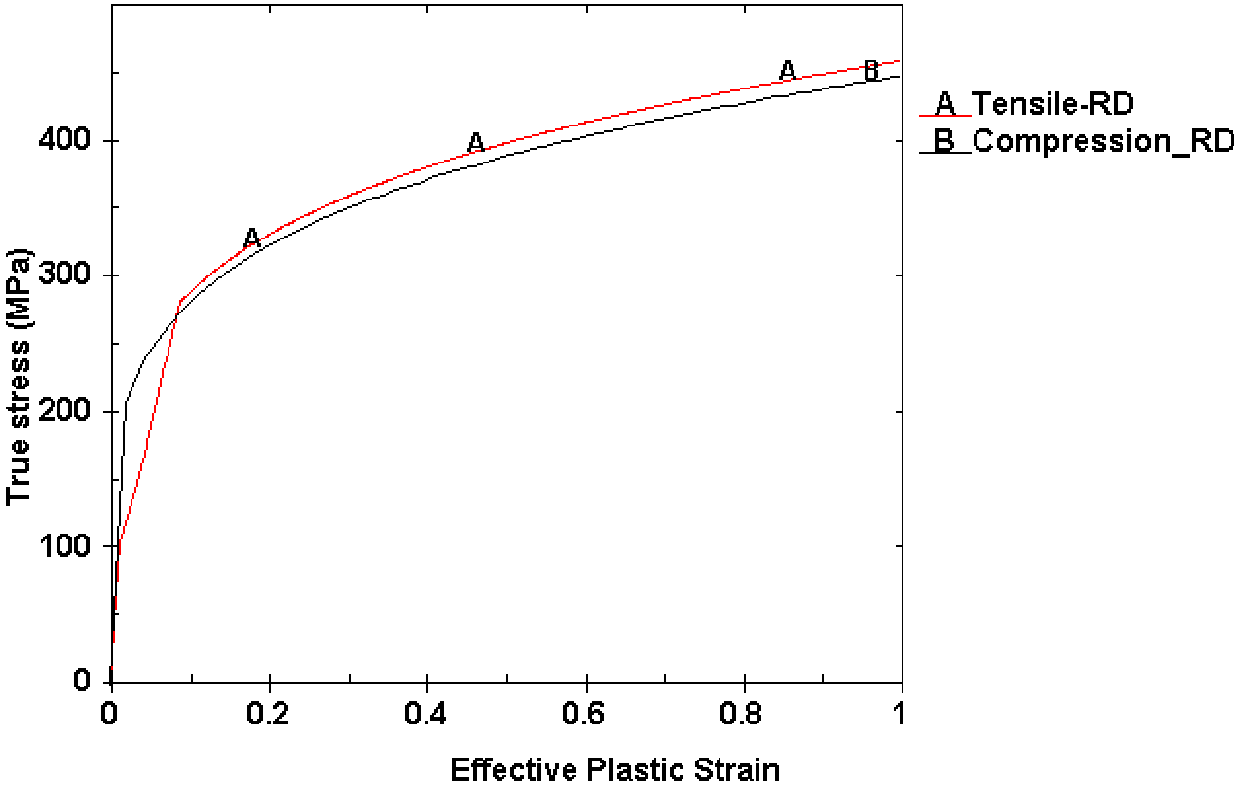

Figure 36. True stress *vs.* effective plastic strain under tensile loading along the rolling direction beyond 8% plastic strain

Appendix H: MathCAD program for calibration of the CPB06ex1ev model

CPB06ex1ev calibration code
By: **Dariush Ghaffari Tari**,

The current code is written within MathCAD software. To use this code, the number of effective plastic strain intervals (*i*) and the magnitude of the effective plastic strain (*ε*) at interval "*i*" need to be defined. The input experiments are introduced as functions of effective plastic strain *ε*. The initial guess for the parameters ($A_0 \ldots A_{20}$, $B_0 \ldots B_2$) are necessary and an improved guess is given as output of this optimization code.

1) Defining effective plastic strain intervals

$$\varepsilon := 0, 0.02 .. 0.08$$

$$\begin{array}{|r|}\hline 0 \\ \hline 0.02 \\ \hline 0.04 \\ \hline 0.06 \\ \hline 0.08 \\ \hline \end{array}$$

$$i := 0 .. 4$$

2) Introducing material response and normalization of the flow stress;
Sigtexθ and *Sigcexθ* represent the normalized uniaxial tensile and compression flow stress curves along arbitrary sheet orientation "*θ*" while *rtexθ* and *rcexθ* are tensile and compression instantaneous *r*-values along sheet orientation "*θ*". *Sabt*, *Sabc* and *tau* are normalized biaxial tensile, biaxial compression and shear flow curves, respectively.

$$\mathrm{Sigtex0}(i) := -37259432.5\cdot\left(\varepsilon_i\right)^6 + 17863423.12\cdot\left(\varepsilon_i\right)^5 - 3336645.77\cdot\left(\varepsilon_i\right)^4 + 351644.8\cdot\left(\varepsilon_i\right)^3 - 29785.9\cdot\left(\varepsilon_i\right)^2 + 2595.22\cdot\left(\varepsilon_i\right) + 161.96$$

$$\mathrm{Sigtex30}(i) := \frac{\left[-19359438.18\cdot\left(\varepsilon_i\right)^6 + 11893538.85\cdot\left(\varepsilon_i\right)^5 - 2938528.15\cdot\left(\varepsilon_i\right)^4 + 394996.22\cdot\left(\varepsilon_i\right)^3 - 35750.05\cdot\left(\varepsilon_i\right)^2 + 2787.83\cdot\left(\varepsilon_i\right) + 165.47\right]}{\mathrm{Sigtex0}(i)}$$

$$\mathrm{Sigtex45}(i) := \frac{\left[-12989369.18\cdot\left(\varepsilon_i\right)^6 + 7989626.33\cdot\left(\varepsilon_i\right)^5 - 2031019.75\cdot\left(\varepsilon_i\right)^4 + 293749.62\cdot\left(\varepsilon_i\right)^3 - 30077.55\cdot\left(\varepsilon_i\right)^2 + 2594.83\cdot\left(\varepsilon_i\right) + 171.75\right]}{\mathrm{Sigtex0}(i)}$$

$$\mathrm{Sigtex60}(i) := \frac{\left[-9416981.53\cdot\left(\varepsilon_i\right)^6 + 4745825.94\cdot\left(\varepsilon_i\right)^5 - 1057282.24\cdot\left(\varepsilon_i\right)^4 + 164749.91\cdot\left(\varepsilon_i\right)^3 - 22053.55\cdot\left(\varepsilon_i\right)^2 + 2354.31\cdot\left(\varepsilon_i\right) + 182.03\right]}{\mathrm{Sigtex0}(i)}$$

$$\mathrm{Sigtex90}(i) := \frac{\left[27472288.68\cdot\left(\varepsilon_i\right)^6 - 15361483.32\cdot\left(\varepsilon_i\right)^5 + 3071885.04\cdot\left(\varepsilon_i\right)^4 - 232112.92\cdot\left(\varepsilon_i\right)^3 - 4299.12\cdot\left(\varepsilon_i\right)^2 + 2022.56\cdot\varepsilon_i + 187.2\right]}{\mathrm{Sigtex0}(i)}$$

$$\mathrm{Sigcex0}(i) := \frac{\left[109925891.94\cdot\left(\varepsilon_i\right)^6 - 96862582.41\cdot\left(\varepsilon_i\right)^5 + 5817684.6\cdot\left(\varepsilon_i\right)^4 + 953806.07\cdot\left(\varepsilon_i\right)^3 - 55066.15\cdot\left(\varepsilon_i\right)^2 + 1777.75\cdot\varepsilon_i + 98.57\right]}{\mathrm{Sigtex0}(i)}$$

$$\mathrm{Sigcex45}(i) := \frac{\left[-297738421.63\cdot\left(\varepsilon_i\right)^6 - 60807857.31\cdot\left(\varepsilon_i\right)^5 + 6199428.96\cdot\left(\varepsilon_i\right)^4 + 1081200.72\cdot\left(\varepsilon_i\right)^3 - 75155.81\cdot\left(\varepsilon_i\right)^2 + 2585.05\cdot\varepsilon_i + 96.69\right]}{\mathrm{Sigtex0}(i)}$$

$$\mathrm{Sigcex90}(i) := \frac{\left[-8615636879.63\cdot\left(\varepsilon_i\right)^6 + 1949705411.28\cdot\left(\varepsilon_i\right)^5 - 174984177.42\cdot\left(\varepsilon_i\right)^4 + 8517029.29\cdot\left(\varepsilon_i\right)^3 - 203708.54\cdot\left(\varepsilon_i\right)^2 + 3239.27\cdot\varepsilon_i + 99.67\right]}{\mathrm{Sigtex0}(i)}$$

$$\mathrm{sabc}(i) := \frac{(\mathrm{Sigcex0}(i) + \mathrm{Sigcex45}(i))}{2}$$

$$\mathrm{sabt}(i) := \frac{\left[-26561615491.50\cdot\left(\varepsilon_i\right)^6 + 6821669682.63\cdot\left(\varepsilon_i\right)^5 - 675234643.56\cdot\left(\varepsilon_i\right)^4 + 32696703.39\cdot\left(\varepsilon_i\right)^3 - 843436.04\cdot\left(\varepsilon_i\right)^2 + 15103.72\cdot\varepsilon_i + 131.24\right]}{\mathrm{Sigtex0}(i)}$$

$$\mathrm{rtex0}(i) := 6489794.03\cdot\left(\varepsilon_i\right)^6 - 2612062.36\cdot\left(\varepsilon_i\right)^5 + 412426.2\cdot\left(\varepsilon_i\right)^4 - 29695.58\cdot\left(\varepsilon_i\right)^3 + 717.84\cdot\left(\varepsilon_i\right)^2 + 20.16\cdot\varepsilon_i + 0.87$$

$$\mathrm{rtex30}(i) := 4386868.57\cdot\left(\varepsilon_i\right)^6 - 2020945.33\cdot\left(\varepsilon_i\right)^5 + 346590.70\cdot\left(\varepsilon_i\right)^4 - 25069.26\cdot\left(\varepsilon_i\right)^3 + 469.46\cdot\left(\varepsilon_i\right)^2 + 27.93\cdot\varepsilon_i + 1.13$$

$$\mathrm{rtex45}(i) := 2283943.15\cdot\left(\varepsilon_i\right)^6 - 1429828.31\cdot\left(\varepsilon_i\right)^5 + 280755.21\cdot\left(\varepsilon_i\right)^4 - 20442.95\cdot\left(\varepsilon_i\right)^3 + 221.07\cdot\left(\varepsilon_i\right)^2 + 35.7\cdot\varepsilon_i + 1.39$$

$$\mathrm{rtex60}(i) := 26004253.9\cdot\left(\varepsilon_i\right)^6 - 9162145.59\cdot\left(\varepsilon_i\right)^5 + 1304894.6\cdot\left(\varepsilon_i\right)^4 - 86935.77\cdot\left(\varepsilon_i\right)^3 + 2211.27\cdot\left(\varepsilon_i\right)^2 + 24.51\cdot\varepsilon_i + 1.59$$

$$\mathrm{rtex90}(i) := 35768086.61\cdot\left(\varepsilon_i\right)^6 - 11913953.96\cdot\left(\varepsilon_i\right)^5 + 1639101.81\cdot\left(\varepsilon_i\right)^4 - 109049.25\cdot\left(\varepsilon_i\right)^3 + 2951.59\cdot\left(\varepsilon_i\right)^2 + 18.15\cdot\varepsilon_i + 2.31$$

$$\mathrm{rcex0}(i) := 132.37\cdot\left(\varepsilon_i\right)^2 - 2.6652\cdot\varepsilon_i + 0.065$$

$$\mathrm{rcex45}(i) := 1740.2\cdot\left(\varepsilon_i\right)^3 + 26.559\cdot\left(\varepsilon_i\right)^2 - 0.3568\cdot\varepsilon_i + 0.0747$$

$$\mathrm{rcex90}(i) := 90308\cdot\left(\varepsilon_i\right)^4 - 10009\cdot\left(\varepsilon_i\right)^3 + 519.85\cdot\left(\varepsilon_i\right)^2 - 6.135\cdot\varepsilon_i + 0.0847$$

$$\mathrm{tau}(i) := \frac{\left[-848.83\cdot\left(\varepsilon_i\right)^2 + 507.89\cdot\varepsilon_i + 104.21\right]}{\mathrm{Sigtex0}(i)}$$

$$\mathrm{XT} := 1$$

$$\mathrm{angc} := \begin{pmatrix} 0 \\ 45 \\ 90 \end{pmatrix}\cdot\frac{\pi}{180}$$

$$\mathrm{rac}(i) := \begin{pmatrix} \mathrm{rcex0}(i) \\ \mathrm{rcex45}(i) \\ \mathrm{rcex90}(i) \end{pmatrix}$$

$$\mathrm{rat}(i) := \begin{pmatrix} \mathrm{rtex0}(i) \\ \mathrm{rtex30}(i) \\ \mathrm{rtex45}(i) \\ \mathrm{rtex60}(i) \\ \mathrm{rtex90}(i) \end{pmatrix}$$

$$\mathrm{sat}(i) := \begin{pmatrix} 1 \\ \mathrm{Sigtex30}(i) \\ \mathrm{Sigtex45}(i) \\ \mathrm{Sigtex60}(i) \\ \mathrm{Sigtex90}(i) \end{pmatrix}$$

$$\mathrm{ang} := \begin{pmatrix} 0 \\ 30 \\ 45 \\ 60 \\ 90 \end{pmatrix} \cdot \frac{\pi}{180}$$

$$\mathrm{sac}(i) := \begin{pmatrix} \mathrm{Sigcex0}(i) \\ \mathrm{Sigcex45}(i) \\ \mathrm{Sigcex90}(i) \end{pmatrix}$$

3) Plotting the input data

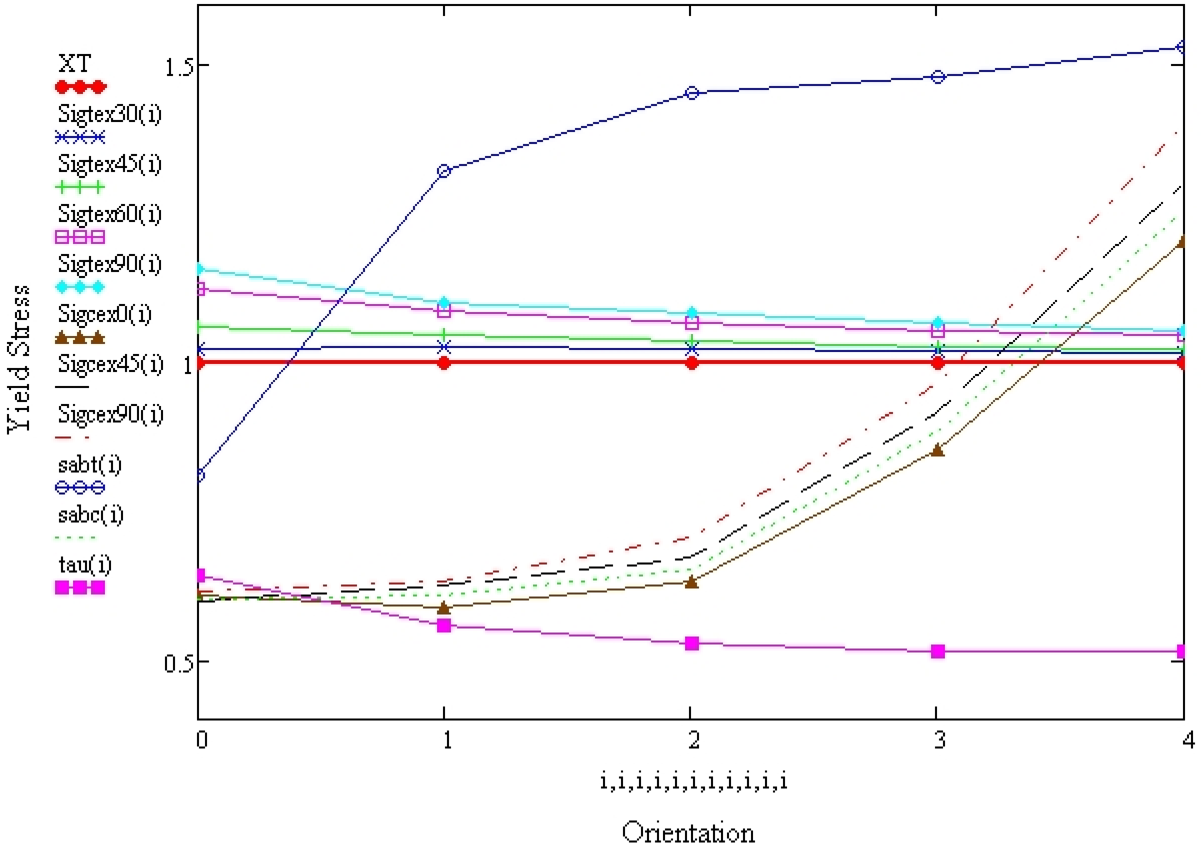

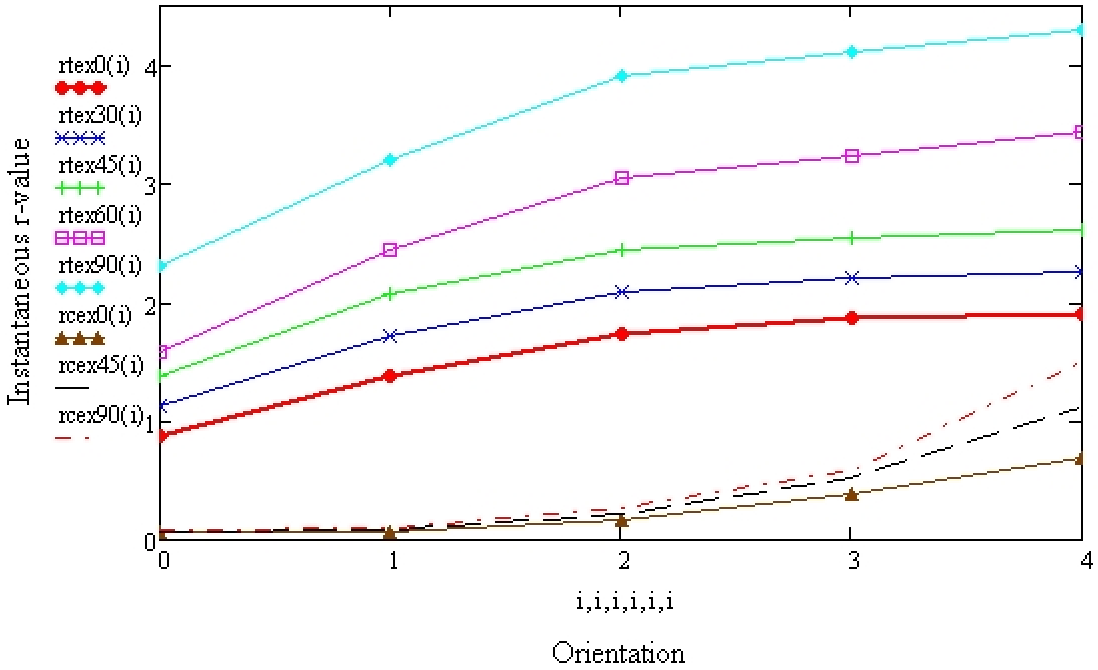

4) Forming C and k functions

$$C11(i,A) := A_0 + A_1 \cdot \left(1 - e^{-A_2 \cdot \varepsilon_i}\right)$$

$$C12(i,A) := A_3 + A_4 \cdot \left(1 - e^{-A_5 \cdot \varepsilon_i}\right)$$

$$C13(i,A) := A_6 + A_7 \cdot \left(1 - e^{-A_8 \cdot \varepsilon_i}\right)$$

$$C22(i,A) := A_9 + A_{10} \cdot \left(1 - e^{-A_{11} \cdot \varepsilon_i}\right)$$

$$C23(i,A) := A_{12} + A_{13} \cdot \left(1 - e^{-A_{14} \cdot \varepsilon_i}\right)$$

$$C33(i,A) := A_{15} + A_{16} \cdot \left(1 - e^{-A_{17} \cdot \varepsilon_i}\right)$$

$$C66(i,A) := A_{18} + A_{19} \cdot \left(1 - e^{-A_{20} \cdot \varepsilon_i}\right)$$

$$k(i,B) := B_0 + B_1 \cdot \left(1 - e^{-B_2 \cdot \varepsilon_i}\right)$$

5) Forming C matrix

$$C(i,A) := \begin{pmatrix} C11(i,A) & C12(i,A) & C13(i,A) & 0 & 0 & 0 \\ C12(i,A) & C22(i,A) & C23(i,A) & 0 & 0 & 0 \\ C13(i,A) & C23(i,A) & C33(i,A) & 0 & 0 & 0 \\ 0 & 0 & 0 & 0 & 0 & 0 \\ 0 & 0 & 0 & 0 & 0 & 0 \\ 0 & 0 & 0 & 0 & 0 & C66(i,A) \end{pmatrix}$$

6) Forming deviatoric stress tensor

$$S(\sigma xx,\sigma yy,\sigma xy) := \begin{bmatrix} \frac{1}{3}(2\sigma xx-\sigma yy) \\ \frac{1}{3}(2\sigma yy-\sigma xx) \\ \frac{-1}{3}(\sigma xx+\sigma yy) \\ 0 \\ 0 \\ \sigma xy \end{bmatrix}$$

7) Calculating Σ tensor

$$\Sigma(i,A,\sigma xx,\sigma yy,\sigma xy) := C(i,A)\, S(\sigma xx,\sigma yy,\sigma xy)$$

8) Calculating principal components of Σ tensor

$$W(\Sigma xx,\Sigma yy,\Sigma zz,\Sigma xy) := \begin{pmatrix} \Sigma xx & \Sigma xy & 0 \\ \Sigma xy & \Sigma yy & 0 \\ 0 & 0 & \Sigma zz \end{pmatrix}$$

$$\Sigma\Sigma(\Sigma xx,\Sigma yy,\Sigma zz,\Sigma xy) := \mathrm{eigenvals}(W(\Sigma xx,\Sigma yy,\Sigma zz,\Sigma xy))$$

$$\Sigma xx(i,A,\sigma xx,\sigma yy,\sigma xy) := \Sigma(i,A,\sigma xx,\sigma yy,\sigma xy)_0$$

$$\Sigma yy(i,A,\sigma xx,\sigma yy,\sigma xy) := \Sigma(i,A,\sigma xx,\sigma yy,\sigma xy)_1$$

$$\Sigma zz(i,A,\sigma xx,\sigma yy,\sigma xy) := \Sigma(i,A,\sigma xx,\sigma yy,\sigma xy)_2$$

$$\Sigma xy(i,A,\sigma xx,\sigma yy,\sigma xy) := \Sigma(i,A,\sigma xx,\sigma yy,\sigma xy)_5$$

$$\Sigma 1(i,A,\sigma xx,\sigma yy,\sigma xy) := \Sigma\Sigma(\Sigma xx(i,A,\sigma xx,\sigma yy,\sigma xy),\Sigma yy(i,A,\sigma xx,\sigma yy,\sigma xy),\Sigma zz(i,A,\sigma xx,\sigma yy,\sigma xy),\Sigma xy(i,A,\sigma xx,\sigma yy,\sigma xy))_0$$

$$\Sigma 2(i,A,\sigma xx,\sigma yy,\sigma xy) := \Sigma\Sigma(\Sigma xx(i,A,\sigma xx,\sigma yy,\sigma xy),\Sigma yy(i,A,\sigma xx,\sigma yy,\sigma xy),\Sigma zz(i,A,\sigma xx,\sigma yy,\sigma xy),\Sigma xy(i,A,\sigma xx,\sigma yy,\sigma xy))_1$$

$$\Sigma 3(i,A,\sigma xx,\sigma yy,\sigma xy) := \Sigma\Sigma(\Sigma xx(i,A,\sigma xx,\sigma yy,\sigma xy),\Sigma yy(i,A,\sigma xx,\sigma yy,\sigma xy),\Sigma zz(i,A,\sigma xx,\sigma yy,\sigma xy),\Sigma xy(i,A,\sigma xx,\sigma yy,\sigma xy))_2$$

9) Forming the CPB06ex1ev function

$$F(i,A,B,\sigma xx,\sigma yy,\sigma xy,a) := \left(\left|\Sigma 1(i,A,\sigma xx,\sigma yy,\sigma xy)\right| - k(i,B)\cdot\Sigma 1(i,A,\sigma xx,\sigma yy,\sigma xy)\right)^a + \left(\left|\Sigma 2(i,A,\sigma xx,\sigma yy,\sigma xy)\right| - k(i,B)\cdot\Sigma 2(i,A,\sigma xx,\sigma yy,\sigma xy)\right)^a + \left(\left|\Sigma 3(i,A,\sigma xx,\sigma yy,\sigma xy)\right| - k(i,B)\cdot\Sigma 3(i,A,\sigma xx,\sigma yy,\sigma xy)\right)^a$$

10) Calculating the derivitives of CPB06ex1ev function

$$F'X(i,A,B,\sigma xx,\sigma yy,\sigma xy,a) := \frac{d}{d\sigma xx}F(i,A,B,\sigma xx,\sigma yy,\sigma xy,a)$$

$$F'Y(i,A,B,\sigma xx,\sigma yy,\sigma xy,a) := \frac{d}{d\sigma yy}F(i,A,B,\sigma xx,\sigma yy,\sigma xy,a)$$

$$\mathrm{F'XY}(i,A,B,\sigma xx,\sigma yy,\sigma xy,a) := \frac{d}{d\sigma xy}\mathrm{F}(i,A,B,\sigma xx,\sigma yy,\sigma xy,a)$$

11) Forming tension and compression model flow stress response functions along arbitrary orientation *θ*

$$\psi1(i,A) := \left(\frac{2}{3}\right)\mathrm{C12}(i,A) - \left(\frac{1}{3}\right)\mathrm{C11}(i,A) - \left(\frac{1}{3}\right)\mathrm{C13}(i,A)$$

$$\psi2(i,A) := \left(\frac{2}{3}\right)\mathrm{C22}(i,A) - \left(\frac{1}{3}\right)\mathrm{C12}(i,A) - \left(\frac{1}{3}\right)\mathrm{C23}(i,A)$$

$$\psi3(i,A) := \left(\frac{2}{3}\right)\mathrm{C23}(i,A) - \left(\frac{1}{3}\right)\mathrm{C13}(i,A) - \left(\frac{1}{3}\right)\mathrm{C33}(i,A)$$

$$\phi1(i,A) := \left(\frac{2}{3}\right)\mathrm{C11}(i,A) - \left(\frac{1}{3}\right)\mathrm{C12}(i,A) - \left(\frac{1}{3}\right)\mathrm{C13}(i,A)$$

$$\phi2(i,A) := \left(\frac{2}{3}\right)\mathrm{C12}(i,A) - \left(\frac{1}{3}\right)\mathrm{C22}(i,A) - \left(\frac{1}{3}\right)\mathrm{C23}(i,A)$$

$$\phi3(i,A) := \left(\frac{2}{3}\right)\mathrm{C13}(i,A) - \left(\frac{1}{3}\right)\mathrm{C23}(i,A) - \left(\frac{1}{3}\right)\mathrm{C33}(i,A)$$

$$\Pi1(i,A) := \left(\frac{-2}{3}\right)\mathrm{C13}(i,A) + \left(\frac{1}{3}\right)\mathrm{C11}(i,A) + \left(\frac{1}{3}\right)\mathrm{C12}(i,A)$$

$$\Pi2(i,A) := \left(\frac{-2}{3}\right)\mathrm{C23}(i,A) + \left(\frac{1}{3}\right)\mathrm{C12}(i,A) + \left(\frac{1}{3}\right)\mathrm{C22}(i,A)$$

$$\Pi3(i,A) := \left(\frac{-2}{3}\right)\mathrm{C33}(i,A) + \left(\frac{1}{3}\right)\mathrm{C13}(i,A) + \left(\frac{1}{3}\right)\mathrm{C23}(i,A)$$

$$\mathrm{Axx}(i,A,\theta) := \phi1(i,A)\cos(\theta)^2 + \psi1(i,A)\sin(\theta)^2$$

$$\mathrm{Ayy}(i,A,\theta) := \phi2(i,A)\cos(\theta)^2 + \psi2(i,A)\sin(\theta)^2$$

$$\mathrm{Azz}(i,A,\theta) := \phi3(i,A)\cos(\theta)^2 + \psi3(i,A)\sin(\theta)^2$$

$$\mathrm{Axy}(i,A,\theta) := \mathrm{C66}(i,A)\sin(\theta)\cos(\theta)$$

$$\mathrm{A1}(i,A,\theta) := \frac{1}{2}\left[(\mathrm{Axx}(i,A,\theta) + \mathrm{Ayy}(i,A,\theta)) + \sqrt{(\mathrm{Axx}(i,A,\theta) - \mathrm{Ayy}(i,A,\theta))^2 + 4(\mathrm{Axy}(i,A,\theta))^2}\right]$$

$$\mathrm{A2}(i,A,\theta) := \frac{1}{2}\left[\mathrm{Axx}(i,A,\theta) + \mathrm{Ayy}(i,A,\theta) - \sqrt{(\mathrm{Axx}(i,A,\theta) - \mathrm{Ayy}(i,A,\theta))^2 + 4(\mathrm{Axy}(i,A,\theta))^2}\right]$$

$$\mathrm{A3}(i,A,\theta) := \mathrm{Azz}(i,A,\theta)$$

$$\sigma t(i,A,B,\theta,a) := \left[\frac{1}{\left[(|\mathrm{A1}(i,A,\theta)| - k(i,B)\cdot \mathrm{A1}(i,A,\theta))^a + (|\mathrm{A2}(i,A,\theta)| - k(i,B)\cdot \mathrm{A2}(i,A,\theta))^a + (|\mathrm{A3}(i,A,\theta)| - k(i,B)\cdot \mathrm{A3}(i,A,\theta))^a\right]}\right]^{\frac{1}{a}}\cdot \mathrm{XT}$$

$$\sigma c(i,A,B,\theta,a) := \left[\frac{1}{\left[(|\mathrm{A1}(i,A,\theta)| + k(i,B)\cdot \mathrm{A1}(i,A,\theta))^a + (|\mathrm{A2}(i,A,\theta)| + k(i,B)\cdot \mathrm{A2}(i,A,\theta))^a + (|\mathrm{A3}(i,A,\theta)| + k(i,B)\cdot \mathrm{A3}(i,A,\theta))^a\right]}\right]^{\frac{1}{a}}\cdot \mathrm{XT}$$

12) Calculating flow stress along *x*, *y* axis under tension and compression

$$\sigma xxt(i,A,B,\theta,a) := \sigma t(i,A,B,\theta,a)\cdot \cos(\theta)^2$$

$$\sigma\mathrm{yyt}(i,A,B,\theta,a) := \sigma\mathrm{t}(i,A,B,\theta,a)\cdot\sin(\theta)^2$$
$$\sigma\mathrm{xyt}(i,A,B,\theta,a) := \sigma\mathrm{t}(i,A,B,\theta,a)\cdot\sin(\theta)\cdot\cos(\theta)$$
$$\mathrm{FXt}(i,A,B,\theta,a) := \mathrm{F'X}(i,A,B,\sigma\mathrm{xxt}(i,A,B,\theta,a),\sigma\mathrm{yyt}(i,A,B,\theta,a),\sigma\mathrm{xyt}(i,A,B,\theta,a),a)$$
$$\mathrm{FYt}(i,A,B,\theta,a) := \mathrm{F'Y}(i,A,B,\sigma\mathrm{xxt}(i,A,B,\theta,a),\sigma\mathrm{yyt}(i,A,B,\theta,a),\sigma\mathrm{xyt}(i,A,B,\theta,a),a)$$
$$\mathrm{FXYt}(i,A,B,\theta,a) := \mathrm{F'XY}(i,A,B,\sigma\mathrm{xxt}(i,A,B,\theta,a),\sigma\mathrm{yyt}(i,A,B,\theta,a),\sigma\mathrm{xyt}(i,A,B,\theta,a),a)$$
$$\sigma\mathrm{xxc}(i,A,B,\theta,a) := -\sigma\mathrm{c}(i,A,B,\theta,a)\cdot\cos(\theta)^2$$
$$\sigma\mathrm{yyc}(i,A,B,\theta,a) := -\sigma\mathrm{c}(i,A,B,\theta,a)\cdot\sin(\theta)^2$$
$$\sigma\mathrm{xyc}(i,A,B,\theta,a) := -\sigma\mathrm{c}(i,A,B,\theta,a)\cdot\sin(\theta)\cdot\cos(\theta)$$
$$\mathrm{FXc}(i,A,B,\theta,a) := \mathrm{F'X}(i,A,B,\sigma\mathrm{xxc}(i,A,B,\theta,a),\sigma\mathrm{yyc}(i,A,B,\theta,a),\sigma\mathrm{xyc}(i,A,B,\theta,a),a)$$
$$\mathrm{FYc}(i,A,B,\theta,a) := \mathrm{F'Y}(i,A,B,\sigma\mathrm{xxc}(i,A,B,\theta,a),\sigma\mathrm{yyc}(i,A,B,\theta,a),\sigma\mathrm{xyc}(i,A,B,\theta,a),a)$$
$$\mathrm{FXYc}(i,A,B,\theta,a) := \mathrm{F'XY}(i,A,B,\sigma\mathrm{xxc}(i,A,B,\theta,a),\sigma\mathrm{yyc}(i,A,B,\theta,a),\sigma\mathrm{xyc}(i,A,B,\theta,a),a)$$

13) Forming tension and compression model r-value response functions along arbitrary orientation *θ*

$$\mathrm{rtt}(i,A,B,\theta,a) := \frac{-\left(\sin(\theta)^2\cdot\mathrm{FXt}(i,A,B,\theta,a) - \mathrm{FXYt}(i,A,B,\theta,a)\cdot\sin(\theta)\cdot\cos(\theta) + \cos(\theta)^2\cdot\mathrm{FYt}(i,A,B,\theta,a)\right)}{\mathrm{FXt}(i,A,B,\theta,a) + \mathrm{FYt}(i,A,B,\theta,a)}$$
$$\mathrm{rc}(i,A,B,\theta,a) := \frac{-\left(\sin(\theta)^2\cdot\mathrm{FXc}(i,A,B,\theta,a) - \mathrm{FXYc}(i,A,B,\theta,a)\cdot\sin(\theta)\cdot\cos(\theta) + \cos(\theta)^2\cdot\mathrm{FYc}(i,A,B,\theta,a)\right)}{\mathrm{FXc}(i,A,B,\theta,a) + \mathrm{FYc}(i,A,B,\theta,a)}$$

14) Forming tension and compression model flow stress response functions for uniaxial, biaxial and shear loading conditions

$$\mathrm{XC}(i,A,B,a) := \left[\frac{1}{\left[\left(|\phi1(i,A)| + k(i,B)\,\phi1(i,A)\right)^a + \left(|\phi2(i,A)| + k(i,B)\,\phi2(i,A)\right)^a + \left(|\phi3(i,A)| + k(i,B)\,\phi3(i,A)\right)^a\right]}\right]^{\frac{1}{a}}\cdot\mathrm{XT}$$

$$\mathrm{YT}(i,A,B,a) := \left[\frac{1}{\left[\left(|\psi1(i,A)| - k(i,B)\,\psi1(i,A)\right)^a + \left(|\psi2(i,A)| - k(i,B)\,\psi2(i,A)\right)^a + \left(|\psi3(i,A)| - k(i,B)\,\psi3(i,A)\right)^a\right]}\right]^{\frac{1}{a}}\cdot\mathrm{XT}$$

$$\mathrm{YC}(i,A,B,a) := \left[\frac{1}{\left[\left(|\psi1(i,A)| + k(i,B)\,\psi1(i,A)\right)^a + \left(|\psi2(i,A)| + k(i,B)\,\psi2(i,A)\right)^a + \left(|\psi3(i,A)| + k(i,B)\,\psi3(i,A)\right)^a\right]}\right]^{\frac{1}{a}}\cdot\mathrm{XT}$$

$$\mathrm{ZT}(i,A,B,a) := \left[\frac{1}{\left[\left(|\Pi1(i,A)| - k(i,B)\,\Pi1(i,A)\right)^a + \left(|\Pi2(i,A)| - k(i,B)\,\Pi2(i,A)\right)^a + \left(|\Pi3(i,A)| - k(i,B)\,\Pi3(i,A)\right)^a\right]}\right]^{\frac{1}{a}}\cdot\mathrm{XT}$$

$$\mathrm{ZC}(i,A,B,a) := \left[\frac{1}{\left[\left(|\Pi1(i,A)| + k(i,B)\,\Pi1(i,A)\right)^a + \left(|\Pi2(i,A)| + k(i,B)\,\Pi2(i,A)\right)^a + \left(|\Pi3(i,A)| + k(i,B)\,\Pi3(i,A)\right)^a\right]}\right]^{\frac{1}{a}}\cdot\mathrm{XT}$$

$$\tau xy(i,A,B,a) := \left[\frac{1}{\left[\left(\left|C66(i,A)\right| + k(i,B)\,C66(i,A)\right)^{a} + \left(\left|C66(i,A)\right| - k(i,B)\,C66(i,A)\right)^{a}\right]}\right]^{\frac{1}{a}} \cdot XT$$

15) Forming the error function for optimization (weighting parameters can be included by multiplying a number into each component.

$$\begin{aligned}
\mathrm{Error}(A,B) := {} & \sum_{i=0}^{4} \left[(XC(i,A,B,6)) - Sigcex0(i)\right]^{2} + \sum_{i=0}^{4} \left(\sigma c\left(i,A,B,\frac{\pi}{4},6\right) - Sigcex45(i)\right)^{2} + \\
& \sum_{i=0}^{4} \left[(YC(i,A,B,6)) - Sigcex90(i)\right]^{2} + \sum_{i=0}^{4} \left(\sigma t\left(i,A,B,\frac{\pi}{4},6\right) - Sigtex45(i)\right)^{2} + \\
& \sum_{i=0}^{4} (\sigma t(i,A,B,0,6) - 1)^{2} + \sum_{i=0}^{4} (ZT(i,A,B,6) - sabt(i))^{2} + \\
& \sum_{i=0}^{4} (ZC(i,A,B,6) - sabc(i))^{2} + \sum_{i=0}^{4} (rtt(i,A,B,0,6) - rtex0(i))^{2} + \\
& \sum_{i=0}^{4} \left(rtt\left(i,A,B,\frac{\pi}{4},6\right) - rtex45(i)\right)^{2} + \sum_{i=0}^{4} \left(rtt\left(i,A,B,\frac{\pi}{2},6\right) - rtex90(i)\right)^{2} + \\
& \sum_{i=0}^{4} (rc(i,A,B,0,6) - rcex0(i))^{2} + \sum_{i=0}^{4} \left(rc\left(i,A,B,\frac{\pi}{4},6\right) - rcex45(i)\right)^{2} + \\
& \sum_{i=0}^{4} \left(rc\left(i,A,B,\frac{\pi}{2},6\right) - rcex90(i)\right)^{2} + \sum_{i=0}^{4} \left(\sigma t\left(i,A,B,\frac{\pi}{6},6\right) - Sigtex30(i)\right)^{2} + \\
& \sum_{i=0}^{4} \left(\sigma t\left(i,A,B,\frac{\pi}{3},6\right) - Sigtex60(i)\right)^{2} + \sum_{i=0}^{4} \left(rtt\left(i,A,B,\frac{\pi}{6},6\right) - rtex30(i)\right)^{2} + \\
& \sum_{i=0}^{4} \left(rtt\left(i,A,B,\frac{\pi}{3},6\right) - rtex60(i)\right)^{2} + \sum_{i=0}^{4} (\tau xy(i,A,B,6) - tau(i))^{2} + \sum_{i=0}^{4} (YT(i,A,B,6) - Sigtex90(i))^{2}
\end{aligned}$$

16) Introducing the initial guess

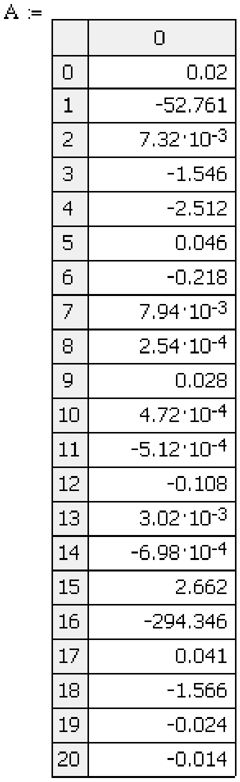

A :=

	0
0	0.02
1	-52.761
2	$7.32\cdot10^{-3}$
3	-1.546
4	-2.512
5	0.046
6	-0.218
7	$7.94\cdot10^{-3}$
8	$2.54\cdot10^{-4}$
9	0.028
10	$4.72\cdot10^{-4}$
11	$-5.12\cdot10^{-4}$
12	-0.108
13	$3.02\cdot10^{-3}$
14	$-6.98\cdot10^{-4}$
15	2.662
16	-294.346
17	0.041
18	-1.566
19	-0.024
20	-0.014

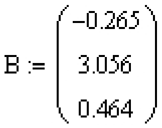

$$B := \begin{pmatrix} -0.265 \\ 3.056 \\ 0.464 \end{pmatrix}$$

17) Checking the initial error (smaller number indicate a more accurate fit; however, the global response of the model has to be checked)

Error(A,B) =

18) Setting the optimization constraints

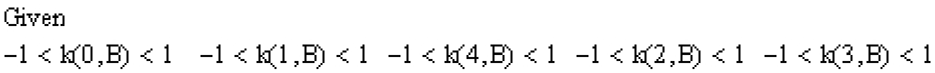

Given

$-1 < k(0,B) < 1 \quad -1 < k(1,B) < 1 \quad -1 < k(4,B) < 1 \quad -1 < k(2,B) < 1 \quad -1 < k(3,B) < 1$

19) Minimizing the error function and obtaining improved calibration parameters

$$\begin{pmatrix} A \\ B \end{pmatrix} := \text{Minimize}(\text{Error}, A, B)$$

20) *A* and *B* are improved parameters. This process should be repeated few times in a loop to reach a local optimum.